**School of Civil and Mechanical Engineering**

# Spatially-Varying Multi-degree-of-Freedom Electromagnetic Energy Harvesting

**Rathishchandra Ramachandra Gatti**

**This thesis is presented for the Degree of**
**Doctor of Philosophy**
**of**
**Curtin University**

**November 2013**

# Abstract

This thesis presents a novel theoretical modelling of a spatially varying multi-degree-of-freedom electromagnetic energy harvester. The unique research outcomes presented herein involved the design of an electromagnetic energy harvester using and manipulating two important physics phenomena: the spatial variation of a magnetic field and a multi-degree-of-freedom based inertial spring-mass damping mechanism.

The working principles of reported electromagnetic vibration energy harvesters are based on the generation of power, from electromagnetic induction, due to the relative periodic motion between electromagnetically active inertial masses. An example of this would be the movement of magnets relative to coils or the movement of coils relative to the magnets. One research question that arises from this is whether or not the isotropic variation of the magnetic field in the direction of the coil motion can beneficially alter the voltage to allow energy harvesting. This research proposes a novel topology of energy harvester involving the effective manipulation of the spatial variation of the magnetic field to obtain favourable voltage output characteristics.

Energy harvesters produce maximum power at resonant frequencies of the transduction mechanisms employed in their designs. A single degree-of-freedom system-based energy harvester characterised by a vibrating single transduction inertial mass typically has only one resonant frequency at which the power production is maximised. From the application perspective of the energy harvester, this is not a favourable proposition since the ambient vibrational sources are in general characterised by multiple frequencies of vibration. Hence, achieving multiple resonant frequencies for energy harvesters, also known as broadband energy harvesters, is a research area that requires further development. This research work proposes that by having multiple degrees-of-freedom, using multiple transduction inertial masses, maximum power across a broadband spectrum of multiple resonant frequencies may be achieved.

The research integrated two transduction mechanisms by including spatial variation of the magnetic field in the design of multi-degree-of-freedom energy harvesters, thus making a very versatile electromagnetic energy harvester model.

In order to gain an in-depth understanding of the spatial variation of the magnetic field, the focus was narrowed to an undamped single degree-of-freedom electromagnetic energy harvesting mechanism. This was then followed by research into single degree-of-freedom energy harvesting and two-degrees-of-freedom energy harvester models. Based on the simulation and experimentation results, a framework for designing multiple degrees-of-freedom energy harvesters was developed.

For both single degree-of-freedom energy harvester and two-degrees-of-freedom energy harvester models, the simulation approach was to initially develop linear models. This was done using the Laplace transform and state-space model techniques for predicting approximate voltage frequency responses, and for performing sensitivity analyses to predict the system's behaviour with respect to the design variables. This was followed by the use of nonlinear models in order to include spatial variation in the system. The nonlinear model solutions were provided by Runge-Kutta based ODE solvers.

To validate the theoretical simulations, the single degree-of-freedom energy harvester and two degree-of-freedom energy harvester prototypes were developed and experimented in the lab environment.

This research attempts to establish a mathematical foundation for the design and future development of multi-degree-of-freedom based energy harvesters.

# Declaration

To the best of my knowledge and belief, this thesis contains no previously published material unless any acknowledgement has been made in the form of stated references.

To the best of my knowledge and belief, this thesis contains no material which has been accepted for the award of any other academic degree or qualification in any university.

Signature

Date

*Dedicated to all those righteous people making this world the best place to live …*

# Acknowledgements

I would like to thank my supervisor A/Prof Ian M Howard for his motivation and valuable guidance throughout my research. Whilst often I would be diverted by related research ideas, his patience and guidance allowed me to keep the focus on my research topic. I am very grateful to him for imparting his technical knowledge regarding vibration, and for his research management wisdom. I owe him my deep thanks for providing me opportunities such as this scholarship, conference attendance and seminars, all of which have enhanced my knowledge.

I would like to thank Curtin University and its friendly staff for their support in my research. I am very grateful to the Australian government and tax-payers whose money was used to fund my research scholarship-Australian Postgraduate (APA) award. Thanks are also due to the Scholarships office, Curtin University for helping me to obtain this award.

I would like to convey my gratitude to the technical officers - Mr David Collier and Mr Russell Wilkinson for their help in manufacturing the prototypes. I would also like to thank Ms Kim Yap, for her enthusiastic support in my research-related activities such as arranging travel and conference attendances.

I would like to express my gratitude to my family including my father Ramachandra Gatti for his guidance throughout my life, my mother Kamala R Gatti, my wife Deeksha and my sister Roopa for their love and support.

Lastly, I would like to thank Mother (God) who has been my main driving force and the reason behind every good thing in my life.

**Rathishchandra R Gatti**

# Contents

# List of figures

# List of tables

# Glossary

**Ambient Energy Resources (AER)**

Energy resources in the vicinity of area of application of the energy harvested sensor. The energy harvester extracts the energy from the resource which is then converted to electrical energy to power the sensors**.**

Example: A generator's vibrations are the ambient energy resource for a remote condition monitoring sensor attached to the generator. A suitable vibration energy harvester would convert the AER to power the attached remote condition monitoring sensor.

**ANSOFT**

ANSOFT is an ANSYS FEA package for performing electromagnetic simulations and analyses. For details, visit

http://www.ansys.com/Support/Platform+Support/ANSOFT+Products+14.0

**Area of Application (AOA)**

Area of application is the area where the energy harvesters are able to produce power for powering sensors. Area of application is determined by two criteria – availability of AERs and requirement of sensors.

**Capacitive effect/electrostatic effect**

Voltage is generated due to the potential difference between two closely placed conductors with a dielectric medium in between.

**Coupling coefficient**

The common coefficient found when two separate linear/nonlinear ordinary differential systems are coupled to each other.

**CRO - Cathode-ray Oscilloscope**

Instrument used to visualise and measure electrical signals.

**EMVEH-Electromagnetic vibration energy harvester**

An energy harvester that converts the ambient vibrations into electric energy by the electromagnetic induction principle.

**FR4**

Glass-reinforced epoxy laminate sheet composed of epoxy-resin-bounded fibreglass cloth. Commonly used to make printed circuit boards. Highly flame-resistant.

**Frequency response**

Variation of a parameter or variable with reference to the frequency of the system. Usually, a plot with frequency on the x-axis and the variable under study on the y-axis.

**Impedance head**

Transducer used to measure acceleration and force. B&K impedance head 8001 is mounted directly to the exciter, and the body to be analysed is then mounted on the impedance head.

**Magnetostatics**

Study of magnetic fields of systems that have steady currents.

**Magnetostrictive effect**

The phenomenon of change in shape and size of ferromagnetic materials by the application of magnetisation.

**MEMS/NEMS - Micro-electromechanical systems/Nano-electromechanical systems**

These are electrical mechanical systems and structures at $10^{-6}$ to $10^{-9}$m level. These structures are manufactured using similar etching processes as for LSI/VLSI semiconductor chips.

**NdFeB - Neodymium magnet**

Made of rare earth element Neodymium, together with Iron and Boron. To date, this is the most common magnetic material used to make strong permanent magnets. The magnetic field strength of NdFeB is the highest of the permanent magnetic materials known to date.

**ODE45**

A solver in MATLAB that makes explicit the Runge-Kutta method to numerically solve nonlinear ordinary differential equations.

**OSI model – Open-Systems Interconnection model**

A communication model proposed by ISO for standardisation of the functions of communication systems consisting of 7 abstract layers. These 7 abstract layers are hierarchical, with the top layer being served by the layer below. The physical, data link and network layers are media layers and occupy the lower region, while the transport, session, presentation and application are the host layers and occupy the top portion of the OSI model.

**Parylene**

Polyxylene polymers formed by chemical vapour deposition. These polymers are typically used as either moisture barriers or as dielectric barriers in PCBs.

**Piezoelectric effect**

Accumulation of charge when mechanical strain is applied to certain crystals and ceramic materials. This effect is used to generate electric energy, or electricity is used to cause mechanical strain.

**Runge-Kutta method**

A system of implicit and explicit numerical methods for solving ordinary differential equations.

**Stack-up tolerance analysis**

Stack-up tolerance analysis is used to fix tolerances of mating assembly parts such that the target process capability is always achieved.

**TEDS Sensor –Transducer Electronic Data Sheet Sensor**

TEDS is a IEEE 1451.4 standard for storing transducer information in the transducer such that it is automatically recognised by devices such as data-loggers without the need for calibration.

**Time domain response**

Response or plot of a variable as a function of time.

**Undamped**

System without damping element.

**VEH-Vibration Energy Harvester**

An energy harvester that converts vibrations into electricity.

**Vibration exciter**

An instrument used to generate vibrations for required amplitude, frequency and waveform by connecting a waveform generator through a power amplifier to control the vibration response.

**Waveform generator**

An instrument used to generate signals for required amplitude, frequency and waveform.

**WSN-Wireless Sensor Node**

Also known as a mote, a wireless sensor node is the node that transmits and receives wireless signals. A typical wireless sensor node consists of a sensing element, a microcontroller, a receiver, transmitter and battery.

**Nomenclature of very commonly used terms**

M = Mass

D = Damping coefficient

K = Spring stiffness

R = Resistance

L = Inductance

C = Capacitance

**B** =Magnetic field strength

B = Magnitude of magnetic field strength.

T = Coupling coefficient.

X = amplitude of the output displacement of the inertial mass.

Y = amplitude of the input displacement of the EMVEH base.

The above terms are often used with suffixes to indicate several entities. Eg: $M_1$ = Mass 1 , $M_2$ = Mass 2.

MDK = Spring-mass-damper mechanical system.

MDKRL = Coupled spring-mass-damper mechanical system and resistance-inductance electrical system.

MDKRLC = Coupled spring-mass-damper mechanical system and resistance-inductance-capacitance electrical system.

**Scalar and vector notations:**

All displacement, velocity and acceleration vectors were unidirectional, hence only their magnitudes were relevant to the equations. Hence, they were considered as scalars throughout the thesis.

**For example:**

$\mathbf{B_x}$ = Magnetic field strength at position $x$ (vector).

$B_x$ = I $\mathbf{B_x}$ I = Magnitude of magnetic field strength at position $x$ (scalar).

**Units**

Unless otherwise specified, all the units mentioned in this thesis are SI units.

# Chapter 1 Introduction

One of the fundamental issues facing the electronics market today is the need to create electronics that are both small and powerful. This applies not only to handheld or household consumer electronics but also to industrial applications like remote monitoring sensors, instrumentation and controls. Whilst both consumer and industrial electronics emphasise portability, there is also the need for superior data quality, accuracy and high precision. Fulfilling these needs requires a greater memory capacity in electronics, and therefore increased power is needed. Hence the goal of power electronics research to create the "small and powerful" takes two approaches. The first approach is to (a) minimise power consumption and the second is to (b) maximise power per unit volume.

Low power consumption in the consumer and industrial electronics field can be achieved with efficient hardware that consumes less power, or by utilising efficient software with efficient algorithms. Current research into efficient hardware includes lower powered circuit designs like ultralow powered microcontrollers (TI, 2012) and Digital Signal Processing (DSPs) and other Very Large Scale Integration (VLSI) technologies. Current research into efficient software includes low powered computing that involves usage of efficient computing protocols with smaller memory and lower time requirements (Minartz, 2012).

The alternative approach of maximising power density can be achieved by high density power storage batteries like thin film batteries (Gambier, 2012) and super capacitors (Yuan, 2012). The power density maximisation approach was thought to be satisfactory until power electronics researchers found some key issues with the batteries. For example, with wireless sensor networks, the replacement of batteries was expensive and cumbersome. In addition, there were limitations in the stretching of the energy density of batteries. Despite this, research is still continuing into thin film NiMH batteries (Dudney, 2009). Another serious concern was found with regard to the hazardous materials used in the manufacture of batteries like NiMH and Pb (Notter, 2010; Chen, 2009). An effective way to solve this problem was found in the creation of an autonomous electronic system which generated its own power from the ambient environment, rather than relying on the replacement of

batteries. This breakthrough led to the birth of a new field of power electronics known as energy harvesting or energy scavenging.

Energy harvesting is important in many fields of low power electronics. Some of the areas where its widespread use is envisaged are as follows:

1. Portable consumer electronics: As the consumer features in mobiles, laptops and desktops increase, power consumption also increases. Mobile companies such as Nokia envisage the use of energy harvesting in mobile phones that would charge the phone from vibrations in the human body (e.g., Nokia Morph Concept, Nokia Research Centre, 2009).

2. Portable industrial electronics: There is an increasing need for portable measurement systems and data loggers for trade personnel to conveniently handle measurement data in a variety of places with increased accuracy along with improving their means of communication (Grant Instruments, 2012). Another serious concern is that of the power supply in measuring instrumentation in an industrial environment. This was often hardwired and exposed to harsh environmental conditions which led to insulation failures causing electrocution, equipment failures and fires (Flammini, 2009). The conversion of wired to wireless operation of the industrial sensors required batteries in each of the sensor nodes. This is one of the reasons why companies would not purchase wireless sensors to replace the conventional hardwired sensors. Moreover, battery operation in wireless systems was thought to be less reliable than the hardwired option, owing to the uncertainty of the wireless system battery life of the *N* number of batteries cascaded in the sensor network. This led to a great opportunity where energy harvesting could power the sensors whenever and wherever the equipment and instruments were in operation. Thus it could be possible to achieve highly reliable wireless sensor networks in industries.

3. Vehicle systems: Vehicle electronics are governed by internal Controller Area Network CAN networks (Leen, 2002) or similar field bus technologies that can be wired or wireless (Green, 2012). Vehicle systems are becoming more and more “intelligent” with more sensors on the vehicles and thus increased demand for power. Fortunately, there are various sources of waste energy in the vehicle, for example, vibrations which can be used to decrease the sensor power requirements. It is envisaged that in the future, vehicles will have advanced telematics where cars will be integrated with intelligent transport networks for the increased safety of vehicles and better control of increasing traffic congestion (Kolls, 2005).

Large trucks like road trains require more sophisticated proximity sensors and improved sensor networks for increased control (Ruff, 2007). Some companies like Google are envisaging cars which are entirely controlled by sensors, actuators and artificial intelligence algorithms, thereby relieving the driver of the need to control the vehicle (Golding, 2009; Hachman, 2011). Such advanced autonomous systems may require a high volume of automotive sensors that are intelligently networked by wireless networks.

4. Wireless sensor networks: Wireless sensor networks are gaining popularity over wired sensor networks in regions where the wiring of sensors is not economically or physically feasible (Gungor, 2009). As wireless sensors consume more power, energy harvesters would alleviate this problem.

There are several other areas such as medical electronics where energy harvesting can be used as an additional power resource for the powering of implants in the human body (Kerzenmacher, 2008; Zurbuchen, 2012). This current research is focused on the increasing need for powering wireless sensor networks.

## 1.1 Energy harvesting needs of wireless sensor networks

A wireless sensor network is generally based around a low-level wireless communication network using the 802.11 communication band, and it usually falls under only the physical and data link layers of the Open System Interconnection (OSI) seven layered communication model. It is not as advanced as other wireless communication networks such as Zigbee, Bluetooth and Wi-Fi since it has to be designed with less bits/sec owing to power limitations. A wireless sensor network is characterised by several wireless sensor nodes (commonly known as motes, nodes or Wireless Sensor Nodes (WSNs)) communicating with each other using the physical layer (Eren, 2005).

A typical WSN is shown in Figure 1.1 and consists of the following fundamental modules: (a) an ultra-low power microcontroller (such as Texas Instruments' MSP430 microcontroller which controls all the other components of the wireless sensor elements (TI, 2012)), (b) a signal communication module to receive and transmit digital signals to other WSNs. The signal communication module consists of a wireless transmitter (TXR) and receiver (RXR), (c) memory such as TI's FRAM to store the data to be transmitted/received along with any

other data that must be processed within the WSN (TI, 2012), (d) a sensor signal conditioner that converts and conditions the analog signals of the sensor or the array of multiple sensors (Eren, 2005), (e) a sensor or array of sensors used to sense the ambient environmental conditions of interest, and (f) energy-storage devices such as NiMH batteries. The self-powered WSN consists of two additional modules; an energy harvester module that converts energy from the ambient energy sources to electrical energy, and a power management module that converts the electrical energy generated by the energy harvester into an acceptable electrical energy input to the battery.

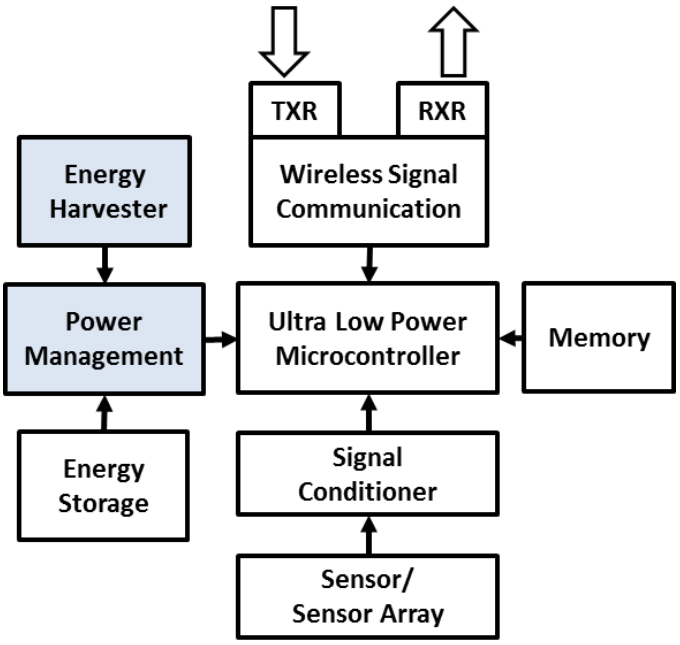


Figure 1.1 Typical wireless sensor node converted to self-powered wireless sensor node by adding energy harvester module and a power management circuit (TI, 2012; Eren, 2005).

## 1.2 Other technologies that motivate energy harvesting research

Some of the contemporary ongoing research areas which directly or indirectly support energy harvesting research and provide additional motivation for advancing energy harvesting research are:

- High density storage research: energy harvesters extract energy but do not store it, hence the need for rechargeable batteries. The advances in research into thin film batteries, super capacitors and Micro-Electro-Mechanical Systems (MEMS) storage devices (Pushparaj, 2007) show promise with regard to shrinking the size of WSNs.
- Ultra-low power microcontrollers: many ultra-low power microcontrollers for WSNs like Texas instruments' MSP430xx, Silicon Lab's C8051F9xx, ATMEL's ATmega165Pxx, and EM Electronics EM6812 focus on reducing power in the order of $10^{-9}$ to $10^{-12}$ A at 0.9-1.5V.
- Ultra-low power DSPs and Analog-to-Digital (A/D) converters: research has advanced into DSPs with regard to shrinking their power consumption. Texas Instruments' 16-bit DSP-TMS320C5000™ (TI, 2012) consumes as little as 0.15 mW/MHz at 1.05V and standby power is less than 0.15 mW but it has a high performance of up to 300MHz (600 MIPS) which extends the overall battery life. Recently Texas Instruments produced an audio capacitive touch booster pack (430BOOST-C55AUDIO1) (TI, 2012), that combines ultra-low power DSP C5000 with ultra-low power microcontrollers. These trends show promise with regard to future decreases in power consumption of WSNs.
- Power management devices for energy harvesters: power management chips for ultra-low power management are a promising trend which may lessen the power requirements of WSNs (Xinping, 2007).
- Energy efficient communication protocols for wireless sensor networks: these include energy efficient protocols such as LEACH (Low Energy Adaptive Clustering Hierarchy) that adapt randomised rotation of cluster heads to evenly distribute the energy load in the sensor network (Mu, 2010).

## 1.3 Energy harvesting sources and types of energy harvesters

Energy harvesting is possible provided two main conditions are met: (a) availability of ambient energy resources that can be harvested in the areas of application, and (b) the actual need for energy harvesting in the particular area of application. Consideration must also be given to economic and technical feasibility.

Until now, the main ambient sources of energy harvesting have been: light, heat, and vibration. For interior locations where sunlight is not available, the only two source options are heat and vibration since the area of research into indoor Photo-Voltaic (PV) cells is still in development. Most current energy harvesting research is focused on vibration. A typical energy harvester converts the ambient energy to the more useful form of electrical energy. The most common technologies which convert ambient vibrations to useful electrical energy are termed: the piezoelectric effect, the magnetostrictive effect, the electrostatic effect and electromagnetic induction. Solar energy harvesters and thermal energy harvesters are also able to convert ambient solar and thermal energy using the photoelectric effect and the thermoelectric effect respectively. It is also possible to harvest energy from radio frequencies emitted by TV signals and wireless radio networks and cell phone towers using floating gate transistor or electrostatic means. The different types of ambient sources and energy harvesters are summarised in Table 1.1 below.

Table 1.1. Types of fundamental energy harvesters.

| **Ambient energy Sources** | **Energy conversion principle** | **Basic types of energy harvesters** |
|---|---|---|
| Light | Photoelectric effect | Solar energy harvesters (SEH) (Win, 2010) |
| Heat/Temperature | Thermoelectric effect | Thermoelectric energy Harvesters (TEH) (Xin, 2010) |
| Vibration | Magnetic induction effect | Electromagnetic vibration energy harvester (EMVEH) (Zorlu, 2011) |
| | Electrostatic effect | Electrostatic vibration energy harvester(ESVEH) (Sidek, 2011) |
| | Magnetostrictive effect | Magnetostrictive vibration energy harvester(MSVEH) (Wang, 2008) |
| | Piezoelectric effect | Piezoelectric vibration energy harvester (PVEH) (Zimmermann, 2012) |
| Radio frequency | Floating gate transistor effect | Floating gate transistor diode RF energy harvester (FGRFEH) (Triet,2006 ) |
| | Electrostatic effect | Capacitive RF energy harvester (CRFEH) (Papotto, 2011) |

However, recent trends in energy harvesting research have been aimed at developing multi-physics models of energy harvesters. These are also known as hybrid energy harvesters and they can generate energy from more than one source such as thermal-vibration energy and solar-thermal energy. It can occur that the combination of two different physics principles will harness only one specific form of ambient energy. A typical

example would be combining piezoelectric and electromagnetic energy to harvest vibrations (Fang, 2011).

## 1.4 A typical electromagnetic vibration energy harvester

The research proposed in this thesis focuses on the development of an Electromagnetic Vibration Energy Harvester (EMVEH). The working principle of the EMVEH is electromagnetic induction which is based on converting the periodic harmonic vibrational energy by moving the coil/magnet relative to the magnet/coil, as illustrated in Figure 1.2.

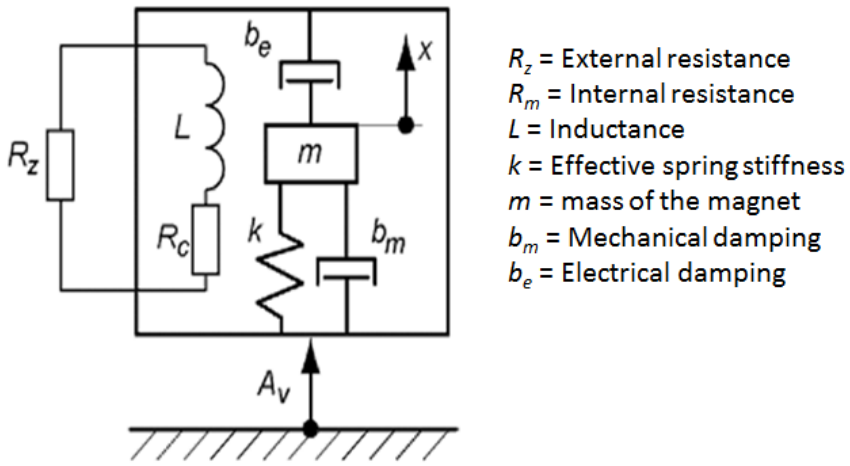


Figure 1.2 Schematic of a basic EMVEH (Beeby, 2009).

## 1.5 Degrees of freedom in an electromagnetic vibration energy harvester

The minimum number of independent coordinates required to completely determine the position of all parts of a system at any instant defines the degree-of-freedom of the system (S Rao, 2004). This thesis deals with unidirectional energy harvesters where the only moving parts are the coils. These coils are constrained by springs such that they form a

prismatic pair with only one translational motion. Hence, the only space vector considered here for moving parts is the translation along the x-axis while all the other movements are constrained. Hence, for the EMVEH systems considered in this thesis, the number of degrees of freedom is defined by the minimum number of coordinates used to describe the motion of moving parts along the x-axis. When only one coil is present, the position of the coil $X_1$ is the only coordinate; hence the system is a one-degree-of-freedom system. When the EMVEH has two coils, coaxial to each other and forming a prismatic constraint with the coaxial ring magnets, it can be defined by a minimum of two coordinates $X_1$ and $X_2$, hence it is a two-degree-of-freedom system. When several such coaxial coils exist in an EMVEH, they require multiple numbers of coordinates to define the dynamic motion, hence the name multi-degree-of-freedom system.

The naming convention used for the energy harvesters in this thesis is as shown in Figure 1.3. Throughout the thesis, only one-directional EMVEHs are considered. The use of multi-directional notation in the nomenclature is kept as an option for future research.

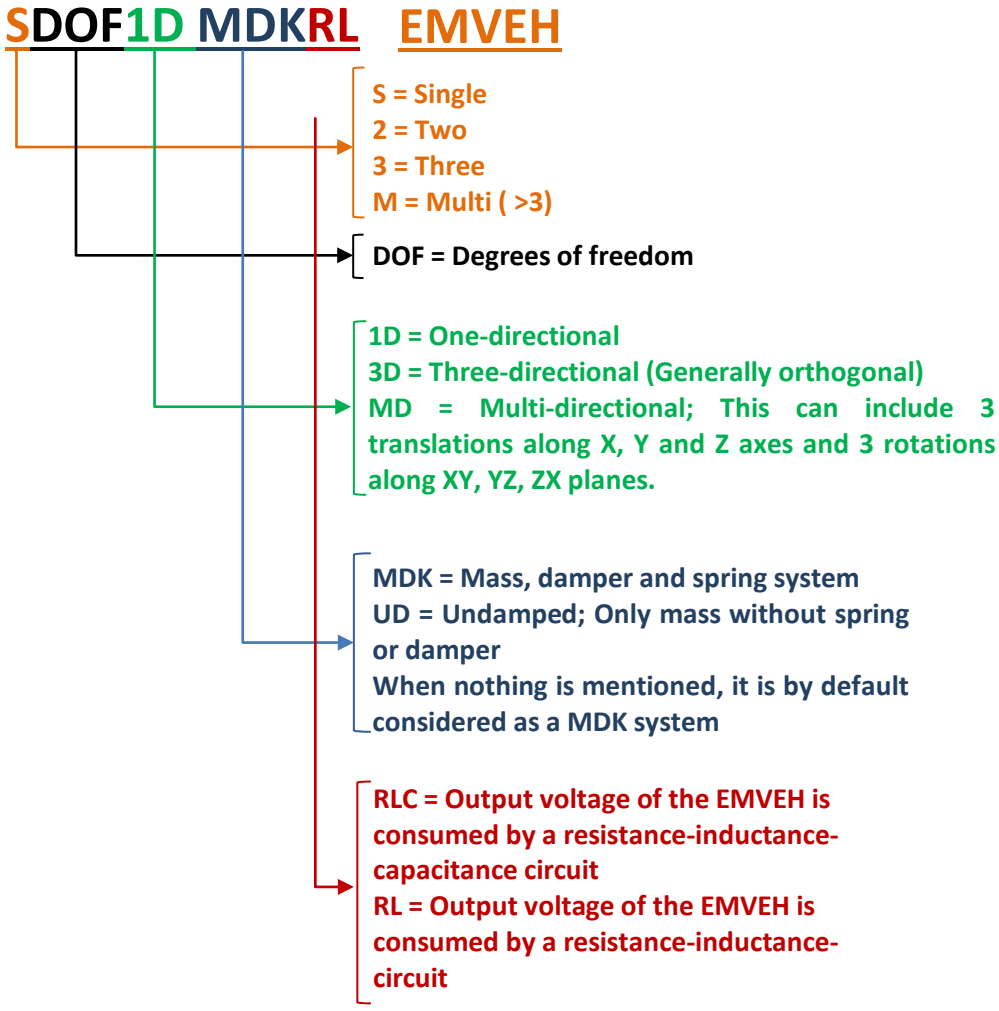


Figure 1.3 EMVEH nomenclature used in this thesis.

## 1.6 Research methodology

The research commences with a literature review of current research in vibration energy harvesting along with formulation of the research topic and its objectives, as discussed in Chapter 2 (see Figure 1.4). In the literature review, it was identified that the EMVEH was a viable option for research compared to other methods. Further literature research was conducted in order to identify possible research challenges regarding EMVEHs. The investigation indicated that the multi-degree-of-freedom system had not been considered as a viable option for modularising the design of the EMVEH. Moreover, the spatial variation of the magnetic field had not been seriously considered as another option for broadband energy harvesting. Hence the research topic chosen was "spatially-varying multi-degree-of-freedom electromagnetic vibration energy harvester". A step-by-step research methodology was designed to study the EMVEH from the simple Single-Degree-of-Freedom-One-Directional EMVEH (SDOF1D EMVEH) aspect to the more complex Multi-Degree-of-Freedom-One-Directional EMVEH (MDOF1D EMVEH).

Following the formulation of the research, investigations were then undertaken into the most basic model of the EMVEH; the undamped SDOF1D EMVEH (Chapter 3), where the spatial variation of the magnetic field was explored to ascertain its use for modularising the EMVEH design. The mathematical model was validated by experiment, showing that the spatial variation in the magnetic field was an effective design parameter for controlling the voltage output of the EMVEH.

The complete form of SDOF1D EMVEH was the damped SDOF1D EMVEH (Chapter 4) with springs attached to the base to control the natural frequency of the EMVEH. The linear Laplace transform analyses and state space analyses were performed without considering the spatial variation. This was followed by the more accurate nonlinear Runge-Kutta method to obtain the theoretical time responses (of vibration and current). Two alternative designs of the coil (single and split coils) were studied to find the best method of coil design for future developments.

The next step was the development of a 2DOF1D EMVEH (Chapter 5) that represented the fundamental multi-degree of freedom system. The linear and nonlinear analytical models were developed along similar lines to the already validated SDOF1D EMVEH. Once the theoretical models of SDOF1D and 2DOF1D EMVEHs were analytically simulated, a number

of sensitivity analyses were performed to analyse how these models behaved when each of the design parameters varied (see Chapter 6). Each sensitivity test consisted of a detailed analysis of the behaviour of the voltage output frequency response for a range of variations of one-design parameters considering the other design parameters as constants.

The next step was to experimentally validate the SDOF1D and 2DOF1D EMVEH system (Chapter 7) before concluding that the mathematical models were correct and could be generalised and extrapolated to a multi-degree of freedom system with a large number of springs and coils.

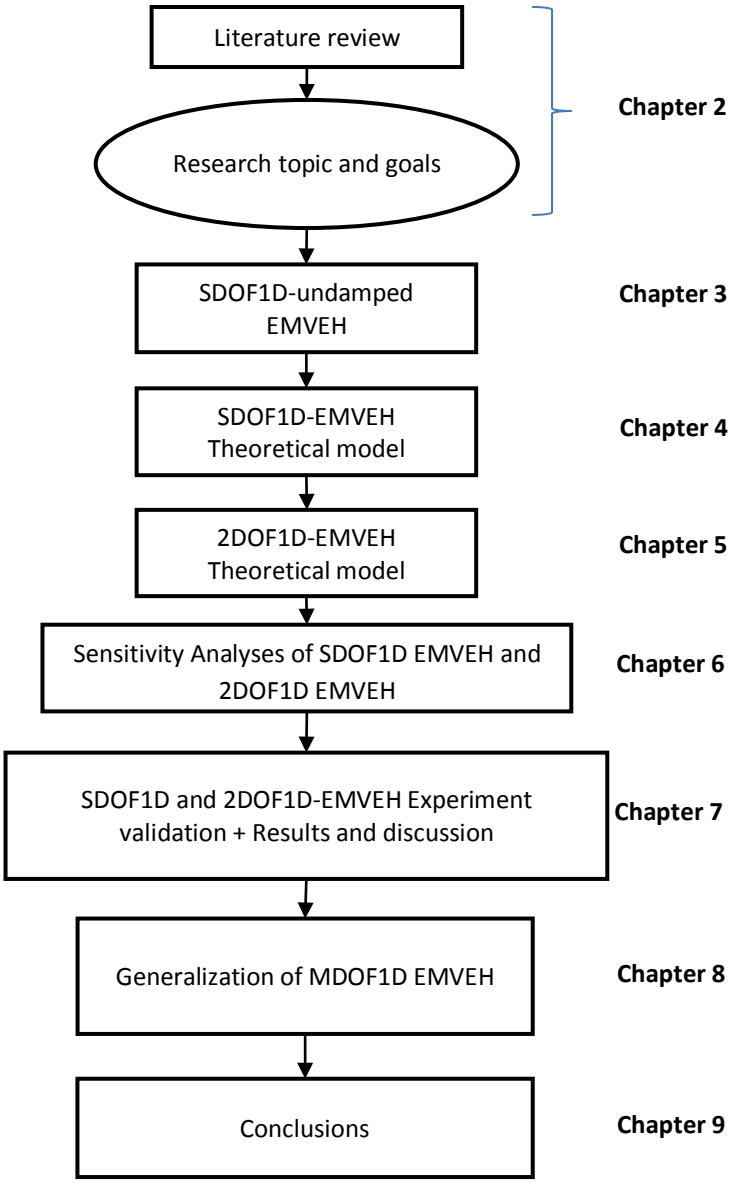


Figure 1.4 Research Methodology.

To validate the systems, two robust prototypes were developed, an SDOF1D EMVEH and a 2DOF1D EMVEH, taking into consideration the practical design values encapsulated by the tolerances obtained from stack-up tolerance analyses. Three sets of experiments were run to obtain the experimental time responses of motion, current and voltage. It was found that the experimental values matched very well with the theoretically obtained values. From the comparison of theoretical and experimental results, some interesting conclusions were drawn indicating how these models can be extrapolated to Multi-Degree-Of-Freedom (MDOF) systems.

The analytical and experimental validation of the SDOF1D and 2DOF1D models prompted the research to generalise the model to MDOF systems (see Chapter 8). For simplicity, a 4DOF1D EMVEH was considered to obtain a mathematical model that was extrapolated to the MDOF1D. The multiplicities of directions were then assumed for the MDOF MD model. The validation of MDOF EMVEH prompted the research to employ this new theory in order to apply it to some of the immediate needs of the research. Due to time and resource constraints, only CAD models and brief details on how they can be applied to solve the commercial problems were documented (see Chapter 9: Conclusions and scope for future work). All MATLAB codes, ANSOFT FEA files and results, and the prototype drawings were recorded in Appendices - with a view that they may be of some help in future related research.

## 1.7 Research output

The main output of this research was the achievement of a modular design of EMVEH that considers the multi-degree of freedom system with due consideration given to the spatial variation of magnetic fields for increased power harvesting. A systematic approach of mathematical modelling of this versatile EMVEH ranged from that of a very basic undamped EMVEH to a damped multi-degree of freedom EMVEH. This was carried out in order to gain a systematic insight into the behaviour of the mechanical design parameters including coil masses, spring constants and damping coefficients along with electrical parameters such as number of coils, coil length, load resistance and coil inductance.

Initially both the SDOF1D and MDOF1D were roughly modelled as linear models using the Laplace transform method and state space method. This was followed by more accurate

nonlinear modelling using the Runge-Kutta method. This approach was also an attempt to establish a computational framework for the future design of EMVEH energy harvesters.

# Chapter 2 Current research into energy harvesting

A comprehensive literature review was conducted into the existing literature regarding energy harvesting. This was undertaken in order to identify the research challenges that exist and to learn more about the different research methodologies and approaches used to overcome these challenges. The literature research led to the formulation of the research topic and its corresponding hypothesis by matching the existing research challenges with available technologies used to solve them.

## 2.1 Literature research methodology

The literature review was conducted as follows:

1. The energy requirements for vibration energy harvesters (VEHs) were reviewed. The objective of this step was to identify sources of vibrations in differing ambient environments to ascertain the amounts of energy available for harvesting.

2. A comparison of different types of VEHs was made and their relative advantages and disadvantages identified. It was found that electromagnetic vibration energy harvesting (EMVEH) was a viable topic of research interest.

3. The current research challenges specific to EMVEHs were identified, along with the most effective research methods and techniques. This step also identified unmet research needs regarding EMVEHs and prompted ideas of possible ways to meet them. Again, this discovery assisted in the formulation of the research topic.

4. Finally the research was formulated, after careful consideration and identification of the unmet research needs mentioned above. The research project's scope and specific research objectives were formulated. A research hypothesis was developed which formed the basis for the entire research described in this thesis. To ensure that this research topic was unique, a prior-art search was conducted to narrow the scope of the topic.

## 2.2 Vibration energy harvesting sources

Two important factors that are necessary for effective energy harvesting are the type of power available (light, heat, vibration) and the power density (power/volume) of the corresponding energy harvester technology. A generic comparison of power density is as shown in Table 2.1.

Table 2.1 Energy and power source comparison (Poulin, 2004).

| Power source | Power ($\mu W$)/cm$^3$ | Energy (Joules)/cm$^3$ | Power ($\mu W$)/cm$^3$/yr |
|---|---|---|---|
| Primary battery | N/A | 2,880 | 90 |
| Secondary battery | N/A | 1,080 | 34 |
| Micro fuel cell | N/A | 3,500 | 110 |
| Ultracapacitor | N/A | 50–100 | 1.6–3.2 |
| Heat engine | $1 \times 10^6$ | 3,346 | 106 |
| Radioactive ($^{63}$Ni) | 0.52 | 1,640 | 0.52 |
| Solar (outside) | 15,000* | N/A | N/A |
| Solar (inside) | 10* | N/A | N/A |
| Temperature | 40*† | N/A | N/A |
| Human power | 330 | N/A | N/A |
| Air flow | 380‡ | N/A | N/A |
| Pressure variation | 17§ | N/A | N/A |
| Vibrations | 375 | N/A | N/A |

The key requirement for deploying wireless sensors over a much wider coverage area in an industrial environment is the presence of ambient energy sources that can be harvested by the energy harvesters embedded to the wireless sensors. For indoor applications, light energy harvesters are not as efficient as vibration, thermal and airflow energy harvesters. Heat engines and airflow are the next best ambient energy sources, but they are not widely found in the industrial environment. In industrial scenarios, most of the machines that have moving parts (especially rotating machinery that needs to be remotely monitored) by default produce vibrations. Table 2.2 details the common vibration sources from machines and their amplitude and frequency range (B&K, 1993).

Table 2.2 Sources of vibration from machinery: amplitude and frequency range.

| Industrial vibration sources | Acceleration ($ms^{-2}$) | Frequency range |
|---|---|---|
| Heavy structural and seismic vibration: Buildings, Ship hulls | 0.1 to 3 | 0.1 Hz-1 kHz |
| Heavy industrial vibration-rotating machinery, jet engines | 0.1 to $10^3$ | 5 Hz-5 kHz |
| Light industrial vibration-domestic appliances, light machines | 1 to $10^4$ | 5 Hz-5 kHz |
| Light structural, medium to high level vibration-thin panels in confined spaces | 1 to $10^4$ | 2 Hz-25 kHz |
| Very high level vibration-hand pneumatic tools, engine valves | 1 to 3 X $10^5$ | 0.001 Hz-60 kHz |

An experimental study was conducted by Gilbert (2008), in order to analyse the vibrations in consumer products, machine tools and cars. It was observed that the majority of vibrations were within a 0.2 $ms^{-2}$ acceleration range with a frequency of less than 100 Hz. Some sources outside this range would be products like blenders and grinding machines. The measured ambient vibration can also be found in Real vibrations database - an online ambient vibration database presented by NISP Labs, Italy (Wang, 2007). A brief summary of the power spectral data in the Real vibrations database of common sources of vibration is summarised in Figure 2.1 below. It can be observed that most of the ambient sources of vibration were either within machines (such as engines, generators and motors) or in structures (such as buildings). Most of the machines and structures also required sensors and wireless sensor networks for intelligent condition monitoring. Powering sensor nodes by batteries alone has become expensive and is impractical for installations with a large number of sensor nodes. This indicates the need for sensor nodes to be self-powered (Chandrakasan, 1998). This can be done by scavenging the available ambient energy (generally vibrations) and coupling it with battery use and suitable power management systems. Also to be considered is the trend toward decreasing power consumption of WSNs (wireless sensor nodes) due to advancements in VLSI and the low-duty cycles of WSNs (Roundy, 2003; Vullers, 2010). All of the abovementioned factors have necessitated the recent research into energy harvesting.

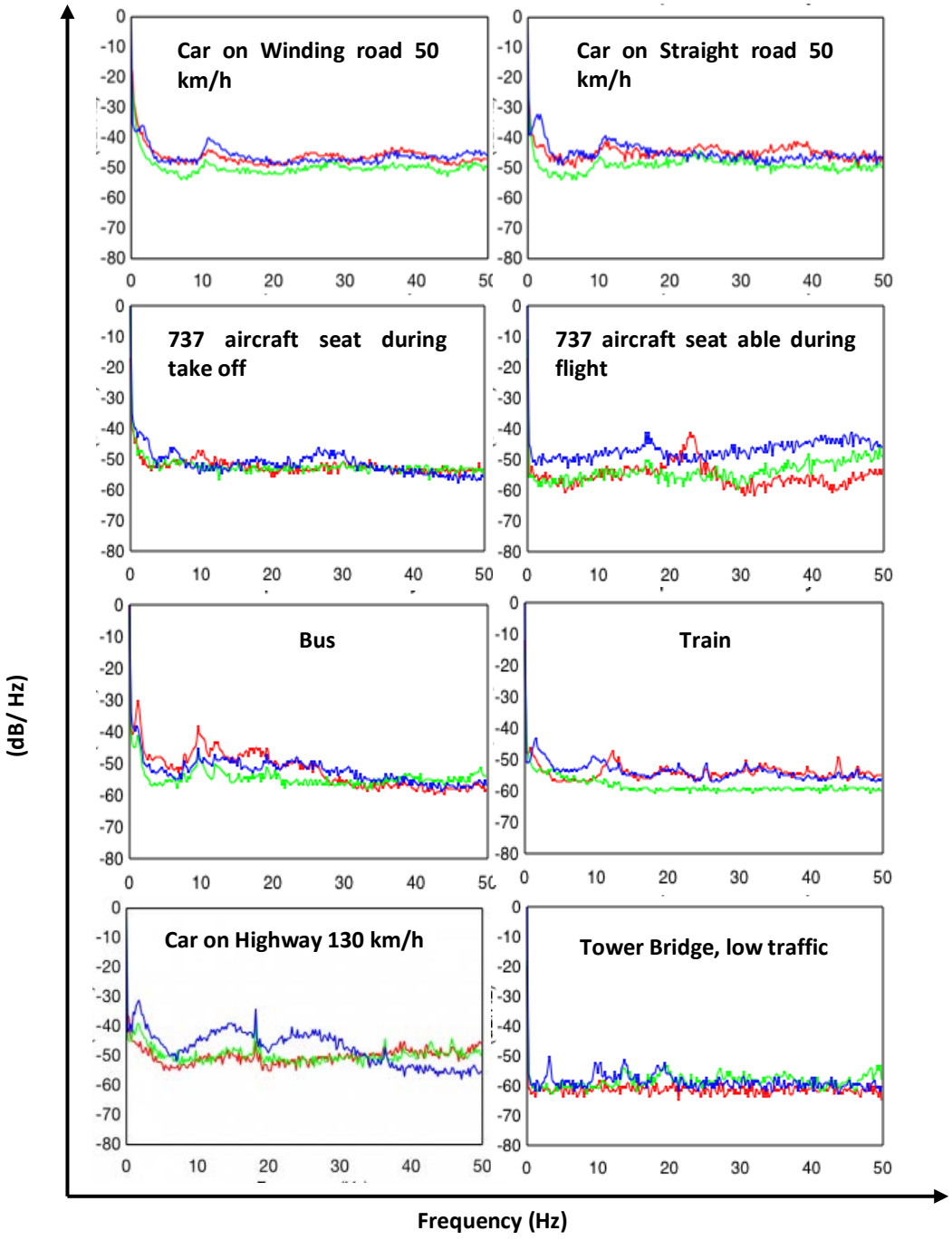


Figure 2.1 Power spectrum data of different sources of vibration extracted from NISP labs Real vibrations database (Real vibrations database, NISP Labs, 2012).

## 2.3 Comparison of vibration energy harvesters

The conversion of vibrational energy to electrical energy can be achieved by employing different transduction methods. Different types of energy harvesters are based on different types of transduction mechanisms. The types and advantages and disadvantages of these vibration energy harvesters are discussed further below.

### 2.3.1 Fundamental types of energy harvesting

Currently, there are four main types of vibration energy harvesting devices, namely piezoelectric, electrostatic, magnetostrictive and electromagnetic (Vullers, 2010). The most widely used vibration energy harvesting method is that of the piezoelectric, due to its scalability to nano levels (Falconi, 2009; Wang, 2007). When piezoelectric materials are subjected to mechanical stress induced by vibrational movement, an electric charge is created (Falconi, 2009; Fang, 2006; Feenstra, 2008; Ferrari, 2008; Howells, 2009; Kuehne, 2008; Lefeuvre, 2006; Liu, 2008; Minazara, 2006). When vibration is used to move one of the electrodes of a capacitor while keeping the other relatively fixed, the difference in capacitance creates electrostatic energy (Kuehne, 2008; Dragunov, 2012; Salem, 2007). This is the principle of electrostatic or capacitive energy harvesting. Another method of energy harvesting is magnetostrictive vibration energy harvesting which uses the Villari effect, where mechanical vibration-inducing strain on MsMs (magnetostrictive materials) like Metglas2605SC result in changes in magnetisation (Wang, 2008) thus generating electrical voltage.

Electromagnetic harvesting relies on electromagnetic induction created by the relative velocity between a coil and a magnet due to vibration-induced motion (Glynne-Jones, 2004). Power harvesting of human kinetic energy using magneto hydrodynamics has also been documented (Jia, 2009), where the changing magnetic fields due to fluid movement is exploited to harvest energy. The use of multi-pole magnet-based topology for EMVEHs has been discussed for both rotating EMVEHs and linear EMVEHs. Recently, Roundy & Takahashi (2013) introduced fine pitch multi-polar magnetic sheets that generate a voltage of 3V. This type of topology is very beneficial for thin film technologies.

### 2.3.2 Comparison of energy harvesters

Currently, there is no accurate information on which energy harvesting method is preferable with regard to a particular scale, although some experimental work has made comparisons between the four methods described previously in Section 2.3.1. Researchers are of the opinion that piezoelectric and electrostatic implementations are suitable for micro and nano-scales owing to their suitability for MEMS fabrication, whereas electromagnetic and magnetostrictive energy harvesting is effective at millimetre scale level. This is due to the practical limitations with regard to the manufacturing of magnets and coils on a micro-scale. Beeby (2006), and O'Donnell (2007), similarly suggest that micro fabricated coils generally have increased coil resistance, thus limiting energy harvesting performance. A consolidated analysis of comparisons in different reviews (Poulin, 2004; Wang, 2007; Beeby, 2006; Gilbert, 2008) is summarised in Table 2.3.

Table 2.3 Consolidated summary of comparison of different types of vibration energy harvesters ( Poulin, 2004; Wang, 2007; Beeby, 2006; Gilbert, 2008).

| | **Electromagnetic** | **Piezoelectric** | **Electrostatic** | **Magnetostrictive** |
|---|---|---|---|---|
| **Displacement** | High. | Low. | Low. | Low. |
| **Voltage** | Low voltage but adjustable. | High voltage (2-10 V). | Very high (>100 V). | Adjustable. |
| **Current** | Adjustable but typically high. | Low. | Very low. | Adjustable. |
| **Resonant frequency** | Adjustable. | High. | Adjustable. | High. |
| **Output impedance** | Resistive (Low). | Capacitive, typically very high (>100 kΩ). | Very high. | Not specified in literature. |
| **Adapted load** | Adjustable | High. | Adjustable. | Not specified in literature. |
| **Mechanical limitations** | Bulky size of magnets and coils. | Required to be strained directly and therefore their mechanical properties will limit the overall performance and lifetime. | Decreasing the distance between plates increases energy density and makes it suitable for MEMS Scale. But, decreasing the area of plates decreases energy density. | High power density. |
| **Transduction efficiency/ Coupling coefficient** | Limited by magnetic field of permanent magnets and the flux linkage | Limited by piezoelectric properties of materials employed; High. | Transduction efficiency is limited by distance between plates, area of plates and input voltage. | Ultra high coupling coefficient >0.9. |
| **Use of force and impact coupled harvesting applications** | Difficult. | Easy. | Difficult. | Difficult. |
| **Material economics** | Can be made from simple materials. | Special smart materials required. | Can be made from simple materials. | Need smart materials. |
| **External voltage source** | No external voltage source. | No external voltage source. | Requires external voltage source. | No external voltage source. |
| **Energy/Volume** | Bulky. | Compact. | Compact. | High flexibility. |
| **MEMS/NEMS scale fabrication** | Difficult. | Easy. | Easy. | Difficult. |

### 2.3.3 Motivation for choosing electromagnetic vibration energy harvesting

There are a number of reasons for choosing electromagnetic vibration energy harvesting, foremost that EMVEHs are economical to manufacture. As can be seen in Table 2.3 above, electromagnetic and electrostatic VEHs do not employ expensive "smart" materials, unlike magnetostrictive and piezoelectric VEHs. Although electrostatic VEHs have proven to be cheaper than electromagnetic EMVEHs, they require external excitation. Hence, the electromagnetic device is the most economical when considering the above factors.

Electromagnetic machines are highly scalable, from macroscopic generators and wind turbines to microscopic electromagnetic energy harvesters abiding by the same basic electromagnetic principles for transduction. Hence any outcomes from this research relating to electromagnetic principles for transduction can possibly be applied to a range of these products. Despite its disputed drawbacks of non-scalability to micro level, electromagnetic energy harvesting is a favourable alternative for millimetre scale sensor applications. Thus any novel method of energy generation can be applied from micro-scale to macro-scale products. Some advances in micro-powered EMVEHs such as the bulk micro-machined EMVEH (Park, 2010) etched using the low-cost KOH wet-etching method, and advances in the micro-machining of NdFeB Magnets (Jiang, 2011), and their improvisation by NdFeB polishing (Miki, 2012) show promise for overcoming the limitations of MEMS Scale fabrication of EMVEHs.

EMVEH technologies are complementary to other electromagnetic energy harvesting technologies including Radio Frequency (RF) energy harvesting, energy harvesting from power cables (Bhuiyan, 2010) and wireless energy transfer. Although RF energy harvesting differs from vibration harnessing, it is based on electromagnetic energy and therefore may possibly be used in conjunction with EMVEH. Wireless energy transfer is another technology, where batteries within a human body implant can be powered by wireless means, using the principles of mutual induction (Shuenn-Yuh, 2012). A body implant with EMVEH can also be used in conjunction with wireless energy transfer to power the batteries when the EMVEH within is not able to generate enough power. Figure 2.2 shows the algorithm and the schematic of such a body implant. To date, no research has been reported in this area.

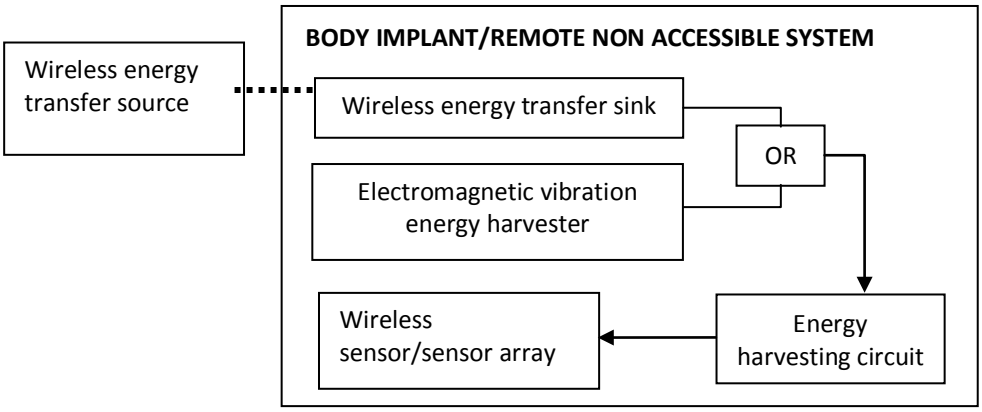


Figure 2.2 Schematic of wireless energy transfer as a parallel redundant system with electromagnetic energy harvester.

The power characteristics of EMVEH have the advantages of low output impedance and adjustable but high current. However, these are offset by the drawback of very low voltage (Beeby, 2009). Electromagnetic energy harvesting can harness various sources of motion energy such as those from wind, wave and human motion. From a vibrational energy perspective, EMVEHs are the best VEHs for harnessing large amplitude, low frequency vibrations that constitute major sources of industrial and structural vibrations (Shen, 2012). Large scale fluidic energy can be harnessed by rotary stator-rotor as observed in wind turbines and water turbines. On a smaller scale, fluid energy can be harnessed by linear energy harvesting mechanisms like the Humdinger wind energy generator (Pimentel, 2010; Frayne, 2009), aero-flutter generator (Ramasur, 2012) or Karman-vortex based EMVEHs (Wang, 2012). Energy from road vibrations can similarly be harvested by novel energy harvesting damping systems in vehicles, as suggested by Zhu (2012). A magneto-rheological damper has also been suggested by Sapiński (2010). EMVEHs can also be built within tyres (Bonisoli, 2010) and on engine blocks (Glynne-Jones, 2004) to harvest energy that can be useful for powering wireless sensor networks within automobiles. A bulk micro-machined EMVEH for harvesting power from human motion was reported to produce 115.1µW at a 54Hz resonance at a voltage of 68.2 mV (Park, 2010).

The main challenge to be addressed in adopting EMVEH is to increase its output voltage. EMVEHs in general have a very low voltage (<1V) owing to their high current. Another important challenge to be addressed is the narrow bandwidth of the operation of resonant generators in general. Typically, a resonance based generator (piezoelectric,

electromagnetic or electrostatic) has only one or a few excitation frequencies, based on the spring elements. Hence, the resonance generator generates maximum power when the vibration that excites it approaches the appropriate resonant frequency. With no resonance conditions, it generates almost zero power. This issue of negligible power during non-resonant conditions has been addressed by researchers using different approaches including the design of broadband frequency VEHs (Sari, 2008), tuneable frequency VEHs (Zhu, 2010), nonlinear resonance (Kai Sun, 2012) and frequency up-conversion methods. The motivation for the research in this thesis was aimed at overcoming these two major drawbacks of EMVEHs - low voltage and lack of broad range of resonant frequencies for maximum power.

## 2.4 Review of current research in electromagnetic vibration energy harvesting - accomplishments and opportunities

The history of the electromagnetic generator dates back to 1831 when Michael Faraday invented the Faraday disk, the first electric generator. The earliest electromagnetic vibration energy harvester was discussed by Williams et al.,(1996) and many transduction mechanisms have been invented since. Trends in construction and strategies for optimum designs have been discussed here.

### 2.4.1 Construction of EMVEHs

There are three topologies of electromagnetic power generators that are generally considered by researchers and authors (Khaligh, 2010). These are shown in Figure 2.2 below and consist of: (a) linear generators that operate in an oscillating mode; found in EMVEHs including wave power generators, (b) rotational generators actuated by a steady torque; such as wind turbines, and (c) hybrid generators that convert both linear and rotational motion into useful energy.

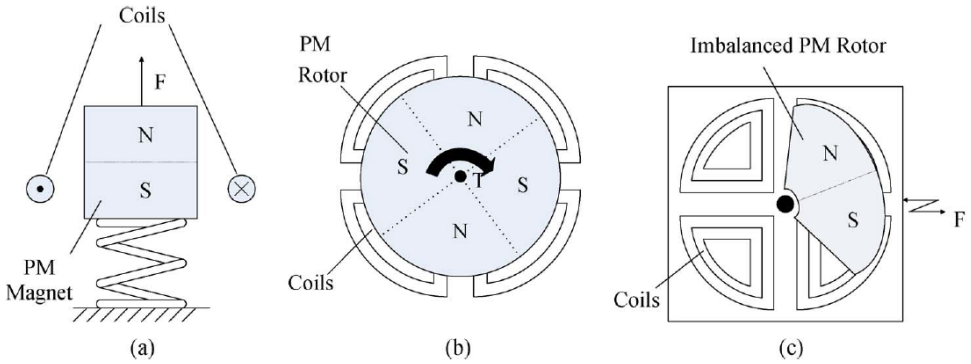


Figure 2.3 Three different categories of EMVEH topologies, namely: (a) Resonant generator operating in oscillating mode under vibration force. (b) Rotational generator operating under steady torque. (c) Hybrid generator to convert linear motion into rotational motion. (Khaligh, et al., 2010).

To date, the linear topology as shown in Figure 2.3 (a) has been employed in most EMVEHs since it is most suitable for resonant transductions from ambient vibrations typically characterised by low frequency and high amplitudes. A resonant linear generator typically consists of three elements, a spring element, a damping element and an active inertial mass. A comprehensive review of the materials being used for EMVEHs has been discussed by Chye (2010).

The conversion of flow-induced vibrations is a relatively new strategy for the harvesting of kinetic energy from fluid motion. Wang, Chiu, & Pham (2012), proposed an EMVEH that would generate around 1.77µW of power from vibration induced by the Karman vortex street flow on a bluff body based energy harvester with volume of 37.9 $cm^3$ (which is caused by repeated patterns of swirling vortices). An electromagnetic energy harvester consisting of a coil and magnet in a 6 inch long tube to be integrated inside the blade structure of turbine blades was reported by Joyce, Farmer, & Inman (2013), to have generated 3.3mW of power at 44 RPM. Zhongjie, Lei, Luhrs, Liangjun, & Yi-xian, (2013) proposed a retrofit regenerative suspension system that consisted of a rack and pinion arrangement to convert linear vehicular vibrations to rotational motion and an internal gearbox within the shock absorber to amplify the rotational energy and feed the built-in generator to produce electricity of about 67W(peak) /19W(average) at 48km/h.

The use of multi-pole magnet-based topology for EMVEHs has been discussed for both rotating EMVEHs and linear EMVEHs. Recently, Roundy et al (2013) introduced fine pitch

multi-polar magnetic sheets and planar coils that generate a voltage of 3V. This type of topology is very beneficial for thin film technologies.

A hybrid EMVEH that generates electric energy from the electromagnetic field of a current-carrying conductor, proposed by Misa et al (2013), uses a simple configuration of piezoelectric material sandwiched between 2 NdFeB magnets. When the NdFeB magnets interact with the magnetic field of the current-carrying conductor, the piezoelectric material is actuated, generating electricity.

The spring element in an EMVEH may be helical, spiral, flat or pneumatic (Khan, 2010). Most micro-EMVEHs have been designed with cantilever beams as springs. Recently, magnetic springs which have magnetic repulsion of like poles have been used in EMVEHs (Kai Sun, 2012). The materials used in helical, spiral and planar springs include copper and steel, whereas the cantilever/beam/paddle springs employ a variety of materials like titanium 55-Ni-45-Ti alloy, silicon, parylene, polymethyl methacrylate (Bouendeu, 2011), acrylic (Yang, 2009), FR4 substrates (Hatipoglu, 2010), and copper and steel. Kapton® membrane has also been used as a spring in a Si-Technology EMVEHs (Fondevilla, 2008).

The damping element in EMVEHs is usually that of viscous damping, due to the presence of the air in-between the coil and magnet, and it may also include Coulomb friction damping. The active inertial mass element is either a magnet or coil, or a mass attached to magnet or coil. Either the coil is surrounded by the magnet or vice-versa, such that there is always a transduction mechanism involving electromagnetic induction due to relative motion. Most of the EMVEHs reported so far use powerful NdFeB magnets. Barton (2010), suggested the use of highly permeable magnets having nonlinear characteristics, and iron cored stators over air cored stators to achieve a high degree of magnetic coupling. The coils are flat, helical or spiral. Copper is the most widely used material for coils in most EMVEHs due to its high conductivity, but the use of gold has also been reported (Kim, 2008).

### 2.4.2 Different strategies used to improve the performance of EMVEHs

A number of intelligent strategies have been adopted in recent years to improve the performance of the EMVEHs. Whilst some strategies target the increase in voltage, others contribute by broadening the operating frequency range and maximising the power output.

Tuning the source frequency of the ambient vibration sources to the sink frequency of the energy harvesting mechanism has always been an interesting strategy to increase the power output of energy harvesters in general. Generally, the tuning is achieved by altering the inertial mass or the spring as observed in state-of-the-art EMVEHs like the PMG from Perpetuum (2012). Another way of tuning has been achieved by the electrical means of altering the load resistance. A novel method of using piezoelectric materials to tune EMVEHs was reported by Wischke (2010). Here, a tuning voltage was applied to the piezoelectric material to vary the oscillator stiffness for tuning. Zhu (2010), reported on a micro-generator where tuning was achieved by varying the axial tensile force by moving the tuning magnet away from the magnet fixed to the electromagnetic transduction mechanism. A similar magnetic approach was employed by Challa (2011) for autonomous resonance frequency tuneability, utilising a magnetic stiffness technique consisting of one attracting magnet and one repelling magnet on either side of the active inertial mass.

Widening the operating frequency range of energy harvesters is another way of maximising the power. This is because the ambient vibration sources consist of random or periodic vibrations characterised by a wide range of frequencies. An EMVEH made of varying lengths of coil carrying parylene cantilevers surrounding a central large magnet was proposed by Sari (2008), for wideband vibration energy harvesting.

Frequency up-conversion is another method of increasing energy harvesting efficiency by up-converting the resonant frequency of the EMVEH system. It has been found that EMVEHs that operate in higher frequencies have higher power densities. Recently, Zorlu (2011), proposed a frequency up-conversion technique wherein the magnet moving on a diaphragm with ambient vibration frequency periodically caught and released a magnetic piece placed on the cantilever. This technique showed an improvement in the energy density from the frequency up-conversion reported by Sari ( 2010).

Unlike piezoelectric VEHs, EMVEHs are low voltage systems and tend to have start-up issues. Hence a novel start-up method was proposed by Dayal (2012) that consisted of a piezo element that generated sufficient voltage for start-up. This method was found to be very suitable from an energy harvesting perspective, and it performed better than the traditional start-up methods such as step-up transformers or battery start-up methods.

A number of non-linearisation methods have been reported recently for achieving broadband resonances of EMVEHs. Owens (2012) suggested that nonlinear coupling was

better than linear coupling for broadening of the frequency response. Cepnik (2011) uses the spatial variation of the magnetic field for calculating the voltage. Barton (2010) validated the use of highly permeable NdFeB magnets characterised by nonlinear magnetic properties.

A number of strategies have recently been proposed for achieving rectification and amplification of the output power obtained from EMVEHs. The synchronised magnetic flux extraction (SMFE) circuit that enabled the rectification and amplification of output voltage of the EMVEH was introduced by Arroyo (Arroyo & Badel, 2011). This was an improvisation on commercially available EMVEHs such as PMG FSH by Perpetuum, where the EMVEHs have an AC-DC rectifier followed by a DC-DC converter. This SMFE circuit removed the dependency of the EMVEH power efficiency upon the load circuit. Marin, Turner, Ha, & Priya (2013) designed a impedance matching circuit consisting of four buck boost DC-DC converters intended to match the electrical and mechanical impedances for obtaining broadband energy harvesting.

## 2.5 Research Formulation

From Section 2.4, it can be observed that the multi-degree-of-freedom vibration system has not been employed in energy harvesting applications to date. Yong (2011), proposed a 2DOF MEMS ultrasonic energy harvester that was capable of extracting ultrasonic energy from all directions by increasing the bandwidth of the operating frequency. However, the proposal was based on the directional degree of freedom and not the degrees-of-freedom of vibration. Although a dual-mass systems-based EMVEH was deemed more effective than a single-degree-of-freedom system (Tang, 2011), it was not further developed to a multiple-degree-of-freedom based electromagnetic energy harvester.

A Prior Art Search was initially conducted to confirm if any inventions had already been conceived of and developed with regard to multi-degree-of-freedom systems. The results of the Prior Art Search are tabulated in Table 2.4. The search results indicated no existing research on the multi-degree-of-freedom strategy of energy harvesting. Hence, it was chosen as the first aspect of research topic.

To be more specific, the spatial variation of the magnetic field with respect to the spatial dimension along the direction of coil motion was considered, rather than the approximate approach of treating the magnetic field of a constant value. This spatial variation of the magnetic field along the direction of coil motion was considered to be the second aspect of the research topic.

Considering these two aspects, the research topic was finalised as “Spatially varying multi-degree-of-freedom electromagnetic dynamic energy harvesting method”. The word dynamic was chosen generically rather than the word “vibrations”, with a view to a method that could be applied to any linear harmonic motion such as vibrations and waves.

Table 2.4 Closest patents to near multi-degree-of-freedom EMVEH systems.

| | |
|---|---|
| US2011/0193428 Al | Electrical Energy Generator; A Single DOF Electromagnetic generator with springs for imparting restorative forces. |
| US2010/0187835 Al | Electromagnetic energy scavenger based on moving permanent magnets; Bi directional EMVEH. |
| WO 2011/092223 A2 | Electromagnetic generator pivoting motion based; Not based on resonance. |

It should be noted that the aim of this project was to understand the behaviour of multi-degree-of-freedom systems and not to design an optimised energy harvester. An optimised MDOF EMVEH could be an extension of this research but it is not covered in this thesis. Table 2.5 summarises the coverage and focus of the research on addressing specific research questions.

Table 2.5 Research scope explained.

| | Inside Scope | Outside scope |
|---|---|---|
| | Research goals that are considered as part of this research project. | Research goals which are not considered as part of this research project (can be future research goals). |
| **Focus of research** | The current research focuses on inventing novel MDOF systems and magnetic spatial variations to electromagnetic vibration energy harvesting. Only the functional prototypes and mathematical models of MDOF1D EMVEHs are considered to study the physics of MDOF systems. | Due to time and resource constraints, the current research does not involve the design evaluation/design optimisation of the best combinations of MDOF design parameters, or the magnet designs that yield the best energy efficient designs. This may later be explored as follow-on to this research. |
| **Spatial variation of magnetic field** | How spatial variation of the magnetic field can enhance the modularity of design of EMVEH. | Spatial variation designs - how can one change the magnetic profiles/which magnetic profiles are the best for producing the most efficient EMVEHs. |
| **What fields does this research cover?** | Focus is on mechanical and core electrical design parameters of energy harvesters are considered. | Electronic design parameters of energy harvester that consist of boost converters, power management. |
| **Scope of development** | Only the energy harvester part of EMVEHs is considered. | Development of an application using energy harvester together with WSN. |
| **Type of vibration energy harvesters** | How electromagnetic energy harvesting with multi-degrees-of-freedom is preferable to equivalent single DOF systems. | The application of the same MDOF principle to other types of energy harvesting like MDOF Piezoelectric Energy Harvesters and MDOF Electrostatic Energy Harvesters is not considered as part of this research project but can be considered for further development. |
| **Broadband energy harvesting to accommodate wide band of frequencies of random vibrations** | How MDOF systems can provide broadband energy harvesting capabilities. | Optimised design of broadband energy harvesting of MDOF EMVEH. |
| **Applications** | Brief about the possible applications of proposed MDOF EMVEH principles at micro-scale, meso-scale and mega-scale. | Complete market-ready design of an application of MDOF EMVEH. |

# Chapter 3 Theoretical and experimental investigation of single-degree-of-freedom undamped electromagnetic vibration energy harvester

As discussed in Chapter 1, the first step in understanding the behaviour of an electromagnetic vibration energy harvester (EMVEH) is to consider the most basic EMVEH model. This model would be a single-degree-of-freedom, one-directional undamped EMVEH (SDOF1DUD EMVEH), consisting of a coil vibrating in the magnetic field where the coil is connected to a vibration source of known amplitude and frequency.

## 3.1 The first principles of electromagnetics

The EMVEH is a coupled electrical–mechanical system wherein electrical energy is derived from the electromagnetic induction of relative coil-magnet movement due to vibration. Hence, it is imperative to understand the basic principles of electromagnetics and vibration dynamics prior to proceeding with the building of a basic EMVEH model.

In 1831, Faraday and Henry discovered that magnetic fields can produce electrical current in a closed loop, provided the magnetic flux linking the surface area of the loop changes over time. Hence, the key to generating electrical energy using electromagnetic induction is "change" (Ulaby, 2005).

Consider a coil of *n* turns (loops) in a magnetic field **B** as shown in Figure 3.1. The magnetic flux, $\mathbf{\Phi}$, passing through each loop of area S is the integral of the normal component of magnetic flux density over the surface area of the loop, and is given by:

$$\mathbf{\Phi} = \int_S \mathbf{B}.d\mathbf{S}. \tag{3.1}$$

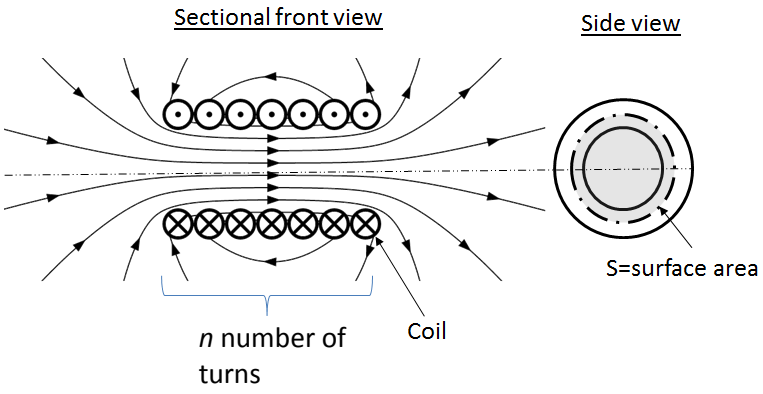


Figure 3.1 Coil in a magnetic field.

When the flux is constant, there is no current in the coil. When the magnetic flux changes, the current is induced and gives rise to an induced electromotive force(EMF) that is proportional to the rate of change of magnetic flux. This is given by Faraday's law as:

$$V_{emf} = -n\frac{d\boldsymbol{\Phi}}{dt}. \tag{3.2}$$

Substitution of equation (3.2) in (3.1) gives,

$$V_{emf} = -n\frac{d}{dt}\int_s \mathbf{B}\cdot d\mathbf{S}. \tag{3.3}$$

It should be noted that the induced EMF is proportional to the total time derivative of the magnetic field **B** as well as the differential surface area *d***S**.

Maxwell summarised the Gaussian law of electric flux and magnetic flux together with Faraday's law of electromagnetic induction and Ampere's law by proposing their use with the following four Maxwell's electromagnetic equations:

Maxwell-Gauss's law of electrical flux given as,

$$\nabla\cdot\mathbf{D} = \rho_{v,} \tag{3.4}$$

Maxwell-Faraday's law of electromotive force given as,

$$\nabla \times \mathbf{E} = -\frac{\partial \mathbf{B}}{\partial t}, \tag{3.5}$$

Maxwell-Gauss's law of magnetism given as,

$$\nabla \cdot \mathbf{B} = 0, \tag{3.6}$$

and Maxwell-Ampere's law given as,

$$\nabla \times \mathbf{H} = \mathbf{J} + \frac{\partial \mathbf{D}}{\partial t}. \tag{3.7}$$

Here, **D** represents the electric flux density and is given by electric field intensity **E** and electric permittivity ε as:

$$\mathbf{D} = \varepsilon \mathbf{E}, \tag{3.8}$$

and $\mathbf{B}$ represents the magnetic flux density and is given by magnetic field intensity $\mathbf{H}$ and magnetic permeability as:

$$\mathbf{B} = \mu \mathbf{H}. \tag{3.9}$$

The current density ($\mathbf{J}$) is the product of electric charge density per unit volume ($\rho_v$) and the velocity of the moving charge particles ($\mathbf{u}$) as:

$$\mathbf{J} = \rho_v \mathbf{u}. \tag{3.10}$$

Of these, the Maxwell-Faraday law of electromotive force is of particular interest in the designing of EMVEHs. The Maxwell-Faraday equation, as described in equation (3.5), can be rewritten in integral form as:

$$\oint_C \mathbf{E} \cdot \mathrm{d}\mathbf{l} = -\int_s \frac{\partial \mathbf{B}}{\partial t} \cdot d\mathbf{S}. \tag{3.11}$$

Equations (3.3) and (3.11) can be combined to obtain the EMF for *n* coils as:

$$V_{emf} = n\oint_C \mathbf{E}\cdot \mathrm{d}\mathbf{l} = -n\int_s \frac{\partial \mathbf{B}}{\partial t}\cdot d\mathbf{S} \tag{3.12}$$

Equation (3.12) suggests that there can be three ways of generating EMF. They are: (a) time-varying magnetic field but stationary coil – commonly known as the transformer EMF ($V_{tr}$), since this is commonly being used in transformers, (b) moving coil in a static magnetic field – commonly known as the motional EMF ($V_m$) and applicable to motors and generators, (c) moving coil in a time-varying magnetic field ($V_{tr}$ + $V_m$). This poses the intriguing question of what happens when a coil is moving a magnetic field that is varying spatially along the trajectory of coil motion. This is similar to Case (c) moving coil in a time-varying magnetic field. This was considered in the design of the basic EMVEH model to consider any advantages in using spatial magnetic field variation.

**Case (a): stationary coil in a time-varying magnetic field.**

Commonly used in transformers, where the conductor does not move but the magnetic flux continuously varies with time, the generated EMF (commonly called transformer EMF) can be given by:

$$V_{emf}^{tr} = -\int_s \frac{\partial \mathbf{B}}{\partial t}\cdot d\mathbf{S}. \tag{3.13}$$

**Case (b): moving conductor in a static magnetic field.**

Commonly used in motors and generators, where the conductor moves in a stationary magnetic field, the EMF generated is due to the motion and hence is called motional EMF which can be given by:

$$V_{emf}^{m} = \oint_c (\mathbf{u}\times\mathbf{B})\cdot d\mathbf{l}\,. \tag{3.14}$$

Combining Case (a) and Case (b), one can think of an interesting Case (c) which represents the moving conductor in a time varying magnetic field.

**Case (c): moving conductor in a time-varying magnetic field**

Here, the EMF generated can be given by:

$$V_{emf}^{m} = V_{emf}^{tr} + V_{emf}^{m} = \oint_{c} \mathbf{E}.\, d\mathbf{l}$$
$$= -\int_{s} \frac{\partial \mathbf{B}}{\partial t} .\, d\mathbf{S} + \oint_{c} (\mathbf{u} \times \mathbf{B}).\, \mathrm{d}\mathbf{l}. \tag{3.15}$$

By Faraday's law, it can also be given that:

$$V_{emf} = -\frac{d\emptyset}{dt} = -\frac{d}{dt}\int_{s} \mathbf{B} \cdot d\mathbf{S}. \tag{3.16}$$

In the SDOF1DUD EMVEH model, it can be seen that if there was a spatial variation of magnetic field **B** with reference to *x*, then as the coil moves (i.e., the position *x* of the coil varies with reference to time *t*), the magnetic field **B** also changes (since **B** was a function of *x*). This was equivalent to Case (c) of Maxwell's equations of electromagnetics. Hence the EMF generated by SDOF1DUD EMVEH model was given by equation (3.16).

## 3.2 The SDOF1DUD EMVEH model

As shown in Figure 3.2, the SDOF1DUD EMVEH model represents the most fundamental electromagnetic energy harvester model with coil and magnet. The moving part is rigidly connected to the vibrating body i.e., the vibration exciter and hence it becomes an undamped (without springs or viscous damping) base-excited system. For this model, there are 2 choices – (a) vibrate the coil keeping the magnets fixed or (b) vibrate the magnets relative to the fixed coil. Either of these cases could have been considered for analysing the SDOF1DUD EMVEH model. The better of the two configuration choices depends on the amount of $\frac{d\emptyset}{dt}$ in the EMVEH being designed. As shown in Figure 3.1, Case (a) configuration was considered with a view to using the same analysis for the SDOF1D EMVEH and 2DOF1D EMVEH models discussed in subsequent chapters. A moving coil configuration design was considered easier for prototype development than the moving magnet design, particularly when suspended by springs. This was also considered based on the state-of-the-art reverse

transduction mechanism that can be seen in moving coil microphones and loud speakers (Figure 3.3) that use moving coil construction (Case (a) type of configuration).

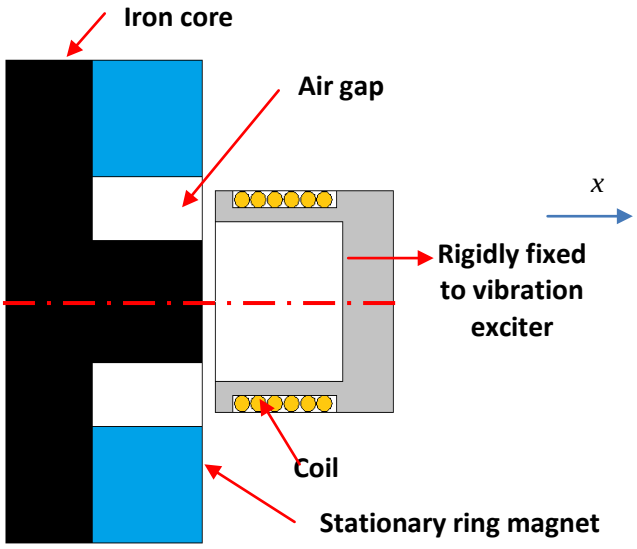


Figure 3.2 Schematic of SDOF1DUD EMVEH model.

It should be noted that both loudspeaker and moving coil microphones, as shown in Figure 3.3, use an iron core to bend the flux lines perpendicular to the direction of coil movement so that the magnitude of the Lorentz force

$$F = BIl\sin\theta = BIl, \tag{3.17}$$

is maximised, where $I$ denotes the current in the conductor of length $l$, $B$ represents the magnitude of magnetic field strength and $\theta$ is the angle between the current $I$ and magnetic field $B$ which is zero for this case.

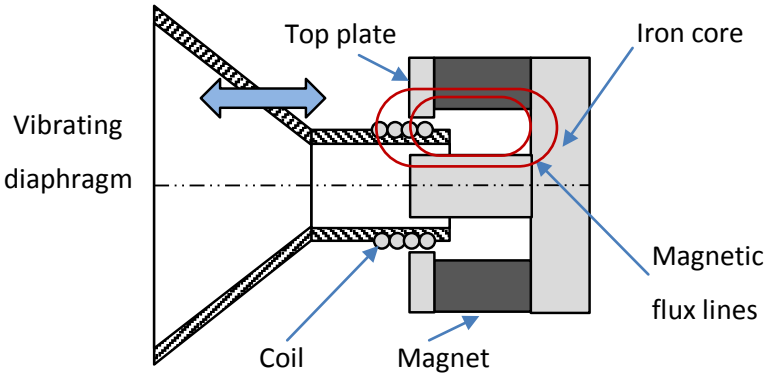


Figure 3.3 Schematic of loud speaker and moving coil microphone construction.

## 3.3 Spatial variation consideration

In the loud speaker and microphone designs as shown in Figure 3.3, the magnetic field strength **B** variation is assumed to be zero with reference to the space. In reality, **B** varies in the direction of the coil motion, having high magnetic field strength at the ends and gradually decreasing at the middle of the ring magnets as shown in Figure 3.4**.** The magnetic field **B** is generally high at the poles and low in the middle portions of the ring magnets. One can play with **B** versus $x$ variation, where $x$ is the direction of coil motion, by altering the geometrical parameters of ring magnets and the central iron core. Whenever there are design space limitations that constrain the geometrical size of the ring magnets and the iron core, then **B** can be varied with reference to $x$ to maximise **B** at the coil movement locations.

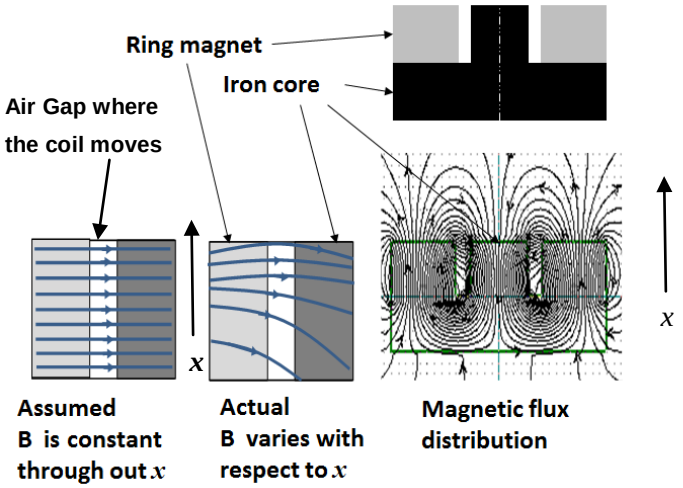


Figure 3.4 Assumed and actual spatial variation of magnetic field in air gap.

## 3.4 Determination of spatial variation – magnetostatic analysis

The analytical determination of the spatial variation in a magnetic field is cumbersome, especially when iron core elements are introduced into the centre of the ring magnets. Hence, the better approach to using numerical simulation was considered. For this, the

magnetostatic analysis was performed using Vizimag software and the magnetic flux distribution obtained, as shown in Figure 3.5. A two-dimensional analysis of the cross-section of a ring magnet with a central iron core was considered using Vizimag software, as the model was assumed to be axisymmetric. It was observed that the magnetic flux lines were denser at the ends than on the inside. This suggested that the coils could be subjected to a higher rate of change of magnetic flux and hence increased generated voltage when the coils vibrated at the ends.

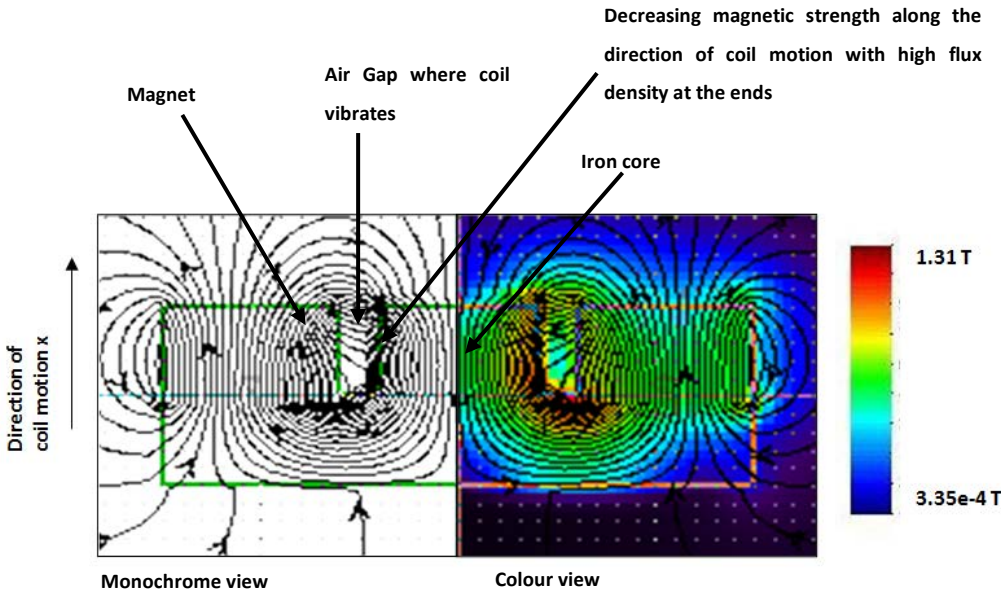


Figure 3.5 Model of numerical magnetostatic analysis using Vizimag software.

To confirm the numerical values, the system as shown in the Figure 3.5 was built using an iron core and a ring magnet. The magnitude of the magnetic field strength at the position $x$ ($B_x$) at different points in the air-gap was measured using a Gauss meter (Range 0-20000Ga, resolution of 1Ga, cross section 5X1 mm head ) every 2 mm along the $x$ direction as shown in Figure 3.6.

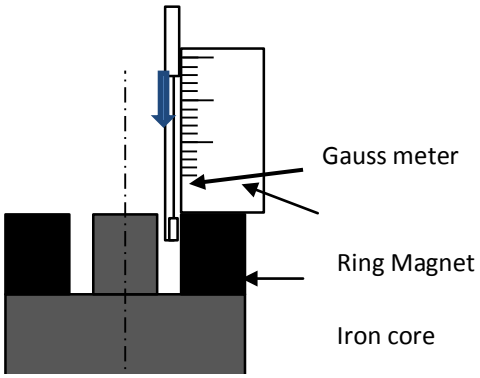


Figure 3.6 Schematic cross-sectional view of experimental Gauss meter measurement of magnetic field strength.

The comparison of the numerical and experimental spatial variation of the magnetic field strength along the axial direction ($x$) of coil motion was plotted as shown in Figure 3.7. The initial position of the coil was centred at $x$ = 5 mm. Curve fitting was used to find an empirical $B_x$ curve that closely fitted the numerical $B_x$ curve.

It was observed that the magnetostatic $B_x$ curve was similar to a sinusoidal curve with $x$ in the operating range of coil motion at $x$ = 2 mm to $x$ = 8 mm for a coil moving at 3 mm amplitude from $x$ = 5 mm. Hence, an empirical $B_x$ curve was assumed as a simple shifted sinusoidal function:

$$B_x = B_0 \sin(gx) + B_i\,, \tag{3.18}$$

that is valid within the operating range of the coil motion $x$ = 2 mm to $x$ = 8 mm. MATLAB's curve fitting tool was used to determine the empirical coefficients $B_i$, $B_0$ and $g$. The best sinusoidal fit was achieved when $B_i$ = 0.5 T, $B_0$ = 0.365 T and $g$ = 872.6 with the following goodness-of-fit statistical parameters: Standard Square Error (SSE) = 0.008, regression square (R-square) error = 0.950, adjusted R-square error = 0.880 and root mean square error = 0.064. The adjusted R-square of 0.880 shows that this approximation is acceptable within the range of $x$ = 2 mm and $x$ = 8 mm.

A better curve fit would have been obtained using a polynomial equation instead of a sinusoidal equation, but that would make the nonlinear voltage calculations cumbersome

and computationally intensive to obtain each voltage value, as discussed in the next section. The objective here was to demonstrate the significance of $B_x$ variation on the generated voltage rather than achieving the perfect fit for the design of an optimised SDOF1DUD EMVEH.

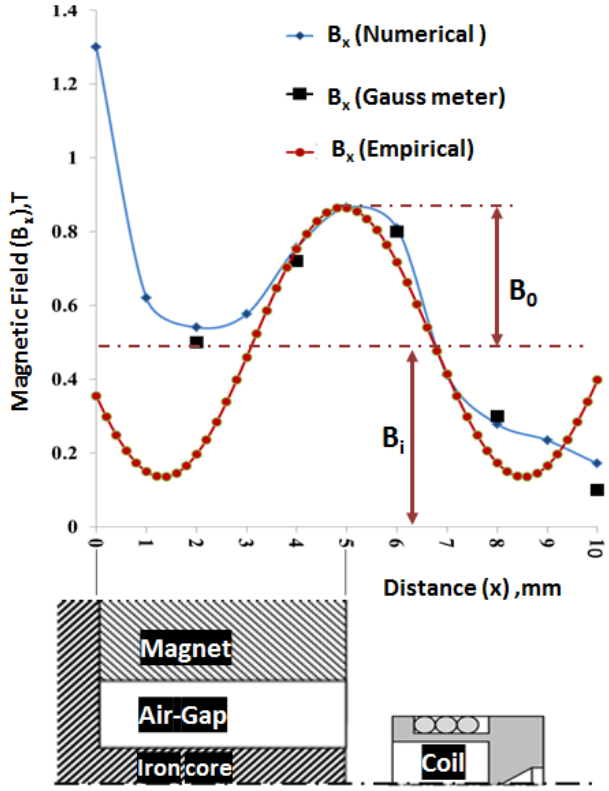


Figure 3.7 Empirical approximation of spatial magnetic field variation with numerical and experimental $B_x$ values - a simple shifted sine curve was chosen (Gatti, 2012).

## 3.5 Derivation of the generated voltage of SDOF1DUD EMVEH model

Consider a coil of $n$ turns and radius ($r_c$) and wire diameter ($d_w$) moving through the spatially varying magnetic field $B_x$ along the $x$ direction as shown in Figure 3.8. The position of the top most coil turn 1 at any point of time, $t$ can be given by:

$$x_1 = A\sin(\omega t), \tag{3.19}$$

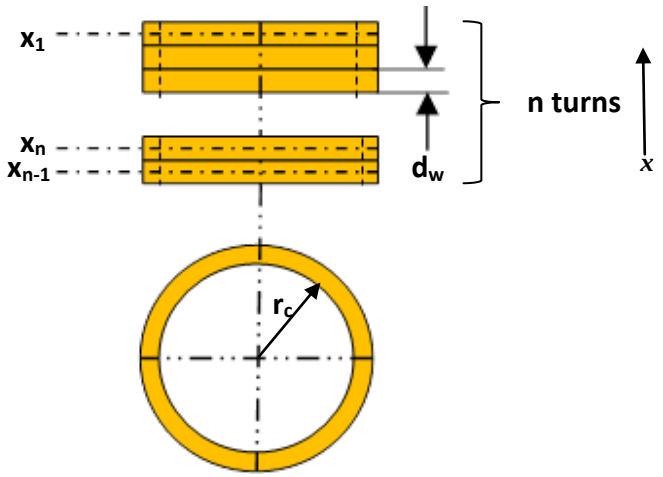


Figure 3.8 Coil of n turns.

assuming harmonic motion of the coil with amplitude $A$ and frequency $\omega$. Since the coil turn 2 is at a distance equal to the wire diameter from coil turn 1, its position along the positive $x$ direction can be given by:

$$x_2 = A\sin(\omega t) - d_w. \tag{3.20}$$

Extending this, the position of the $n^{th}$ coil turn can be given by:

$$x_n = A\sin(\omega t) - d_w(N-1). \tag{3.21}$$

Let the magnetic flux at position $x_1$ be $\boldsymbol{\phi}(x_1)$ that generates a magnetic field $\mathbf{B}(x_1)$. According to Faraday's law, the voltage generated by coil turn 1 when it was at $x_1$ can be given by:

$$V_1 = \frac{\partial \boldsymbol{\phi}(x_1)}{\partial t} = \frac{\partial}{\partial t}\int_s \mathbf{B}(x_1).\, d\mathbf{s}. \tag{3.22}$$

Assuming the magnetic field varies as a sinusoidal function as in equation 3.18, the magnetic field at $x_1$ can be given by:

$$B(x_1) = B_0 \sin(g x_1) + B_i, \tag{3.23}$$

where, $B_i$ = 0.5 T, $B_0 = B_{max2} - B_i$ = 0.865 – 0.5 = 0.365 T and g = 872.6 were determined empirically as discussed previously in equation(3.18).

Using equations (3.18) and (3.21), the magnetic field at the $N^{th}$ coil turn becomes:

$$\begin{aligned} B(x_n) &= B_0 \sin(g x_N) \\ &= B_0 \sin\big(g(A sin(\omega t) - d_w(N-1)\big) + B_i \end{aligned} \tag{3.24}$$

The voltage generated at the $N^{th}$ coil turn will be given by:

$$V_n = \frac{\partial \boldsymbol{\Phi}(x_N)}{\partial t} = \frac{\partial}{\partial t}\int_s \mathbf{B}(x_N).d\mathbf{s} \tag{3.25}$$

$$= -\pi r_c^2 B_0 g A\omega \ \sin(gA\sin(\omega t) - g d_w(N-1))\cos(\omega t)\,. \tag{3.26}$$

Since coils 1 to coil *n* represent *n* coils connected in series, the total EMF can be given by:

$$\begin{aligned} V_{emf} = -\sum_{n=1}^{N} \pi r_c^2 B_0 g A\omega \ \sin(gA\sin(\omega t) - g d_w(n-1) \\ + C_f)\cos(\omega t) \end{aligned} \tag{3.27}$$

where, $C_f$ represents a correction factor that accommodates the space limitation to accurately position the coil's initial position in the region of $B_{max}$. From first principles, it is evident that the generated EMF opposes the direction of motion; hence the negative sign in equation (3.18).

## 3.6 Experimentation of SDOF1DUD EMVEH model

To validate the theoretical SDOF1DUD EMVEH model as discussed in the previous Section 3.5, the SDOF1DUD EMVEH prototype was designed with the same coil and magnet design

parameters as the coil and the magnet as assumed in the theoretical model, and then tested in a laboratory environment. The prototype coil was rigidly mounted to the B&K vibration exciter that acted as a vibration source and made to vibrate to and fro from the stationary ring magnet-iron core assembly that was fixed coaxially to the mounted coil. The experimentation included the following steps: prototype design and development, stack-up tolerance analysis, impedance head calibration – to reduce sensor calibration errors (discussed in detail in Appendix A), filter design to reduce unwanted noise in the data-capturing instrument, and experiment setup and experimentation.

### 3.6.1 Prototype Design and Development

The prototype design was initially designed using SolidWorks CAD and is as shown in the experimental setup as illustrated in Figure 3.9. A ring magnet of N35 grade NdFeB material and strength of 11.7 - 12.1 mT was obtained from the standard sizes available in the market. Its inner diameter (ID = 10 mm), outer diameter (OD = 30 mm ) and height (H = 5 mm) were the fundamental driving dimensions of the design of other parts, such as the iron core and coil. An air gap of about 3 mm was considered suitable for vibration motion of the coil in and out of the magnet-iron core assembly. The dimensional drawings of the individual parts are provided in the Appendix C of this thesis.

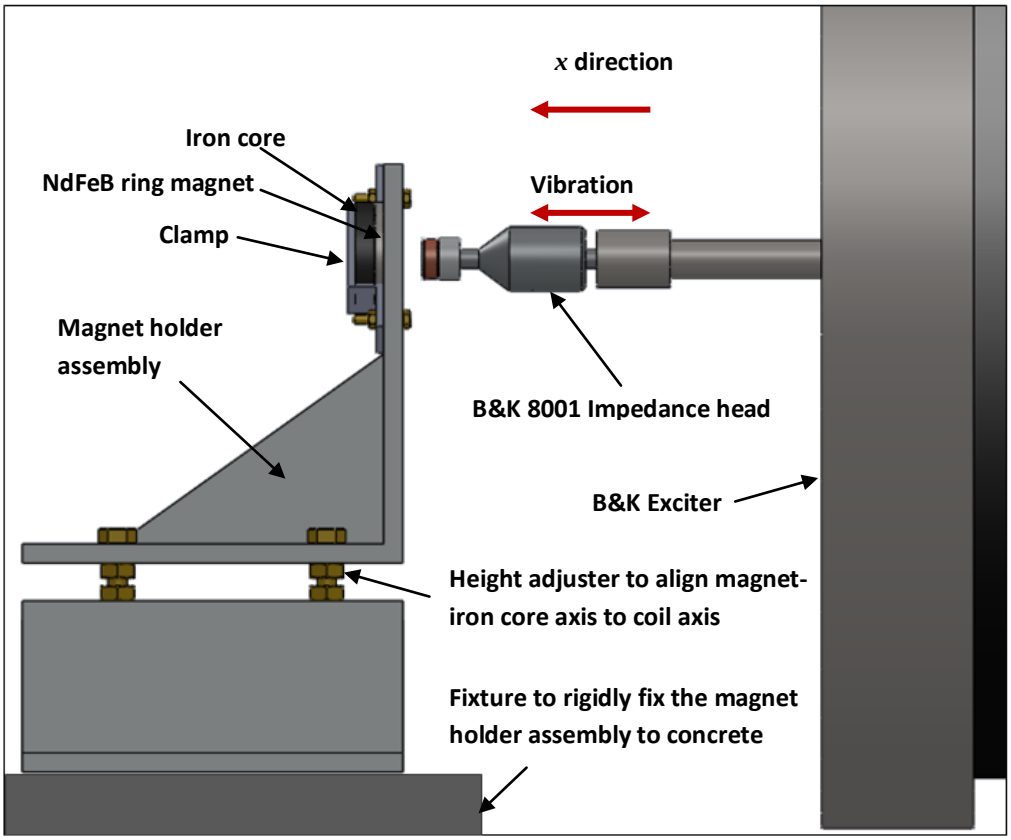


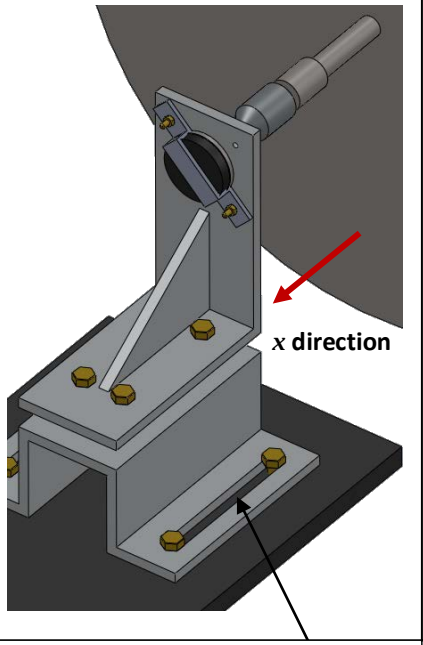


Slot for slide adjustment of initial spacing between coil and the magnet in the x direction


Actual photo of prototype –Detailed drawings and more pictures in Appendix C

Figure 3.9 SDOF1D UD EMVEH prototype design.

### 3.6.2 Stack-up tolerance analysis for initial position of the coil

To ensure correct experimental results, it was very important that the coil be positioned correctly in its initial position to have the required magnetic field $B_x$ in the 1st turn of coil. In addition, adequate safe distance was required between the coil face and the iron core at the maximum amplitude to prevent collision between the coil and the iron core. Hence a stack-up tolerance analysis was performed for the coil-magnet-iron core assembly to ensure that there was a safe distance of at least 0.5 mm between the front face of the coil and the corresponding face of the iron core (dimension x4) as shown in Figure 3.10. The worst case of maximum amplitude vibration was considered. From a safety perspective, x4 = 3.5 mm was considered because at the amplitude of 3 mm, the coil moves 3 mm forward adding to the 0.5 mm safety clearance. But since, at the 1st turn of the coil, it had to start vibrating from the initial position at maximum $B_x$ region, the dimension x4 should be equal to x5 in the tolerance analysis. Thus $Y_{mean}$ was obtained as 6.875 mm as can be seen in Table 3.1.

It is important to understand that the individual tolerances of the parts can contribute significantly to the predicted Y. Hence a Monte-Carlo simulation was conducted to simulate the variation of individual part tolerances, based on their assumed standard deviation. The Monte-Carlo simulation iterates each individual predicting dimension (Xs) within their tolerances to predict the output Y and its standard deviation. For this, the standard deviations of the individual part dimensions were assumed to be 25% of the tolerance, in accordance with the range rule that is frequently used for prototype design. From the tolerance analysis, the standard deviation of Y was found to be 0.01 and the predicted Y as 6.925. The process capability was calculated as:

$$\text{Process capability} = (Y_{mean} - Y_{predicted})/\sigma = (6.935\text{-}6.875)/0.01 \approx 5 \quad (3.28)$$

The 5σ process capability was considered sufficient to carry out the experiment safely without assembly interference.

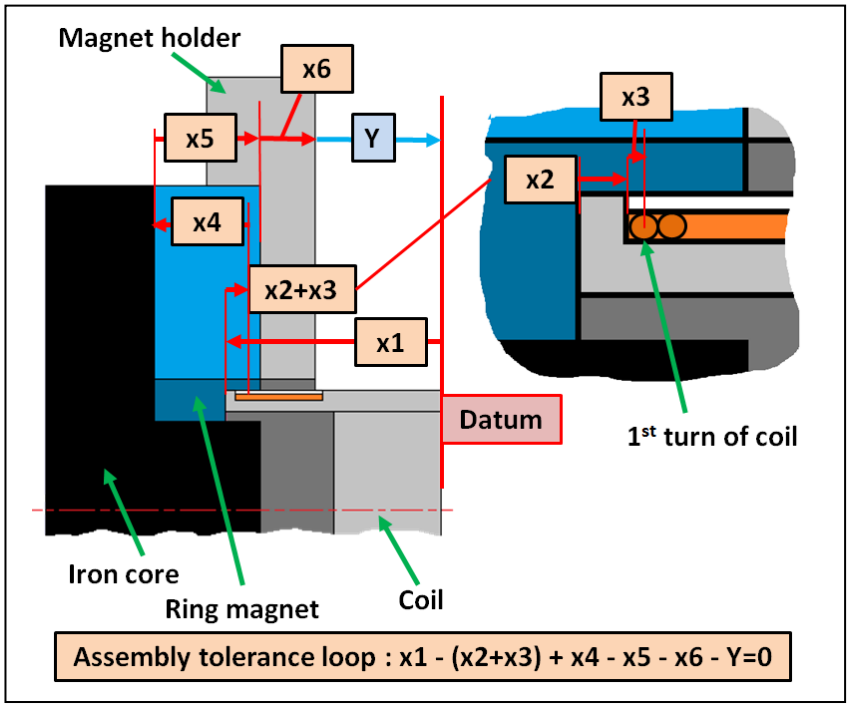


Figure 3.10 Stack-up tolerance analysis for correct initial position of the coil.

Table 3.1. Stack-up tolerance analysis using Monte-Carlo simulation.

| Dimension | length(mm) | Std deviation | tolerance |
|---|---|---|---|
| X1 | 10.00 | 0.0025 | 0.01 |
| X2 | 0.50 | 0.0025 | 0.01 |
| X3 | 0.125 | 0.0025 | 0.01 |
| X4 | 5.00 | 0.0025 | 0.01 |
| X5 | 5.00 | 0.0025 | 0.01 |
| X6 | 2.00 | 0.0025 | 0.01 |
| Y | 6.875 | 0.01 | |
| | Process capability > | 5σ | |

### 3.6.3 Filter design

One of the key issues of signal analysis during the experiment was the electrical noise level in the coil. This noise was due to high frequency electromagnetic signals present in the ambient confines of the laboratory. This was identified in an initial setup where the coil was made to vibrate in and out of the magnet and the voltage generated was captured and shown on a cathode ray oscilloscope. When the signal was significantly zoomed, it was

observed that most of the noise was above 15 kHz. Hence, a low pass RC-filter was designed to cut off the extraneous high frequency noise as shown in Figure 3.11.

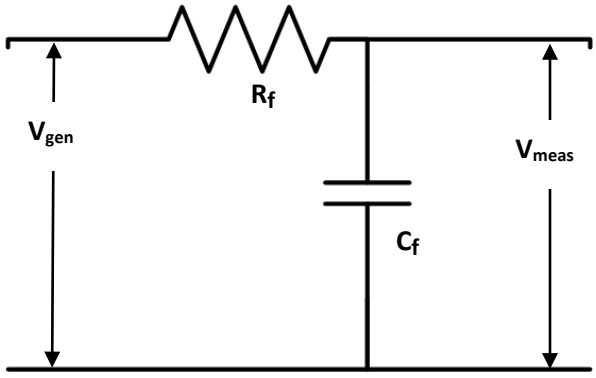


Figure 3.11 Low pass first order RC filter between the generating coil and the measuring circuit.

Hence,

$$f_c = 15000 = \frac{1}{2\pi R_f C_f} \tag{3.29}$$

Thus, $R_f C_f = 1.06 \times 10^{-5}\text{F}\Omega$. By carefully choosing $C_f = 1\text{nF}$ and $R_f = 1000\Omega$, $R_f C_f = 1X10^{-5}$ gave a cut off frequency of 15.9 kHz.

Once the filter was added to the voltage generation circuit the measured output voltage after the filter will be given by:

$$V_{meas} = V_{gen}\left(\frac{X_c}{Z}\right) \tag{3.30}$$

where, $X_c = \left(\frac{1}{2\pi f C_f}\right)$ represents the capacitive reactance and $\text{Z} = \sqrt{R_f^2 + X_L^2}$ represents the impedance. The filter cut off unwanted high frequency noise and given this, it was important to ascertain that the measured output voltage was not altered by the filter. In other words, $V_{gen}$ should almost be the same as $V_{meas}$. If not, the filter would alter the measurement and a gain factor would be multiplied every time. Hence the gain was evaluated for the operable (interested) frequency range of 6-31Hz and was found to be

equal to 1.The subsequent waveform analysis of the $V_{gen}$ during the experiments indicated a typical noise level of 0.1 mV which was considered satisfactory and a large improvement over the unfiltered signal.

### 3.6.4 Experiment

The schematic of the experimental setup is shown in Figure 3.12. The calibrated B&K Impedance head 8001 was mounted to the B&K 4825 vibration exciter which was powered using a B&K type 2720 power amplifier. The 'A' port of the impedance head (used to measure acceleration) was connected to a TDS210 Digital CRO through a B&K charge amplifier (CA) of type 2635. The exciter was powered by an Agilent wave form generator that generates sinusoidal waves for harmonic vibration of the exciter.

The coil was mounted on the impedance head. The coil circuit was connected to a HBM MX410 data acquisition device through a TEDS voltage sensor connector since this was the only way to connect to the RS232 input pin of the MX410 data acquisition device. The magnet assembly was mounted on the mounting base. The sliding slot adjustment of the magnet assembly was used to ensure alignment of the magnet assembly axis to the coil axis.

The magnet assembly was fixed such that the coil was almost at its initial corner position. The electrical circuit for measuring the output voltage is shown in Figure 3.13. This included the filter circuit and the load resistance. The electrical values are, Coil resistance = $R_c$ = 0.3 Ω, Coil inductance= $L_c$ = 2.4 mH, Load resistance = $R_L$ = 10000 Ω, Filter resistance = $R_f$ = 10000 ohm and filter capacitance = $C_f$ = 1 nF respectively.

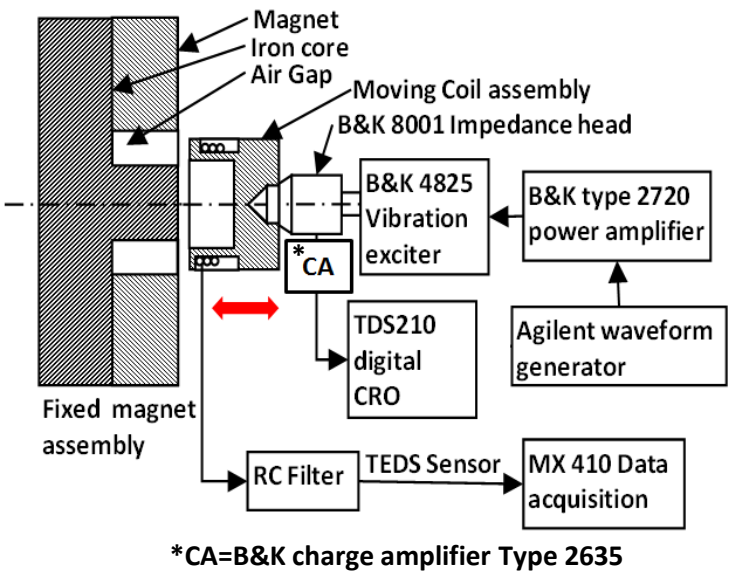


Figure 3.12 Experiment setup of undamped SDOF1D EMVEH.

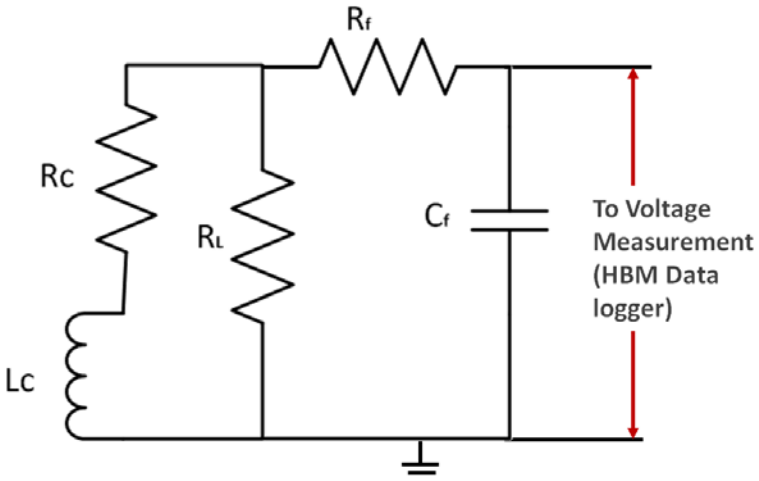


Figure 3.13 Circuit for measuring voltage output of SDOF1D UD EMVEH prototype.

To obtain a broad understanding of the variation of the induced voltage using spatial variation of the magnetic field, four cases were considered:

Case 1: Movement of coil in constant magnetic field. For this, the coil was made to oscillate with an amplitude of 0.75 mm measured using the accelerometer signal in the $x$ = 3 mm - 7 mm region, where $B_x$ was relatively constant and $\frac{\partial \mathbf{B}}{\partial x}$ trends towards zero.

Case 2: The movement of the coil in the varying magnetic field was in the region defined by $x$ = 5 mm - 7 mm. For this, the coil was made to oscillate with an amplitude of 0.75 mm in the $x$ = 5 mm - 7 mm region, where $B_x$ varied considerably and $\frac{\partial \mathbf{B}}{\partial x}$ was very high.

An amplitude of 0.75 mm and a coil of 14 turns were used for both Cases 1 and 2 for fair comparison.

Case 3: This consisted of the movement of the coil within the sinusoidal region wherein the entire coil did not leave this region. For this, the amplitude was 0.875 mm and the number of coils was 7. This case was used mainly for the study of energy harvesting with regard to small amplitude and higher frequencies.

Case 4: This consisted of the movement of the coil in and out of the sinusoidal region wherein the entire coil oscillated in and out of this region. For this, the amplitude was 3 mm and the number of coils was 14. This case was also intended for studying the energy harvesting for large amplitudes and lower frequencies.

Since the $B_x$ curve was not perfectly sinusoidal, a Correction factor ($C_f$) was used to apply corrections in $x$ for Cases 1 and 2 to improve modelling accuracy.

The procedure for all of these cases is given below:

a) Set the frequency (for example, 6Hz) and amplitude in the waveform generator. For amplitude, set the amplitude coarsely, using the power amplifier voltage knob. For fine adjustment of required amplitude, use the amplitude settings in the waveform generator.
b) Adjust the CRO signals until a stable sinusoidal voltage signal is observed.
c) Once the correct amplitude signal is observed in the CRO, commence data acquisition over a period of ten seconds. Save the data (Voltage) file as an excel file export.
d) Repeat a, b and c for steps of different frequencies over the range 6 Hz - 31 Hz.

## 3.7 Results and Discussion

To determine the element of uncertainty in the experiment, and the theoretical assumptions, an uncertainty analysis using a first order Taylor's series expansion was performed to identify the major uncertainties. This was followed by comparison of the signal shapes of the experimentally measured voltages with the theoretically simulated voltage signals in the time domain. The theoretical RMS voltage values were then compared to the experimental RMS voltage values in the frequency domain. Finally, the curve-fitness tests were performed between the theoretical and the experimental voltage signals to measure the goodness-of-fit statistics and validate the theory. The power-frequency curve of both the theoretical and experimental values were plotted to identify the power characteristics of SDOF1DUD EMVEH.

### 3.7.1 Uncertainty analysis

The total uncertainty in the voltage waveform is the result of all the possible uncertainties of the dependent variables of the voltage output. Hence, the total voltage uncertainty of the output voltage was determined by applying first order Taylor series expansion (Beckwith, 2007) to the major input parameters including the radius of the coil ($r_c$), sinusoidal spread function ($g$), amplitude of vibration ($A$), angular frequency of vibration ($\omega$), height of $B_x$ sinusoidal region ($B_0$), spatial variation along $x$ axis ($x_n$), time function ($t$) in the voltage equation (3.27) to get,

$$\frac{U_v}{V} = U_{r_c}\frac{\partial V}{\partial r_c} + U_A\frac{\partial V}{\partial A} + U_\omega\frac{\partial V}{\partial \omega} + U_{B_0}\frac{\partial V}{\partial B_0} + U_{x_n}\frac{\partial V}{\partial x_n} + U_t\frac{\partial V}{\partial t}, \tag{3.31}$$

where $U_p = \{U_{r_c}, U_A, U_\omega, U_{B_0}, U_{x_n}, U_t\}$ represent uncertainties of input parameters that contribute to the overall output uncertainty $U_v$ of voltage and $\frac{\partial V}{\partial p} = \{\frac{\partial V}{\partial r_c}, \frac{\partial V}{\partial A}, \frac{\partial V}{\partial \omega}, \frac{\partial V}{\partial B_0}, \frac{\partial V}{\partial x_n}, \frac{\partial V}{\partial t}\}$ represent the partial derivatives of the voltage output function to each of these input parameters. Each of these uncertainties is determined by the relation:

$$U_p = \sqrt{P_z^2 + B_z^2} \tag{3.32}$$

where, $P_z$ = precision uncertainty and $B_z$ = bias uncertainty of each of the input parameters. The precision uncertainty of each input parameter is due to environmental disturbances that affect the experimental setup and is usually given by 1.9σ for a single sample precision sample at a 95% confidence interval (2σ level). The bias uncertainty of input parameters may be caused by calibration errors, human error and defective equipment. The bias errors were suitably assumed based on the resolution of the instruments controllable by humans. The partial derivative individual errors, $\frac{\partial V}{\partial p}$ (where p = one of the parameters) of each input parameter were determined using different criteria and methods as shown in Table 3.2 and allowance for the final error was calculated.

Table 3.2. Experimental error analysis.

| **Transfer function Parameters** | **Basis** | **Precision error, Pz=1.96σ** | **Bias error, Bz** | **Up** | **∂V/∂p** | **Up*∂V/∂p (%)** |
|---|---|---|---|---|---|---|
| **Radius of the coil ($r_c$)** | Manufacturing tolerance. | 2.22E-03 | 0 | 2.22E-03 | 5.575 | 0.012% |
| **Sinusoidal spread function (g)** | Theoretical shift factor. | 7.84E-03 | 0 | 7.84E-03 | 1.25E-02 | 0.00010% |
| **Amplitude of vibration (A)** | Calibration of 8001 accelerometer. | 0.357 | 2.000E-02 | 3.577E-01 | 3.584E+00 | 1.282% |
| **Angular frequency of vibration (ω)** | Waveform generator. | 2E-03 | 0.02 | 0.02 | -1.27E-08 | -2.55E-12 % (~0) |
| **Height of $B_x$ sinusoidal region ($B_0$)** | Magnetic tolerance of NdFeB magnet used. | 2E-03 | 3.200E-02 | 3.206E-02 | 3.437E-02 | 0.001% |
| **Spatial variation along $x$ axis ($x_n$)** | Tolerance stack-up analysis (Monte-Carlo simulation) and coil fill factor. | 0.202 | 0.05 | 0.208 | 35.57 | 7.399% |
| **Time function ($t$)** | Data logger sampling rate and dynamicity. | 2E-03 | 0 | 2.000E-03 | -1.321 | -0.003% |
| **Voltage ($V$)** | | | | | **Uv/V** | 8.7% |

The experimental error at worst case analysis was found to be 8.7%, of which the distance error was the highest contributing factor (7.39%) mainly due to a) limited control of

establishing initial static position of coil, b) mechanical design deviation and c) hand wound coil.

### 3.7.2 Signal analyses

Signal analyses were performed to compare if the theoretically determined voltages using equation (3.27) obtained for the four cases as discussed in Section 3.6.4 had similar waveforms as the experimental voltages in the time domain as can be seen in Figure 3.14. Cases 1, 2 and 3 were found to have approximately the same shape and peak values. It was observed that the experimental signal was phase-shifted towards one side and had two sine components of the form sin (A) +sin (B) that validated the theoretical voltage function as described in equation (3.27). It can also be seen that Case 4 was the outlier with no match of theoretical and experimental voltage signals since it vibrates outside the boundary of the $B_x$ sine curve considered. This again was expected and confirmed the importance of including an accurate representation of the spatial variation of the magnetic field $B_x$ in the model.

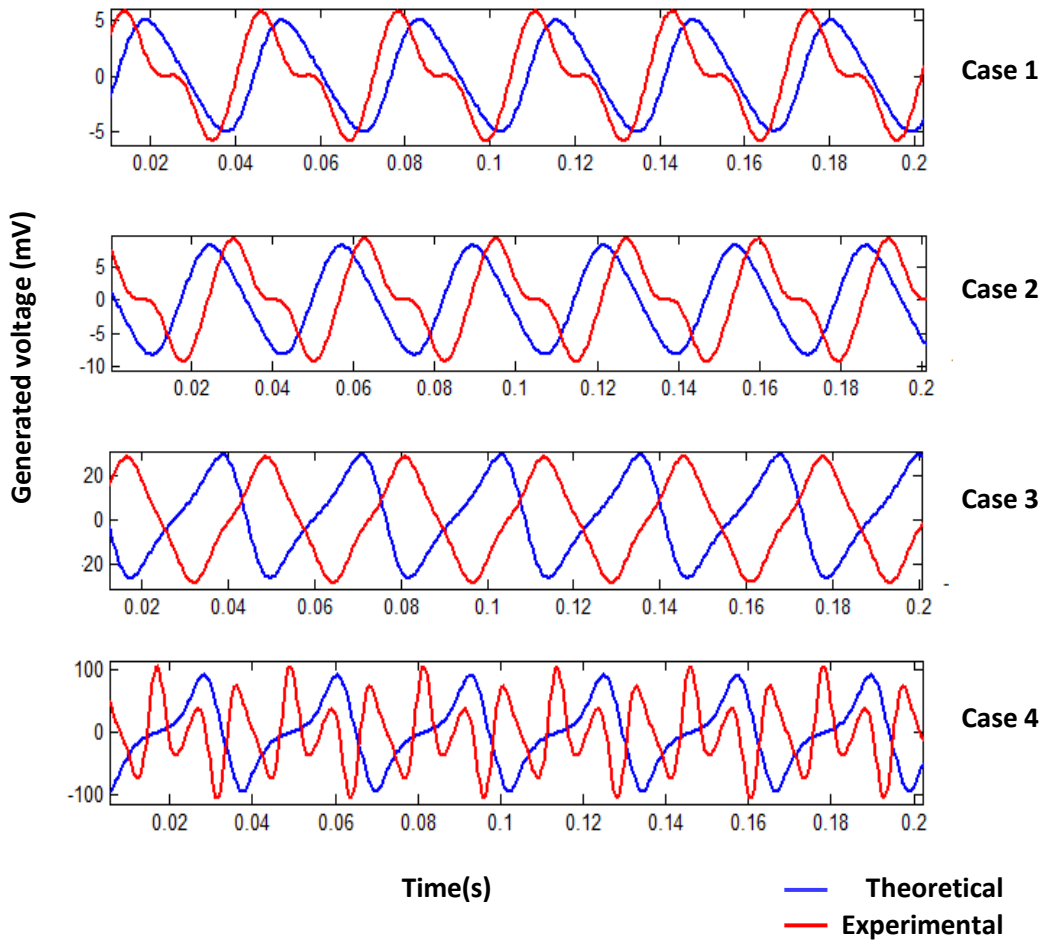


Figure 3.14 Signal analyses of theoretical and experimental voltages generated in the coil of SDOF1DUD EMVEH for all 4 cases at 31 Hz.

### 3.7.3 Voltage comparison analyses

The theoretical and experimental root mean square voltages were plotted in voltage plots as shown in Figure 3.15 for all the 4 cases as considered in Section 3.6.4. It was observed that the theoretical voltage values matched very well with the experimental voltage values, thus validating the model within the low frequency range of 7-31Hz.

To further ascertain the extent of the fitness, curve fitness tests were conducted (Figure. 3.16, Case 1 to Case 4) to determine the following goodness-of-fit statistical measures - Standard square error (SSE), R-square, adjusted R-square and root mean square error (RMSE) as tabulated in Table 3.3. The curve fitness values obtained in the Table 3.3

Goodness-of-fit statistics indicate a good fitness in the range of the adjusted R-square = 0.99 in all 4 cases.

(a)

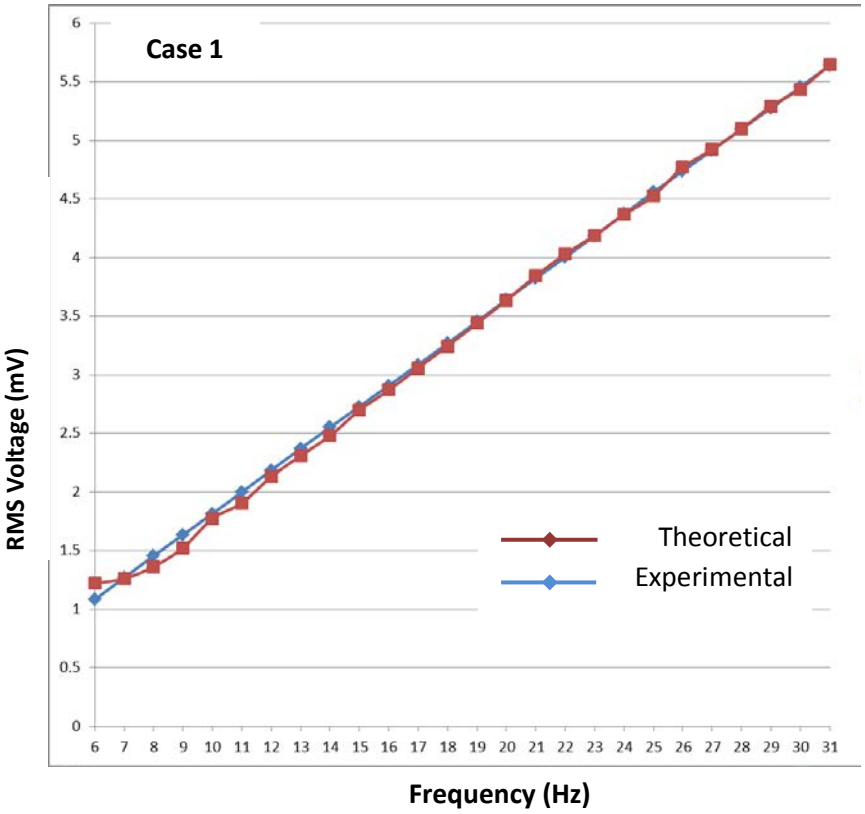


(b)

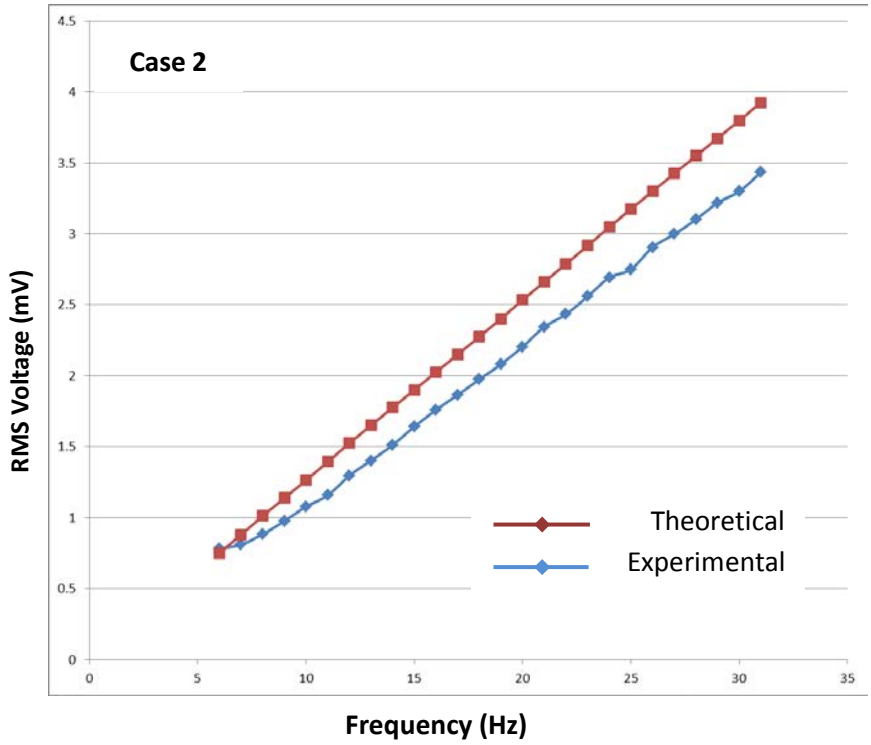

(c)

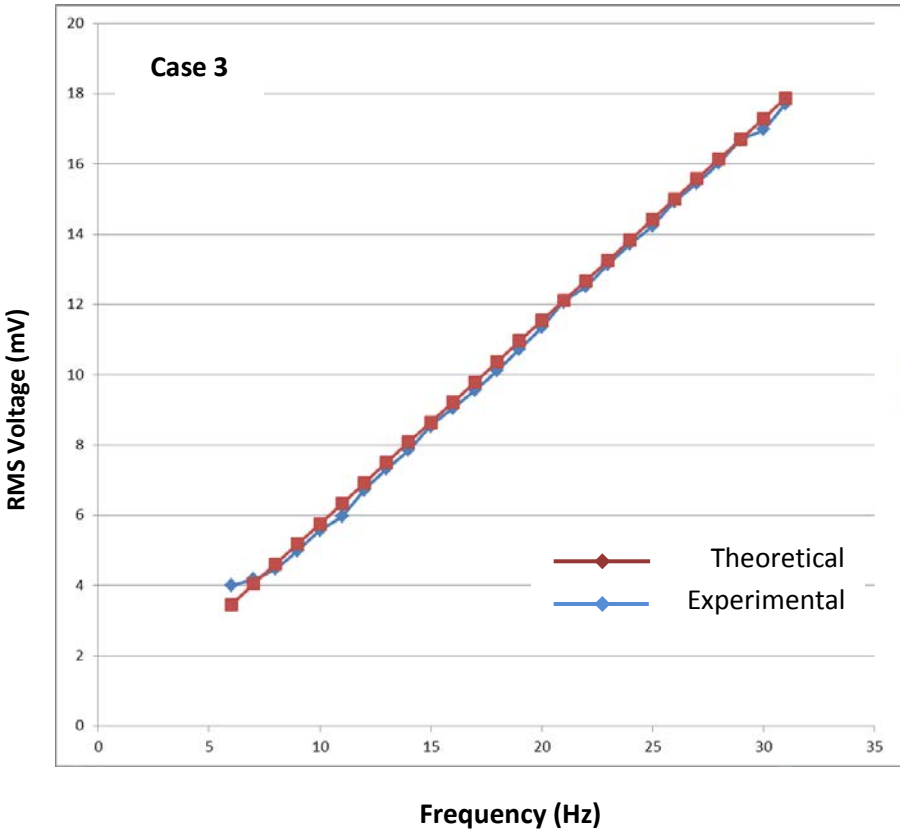


(d)

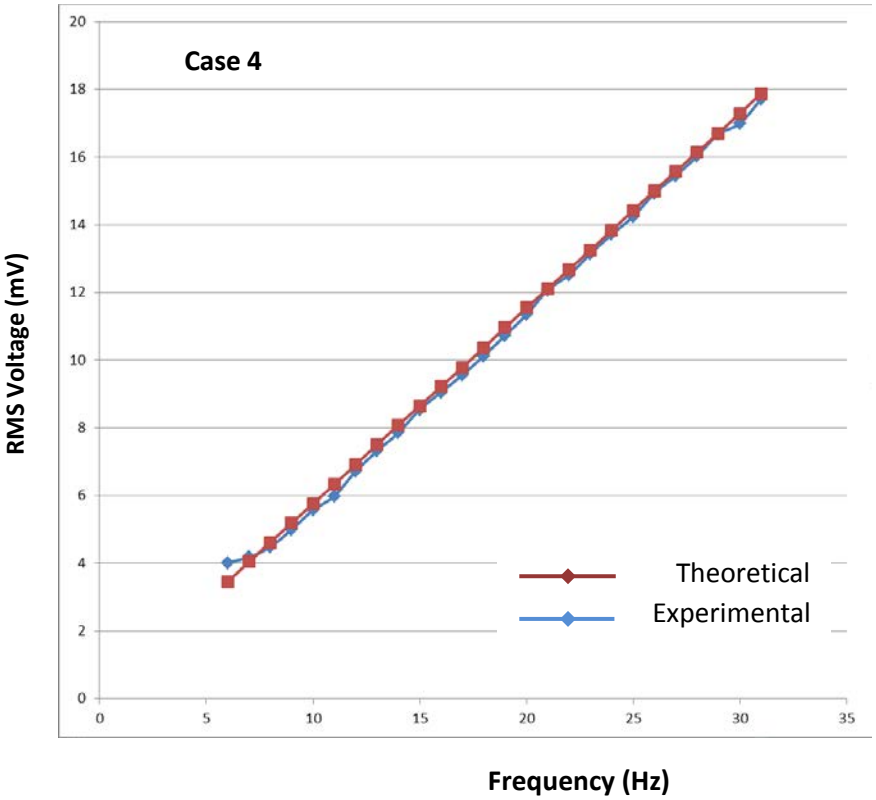


Figure 3.15 Plots of theoretical and experimental voltages simulated at different frequencies for all the 4 cases. (a) Case 1 for amplitude = 0. 75 mm at $x$ = 3 mm to $x$ = 5 mm, (b) Case 2 for amplitude = 0.75 mm at $x$ = 5mm to $x$ = 7 mm, (c) Case 3 for amplitude = 0.875 mm at $x$ = 3 mm to $x$ = 7 mm, (d) Case 4 for amplitude = 3 mm at $x$ = 2 mm to $x$ = 8 mm.

(a)

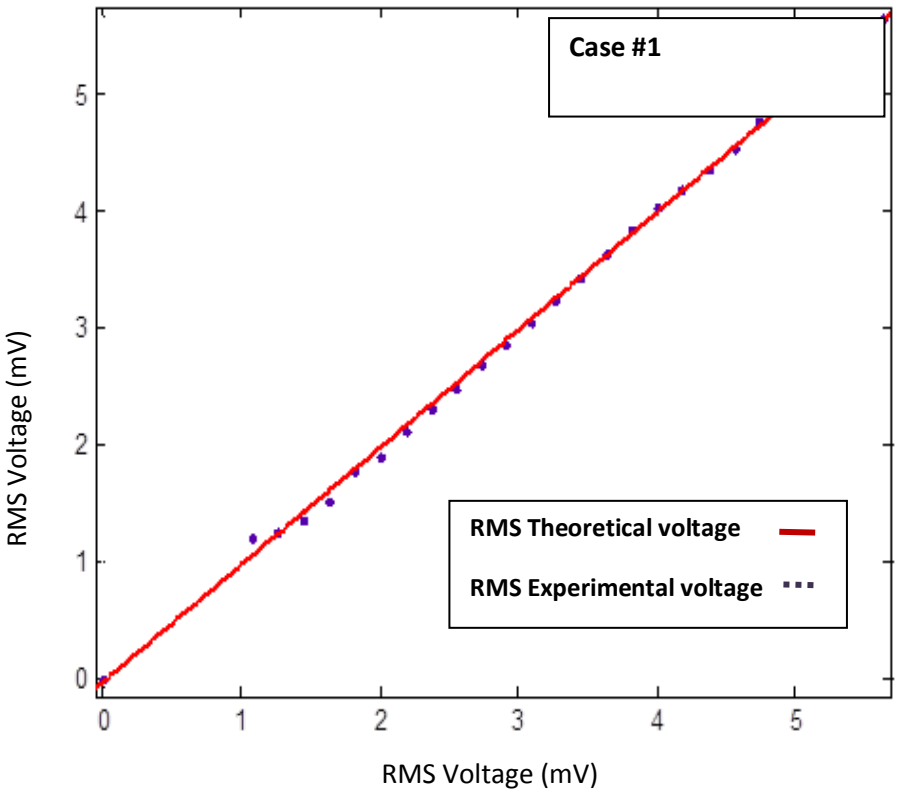
Case #1
RMS Theoretical voltage
RMS Experimental voltage
RMS Voltage (mV)
RMS Voltage (mV)
0
1
2
3
4
5

(b)

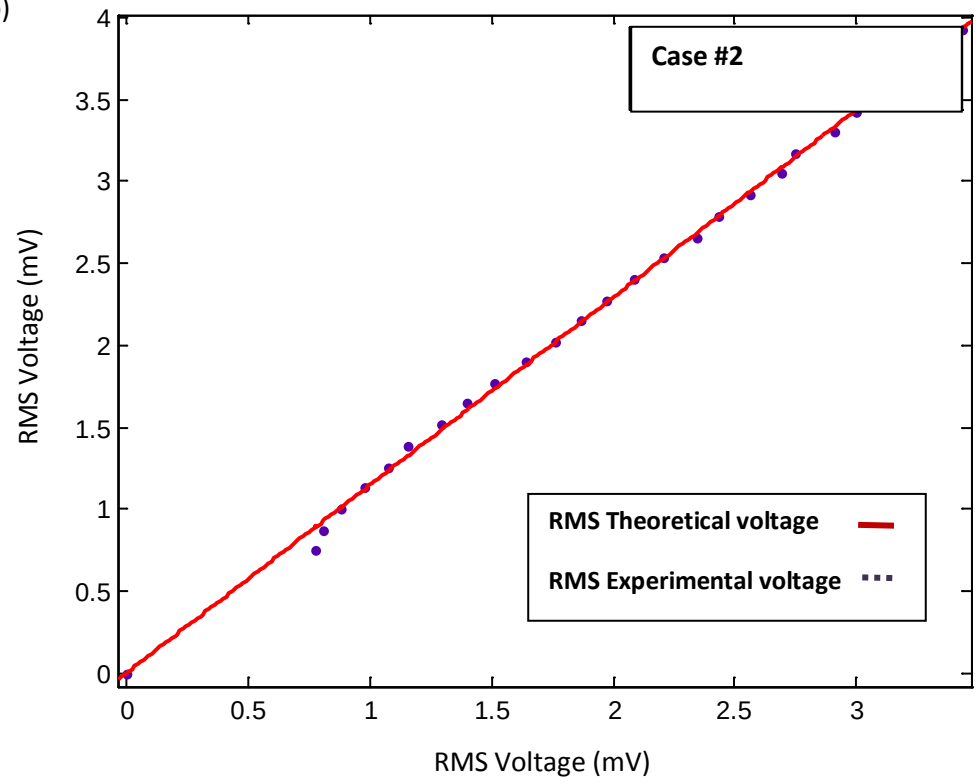
Case #2
RMS Theoretical voltage
RMS Experimental voltage
RMS Voltage (mV)
RMS Voltage (mV)
0
0.5
1
1.5
2
2.5
3
3.5
4

(c)

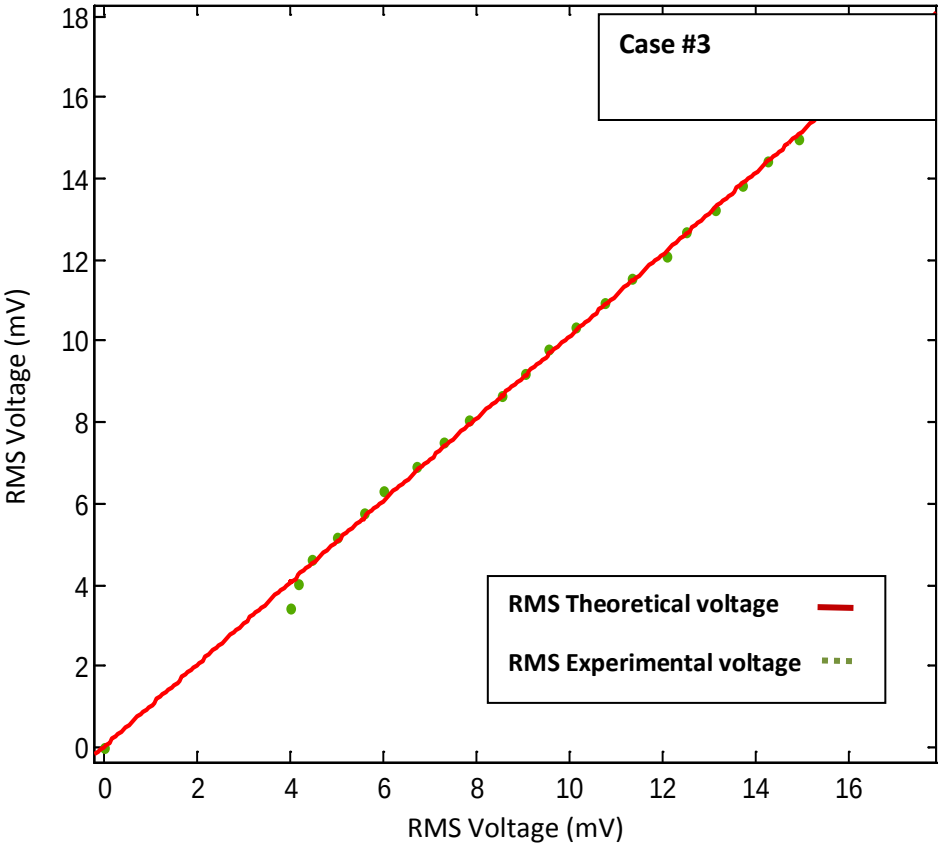


(d)

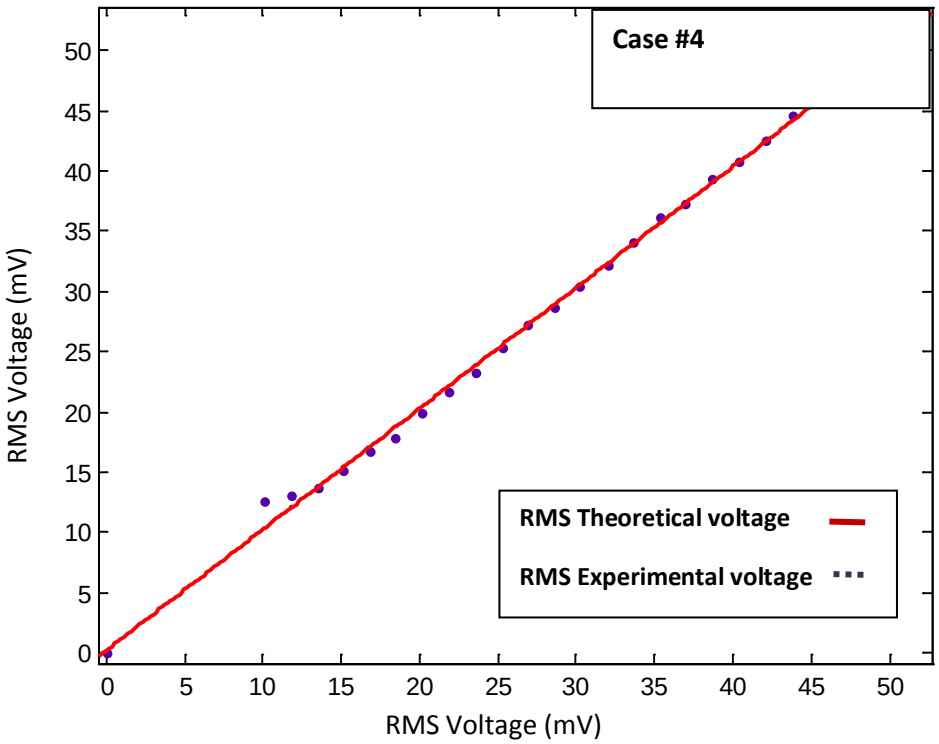


Figure 3.16 Curve fitness test to validate experimental results against theoretical value of voltage for all the 4 cases. (a) Case 1 for amplitude = 0.75 mm at $x$ = 3 mm to $x$ = 5 mm, (b) Case2 for amplitude = 0.75 mm at $x$ = 5 mm to $x$ = 7 mm, (c) Case 3 for amplitude = 0.875 mm at $x$ = 3 mm to $x$ = 7 mm, (d) Case 4 for amplitude = 3 mm at $x$ = 2 mm to $x$ = 8 mm. All voltages in mV.

Table 3.3. Goodness-of-fit statistics for Cases 1 to 4.

| Experiment | SSE | R-Square | Adjusted R-Square | RMSE |
|---|---|---|---|---|
| Case 1 | 0.06215 | 0.9994 | 0.9993 | 0.04629 |
| Case 2 | 0.04018 | 0.9991 | 0.9991 | 0.03722 |
| Case 3 | 0.6848 | 0.9993 | 0.9993 | 0.1536 |
| Case 4 | 10.39 | 0.9987 | 0.9987 | 0.5986 |

### 3.7.4 Power frequency responses SDOF1DUD EMVEH

The theoretical and experimental values of the average power generated for each of the four different cases were obtained, as in Figure 3.17**,** using the formula,

$$P_{rms} = \mathrm{VI}\ \cos\varphi\ = \frac{\mathrm{V}^2}{\mathrm{Z}}\cos\varphi \tag{3.33}$$

where $\cos\varphi$ is the power factor and $\varphi$ is the phase difference between the current and voltage. The power factor is given by the relation,

$$\cos\varphi = \frac{\mathrm{R}}{\mathrm{Z}} \tag{3.34}$$

where, R is the resistance of the circuit and Z is the total impedance of the circuit.

It was observed that Case 4 produced a great deal of power due to high amplitude. Also the power achieved in Case 3 was greater than Case 1, showing that the spatial variation of the magnetic field had a significant effect on power generation.

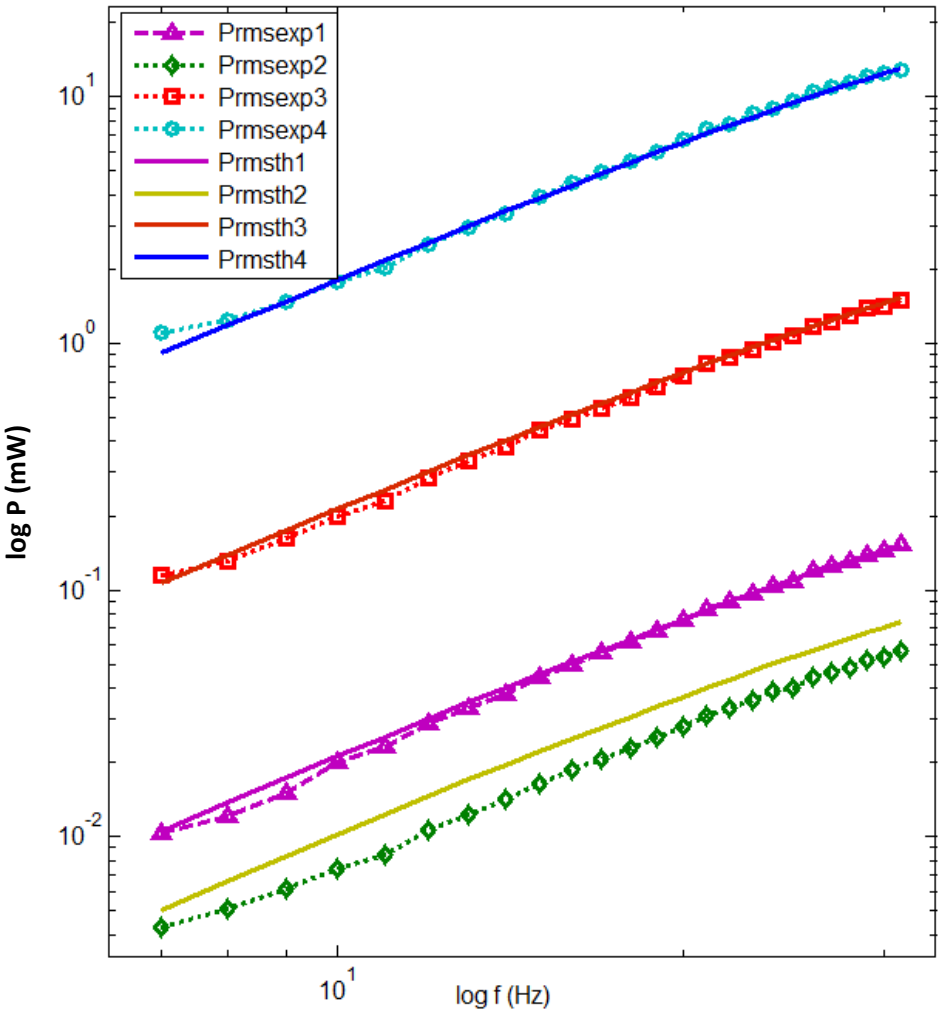


Figure 3.17 Logarithmic plot of theoretical and experimental power generated by SDOF1DUD EMVEH in mW for all the 4 cases. Prmsexp1 = experimental power for Case 1, Prmsth1 = theoretically obtained power for Case 1, Prmsexp2 = experimental power for Case 2, Prmsth2 = theoretically obtained power for Case 2, Prmsexp3 = experimental power for Case 3, Prmsth3 = theoretically obtained power for Case 3, Prmsexp4 = experimental power for Case 4, Prmsth4 =theoretically obtained power for Case 4.

## 3.8 Conclusions

The spatial variation of the magnetic field along with the governing analytical equations were derived and analysed for the SDOF1DUD EMVEH in this chapter. Comparison between empirical and experimental results confirmed the validity of the models. The magnetic field was considered as constant during the derivation of the voltage generated in the case of transformers and generators. This opens up new possibilities for the designing of EMVEHs.

A unique approach encompassing multiple methods can be used as a guideline for the design of electromagnetic vibration energy harvesting. The SDOF1D-UD design protocol consisted of: (a) finding the $B_x$ versus $x$ variation numerically, using Magnetostatic software such as Vizimag or ANSOFT, (b) fitting an analytical equation derived by including magnetostatic findings in the Maxwell-Faraday equation for generated EMF; this included an approximate $B_x$ variation within the range of coil motion, and (c) designing the prototype. Comparing the analytical results with those values obtained from experimentation with the prototype, it was confirmed that the approach is suitable for the designing of new energy harvesters.

One of the key design concerns with regard to any energy harvester is to generate maximum power without the energy harvester being bulky. This is technically known as the power to volume ratio. This ratio is vital, particularly with regard to the electromagnetic energy harvester design. The reason for this is that the density of the iron core and magnet material makes the EMVEH not only voluminous but also heavy. To combat this problem, the EMVEH must be compact in design and space constraints must be considered. The current research into spatial variation was useful in showing that greater power can be produced in a compact design by altering the spatial variation. This finding has assisted in the growth of EMVEH research. The current study into spatial variation of the magnetic field can be utilised to design compact electromagnetic energy harvesters by changing the profiles of the magnets along the direction of coil motion as shown in Figure 3.18.

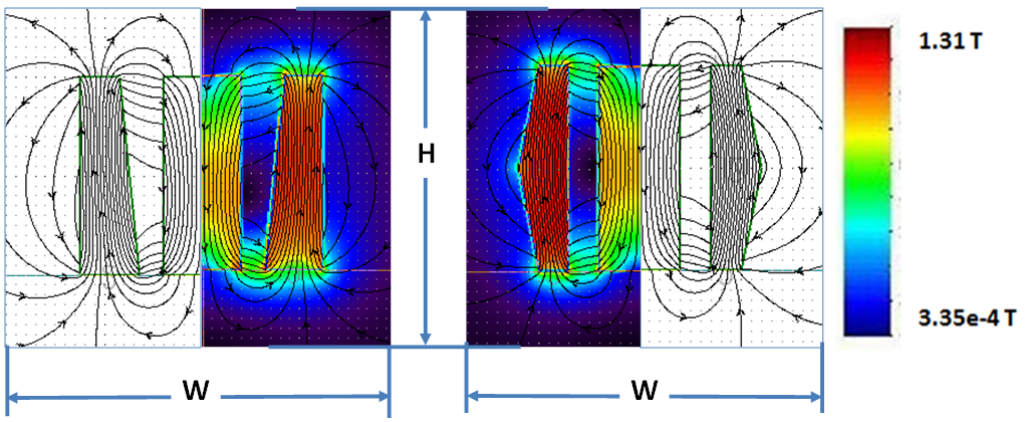


Figure 3.18 A schematic of the cross-sections of the magnet and iron-core profile designs to maximise the spatial variation for maximising generated voltage at minimum volume.

The most important conclusion, particularly relevant to this research, was that the analytical formulation of SDOF1DUD EMVEH and its accurate validation proves that similar research methodology and analytical assumptions can be applied to MDOF systems. This is discussed in subsequent chapters.

# Chapter 4 Theoretical investigation into single-degree-of-freedom damped (SDOF1D) electromagnetic vibration energy harvester

The previous chapter presented the derivation and model showing how spatial variation in a magnetic field influenced the voltage generated by an energy harvester. In that chapter, the model incorporated the coil which was directly mounted onto the vibration exciter which simulated the vibration source. This method however, is not of practical consideration where an EMVEH must be designed for a particular resonant frequency, where the amplitude of vibration and hence the generated power, is maximised. This can be achieved by mounting the coil mass onto a spring and connecting the spring base to the vibration source. The current chapter deals with the theoretical modelling and analysis of SDOF1D EMVEH – the basic model of the spring-mass-damper mechanical system coupled to the resistance-inductance-capacitance (RLC) electrical system with only one-degree-of-freedom.

## 4.1 Research methodology

The research methodology, as shown in Figure 4.1 illustrates the design of the SDOF1D model in its most basic form – the spring-mass-damper system; also referred to as the MDK system, where *M* = Mass, *D* = Damping coefficient and *K* = Spring stiffness to understand the mechanical frequency response behaviour. The MDK system with base excitation was used to choose the practical values of spring, coil and magnet dimensions for the prototype. The same design values were chosen for both analytical and experimental methods to facilitate comparison of the results.

After the study of the MDK base excitation model, the same model was coupled with the electrical RLC system, where *R* = resistance, *L* = inductance and *C* = capacitance, and RL circuits to form the SDOF1D MDKRLC EMVEH and SDOF1D MDKRL EMVEH models with identical values of *M, D, K, R* and *L*. Both of these models were compared, in order to

understand which would be the most effective model for future use in multi-degree-of-freedom EMVEH models. In Section 3.6 in Chapter 3, the magnetostatic results showed that the ends of the iron-core and magnet combination showed a significantly high rate of change of magnetic field strength as a function of position, $\partial \mathbf{B}/\partial x$. Considering this observation, an initial magnetostatic analysis was performed to determine the spatial variation of magnetic field strength in the region of the coil vibration. On the electrical side, the RL circuit and RLC circuit were compared, showing that the RL circuit was appropriate for measuring an open circuit voltage. The sensitivity analyses of the design parameters of SDOF1D EMVEH are discussed in Chapter 6 and the experimental validation of the SDOF1D EMVEH is discussed in Chapter 7.

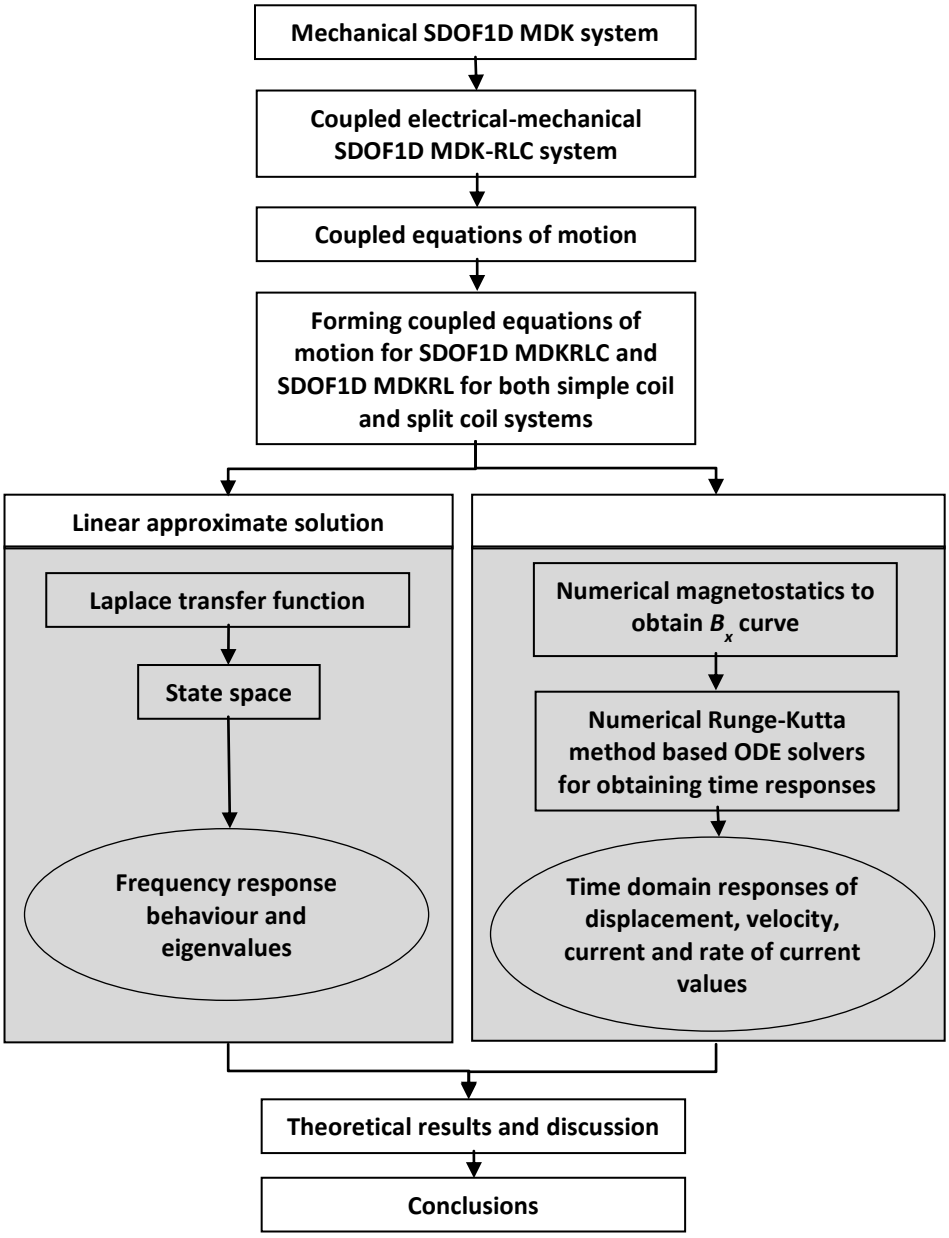


Figure 4.1 Research methodology of SDOF1D system.

The coupled equations of the SDOF1D system showed that the system is non-linear when the spatial variation is considered. Hence the coupled equations were solved using both linear and nonlinear methods as described in the steps below:

1. Initially, an approximate linear method was considered, where the magnetic field was assumed to be constant. The coupling coefficient, ($T$) was used to develop the linear system that was then solved by the Laplace transform and state space methods. The state space method was chosen for extra validation. The linear methods were used to derive the frequency response behaviour of the system and also its eigenvalues.
2. The next step was to progress to the more accurate non-linear method where the magnetic field was considered as realistic and spatially varying in every region. For this, the coupling coefficient was modelled as a function of $x$, which was the position of the coil at any instant. This was determined from the variation of the magnetic field with respect to $x$. This required an accurate profile of the magnetic field variation in the region of the coil movement. This was achieved by performing a magnetostatic numerical simulation to obtain a $B$ versus $x$ profile output. Meanwhile, since the resulting equations are non-linear, the Runge-Kutta numerical method was used. Hence, MATLAB's ODE45 was selected to use the ANSOFT MAXWELL 14.0 software's $B$ versus $x$ profile data, and to interpolate the coupling coefficient $T$ for any value of $x$ corresponding to the time instant $t$. The time responses of displacement, velocity, current and rate of current were output from the ODE45 simulation.
3. Finally, the theoretically developed and simulated SDOF1D EMVEH was experimentally validated by designing a prototype and experimenting with it in laboratory conditions. The experimental part of SDOF1D EMVEH will be discussed in detail in Chapter 6.

## 4.2 SDOF1D damped EMVEH model and design options

The SDOF1D damped EMVEH model consisted of a spring-mass-damper mechanical system coupled to the electrical resistance-inductance-capacitance circuit, as shown in Figure 4.2. The mechanical system consisted of a coil of mass, $M$, connected to the base using a spring of stiffness, $K$. The base was set into vibration motion by connecting it to the vibration

source *y*. The viscous damping of air in the assembly was modelled as damping parameter *D*. The electrical system consisted of the resistance *R*, which is the equivalent resistance of the coil and any external load resistance; inductance *L* of the coil and an external capacitor *C*.

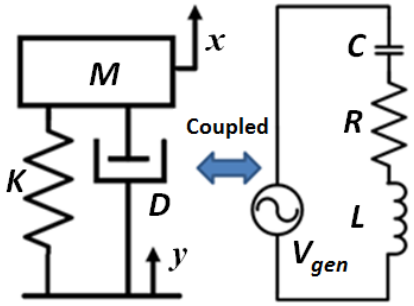


Figure 4.2 General schematic of SDOF1D model showing the mechanical MDK system coupled to the electrical RLC system.

The coil vibrates in a magnetic field created by a ring magnet and a central iron-core, both coaxial to each other, as shown in Figure 4.3. For such a magnet and iron-core configuration, an initial magnetostatic analysis was performed to obtain the magnetic field distribution throughout the direction of the coil movement.

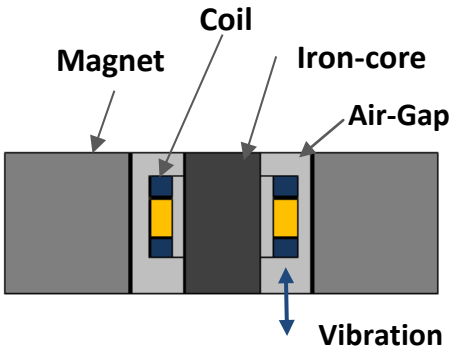


Figure 4.3 Schematic of the cross section of the SDOF1D coil vibrating in the air gap between the central iron-core and ring magnet.

It was found that the magnetic field strength was highest ($B_{max}$) at the planes corresponding to the top and bottom surface of the magnets and was least ($B_{min}$) in the middle. Hence, two methods of designing the coil were observed : a) single coil design, with a single coil at the centre, that moves from the centre towards the surface planes of $B_{max}$ or, b) split coil

design having a coil split into two with each centre fixed at the $B_{max}$ positions, as shown in Figure 4.4.

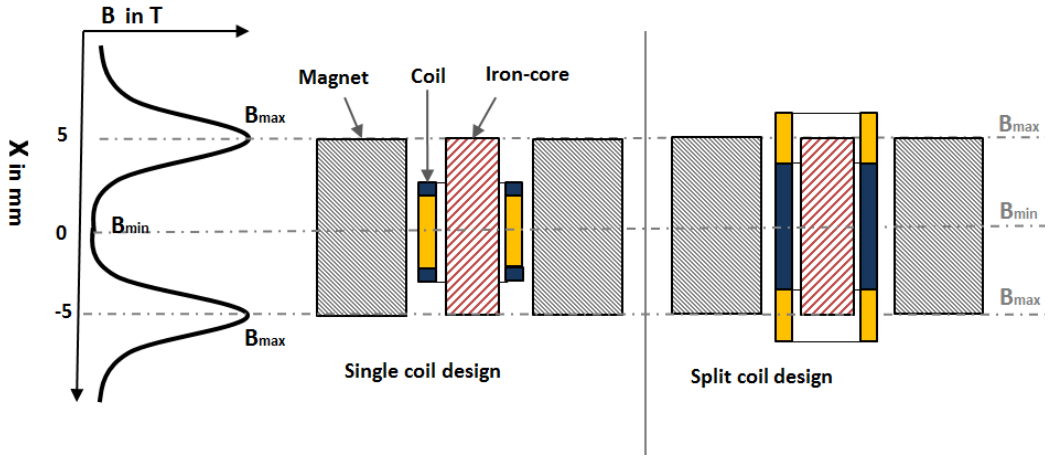


Figure 4.4 Schematic cross-sectional views of two coil design options for SDOF1D EMVEH.

The other design option was in the electrical RLC system of the SDOF1D EMVEH model. Since the inductance and resistance of the coil was fixed, one could achieve variability in the electrical system by having a capacitor with varying value, as shown in Figure 4.5. Hence, there were two options for the electrical system: a) RLC circuit and b) RL circuit.

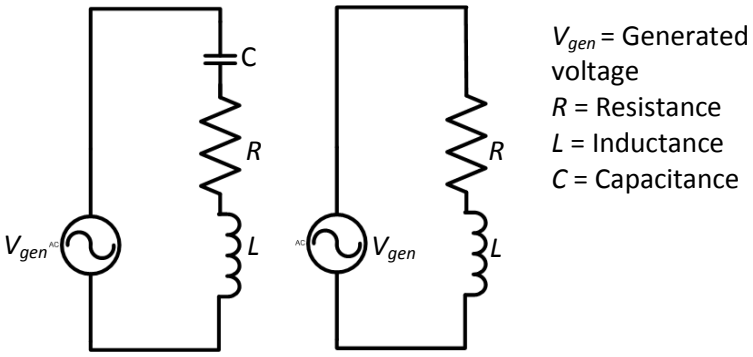


Figure 4.5 RLC and RL design options.

For simplicity, a single coil SDOF1D EMVEH was chosen, although the split coil was a better design in that it effectively utilised the high spatial variation range of the magnetic field. Taking into account all of these design alternatives, the theoretical simulation of SDOF1D was divided into nine analyses, as shown in Table 4.1. The SDOF1D EMVEH model was initially analysed in its basic SDOF MDK system form which consisted of the mechanical system only, i.e., without the electrical transduction mechanism. The next model under

study was the SDOF1D MDKRLC system wherein the mechanical MDK system was coupled to the RLC circuit. The third model to be considered was the SDOF1D MDK RL system where the RL circuit was coupled to the mechanical MDK system. The values of the design parameters *M, D, K, R, L, C* and *T* were constants, in all nine analyses to ensure fair comparison of the results (see Table 4.1).

Table 4.1. Theoretical simulations of SDOF1D Model.

| | | | Mass | Damping coefficient | Spring stiffness | Resistance | Inductance | Capacitance | Coupling coefficient |
|---|---|---|---|---|---|---|---|---|---|
| | | | ***M*** **(kg)** | ***D*** **(Ns/m)** | ***K*** **(N/m)** | ***R*** **(Ohm)** | ***L*** **(H)** | ***C*** **(F)** | ***T*** **(NC/s)** |
| **SDOF1D MDK** | **1** | **Laplace** | 0.0015 | 0.1 | 160 | N/A* | N/A | N/A | N/A |
| | **2** | **State space** | 0.0015 | 0.1 | 160 | N/A | N/A | N/A | N/A |
| | **3** | **Non-linear** | 0.0015 | 0.1 | 160 | N/A | N/A | N/A | N/A |
| **SDOF1D MDKRLC** | **4** | **Laplace** | 0.0015 | 0.1 | 160 | 0.3 | 0.016 | 1 X $10^{-9}$ | 0.4916 |
| | **5** | **State space** | 0.0015 | 0.1 | 160 | 0.3 | 0.016 | 1 X $10^{-9}$ | 0.4916 |
| | **6** | **Non-linear** | 0.0015 | 0.1 | 160 | 0.3 | 0.016 | 1 X $10^{-9}$ | Variable |
| **SDOF1D MDKRL** | **7** | **Laplace** | 0.0015 | 0.1 | 160 | 0.3 | 0.016 | N/A | 0.4916 |
| | **8** | **State space** | 0.0015 | 0.1 | 160 | 0.3 | 0.016 | N/A | 0.4916 |
| | **9** | **Non-linear** | 0.0015 | 0.1 | 160 | 0.3 | 0.016 | N/A | Variable |

*N/A = Not applicable

## 4.3 Simulation of the SDOF1D MDK system

Consider a coil of mass *M* suspended by spring *K* in a base moving with acceleration $\ddot{y}$ and displacement at any time *t*, as shown in Figure 4.6. Let the displacement of the coil mass *M* be $x$ due to the base motion $y$.

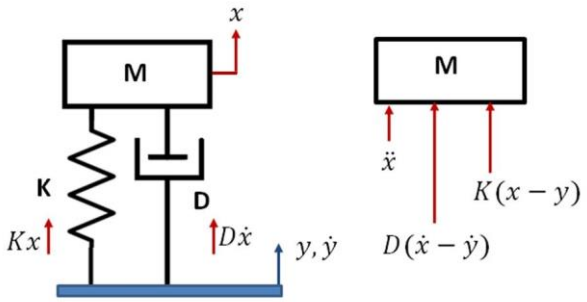


Figure 4.6 A simple SDOF1D MDK system.

The resulting equations of motion will be given by:

$$M\ddot{x} + D(\dot{x} - \dot{y}) + K(x - y) = 0. \tag{4.1}$$

This can be rewritten as:

$$M\ddot{x} + D\dot{x} + Kx = D\dot{y} + Ky. \tag{4.2}$$

### 4.3.1 Laplace transform analysis of SDOF1D MDK system

The equation (4.2) becomes,

$$Ms^2X(s) + DSX(s) + KX(S) = DSY(s) + KY(s) \tag{4.3}$$

after applying Laplace transforms and ignoring initial conditions. Here, the Laplacian operator, $s$ is defined as a complex number $s = j\omega$, where $\omega$ is the angular velocity of the coil motion $y$. The resulting transfer function of the system can be given by:

$$H(s) = \frac{X(s)}{Y(s)} = \frac{Ds + K}{Ms^2 + Ds + K} \tag{4.4}$$

The resulting frequency response is obtained from $H(j\omega) = H(s)$ where $s = j\omega$ and $\omega$ is the excitation frequency (rad/s). A theoretical simulation was run to yield the following results (See Appendix B for MATLAB code) using the following realistic design values of $M$ = 0.0015 kg, $D$ = 0.10 Ns/m and $K$ = 160 N/m. The results of the simulation are shown in Figure 4.7.

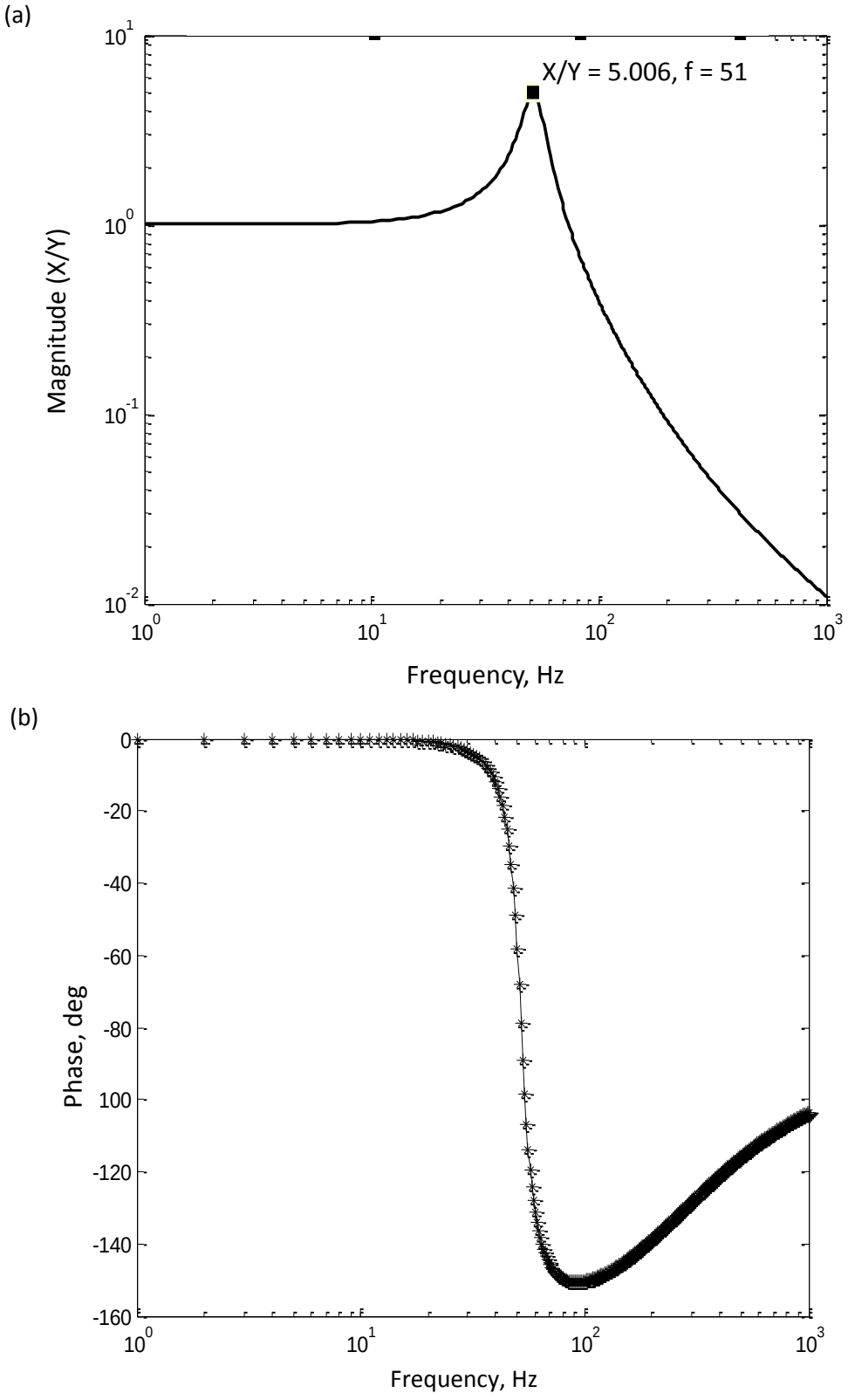


Figure 4.7 Frequency response of SDOF1D MDK system.

### 4.3.2 State space analysis of SDOF1D MDK only system

Equation (4.2) can be written in state space form by considering the state variables $V_1$ and $V_2$. This gives:

$$V_1 = x, \tag{4.5}$$

and

$$V_2 = \dot{x}, \tag{4.6}$$

respectively.

Differentiating (4.5) and (4.6) and applying (4.2),

$$\frac{dV_1}{dt} = \dot{x} = V_2 \tag{4.7}$$

$$\frac{\mathrm{dV_2}}{\mathrm{dt}} = \ddot{x} = \frac{1}{\mathrm{M}}[\mathrm{D\dot{y} + Ky - DV_2 - KV_1}] \tag{4.8}$$

the resulting state space matrix form of the differential equation gives:

$$\begin{bmatrix} \frac{dV_1}{dt} \\ \frac{dV_2}{dt} \end{bmatrix} = \begin{bmatrix} 1 & 0 \\ \frac{-K}{M} & \frac{-D}{M} \end{bmatrix} \begin{bmatrix} V_1 \\ V_2 \end{bmatrix} + \begin{bmatrix} 0 & 0 \\ \frac{K}{M} & \frac{D}{M} \end{bmatrix} \begin{bmatrix} y \\ \dot{y} \end{bmatrix} \tag{4.9}$$

The theoretical simulation was run to yield the following results (See Appendix B for MATLAB code) using the following realistic design values of $M$ = 0.0015 Kg, $D$ = 0.10 Ns/m, $K$ = 160 N/m.

The resulting eigenvalues obtained were $\lambda_{i=1\ to\ 4}$ = -33.33 + 324.9i, 0, 0 and -33.33 -324.9i as shown in Figure 4.8. The corresponding natural frequencies were obtained using the formula:

$$\omega_i = \sqrt{Re(\lambda_i)^2 + Im(\lambda_i)^2} = 326.6 \text{ rad/s} \tag{4.10}$$

or $f_i$ = 51.97Hz close to Laplace's transform frequency response. Similarly, the damping ratios $\zeta_i$ , $\zeta_{i+1}$ , $\zeta_{i+2}$ and $\zeta_{i+3}$ can be given by:

$$\zeta_i, \zeta_{i+1} = Re(\lambda_i)/\sqrt{Re(\lambda_i)^2 + Im(\lambda_i)^2} = 0.102 \quad (4.11)$$

$$\zeta_{i+2}, \zeta_{i+3} = Re(\lambda_i)/\sqrt{Re(\lambda_i)^2 + Im(\lambda_i)^2} = 0 \quad (4.12)$$

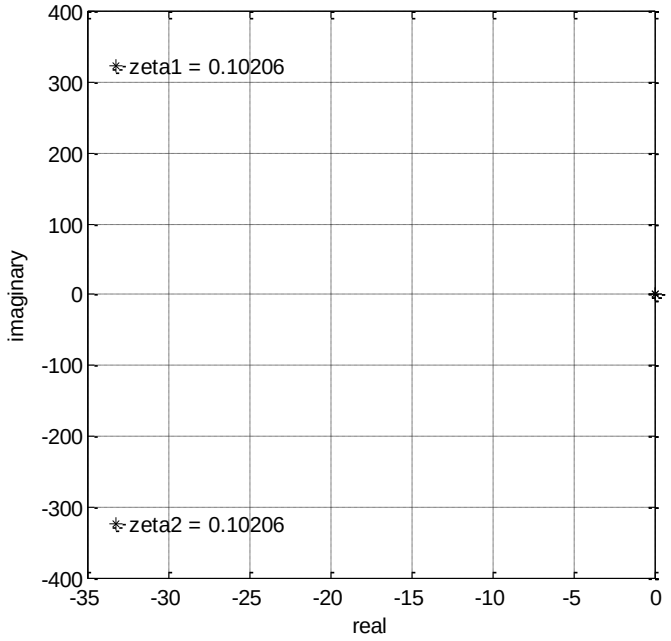


Figure 4.8 Plot of eigenvalues of SDOF1D MDK state space analysis.

### 4.3.3 Numerical simulation analysis

Although the SDOF1D MDK system is linear, a numerical simulation was used to obtain the time response of the coil displacement and velocity. The theoretical simulation was run to yield results (See Appendix B for MATLAB code) using the following realistic design values of $M$ = 0.0015 kg, $D$ = 0.10 Ns/m, $K$ = 160 N/m, $f$ = 51.97Hz, amplitude $A$ = 0.1 mm. The base excitation was assumed to have the initial displacement $y$ = 0 and its corresponding velocity, $\dot{y} = 0$. The results of the simulation are given in Figure 4.9.

As expected, the displacement $x$ and the velocity $\dot{x}$ were sinusoidal and were 90° out of phase with one another. The amplitude of displacement was $x = 0.1$ mm. From Figure 4.6, $X/Y$ = 5.006 at 51.97 Hz, thus $x$ = 5.006 × 0.0001 = 0.0005 m. This confirms the amplitude of the displacement signal, as shown in Figure 4.9 (b).

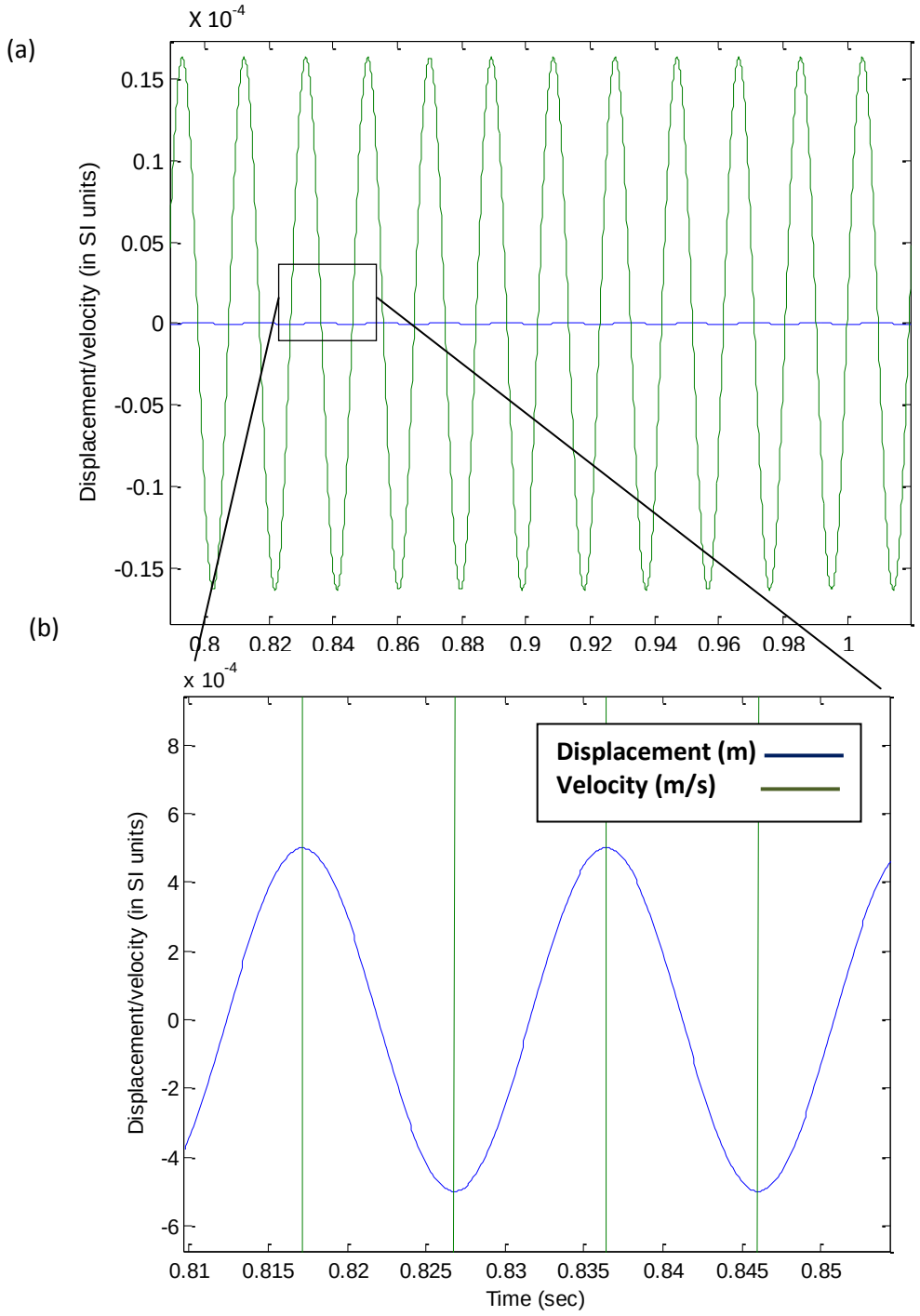


Figure 4.9 SDOF1D MDK coil (a) displacement and velocity response (b) displacement versus time zoomed in.

## 4.4 SDOFID energy harvester –MDK RLC /RL system derivation

In Section 4.4, only the mechanical part of the SDOF1D EMVEH, namely, the MDK system was analysed. The SDOF1D EMVEH, as shown in Figure 4.2 was a coupled mechanical-electrical system. Hence, the next step was to consider the coupled mechanical and electrical systems of the SDOF1D EMVEH.

The SDOF1D EMVEH system was assumed to be vibrating in the $x$ direction with a base motion $y$. Let $D$ = viscous damping due to air in the coil gap and $K$ = spring stiffness. Considering the free body diagram of the coil mass $M$ as shown in Figure 4.10, Newton's second law states that the sum of all the forces is equal to the mass multiplied by the acceleration. This can be written as:

$$\sum F = M\ddot{x}. \tag{4.13}$$

Therefore,

$$M\ddot{x} + D(\dot{x} - \dot{y}) + K(x - y) + F_L = 0, \tag{4.14}$$

where $F_L$= the Lorentz force which is the electrical damping force. Equation (4.13) can be rearranged as:

$$M\ddot{x} + D\dot{x} + Kx + F_L = D\dot{y} + Ky. \tag{4.15}$$

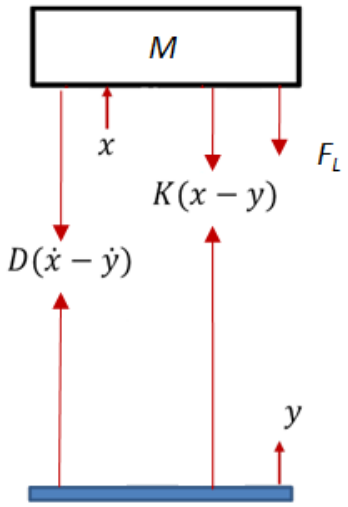


Figure 4.10 Free body diagram of SDOF1D MDK RLC system.

Consider the voltage across the RLC circuit, as shown in Figure 4.2. The induced voltage generated by the induction ($V_{gen}$) is given by *R*, *L* and *C* as $V_R$, $V_L$ and $V_C$ respectively as:

$$V_{gen} = V_R + V_L + V_{c.} \tag{4.16}$$

In terms of current $I$, Equation 4.16 becomes:

$$V_{gen} = RI + L\dot{I} + (1/C)\int_0^{\tau} Idt. \tag{4.17}$$

Consider that there are *n* turns in the coil moving in the positive $x$ direction, as in Figure 4.11.

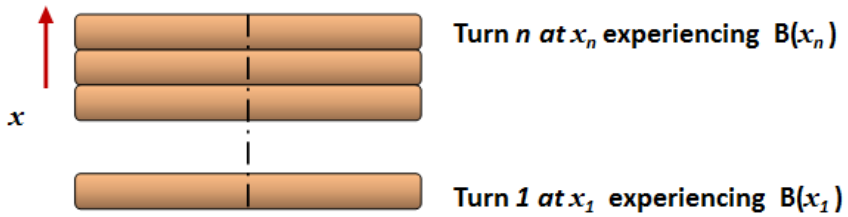


Figure 4.11 Schematic representation of the coil of n turns.

For turn 1 of the coil, Faraday's law gives the voltage generated as:

$$V_1 = 2\pi r_c B(x_1).\dot{x}_1, \tag{4.18}$$

where $r_c$ is the radius of the coil, $B(x_1)$ represent the magnitude of the magnetic field at $x_1$, $\dot{x}_1$ the velocity of the coil at turn 1.

Equation (4.18) is valid only when the magnet is in a static position and the coil is moving to a position $x_1$ relative to the magnet. In the current SDOF1D EMVEH design, the entire energy harvester is mounted onto a vibration source having motion $y$. Since the magnet is assumed to be rigidly fixed to the base, it also moves with base motion $y$. Hence turn 1 of the coil is located at position ($x_1$-$y$).

Equation (4.18) can then be modified to:

$$V_1 = 2\pi r_c B(x_1 - y)(\dot{x}_1 - \dot{y}), \tag{4.19}$$

where $B(x_1\text{-}y)$ represents the magnetic field at $(x_1\text{-}y)$.

Similarly, the generated voltage at coil turn 2 will be

$$V_2 = 2\pi r_c B(x_2 - y)(\dot{x}_2 - \dot{y}), \tag{4.20}$$

and

$$V_n = 2\pi r_c B(x_n - y)(\dot{x}_n - \dot{y}), \tag{4.21}$$

for the coil turn *n*.

Since the *n* turns of the coil are in series, the total voltage of the entire coil can be given by:

$$V = \sum_{i=1}^{n} V_i, \tag{4.22}$$

which can be written as:

$$V = 2\pi r_c \sum_{i=1}^{n} B(x_i - y).(\dot{x}_i - \dot{y}), \tag{4.23}$$

The second coil turn position can be given by:

$$x_2 = x_1 - d. \tag{4.24}$$

Similarly, the $n^{th}$ coil turn position can be given by:

$$x_n = x_1 - (n-1)d. \tag{4.25}$$

If $x$ is the position of the entire coil at any instant in time, the positions $x_1$, $x_2$, $x_3 \ldots x_n$ are at distances $d_1$, $d_2$, $d_3 \ldots d_n$ from the coil's absolute coordinates system. The velocities of each of these turns are the same. Hence, this can be expressed as:

$$\dot{x}_1 = \dot{x}_2 = \dot{x}_3 = \ldots = \dot{x}_n = \dot{x}, \tag{4.26}$$

where $\dot{x}$ *is* the velocity of the coil. The voltage generated by the entire coil can then be written as:

$$V = 2\pi r_c \sum_{i=1}^{n} B(x_i - y).(\dot{x} - \dot{y}) \tag{4.27}$$

Now, consider the Lorentz force generated due to the coil motion. This force is responsible for electromagnetic damping and gives the electromagnetic damping force in the SDOFID system context.

Each turn in the coil exerts a Lorentz force that opposes the motion of the coil.

The Lorentz force is given by:

$$F_L = BIl \sin\theta = BIl \tag{4.28}$$

where, $B$ represents the magnetic field, $l$ represents the length of the conductor, and $I$ represents the current. The angle between the magnetic field and the direction of coil motion represented by $\theta$ is 90° as the motion of the coil is assumed to be perpendicular to the magnetic field.

Hence for the first turn of the coil, the Lorentz force can be written as:

$$F_{L_1} = B(x_1 - y).I(2\pi r_c) \tag{4.29}$$

Similarly, the Lorentz force for the second turn of the coil can be written as:

$$F_{L_2} = B(x_2 - y).I(2\pi r_c) \tag{4.30}$$

and for the $n^{th}$ turn of the coil can be written as:

$$F_{L_n} = B(x_n - y).I(2\pi r_c). \tag{4.31}$$

Since these Lorentz forces of individual coil turns are in the same direction, they can be summed up using the principle of superposition of forces. The effective Lorentz force of the entire coil is then given by:

$$F_L = F_{L_1} + F_{L_2} + \cdots F_{L_n} = \sum_{i=1}^{n} F_{L_n} \tag{4.32}$$

Using equation (4.31), equation (4.32) becomes,

$$F_L = 2\pi r_c I. \sum_{i=1}^{n} B(x_i - y) \tag{4.33}$$

The voltage generated (equation (4.27)) and the total Lorentz force (equation (4.33)) have one term in common which was designated as the coupling coefficient $T(x, y)$, which is given by:

$$T(x,y) = 2\pi r_c \sum_{i=1}^{n} B(x_i - y) \tag{4.34}$$

Substituting $T(x, y)$, one can obtain the SDOF1D MDKRLC coupling system in the form of the two systems of equations:

### 4.4.1 SDOF1D MDKRLC coupled EMVEH system

The single-degree-of-freedom system with RLC electric circuit can be considered by the following analysis:

The force equation can be given by:

$$M\ddot{x} + D\dot{x} + Kx + T(x,y)I = D\dot{y} + Ky, \tag{4.35}$$

and the voltage equation by:

$$L\ddot{I} + R\dot{I} + {}^{1}/_{C}\, I = T(x,y).(\ddot{x} - \ddot{y}). \tag{4.36}$$

In matrix form, equations (4.35) and (4.36) can be written as:

$$\begin{bmatrix} M & 0 \\ -T(x,y) & L \end{bmatrix}\begin{bmatrix} \ddot{x} \\ \ddot{I} \end{bmatrix} + \begin{bmatrix} D & 0 \\ 0 & R \end{bmatrix}\begin{bmatrix} \dot{x} \\ \dot{I} \end{bmatrix} + \begin{bmatrix} K & T(x,y) \\ 0 & 1/C \end{bmatrix}\begin{bmatrix} x \\ I \end{bmatrix} = \begin{bmatrix} K & D & 0 \\ 0 & 0 & -T(x,y) \end{bmatrix}\begin{bmatrix} y \\ \dot{y} \\ \ddot{y} \end{bmatrix} \tag{4.37}$$

### 4.4.2 SDOF1D MDKRL coupled EMVEH system

In the absence of capacitance, the system SDOF1D MDKRLC described in equations (4.35) to (4.37) reduces to the SDOF1D MDKRL system. The coupled system equations for SDOF1D MDKRL will thus have:

force equation as,

$$M\ddot{x} + D\dot{x} + Kx + T(x,y)I = D\dot{y} + Ky, \tag{4.38}$$

and the voltage equation as:

$$L\ddot{I} + R\dot{I} = T(x,y).(\ddot{x} - \ddot{y}). \tag{4.39}$$

Integrating with respect to time, (4.39) reduces to

$$L\dot{I} + RI = T(x,y).(\dot{x} - \dot{y}). \tag{4.40}$$

In matrix form, (4.38) and (4.40) can be written as

$$[M][\ddot{x}] + \begin{bmatrix} D & 0 \\ -T(x,y) & L \end{bmatrix}\begin{bmatrix} \dot{x} \\ \dot{I} \end{bmatrix} + \begin{bmatrix} K & T(x,y) \\ 0 & R \end{bmatrix}\begin{bmatrix} x \\ I \end{bmatrix} = \begin{bmatrix} K & D \\ 0 & -T(x,y) \end{bmatrix}\begin{bmatrix} y \\ \dot{y} \end{bmatrix}. \tag{4.41}$$

### 4.4.3 SDOF1D EMVEH coil design alternatives

The coil of the SDOF1D EMVEH can be designed in two ways: (a) a single coil assembly that can be at the middle of the coil holder, (b) a split coil assembly wherein the coil is split at the top and bottom of the coil holder with a spacer in between. The coil designs only change the spatial variation of the magnetic field as experienced by the coil and hence will affect only *T*.

The single coil design is straightforward and the coupling coefficient for the single coil design is given by,

$$T(x,y) = 2\pi r_c \sum_{i=1}^{n} B(x_i - y) \approx 2\pi n r_c B(x_m - y), \tag{4.42}$$

where $B(x_m - y)$ is the magnetic field experienced at the middle turn of the entire coil. This yields an approximate magnetic field strength experienced by the entire coil, but is better than considering magnetic field *B* as a constant (discussed in detail in Section 4.7).

The split coil design is different and requires separate derivation. Consider the split coil design vibration wherein the position of the coil centre is known at any instant *t*. Consider the split coil as having two coils, Coil 1 and Coil 2 as shown in Figure 4.12.

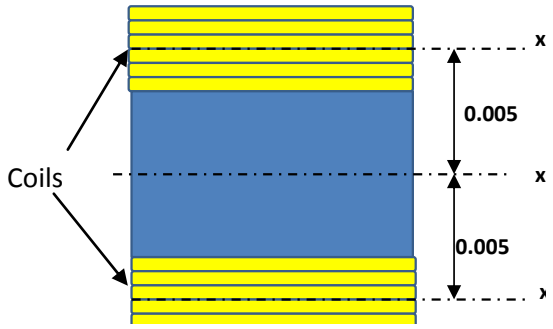


Figure 4.12 Split coil design.

Since the coil is made from two parts; coil 1 and coil 2, where the number of turns (*n*) can be equally divided into each of these coils. These coils are assumed to be spaced 10 mm apart. The coil positions can be given by $x_1$ and $x_2$ where:

$$x_1 = x - 0.005, \tag{4.43}$$

and

$$x_2 = x + 0.005. \tag{4.44}$$

If the voltage generated by the entire coil is the sum of the voltages of the individual coils $V_{gen1}$ and $V_{gen2}$, then it can be given by:

$$V_{gen1} = 2\pi(n/2)rB(x_1 - y)\dot{x}_1, \tag{4.45}$$

and

$$V_{gen2} = 2\pi(n/2)\,rB(x_2 - y)\dot{x}_2, \tag{4.46}$$

as the velocities of both the coils are the same as shown earlier in (4.26).

The Lorentz force of each of these coils can be considered to be $F_{L1}$ and $F_{L2.}$

The Lorentz force at coil 1 can be written as:

$$F_{L_1} = BIl\sin\theta = BIl,$$

since the magnetic flux lines are assumed to be perpendicular to the direction of coil motion. Hence, this becomes:

$$F_{L_1} = B(x_1 - y)I_1[2\pi(n/2)r_c] = \pi n r_c B(x_1 - y).I_1 \quad (4.47)$$

Similarly, the Lorentz force at coil 2 can be given by,

$$F_{L_2} = \pi n r_c B(x_2 - y).I_2 \quad (4.48)$$

If both the coils are in same phase, then the total Lorentz force for the two coils then becomes:

$$F_L = F_{L_1} + F_{L_2} = \pi n r_c\big(B(x_1 - y) + B(x_2 - y)\big)I, \quad (4.49)$$

where $I_1 = I_2 = I$.

Equations (4.45) (4.46) and (4.49) have a common term: $\pi n r_c(B(x_1 - y) + B(x_2 - y))$ which can be represented as the coupling coefficient.

Hence, for the split coil, the coupling coefficient $T(x,y)$ is given by:

$$T(x, y) = \pi n r_c\big(B(x_1 - y) + B(x_2 - y)\big) \quad (4.50)$$

For simplicity, a simple coil design was considered in the SDOF1D theoretical analyses and the experimental validation shown in subsequent chapters.

## 4.5 Methods of simulating the SDOF1D MDK RL/RLC system

The coupling coefficient $T(x, y)$ as defined in equation (4.27) is highly accurate, but computationally it is very intensive. This is because it has to iterate the value for every $B(x_i\text{-}y)$, $i$ = 1 to $n$ for each of the coil turns and then sum them.

Three approaches can be considered for obtaining the solution to the SDOF1D MDK RL coupled equations:

The first method is to consider $T(x,y)$ = constant = $2\pi r_c n B_{max}$. This converts the coupled equations to linear format that can be solved by the Laplace transform and state space methods. The solution is approximate, but it is sufficient for understanding the frequency response and the system eigen values.

The second method is to consider $T(x, y) = 2\pi r_c n B(x - y)$ where,

$$B(x_1 - y) = B(x_2 - y) = \cdots B(x_n - y) = B(x - y), \tag{4.51}$$

and $x$ is the position of the centre of the coil. This method retains the coupled equations as non-linear, but drastically reduces the computational time. The simulation time is reduced by (*1/n*) times by negating the computation of each value of $B(x, y)$ to get $T(x,y)$ for every time step.

The non-linear equation can be solved using the numerical Runge-Kutta method based on ordinary differential equation solvers like MATLAB's ODE45. $T(x, y)$ can be obtained from the value of $B(x)$ versus $x$ profile that can be obtained by numerical magnetostatic finite element analysis. The $B$ versus $x$ data can then be fed to the ODE solver to obtain time domain responses.

The third method is to consider $T(x, y) = 2\pi r_c \sum_{i=1}^{n} B(x_i - y)$. This can also be solved using a numerical ODE solving and magnetostatic approach and is the most accurate approach, but again computationally it is very intensive and practically not possible if there are more number of coils. Hence the method was not considered in this thesis and the second method, as discussed above, was considered for the non-linear analysis. In summary, the coupling coefficient approximations and its uses are as shown in Table 4.2.

Table 4.2. Coupling coefficient assumptions and the accuracy of solutions.

| **Coupling coefficient** | **Solution methods** | | **Accuracy** |
|---|---|---|---|
| $T(x,y) = \text{Constant} = 2\pi r_c n B$ | Linear. | Laplace, state space. | Very approximate. |
| $T(x,y) = 2\pi r_c n B(x - y)$ | Non-linear. | Runge-Kutta (ODE45) + FEA. | Optimum. |
| $T(x,y) = 2\pi r_c \sum_{i=1}^{n} B(x_i - y)$ | Non-linear. | Runge-Kutta (ODE45) + FEA, Not considered in this thesis. | Very accurate. |

## 4.6 Theoretical analyses of SDOF1D MDKRLC EMVEH system

In the previous section (Section 4.6), the SDOF1D MDKRLC EMVEH system was modelled as a set of coupled electrical-mechanical equations as described in Section 4.5.1. In this section, the Laplace transform analysis was used to find out an approximate solution for the voltage output followed by state space analysis. This was followed by a more accurate nonlinear method using magnetostatic data to find the coupling coefficient (*T*) and Runge-Kutta based ODE solvers for the nonlinear ODE thus formed.

### 4.6.1 Linear Laplace transform analysis for SDOF1D MDK RLC single coil coupled system

The coupling coefficient $T(x,y)$ is modelled here to be a constant given by $T = Constant = 2\pi r_c NB$. The coupled equations of the energy harvester in Laplace transform form ignoring initial conditions are given by,

$$\begin{bmatrix} (Ms^2 + Ds + K) & T \\ -CTs^2 & LCs^2 + RCs + 1 \end{bmatrix} \begin{bmatrix} X(s) \\ I(s) \end{bmatrix} = \begin{bmatrix} Ds + K \\ -CTs^2 \end{bmatrix} [Y(s)], \tag{4.52}$$

where $s = j\omega$ and $\omega$ = angular velocity of the base motion $y$.

This is of the form $[A][\alpha] = [B][\beta]$, where

$$[A] = \begin{bmatrix} a_{11} & a_{12} \\ a_{21} & a_{22} \end{bmatrix} = \begin{bmatrix} Ms^2 + Ds + K & T \\ -CTs^2 & LCs^2 + RCs + 1 \end{bmatrix}, [B] = \begin{bmatrix} b_1 \\ b_2 \end{bmatrix} = \begin{bmatrix} Ds + K \\ -CTs^2 \end{bmatrix}, [\alpha] = \begin{bmatrix} X(s) \\ I(s) \end{bmatrix} \; and \; [\beta] = [Y(s)].$$

Then Laplace solution for $[\alpha]$ then becomes, $[\alpha] = [A^{-1}][B][\beta]$, which gives the transfer function relationship, $\frac{[\alpha]}{[\beta]} = A^{-1}B$.

This can be rewritten as:

$$\begin{bmatrix} \frac{X(s)}{Y(s)} \\ \frac{I(s)}{Y(s)} \end{bmatrix} = A^{-1}B.$$

This can be expanded by taking the inverse of $A$ to give,

$$\begin{bmatrix} \frac{X(s)}{Y(s)} \\ \frac{I(s)}{Y(s)} \end{bmatrix} = \frac{1}{|A|}\begin{bmatrix} a_{22} & -a_{12} \\ -a_{21} & a_{11} \end{bmatrix}\begin{bmatrix} b_1 \\ b_2 \end{bmatrix},$$

which can be simplified as:

$$\begin{bmatrix} \frac{X(s)}{Y(s)} \\ \frac{I(s)}{Y(s)} \end{bmatrix} = \frac{1}{|A|}\begin{bmatrix} a_{22}b_1 & -a_{12}b_2 \\ -a_{21}b_1 & +a_{11}b_2 \end{bmatrix}$$

Hence the transfer functions are given by:

$$\frac{X(s)}{Y(s)} = \frac{1}{|A|}(a_{22}b_1 - a_{12}b_2) \tag{4.53}$$

and

$$\frac{I(s)}{Y(s)} = \frac{1}{|A|}(a_{11}b_2 - a_{21}b_1), \tag{4.54}$$

where, $a_{11}$ = Ms$^2$+Ds+K, $a_{12}$ = *T*, $a_{21}$ = *-CTs*$^2$, $a_{22}$ =*LCs*$^2$*+RCs+1*, $b_1$ = *Ds+K* and $b_2$ = -C*T*s$^2$.

The theoretical simulation was run to yield the following results (See Appendix *B* for MATLAB code) using the following realistic design values of *M* = 0.0015, *D* = 0.10, *K* = 160, *R* = 0.3Ω, *L* = 0.016H, *C* = 1nF. The results of the simulation are given in Figure 4.13.

It was observed that the SDOF1D MDKRLC had two resonant peaks at *f* = 51.71Hz and f = 3.977e+4 Hz corresponding to the resonances of the coupled mechanical resonance, where the natural frequency is $\sqrt{(K/m)}$ = 51.97Hz and the coupled electrical resonance whose natural frequency is $\sqrt{(1/LC)}$ = 3.977e+4 Hz.

(a)

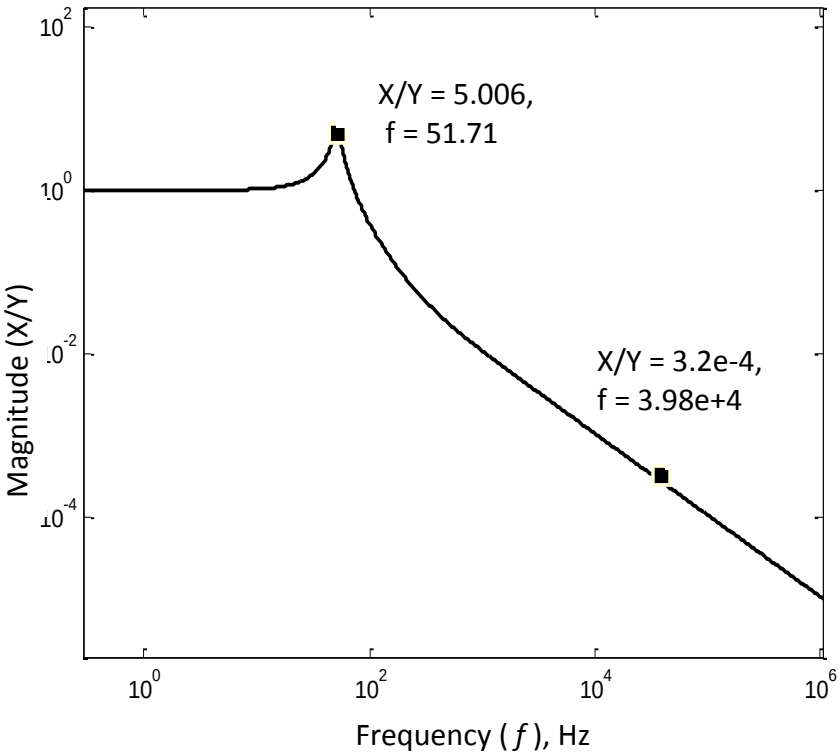
X/Y = 5.006,
f = 51.71
X/Y = 3.2e-4,
f = 3.98e+4
Magnitude (X/Y)
Frequency ( f ), Hz

(b)

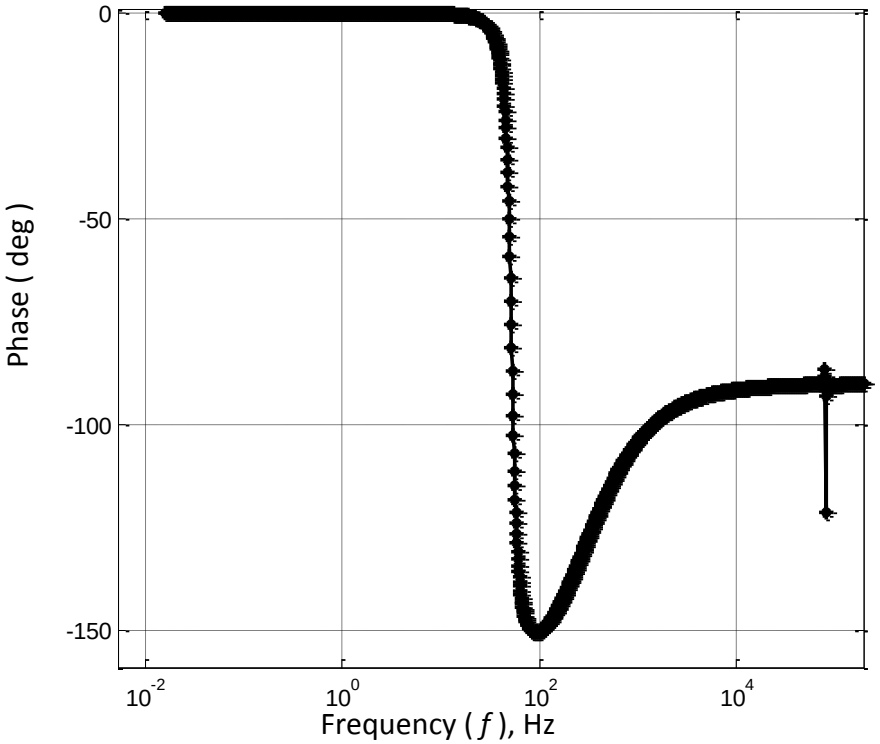
Phase ( deg )
Frequency ( f ), Hz

( c )

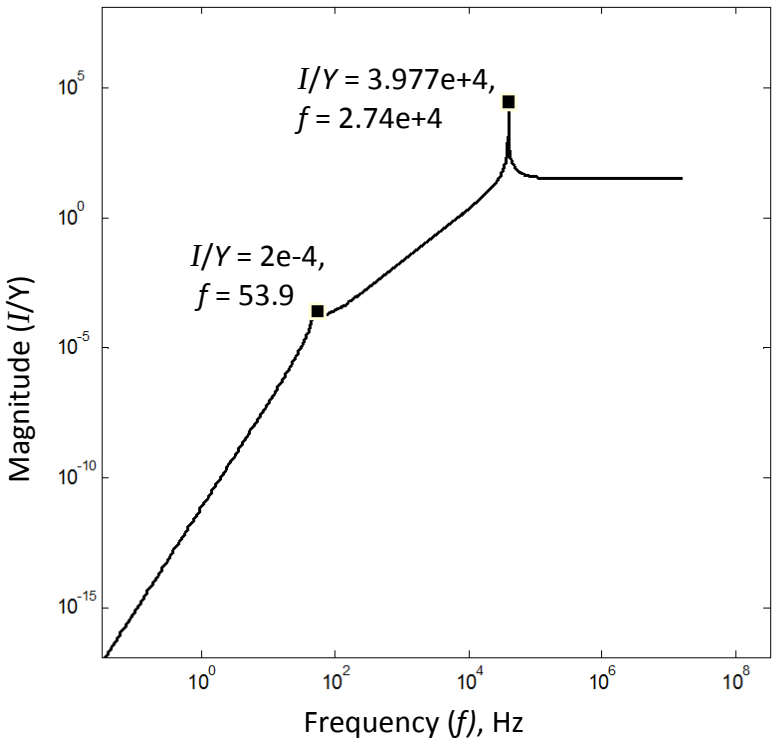


(d)

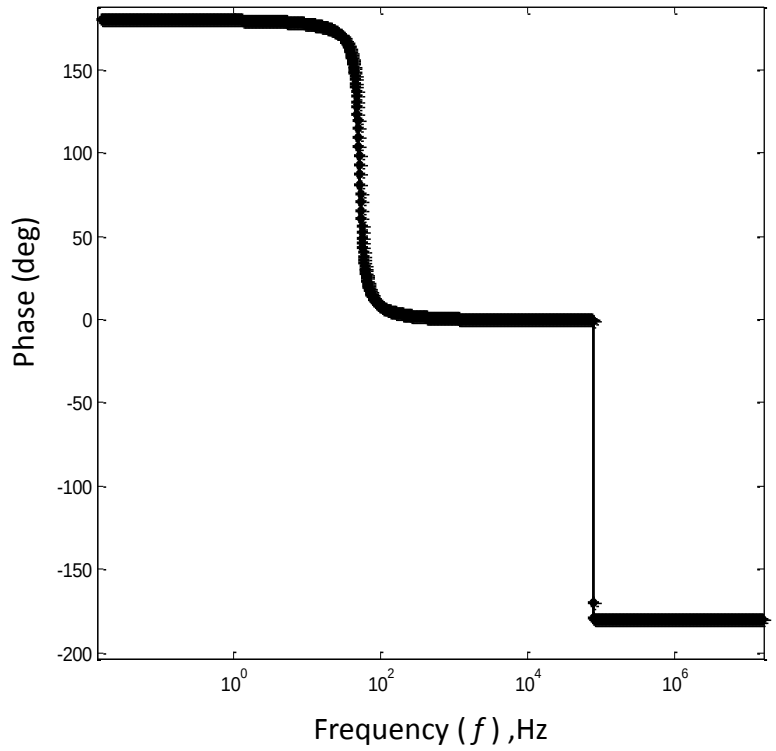


Figure 4.13 Laplace transform frequency response curves for SDOF1D MDKRLC system: (a) frequency response of the transfer function $X(s)/Y(s)$, (b) frequency response of the phase of $X(s)/Y(s)$, (c) frequency response of the transfer function $I(s)/Y(s)$, (d) frequency phase response of the transfer function $I(s)/Y(s)$.

From the Laplace transform, it can thus be concluded that the behaviour of the overall electromechanically coupled SDOF1D MDKRLC system is influenced by the mechanical resonance and the electrical resonance of the mechanical and electrical subsystems respectively. It was observed that at low frequency range (say <100 Hz) of operation, the SDOF1D EMVEH is influenced by mechanical resonance. Hence, the mechanical design parameters *M, D* and *K* have a major role in the design of vibration energy harvesters that operate at low frequency range of 1-100 Hz.

### 4.6.2 Linear state space analysis for SDOF1D MDK RLC system

State space methods can be used to solve equations (4.35) and (4.36). State space variables can be defined as,

$$V_1 = x, \tag{4.55}$$

$$V_2 = \frac{dV_1}{dt} = \dot{x}, \tag{4.56}$$

$$V_3 = I, \tag{4.57}$$

and

$$V_4 = \frac{dV_3}{dt} = \dot{I}. \tag{4.58}$$

The four state derivative equations then become:

$$\frac{dV_1}{dt} = V_2, \tag{4.59}$$

$$\frac{dV_2}{dt} = \ddot{x} = \frac{1}{M}\left[D\dot{Y} + KY - DV_2 - KV_1 - TV_3\right], \tag{4.60}$$

$$\frac{dV_3}{dt} = V_4, \tag{4.61}$$

and,

$$\frac{dV_4}{dt} = \ddot{I} = \frac{1}{L}\left[\frac{T}{M}\left(D\dot{Y} + KY - DV_2 - KV_1 - TV_3\right) - T\ddot{Y} - RV_4 - \frac{1}{C}V_3\right] \tag{4.62}$$

Hence, the state space matrix differential equation is given by:

$$\begin{bmatrix} \frac{dV_1}{dt} \\ \frac{dV_2}{dt} \\ \frac{dV_3}{dt} \\ \frac{dV_4}{dt} \end{bmatrix} = \begin{bmatrix} 0 & 1 & 0 & 0 \\ \frac{-K}{M} & \frac{-D}{M} & \frac{-T}{M} & 0 \\ 0 & 0 & 0 & 1 \\ \frac{-KT}{ML} & \frac{-TD}{ML} & \frac{-T^2}{ML} - \frac{1}{CL} & \frac{R}{L} \end{bmatrix} \begin{bmatrix} V_1 \\ V_2 \\ V_3 \\ V_4 \end{bmatrix} + \begin{bmatrix} 0 & 0 & 0 \\ \frac{K}{M} & \frac{D}{M} & 0 \\ 0 & 0 & 0 \\ \frac{TK}{ML} & \frac{TD}{ML} & \frac{-T}{L} \end{bmatrix} \begin{bmatrix} Y \\ \dot{Y} \\ \ddot{Y} \end{bmatrix} \tag{4.63}$$

MATLAB software was written to yield the following results (See Appendix B for MATLAB code) using the realistic design values of *M* = 0.0015 Kg, *D* = 0.10 Ns/m, *K* = 160 N/m, *R* = 0.3 Ω, *L* = 0.016 H, *C* = 1 nF. The results of the simulation are given in Figure 4.14, showing the eigen value solutions and the damping ratios. Since this was a coupled mechanical electrical system, there were four eigenvalues, $\lambda_1$ = -33.33 + 324.9i, $\lambda_2$ = -33.33 - 324.9i corresponding to the coupled mechanical resonance with frequency *f* = 51.97Hz and $\lambda_3$=-18.75 + 250000i and $\lambda_4$= -18.75 - 250000i, corresponding to the coupled electrical resonance with frequency *f* = 39,788Hz. These results are near to the Laplace transform frequency response values. It can be seen that the peaks of the Laplace transform frequency response results confirm the natural frequencies obtained from state space analysis.

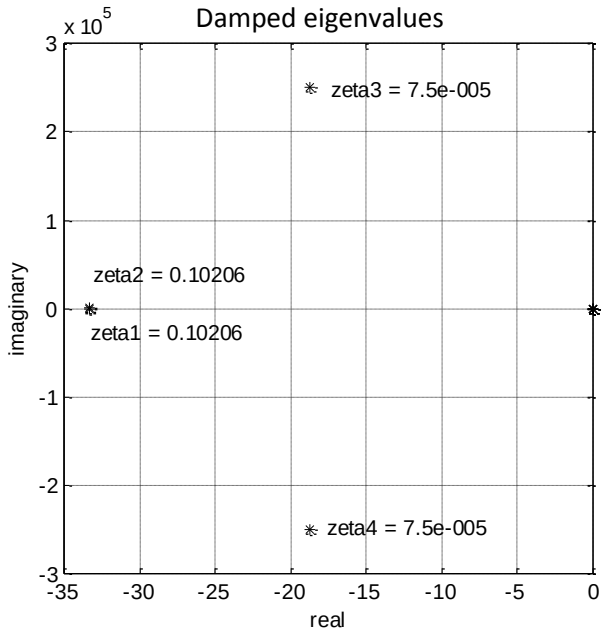


Figure 4.14 Eigenvalues of SDOF1D MDKRLC from state space method.

### 4.6.3 Non-linear–SDOF1D MDK RLC system

By employing the second method discussed in equation (4.51), the coupling coefficient T($x$,y) can be modelled as a function of $B$($x$-y) given by $T(x,y) = 2\pi NrB(x-y)$. The magnetic field strength, $B$($x$-$y$) can be obtained from ANSOFT Numerical Magnetostatic analysis, using interpolation to solve the exact $B$($x$-$y$) values as a function of $x$ and $t$ for time domain simulation of the system behaviour.

The state variables for the coupled simulation were given by:

$$Z(1) = x, \tag{4.64}$$

$$Z(2) = \dot{x} = \frac{d(Z(1))}{dt}, \tag{4.65}$$

and

$$Z(3) = I, \tag{4.66}$$

$$Z(4) = \dot{I} = \frac{d(Z(3))}{dt} \tag{4.67}$$

This gives:

$$\frac{d(Z(2))}{dt} = \ddot{x} = \frac{1}{M}[D\dot{y} + Ky - DZ(2) - KZ(1) - T(Z(1) - y)Z(3)] \tag{4.68}$$

and:

$$\frac{d(Z(4))}{dt} = \ddot{I} == \frac{T(Z(1)-y)}{ML}.D\dot{Y} + \frac{T(Z(1)-y).KY}{ML} - \frac{T(Z(1)-y)}{ML}.DZ(2) - \frac{T(Z(1)-y)}{ML}KZ(1) - \frac{T^2}{L}(Z(1)-y)Z(3) - \frac{T}{L}(Z(1)-y)\ddot{Y} - \frac{R}{L}Z(4) - \frac{1}{CL}Z(3). \tag{4.69}$$

MATLAB software was written (See Appendix B for MATLAB code) using the following realistic design values of *M* = 0.0015kg, *D* = 0.10 Ns/m, *K* = 160 N/m, *R* = 0.6 Ω, *L* = 0.016 H, *C* = 1 nF, *A* = 0.0001 m and frequency of *f* = 53.9 Hz to compare them with the Laplace transform results as obtained in Figure 4.13(c, d). The results of this time domain simulation are given in Figure 4.15. It was observed that the current was fluctuating and the current was not centred at zero. Hence, The RMS current was calculated and found to be 1.814e-6 A. The averaged peak current was found as $I_{pk} = \sqrt{2}\,.I_{rms}$ =2.55e-6 A. From Laplace transform, *I/Y*=0.00026 where *Y* = 0.1 mm=1e-4 m. Hence the Laplace transform value of current was *I*=2.6e-6 A and conforms to this value.

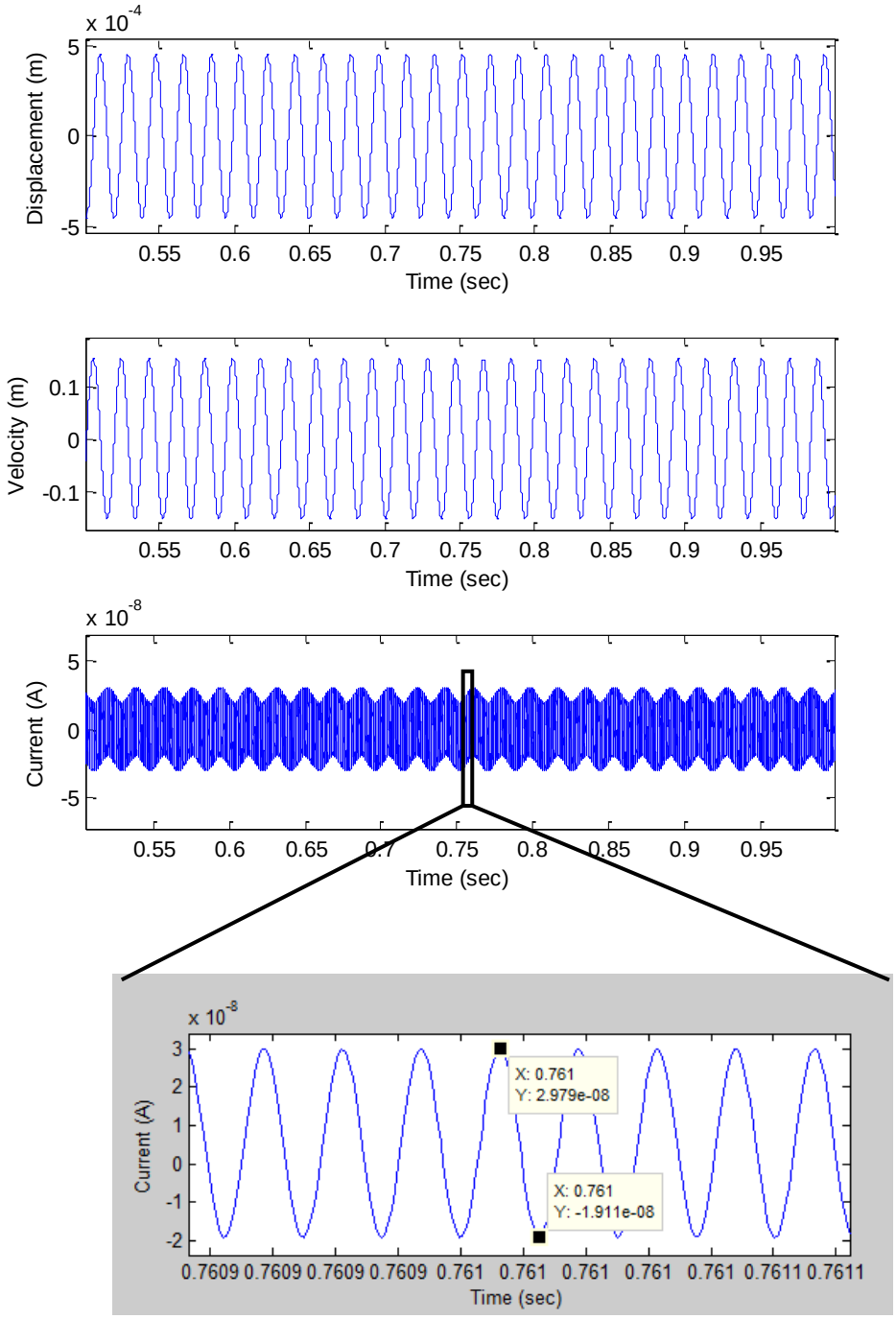


Figure 4.15 Time response of the displacement of the coil, coil velocity and the current generated in the coil.

## 4.7 Theoretical analyses of SDOF1D MDKRL EMVEH system

Similar to the theoretical analyses of SDOF1D MDKRLC EMVEH, as discussed in section 4.7, a series of theoretical analyses from Laplace analysis, state space analysis and non-linear

Runge-Kutta based numerical analysis was performed for the SDOF1D MDKRL EMVEH model.

### 4.7.1 Linear –Laplace transform for SDOF1D MDK RL system

Applying Laplace transforms to the SDOF1D MDK RL equation (4.40) after ignoring the initial conditions gives:

$$\begin{bmatrix} (Ms^2 + Ds + K) & T \\ -Ts & Ls + R \end{bmatrix} \begin{bmatrix} X(s) \\ I(s) \end{bmatrix} = \begin{bmatrix} Ds + K \\ -Ts \end{bmatrix} [Y(s)] \tag{4.70}$$

This is of the form $[A][\alpha] = [B][\beta]$,

where, $[A] = \begin{bmatrix} a_{11} & a_{12} \\ a_{21} & a_{22} \end{bmatrix} = \begin{bmatrix} Ms^2 + Ds + K & T \\ -Ts & Ls + R \end{bmatrix}$, $[B] = \begin{bmatrix} b_1 \\ b_2 \end{bmatrix} = \begin{bmatrix} Ds + K \\ -Ts \end{bmatrix}$, and

$[\alpha] = \begin{bmatrix} X(s) \\ I(s) \end{bmatrix}$ and $[\beta] = \begin{bmatrix} \dot{Y}(s) \end{bmatrix}$. Then, $[\alpha] = [A^{-1}][B][\beta]$.

This can also be written as:

$$\begin{bmatrix} \frac{X(s)}{Y(s)} \\ \frac{I(s)}{Y(s)} \end{bmatrix} = A^{-1}B.$$

This can be written in the form:

$$\begin{bmatrix} \frac{X(s)}{Y(s)} \\ \frac{I(s)}{Y(s)} \end{bmatrix} = \frac{1}{|A|} \begin{bmatrix} a_{22} & -a_{12} \\ -a_{21} & a_{11} \end{bmatrix} \begin{bmatrix} b_1 \\ b_2 \end{bmatrix}.$$

which becomes:

$$\begin{bmatrix} \frac{X(s)}{Y(s)} \\ \frac{I(s)}{Y(s)} \end{bmatrix} = \frac{1}{|A|} \begin{bmatrix} a_{22}b_1 & -a_{12}b_2 \\ -a_{21}b_1 & +a_{11}b_2 \end{bmatrix}.$$

Hence the transfer functions are given by:

$$\frac{X(s)}{Y(s)} = \frac{1}{|A|}(a_{22}b_1 - a_{12}b_2), \tag{4.71}$$

and

$$\frac{I(s)}{Y(s)} = \frac{1}{|A|}(a_{11}b_2 - a_{21}b_1), \tag{4.72}$$

where, $a_{11} = Ms^2 + Ds + K$, $a_{12} = T$, $a_{21} = -Ts$, $a_{22} = Ls + R$ and $b_1 = Ds + K$, $b_2 = Ts$. MATLAB software was written to yield the following results (See Appendix B for MATLAB code) using the following realistic design values of *M* = 0.0015 kg, *D* = 0.10 Ns/m, *K* = 160 N/m, *R* = 0.3 Ω, *L* = 0.016 H. The results of the simulation are given in Figure 4.16.

(a)

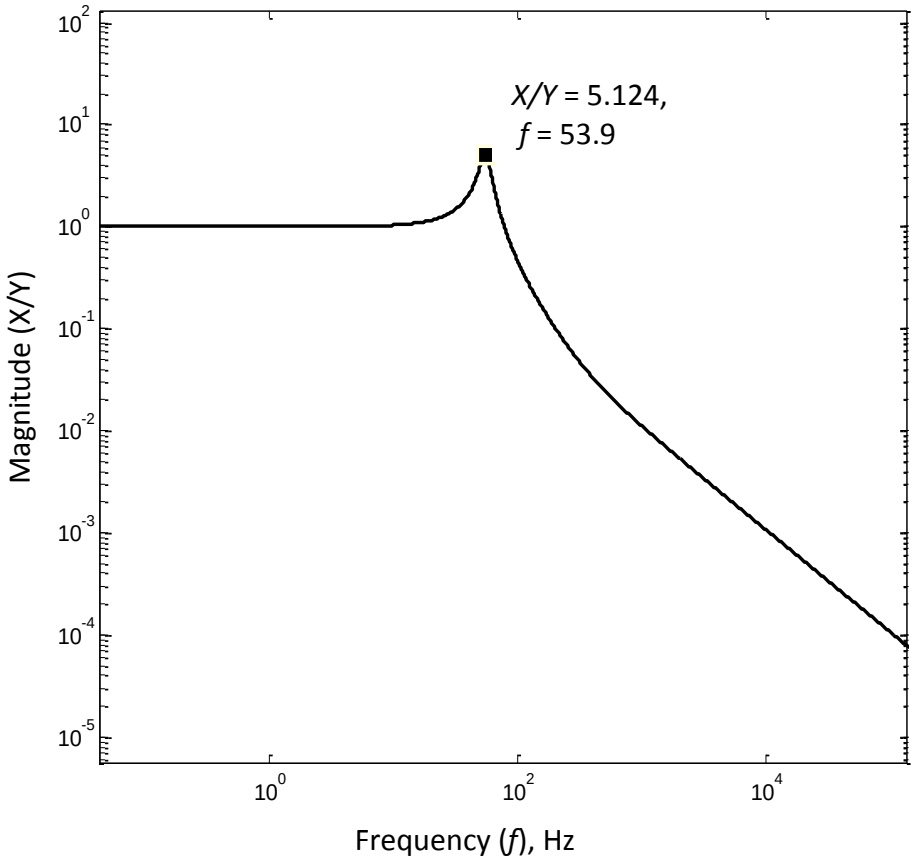

(b)

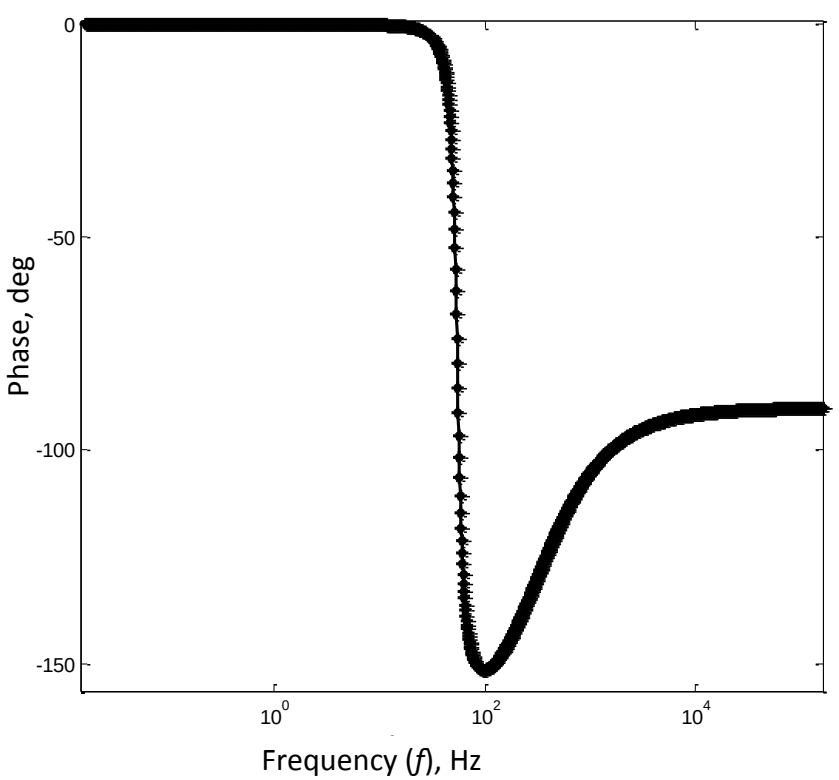
0
-50
-100
-150
Phase, deg
$10^0$
$10^2$
$10^4$
Frequency (*f*), Hz

( c )

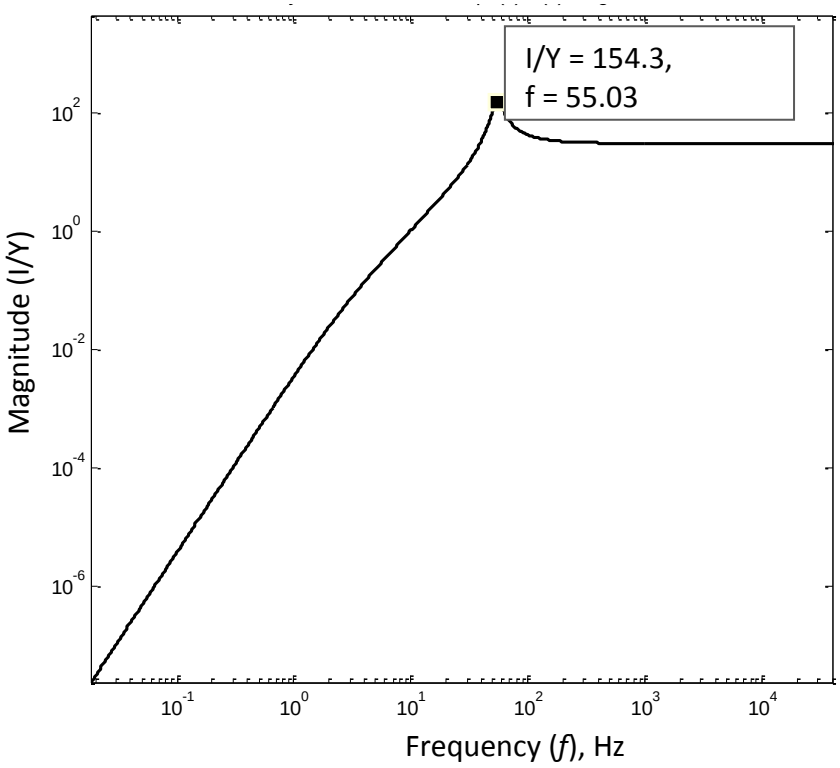
I/Y = 154.3,
f = 55.03
$10^2$
$10^0$
$10^{-2}$
$10^{-4}$
$10^{-6}$
Magnitude (I/Y)
$10^{-1}$
$10^0$
$10^1$
$10^2$
$10^3$
$10^4$
Frequency (*f*), Hz

(d)

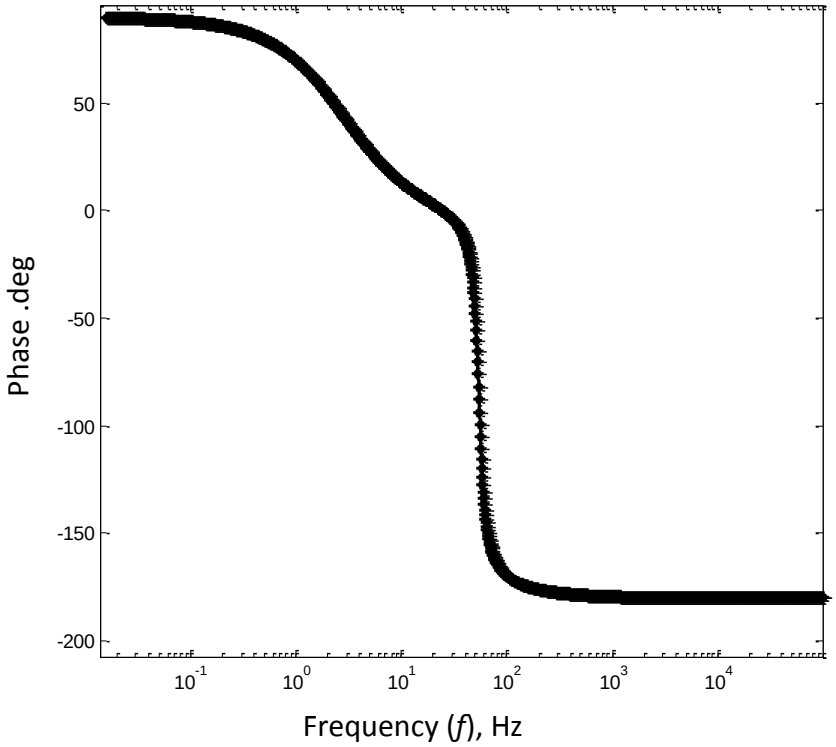


Figure 4.16 Laplace transform - frequency response curves for SDOF1D MDKRL system: (a) frequency response of the transfer function X(s)/Y(s), (b) frequency response of the phase of X(s)/Y(s), (c) frequency response of the transfer function I(s)/Y(s), (d) frequency phase response of the transfer function I(s)/Y(s).

From the results as observed in Figure 4.16, the resonance occurred at $f$ = 55 Hz for the SDOF1D MDKRL EMVEH system. The first resonant frequency was near the value of mechanical resonance of a pure SDOF1D MDK system as discussed earlier in Section 4.3.1.

### 4.7.2 Linear state space analysis for SDOF1D MDK RL system

Applying state space methods to solve equations (4.38) and (4.40), the state space variables can be defined as:

$$V_1 = x, \tag{4.73}$$

$$V_2 = \frac{dV_1}{dt} = \dot{x}, \tag{4.74}$$

and

$$V_3 = I. \tag{4.75}$$

The state derivative equations then become:

$$\frac{dV_2}{dt} = \ddot{x} = \frac{1}{M}[D\dot{y} + Ky - DV_2 - KV_1 - TV_3],$$

and,

$$\frac{dV_3}{dt} = \dot{I} = \frac{1}{L}[TV_2 - T\dot{y} - RV_3].$$

The resulting state space derivative matrix equation can be written as:

$$\begin{bmatrix} \frac{dV_1}{dt} \\ \frac{dV_2}{dt} \\ \frac{dV_3}{dt} \end{bmatrix} = \begin{bmatrix} 0 & 1 & 0 \\ \frac{-K}{M} & \frac{-D}{M} & \frac{-T}{M} \\ 0 & \frac{T}{L} & \frac{-R}{L} \end{bmatrix} \begin{bmatrix} V_1 \\ V_2 \\ V_3 \end{bmatrix} + \begin{bmatrix} 0 & 0 \\ \frac{K}{M} & \frac{D}{M} \\ 0 & \frac{-T}{L} \end{bmatrix} \begin{bmatrix} y \\ \dot{y} \end{bmatrix}. \tag{4.76}$$

The theoretical simulation was run to yield the following results (See Appendix B for MATLAB code) using the following realistic design values of $M$ = 0.0015kg, $D$ = 0.1 Ns/m, $K$ = 160 N/m, $R$ = 0.3 Ω, $L$ = 0.016 H. The results of the simulation are shown in Figure 4.17.

The eigen values obtained were $\lambda_1$ = -17.47 + 341.26i, $\lambda_2$ = -17.47 + 341.26i and $\lambda_3$ = -17.13 and their corresponding natural frequencies were $f_{n2}$ = 0Hz and $f_{n2}$ = 54.38Hz respectively. It should be noted the resonant frequency was close to the peak of the Laplace transform thus confirming the validity of the state space results. It was noted that the SDOF1D MDKRL system did not have a frequency resonance at high frequency range as was found in the SDOF1D MDK RLC system. This was due to the fact that electrical resonance could not be achieved since the circuit was RL and the resonant frequency was $1/\sqrt{LC}$ .

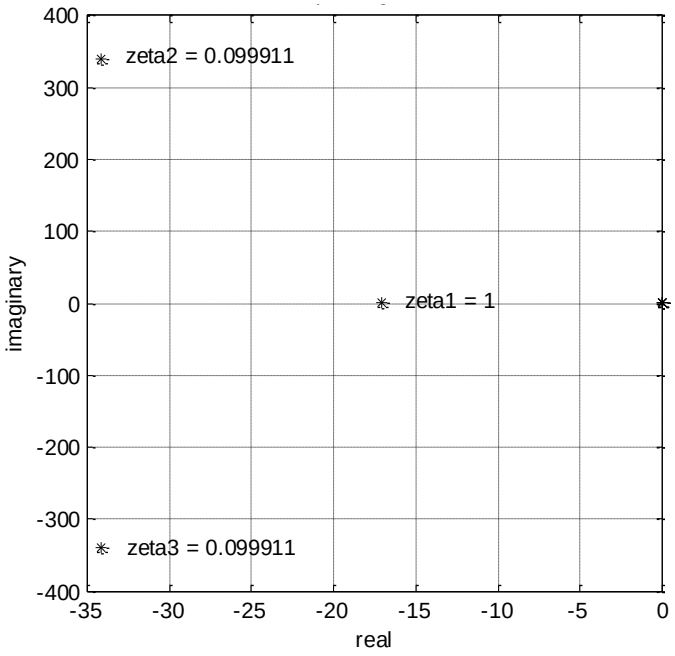


Figure 4.17 Eigen values of SDOF1D MDKRL from state space method.

### 4.7.3 Non-linear simulation of SDOF1D MDK RL system

The derivative equations for the SDOF1D MDKRL system can be written as:

$$Z(1) = x, \tag{4.77}$$

$$Z(2) = \dot{x} = \frac{d(Z(1))}{dt}, \tag{4.78}$$

and $Z(3) = I.$ (4.79)

The state derivative functions then becomes:

$$\frac{d(Z(2))}{dt} = \ddot{x} = \frac{1}{M}[D\dot{y} + Ky - DZ(2) - KZ(1) - T(Z(1) - y)Z(3)], \tag{4.80}$$

and $$\frac{d(Z(3))}{dt} = \dot{I} = \frac{1}{L}[T(Z(1) - y)(Z(2) - \dot{y}) - RZ(3)]. \tag{4.81}$$

MATLAB software was written to simulate the system behaviour (See Appendix B for MATLAB code) using the following realistic design values of $M$ = 0.0015 kg, $D$ = 0.10 Ns/m, $K$ = 160 N/m, $R$ = 0.3 ohm, $L$ = 0.016 H, $f$ = 51.97 Hz, $A$ = 0.0001 m. The results of the simulation are given in Figure 4.18. The frequency of 51.97 Hz was selected to compare it with the SDOF1D MDKRLC system. It was observed that the current was higher in the SDOFMDK RL system when compared to the SDOF1D MDK RLC system.

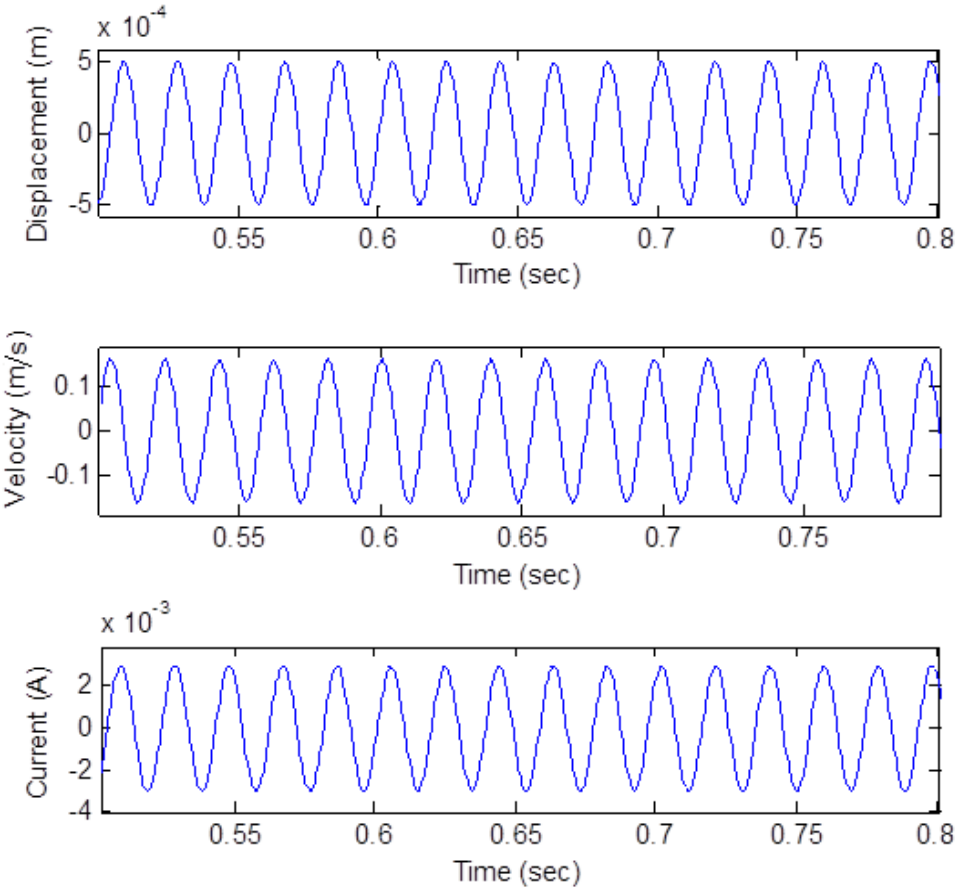


Figure 4.18 Time domain responses of the displacement of the coil, coil velocity, current generated in the coil for the SDOF1D MDK RL system at f = 51.97Hz.

It is important to understand that the time domain behaviour of the SDOF1D MDKRL system at its resonant frequency of 54.38 Hz was obtained as in Figure 4.19. There was no significant difference observed between the currents obtained at $f$ = 51.97 Hz and $f$ = 54.38 Hz.

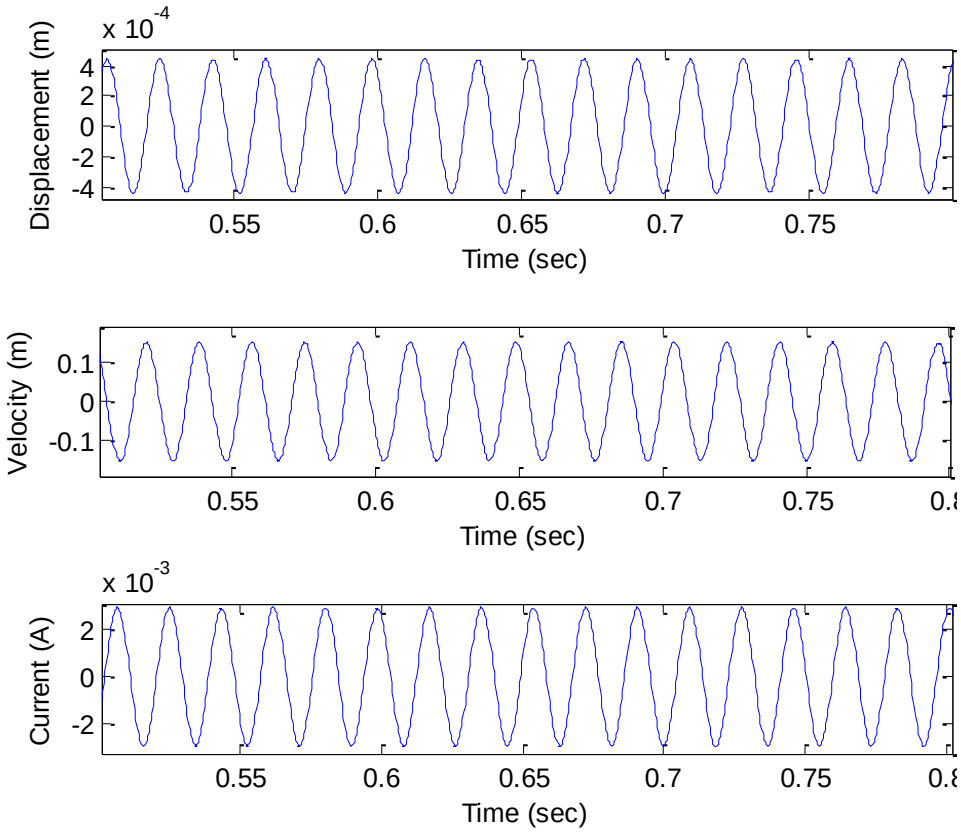


Figure 4.19 Time domain responses of the displacement of the coil, coil velocity, current generated in the coil for the SDOF1D MDK RL system at f = 54.38 Hz.

## 4.8 Theoretical electrical output frequency responses of SDOF1D EMVEH at different amplitudes

It was assumed that the voltage measurement apparatus was similar to the circuit employed in SDOF1D UD EMVEH, as in Figure 3.15, Chapter 3. Therefore, only the impedance of the coil was considered since a very high load resistance of 10000 ohms was connected across the coil, similar to the voltage measuring circuit. Initially, the impedance values at different frequencies were calculated, as in Figure 4.20. It can be seen from Fig 4.20 that the impedance of the system is predominantly inductive reactance. The currents at different frequencies were found using the ODE45 non-linear simulation, and are shown in Figure 4.21. The voltage frequency response was then found using Ohm's law $V = IZ_{coil}$, where $Z_{coil}$ represents the impedance of the coil, as shown in Figure 4.22.

The average power at different frequencies is obtained using the equation (3.33) as described in Chapter 3 that includes the power factor $\cos\varphi$ where $\varphi$ is the phase difference between current and voltage. The theoretical average power responses for 1 mm to 3 mm amplitude were plotted both in normal scale and semi-log scale as shown in Figure 4.23. It can be observed that the minor increase in amplitude causes a very high surge in power. It can also be observed that the power obtained in the SDOF1D EMVEH is higher than its undamped version SDOF1D UD EMVEH at 3 mm.

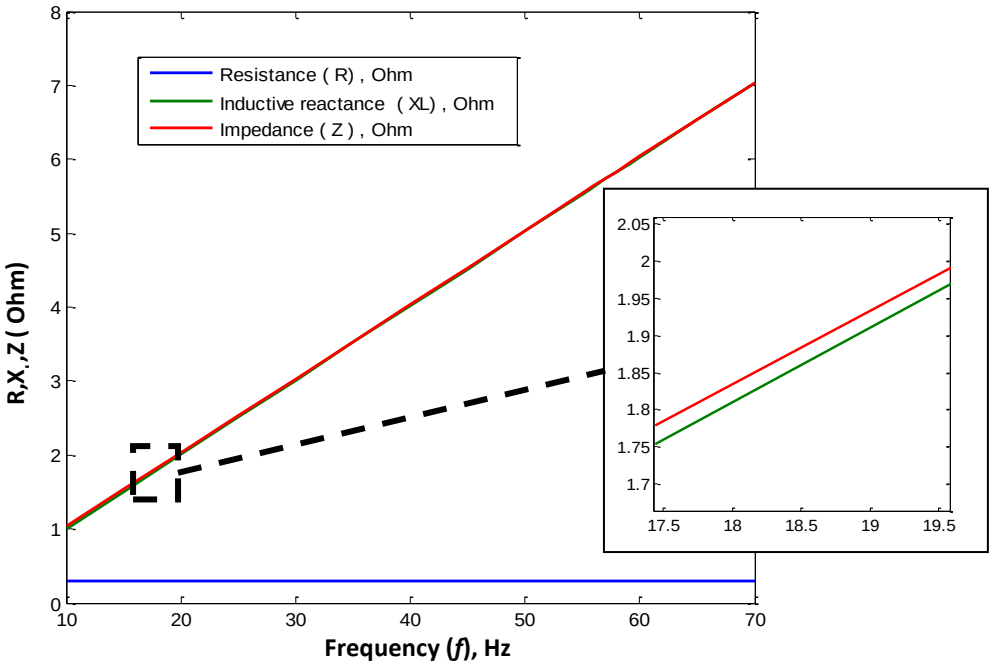


Figure 4.20 Theoretical impedance calculations at different frequencies of SDOF1D EMVEH.

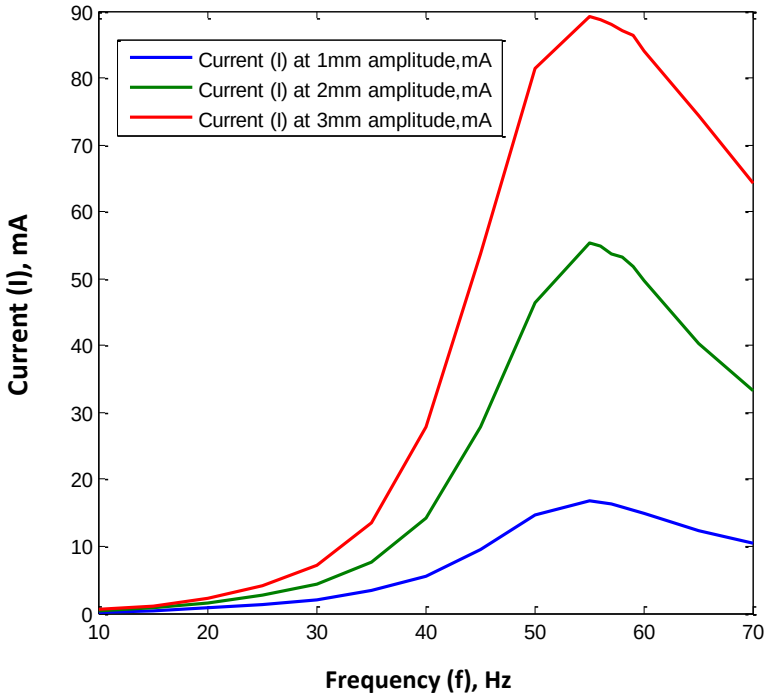


Figure 4.21 Theoretical currents of SDOF1D EMVEH at 1mm to 3mm amplitude.

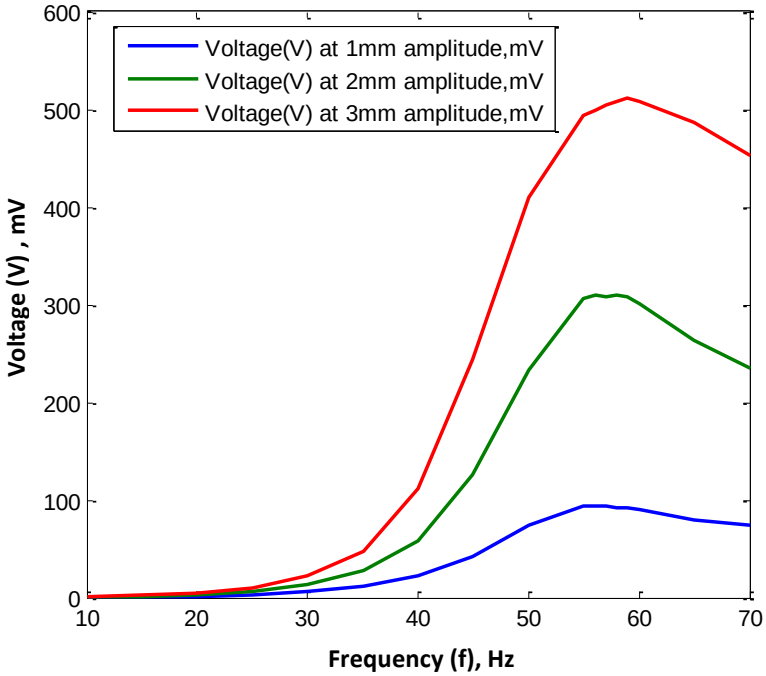


Figure 4.22 Theoretical voltages of SDOF1D EMVEH at 1mm to 3mm amplitude.

**(a)**

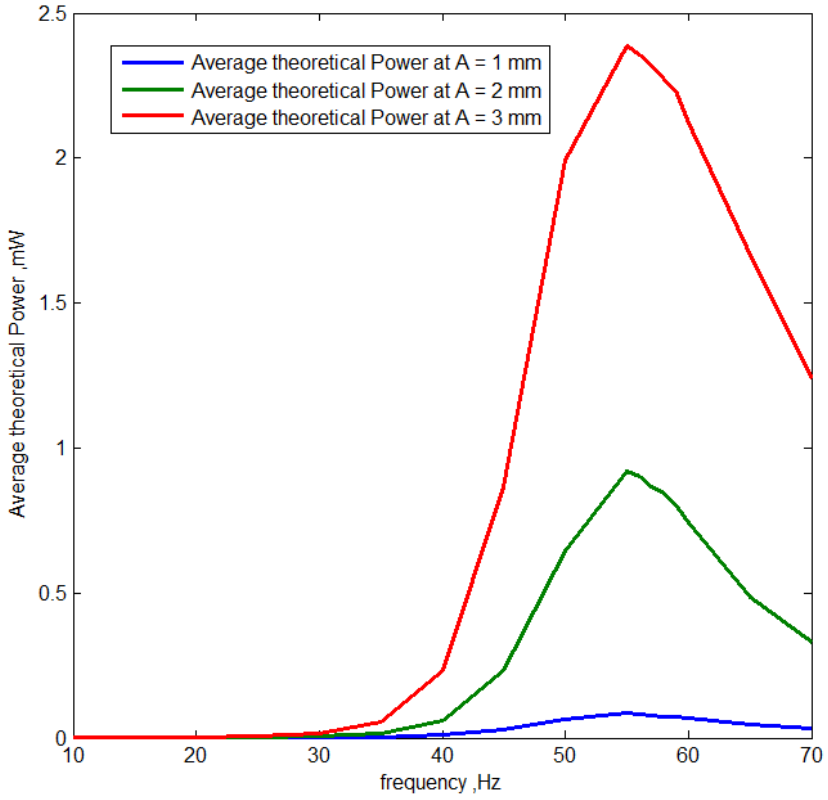


**(b)**

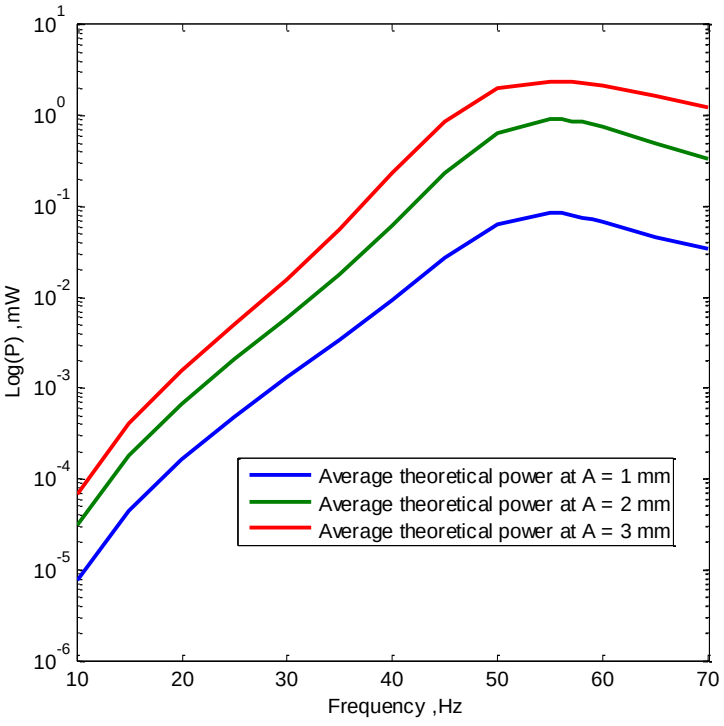


Figure 4.23 Theoretical Power responses of SDOF1D EMVEH at 1mm to 3mm amplitude at (a) power versus frequency, (b) log (power) versus frequency.

## 4.9 Discussion

For the study of SDOF1D EMVEH, three models were considered, namely, the SDOF1D MDK system, the SDOF1D MDK RLC EMVEH system and the SDOF1D MDKRL EMVEH. Initially, simple linear analyses were performed on these models, disregarding the spatial variation of the magnetic field. This was achieved by Laplace transform analyses and state space analyses. It was followed by non-linear analyses using a hybrid method consisting of the non-linear Runge Kutta method (MATLAB ODE45 function) and magnetostatic data for spatial variation of the magnetic field.

The Laplace and the state space analyses of SDOF1D MDKRLC and SDOF1D MDKRL EMVEH systems were summarised, as can be seen in Table 4.3. The SDOF1D MDKRLC EMVEH system has two resonant peaks with $f_{n1}$ = 51.71Hz corresponding to the coupled mechanical resonance ($1/2\pi\sqrt{K/m} = 51.97\text{Hz}$) and $f_{n2}$ = 3.977e+4Hz corresponding to the coupled electrical resonance (${}^{1}/_{2\pi\sqrt{LC}} = 3.98e+4\text{Hz}$). One can observe that both the transfer functions *X*/*Y* and *I*/*Y* deviated from their corresponding mechanical and electrical resonances. Hence, one can conclude that the electrical system caused an additional damping effect on the mechanical damping and vice-versa. Thus one can conclude that provided coupling occurs between the mechanical and electrical system to form a combined electromechanical system, the electromechanical system will have its own resonances that differ to the independent mechanical and electrical system before coupling. This is further validated by the fact that the SDOF1D MDK RL EMVEH did not have any second resonance as there was no electrical resonance. However, the resonant frequencies of both the independent MDK and RLC systems were observed with the state space analyses, as can be seen from Table 4.3. Although Laplace and state space provided these interesting observations, detailed investigations were made from the time domain results of non-linear ODE solver based analyses.

Table 4.3. Summary of linear theoretical simulation results of SDOF1D MDK RLC and SDOF1D MDK RL EMVEH systems.

| | | **SDOF1D MDK RLC** | **SDOF1D MDK RL** |
|---|---|---|---|
| **Laplace transform analysis** | X/Y peak coordinates | (51.71,5.019), (3.977e+4,3.112e-4) | (53.9,5.124) |
| | X/Y frequency | 51.71Hz , 3.977e+4 Hz | 53.9 Hz |
| | X/Y magnitude | 5.019 , 0.0003112 | 5.124 |
| | X | 5.02e-4, 3.112e-6 | 5.12E-04 |
| | I/Y peak coordinates | (53.9,2.699e-4), (3.977e+4,2.758e+4) | (55.03,154.3) |
| | I/Y frequency | 53.9 Hz,39770 Hz | 55.03 Hz |
| | I/Y Magnitude | 0.00027,2.758e+4 | 154.3 |
| | I | 2.699e-6A,2.758A | 0.1543A |
| **State space analysis** | $\lambda_1$ | -33.33 + 324.9i | -34.148 + 340.075i |
| | $\lambda_2$ | -33.33- 324.9i | -34.148 - 340.075i |
| | $\lambda_3$ | -9.37 + 250000i | -17.12 |
| | $\lambda_4$ | -9.37 - 250000i | |
| | $f_1$ | 51.98Hz | 2.72Hz |
| | $f_2$ | 39789Hz | 54.39Hz |
| | **Resonances** | Mechanical and Electrical Resonances. | Only Mechanical Resonance. |

The non-linear analyses of both SDOF1D MDK RLC and SDOF1D MDK RL were simulated for resonant responses in the time domain based signal analyses of displacement and current. The resonant frequencies of both the SDOF1D MDK RL and SDOF1D MDKRLC systems were considered for both the systems for better comparison. The observed peak currents and the RMS currents were tabulated, as shown in Table 4.4. The electrical Impedances of both the systems were calculated using the formula:

$$Z = \sqrt{R^2 + (X_L - X_c)^2} \tag{4.82}$$

where, $X_L = 2\pi fL$ and $X_c = 1/2\pi fC$ . It should be noted that $X_c = 0$ for SDOF1D MDK RL EMVEH. The peak voltages and the RMS voltages were then obtained using Ohm's Law *V* = *IZ*.

Table 4.4. Summary of linear theoretical simulation results of SDOF1D MDK RLC and SDOF1D MDK RL EMVEH systems at 0.1mm amplitude.

| | | **SDOF1D MDK RLC EMVEH** | **SDOF1D MDK RL EMVEH** |
|---|---|---|---|
| At 1st resonance of SDOF1D MDK RLC EMVEH system where $f_n$ = 51.71Hz. | Peak current at 51.71 Hz(mA). | 1.81E-05 | 2.986 |
| | RMS Current at 51.71 Hz(mA). | 1.28E-05 | 2.111 |
| | Impedance at 51.71 Hz(Ohm). | 3.08E+06 | 5.207 |
| | Peak voltage at 51.71 Hz(mV). | 55.709 | 15.548 |
| | RMS voltage at 51.71 Hz(mV). | 39.386 | 10.993 |
| | Power factor , cosφ = R/Z | 9.74711E-08 | 0.057 |
| | Average power at 51.71 Hz (mW). | 4.91E-14 | 1.323E-03 |
| At 1st resonance of SDOF1D MDK RI EMVEH System where $f_n$ = 54.39 Hz. | Peak current at 54.39 Hz (mA). | 1.44E-05 | 2.984 |
| | RMS current at 54.39 Hz (mA). | 1.02E-05 | 2.11 |
| | Impedance at 54.39 Hz (Ohm). | 2.93E+06 | 5.476 |
| | Peak voltage at 54.39 Hz (mV). | 42.178 | 16.341 |
| | RMS voltage at 54.39 Hz (mV). | 29.82 | 11.553 |
| | Power factor , cosφ = R/Z | 1.02523E-07 | 0.054 |
| | Average power at 54.39 Hz (mW). | 3.12E-14 | 1.32E-03 |
| Practical Perspective | Good for EMVEH design | OK for EMVEH design | Bad for EMVEH design |

It was observed that the SDOF1D MDK RLC EMVEH system produced a higher voltage than the SDOF1D MDK RL EMVEH system. But it should be noted that this was due to the high impedance of the RLC system, thus reducing power output. The SDOF1D MDK RL system produced higher power levels than the equivalent SDOF1D MDKRLC system. Although the voltage of SDOF1D MDK RL was smaller than the SDOF1D MDKRLC, it was still of a good value in the order of 10 mV to 16 mV for an amplitude of 0.1 mm. Even the current output of the SDOF1D MDKRL system was better than its equivalent SDOF1D MDKRLC system due to its high electrical impedance. Thus, it can be summarised that the SDOF1D MDK RL EMVEH is a better design alternative than the SDOF1D MDK RLC EMVEH due to its relative merits in current and power and moderately good voltage output.

In Chapter 5, only the 2DOF1D MDKRL EMVEH will be considered due to its relative advantages. A comprehensive review of the linear and non-linear analyses of the SDOF1D EMVEH provided a framework and ground for further research towards an advanced 2DOF1D EMVEH and subsequent MDOF1D EMVEH systems.

# Chapter 5 Theoretical investigation into two-degrees-of-freedom damped electromagnetic vibration energy harvester (2DOF1D EMVEH)

In the previous chapter (Chapter 4), the SDOF1D and its various design options were identified. However the SDOF1D system had only one degree of freedom and was limited to only one resonant natural frequency. Ideally, the energy harvester should be able to pick up and resonate at every frequency present in the source vibration. By employing MDOF systems, one can use multiple resonant frequencies and achieve maximum power. The simplest form of a multi-degree-of-freedom system is a two-degrees-of-freedom one-directional system (2DOF1D) with two coil masses. This chapter deals with 2DOF1D EMVEH systems and their behaviour with regard to various design criteria. The study of 2DOF1D is a prerequisite to the designing of complex MDOF systems that will be discussed in Chapter 7 and Chapter 8.

## 5.1. Research methodology

The research methodology is as shown in Figure 5.1. The research methodology was similar to the SDOF1D EMVEH system as discussed in the previous chapter (Chapter 4). It was already established in the previous chapter that the MDKRL system achieved better performance than the MDKRLC system for measuring open circuit voltage and power. Hence in this 2DOF1D study, only the 2DOF1D MDKRL EMVEH system was theoretically explored.

The 2DOF1D EMVEH study began with a simple linear analytical simulation using the Laplace and state space methods to understand the behaviour of the system at various frequencies. The frequency response and eigenvalues were initially obtained for the 2DOF1D MDK system without the electrical system in order to understand the mechanical system and its resonant behavior. This was followed by a linear simulation of the coupled 2DOF1D MDK RL system. As in the previous chapter (Chapter 4), the linear simulation was

approximate since it neglected the spatial variation of the magnetic field along the direction of the coil motion. Hence, this was followed by the non-linear hybrid numerical-analytical simulation of SDOF1D MDKRL EMVEH by using the magnetic spatial variation data from numerical magnetostatics. The effect of the design variables on the frequency response of the voltage output of 2DOF1D EMVEH is discussed in detail in Chapter 6. To validate the theoretical models of the 2DOF1D EMVEH, a 2DOF1D prototype was developed and experimentally validated, which shall be discussed in Chapter 7.

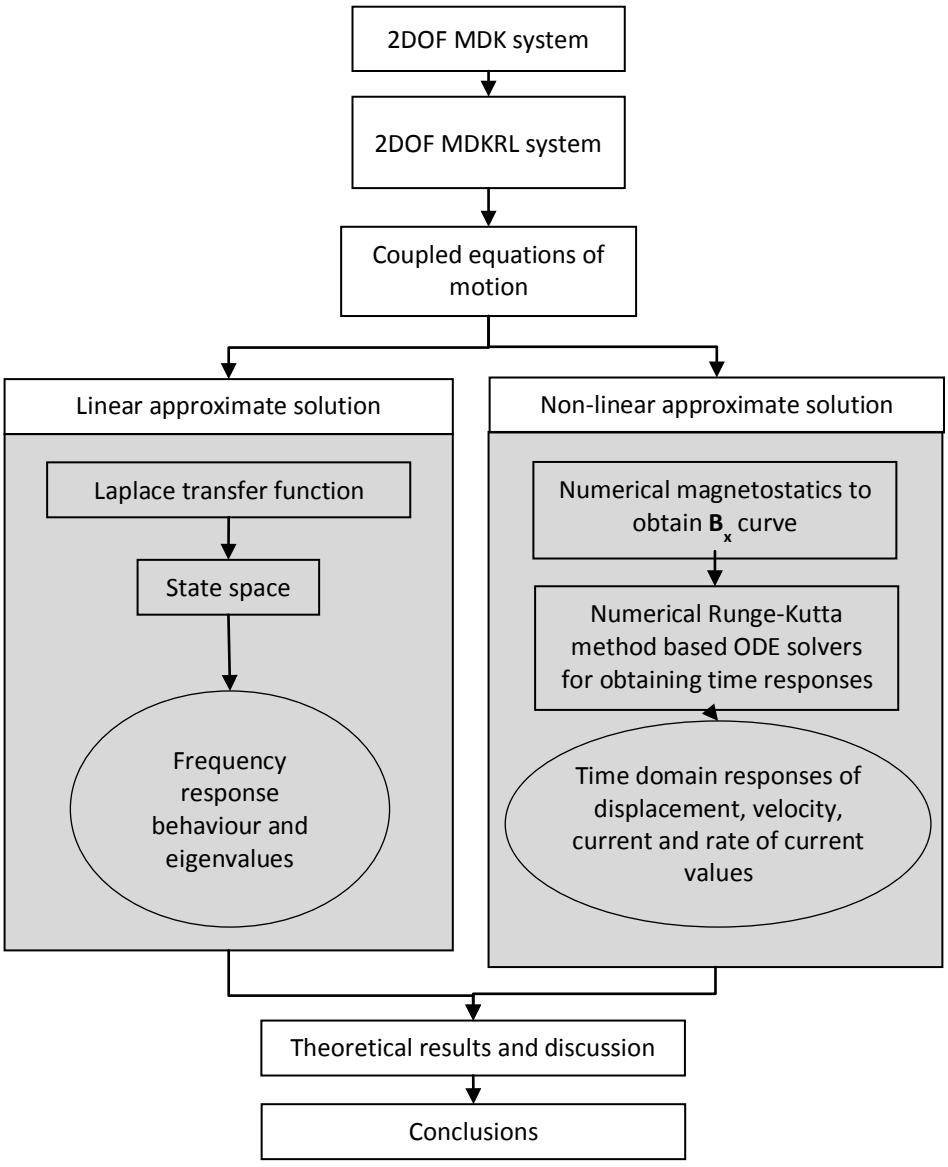


Figure 5.1 Research methodology of 2DOF1D EMVEH system.

## 5.2 The 2DOF1D damped EMVEH model:

The 2DOF1D EMVEH system consists of two active electromagnetic masses $M_1$ and $M_2$ as shown in Figure 5.2. Each of these masses can either be a moving magnet if the magnet oscillates inside a surrounding coil or vice-versa. In this research, the coil masses are considered as the active electromagnetic masses $M_1$ and $M_2$ which are surrounded by a ring magnet as shown in Figure 5.3. The mass $M_1$ is connected to the base by a spring $K_3$ and has a total damping of $D_3$. Mass $M_2$ is connected to the base by $K_2$ and has the total damping $D_2$. $M_1$ is also connected to $M_2$ by spring $K_1$ and with damping $D_1$. The two coils are connected in series and the output voltage is obtained from them.

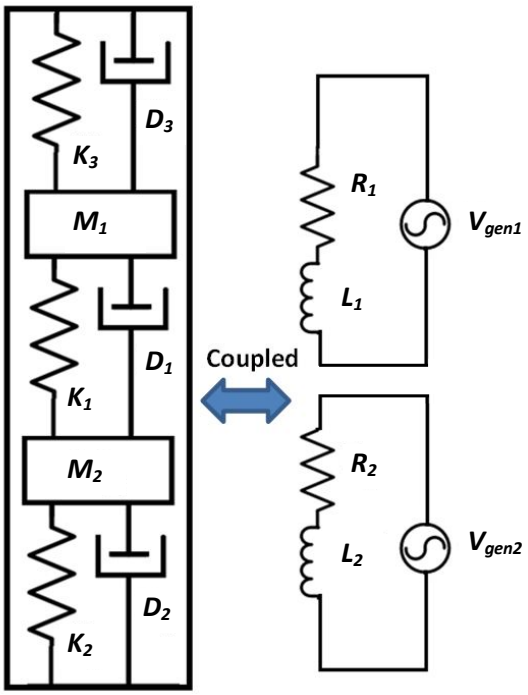


Figure 5.2 General schematic of 2DOF1D EMVEH model showing the mechanical MDK system being coupled to electrical RL system.

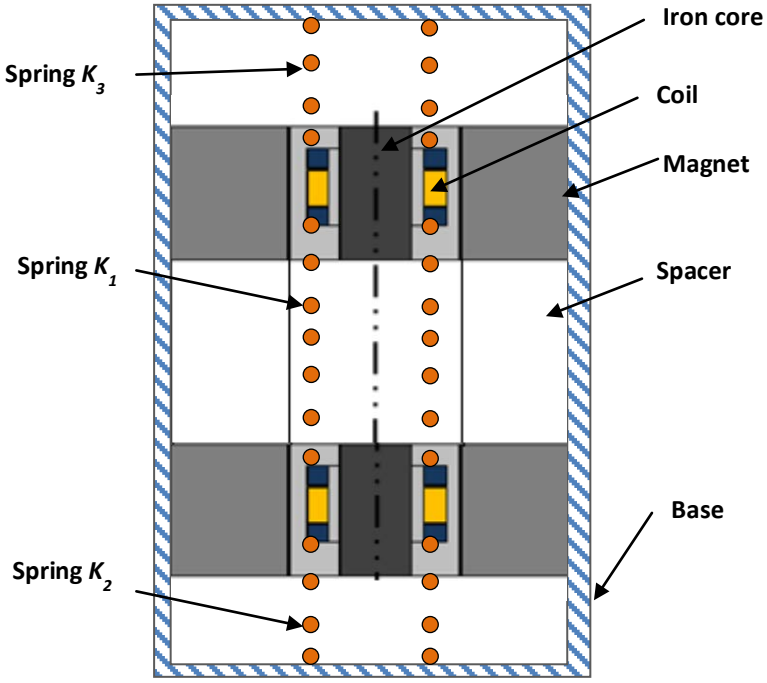


Figure 5.3 Cross-section of a magnet coil and iron-core arrangement.

The theoretical simulation of 2DOF1D was divided into seven analyses, as shown in Table 5.1. The 2DOF1D model was analysed initially in its basic form; a 2DOF1D MDK system that consisted of only the mechanical system without an electrical transduction mechanism. The next model was the 2DOF1D MDKRL system wherein the mechanical MDK system was coupled to the RL circuit. The values of the design parameters *M, D, K, R, L* and *T* constants were assumed as shown in Table 5.1, in all the seven analyses to ensure fair comparison of the results. Initially, Analysis 1 was performed with identical spring stiffnesses $K_1 = K_2 = K_3$ followed by different spring stiffnesses in Analysis 2 where $K_1 = K_3 = 80$ N/m and $K_2 = 20$ N/m. It was found that having different spring stiffnesses proved advantageous from a broadband energy harvesting point of view. Hence, the same configuration of spring stiffnesses with $K_1 = K_3 = 80$ N/m and $K_2 = 20$ N/m were assumed for the rest of the analyses from Analysis 3 to Analysis 7. Also, the value of 0.0001m was assumed for the input base motion $y$ for analysis from Analysis 3 to Analysis 7. Since it was found that the MDKRL system was better than the MDKRLC system (see Chapter 4), in terms of measuring voltage outputs, only the 2DOF1D MDKRL EMVEH was considered in this current chapter.

Table 5.1 Theoretical simulations of 2DOF1D EMVEH model

| | | 2 DOF1D MDK | | | | 2D0F1D MDKRL | | |
|---|---|---|---|---|---|---|---|---|
| | | Analysis 1 | Analysis 2 | Analysis 3 | Analysis 4 | Analysis 5 | Analysis 6 | Analysis 7 |
| Variables | | Laplace | Laplace | State space | Nonlinear | Laplace | State space | Nonlinear |
| Coil masses | $M_1$ (kg) | 0.0015 | 0.0015 | 0.0015 | 0.0015 | 0.0015 | 0.0015 | 0.0015 |
| | $M_2$ (kg) | 0.0015 | 0.0015 | 0.0015 | 0.0015 | 0.0015 | 0.0015 | 0.0015 |
| Damping coefficients | $D_1$ (Ns/m) | 0.05 | 0.05 | 0.05 | 0.05 | 0.05 | 0.05 | 0.05 |
| | $D_2$ (Ns/m) | 0.05 | 0.05 | 0.05 | 0.05 | 0.05 | 0.05 | 0.05 |
| | $D_3$ (Ns/m) | 0.05 | 0.05 | 0.05 | 0.05 | 0.05 | 0.05 | 0.05 |
| Spring Stiffnesses | $K_1$ (N/m) | 80 | 80 | 80 | 80 | 80 | 80 | 80 |
| | $K_2$ (N/m) | 80 | 20 | 20 | 20 | 20 | 20 | 20 |
| | $K_3$ (N/m) | 80 | 80 | 80 | 80 | 80 | 80 | 80 |
| Resistances | $R_1$ (Ohm) | NA* | NA | NA | NA | 0.3 | 0.3 | 0.3 |
| | $R_2$ (Ohm) | NA | NA | NA | NA | 0.3 | 0.3 | 0.3 |
| Inductances | $L_1$ (H) | NA | NA | NA | NA | 0.016 | 0.016 | 0.016 |
| | $L_2$ (H) | NA | NA | NA | NA | 0.016 | 0.016 | 0.016 |
| Coupling coefficient | $T$ (Tm) | 0.492 | 0.492 | 0.492 | 0.492 | 0.492 | 0.492 | 0.492 |

*NA =Not Applicable.

## 5.3 A Simple 2DOF1D MDK system

As dealt with previously in Chapter 4, a similar methodology of moving from the simplest MDK only system to the MDK RL is seen as beneficial to a comprehensive understanding of

the 2DOF1D system. Therefore, only the 2DOF1D MDK system, as shown in Figure 5.4, was initially considered.

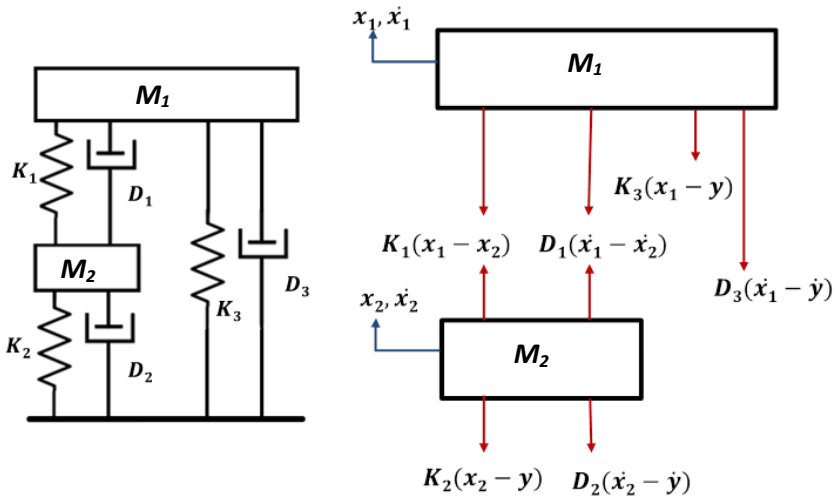


Figure 5.4 2DOF1D MDK system.

Considering the free body diagrams of masses $M_1$, the force equation can be given by:

$$M_1\ddot{x}_1 + K_1(x_1 - x_2) + D_1(\dot{x}_1 - \dot{x}_2) + K_3(x_1 - y) + D_3(\dot{x}_1 - \dot{y}) = 0,$$

which can be rearranged as:

$$M_1\ddot{x}_1 + (K_1 + K_3)x_1 + (D_1 + D_3)\dot{x}_1 - K_1x_2 - D_1\dot{x}_2 = D_3\dot{y} + K_3y. \quad (5.1)$$

Similarly, the force equation for mass $M_2$ can be given by:

$M_2\ddot{x}_2 - K_1(x_1 - x_2) - D_1(\dot{x}_1 - \dot{x}_2) + K_2(x_2 - y) + D_2(\dot{x}_2 - y) = 0$, which can be rearranged as:

$$M_2\ddot{x}_2 + (K_1 + K_2)x_2 + (D_1 + D_2)\dot{x}_2 - K_1x_1 - D_1\dot{x}_1 = D_2\dot{y} + K_2y. \quad (5.2)$$

Equations (5.1) and (5.2) can be rewritten in matrix form as:

$$\begin{bmatrix} M_1 & 0 \\ 0 & M_2 \end{bmatrix}\begin{bmatrix} \ddot{x}_1 \\ \ddot{x}_2 \end{bmatrix} + \begin{bmatrix} D_1 + D_3 & -D_1 \\ -D_1 & D_1 + D_2 \end{bmatrix}\begin{bmatrix} \dot{x}_1 \\ \dot{x}_2 \end{bmatrix} + \begin{bmatrix} K_1 + K_3 & -K_1 \\ -K_1 & K_1 + K_2 \end{bmatrix}\begin{bmatrix} x_1 \\ x_2 \end{bmatrix} = \begin{bmatrix} D_3 & K_3 \\ D_2 & K_2 \end{bmatrix}\begin{bmatrix} \dot{y} \\ y \end{bmatrix}. \quad (5.3)$$

### 5.3.1 Laplace transform analysis of 2DOF1D MDK system

Applying the Laplace transform to equation (5.3) gives:

$$\begin{bmatrix} M_1 & 0 \\ 0 & M_2 \end{bmatrix}\begin{bmatrix} s^2x_1 \\ s^2x_2 \end{bmatrix} + \begin{bmatrix} D_1+D_3 & -D_1 \\ -D_1 & D_1+D_2 \end{bmatrix}\begin{bmatrix} sx_1 \\ sx_2 \end{bmatrix} + \begin{bmatrix} K_1+K_3 & -K_1 \\ -K_1 & K_1+K_2 \end{bmatrix}\begin{bmatrix} x_1 \\ x_2 \end{bmatrix} = \begin{bmatrix} D_3 & K_3 \\ D_2 & K_2 \end{bmatrix}\begin{bmatrix} sy \\ y \end{bmatrix}, \quad (5.4)$$

and ignoring initial conditions. Here, $s = j\omega$ where ω represents the excitation frequency of the system in rad/s. This can be rewritten as:

$$\begin{bmatrix} M_1s^2+(D_1+D_3)s+(K_1+K_3) & -D_1s-K_1 \\ -D_1s-K_1 & M_2s^2+(D_1+D_2)s+(K_1+K_2) \end{bmatrix}\begin{bmatrix} x_1 \\ x_2 \end{bmatrix} = \begin{bmatrix} D_3s+K_3 \\ D_2s+K_2 \end{bmatrix}[y] \quad (5.5)$$

This is of the form $[A][\alpha] = [B][\beta]$,which can be rearranged as:

$$\begin{bmatrix} \alpha \\ \beta \end{bmatrix} = \begin{bmatrix} \frac{x_1}{y} \\ \frac{x_2}{y} \end{bmatrix} = [A]^{-1}[B],$$

where,

$$A = \begin{bmatrix} a_{11} & a_{12} \\ a_{21} & a_{22} \end{bmatrix} = \begin{bmatrix} M_1s^2+(D_1+D_3)s+(K_1+K_3) & -D_1s-K_1 \\ -D_1s-K_1 & M_2s^2+(D_1+D_2)s+(K_1+K_2) \end{bmatrix},$$

$B = \begin{bmatrix} b_1 \\ b_2 \end{bmatrix} = \begin{bmatrix} D_3s+K_3 \\ D_2s+K_2 \end{bmatrix}$, $\alpha = \begin{bmatrix} x_1 \\ x_3 \end{bmatrix}$ and $\beta = [y]$.

Equation (5.5) can then be written as:

$[A][\alpha] = [B][\beta]$,

$$\Rightarrow \frac{[\alpha]}{[\beta]} = \begin{bmatrix} x_1/y \\ x_2/y \end{bmatrix} = [A^{-1}][B],$$

$$\Rightarrow \begin{bmatrix} x_1/y \\ x_2/y \end{bmatrix} = \frac{1}{|A|}\begin{bmatrix} a_{22} & -a_{12} \\ -a_{21} & a_{11} \end{bmatrix}\begin{bmatrix} b_1 \\ b_2 \end{bmatrix} = \frac{1}{|A|}\begin{bmatrix} a_{22}b_1 & -a_{12}b_2 \\ -a_{21}b_1 & +a_{11}b_2 \end{bmatrix}.$$

Hence the transfer functions are given by:

$$G(s) = \frac{x_1(s)}{y(s)} = \frac{1}{|A|}(a_{22}b_1 - a_{12}b_2), \tag{5.6}$$

and

$$H(s) = \frac{x_2(s)}{y(s)} = \frac{1}{|A|}(a_{11}b_2 - a_{21}b_1), \tag{5.7}$$

where $a_{11} = M_1s^2 + (D_1 + D_3)s + (K_1 + K_3)$, $a_{12} = a_{21} = -D_1s - K_1$, $a_{22} = M_2s^2 + (D_1 + D_2)s + (K_1 + K_2)$ and $b_1 = D_3s + K_3$, $b_2 = D_2s + K_2$ respectively.

The theoretical simulation was run to yield the following results (see Appendix B – Analysis 5.1 for MATLAB code) using the following realistic design values: $M_1 = M_2 = 0.0015$ kg, $D_1 = D_2 = D_3 = 0.05$ Ns/m, $K_1 = K_2 = K_3 = 80$ N/m and the results are given in Figure 5.5. Only the frequency response of mass $M_1$ motion is shown since both were found to be identical.

(a)

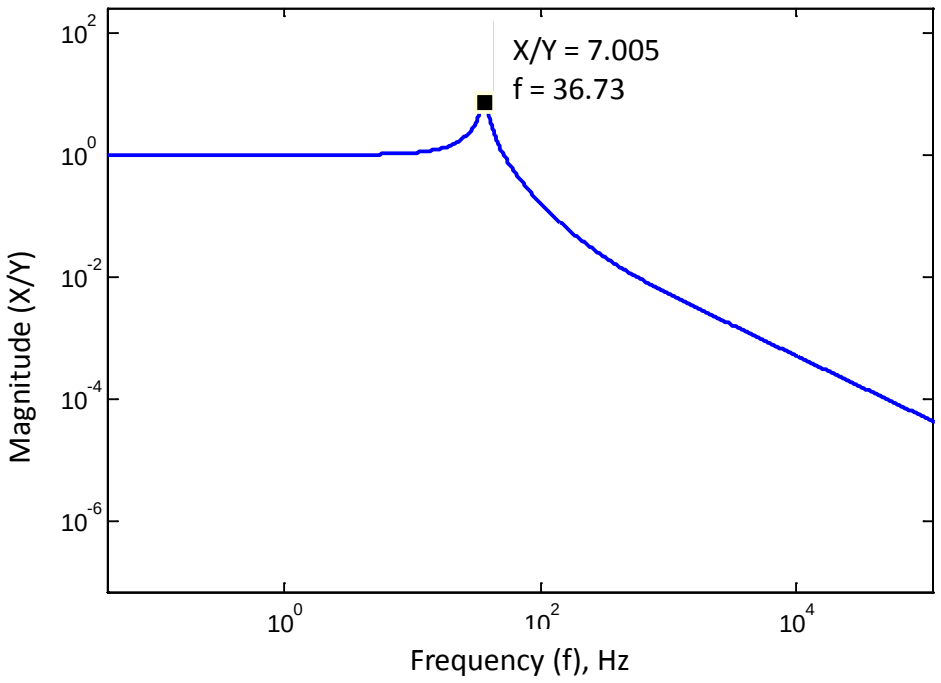

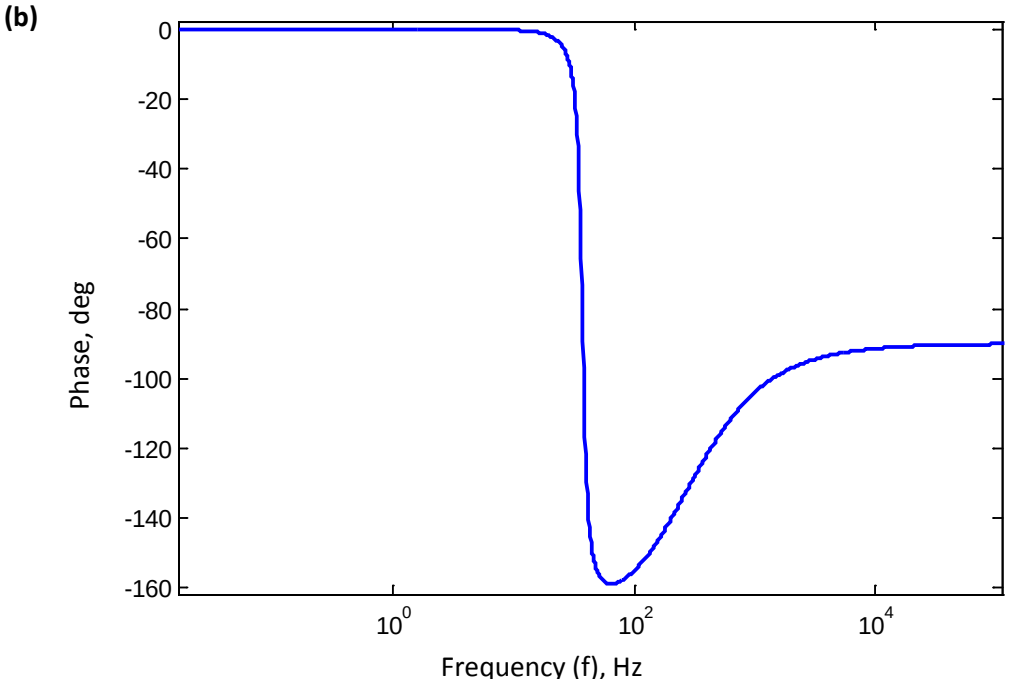


Figure 5.5 Frequency response of 2DOF1D MDK system with $K_1 = K_2 = K_3 = 80$ N/m.

It was observed that both the coil masses $M_1$ and $M_2$ had identical frequency responses. This was not deemed favourable from a practical standpoint, since the very purpose of a multi-degree-of-freedom system is to have multiple resonant frequencies to ensure maximum power output at different frequencies. The above results are due to the reason that the both the top and bottom springs $K_2$ and $K_3$ are identical.

If one of the springs, for example, the bottom spring $K_2$ has relatively low stiffness compared to the springs $K_1$ and $K_3$, then it may make the system vibrate at two different resonances. Hence, another 2DOF1D MDK analysis was run using the same values with the middle spring of stiffness $K_2$ = 20 N/m. The Laplace transform based frequency response results showed two peak resonances for both $x_1$ and $x_2$ as can be observed in Figure 5.6. The two resonant peaks in both the masses were similar to each other. This is expected since only two resonant frequencies can occur in an EMVEH consisting of two coil masses. The first resonant peaks for $x_1$ and $x_2$ were at 27 Hz where ($x_1/y$) peak was 4.094 at 26.91Hz and ($x_2/y$) peak was 5.643 at 27.19Hz. The second resonant peak for $x_1$ and $x_2$ was at 60.5Hz where ($x_1/y$) peak was 0.9545 at 60.41Hz but ($x_2/y$) peak was not clear due to damping,

although significant transition occurred at this frequency. Henceforth, changes to the middle spring stiffness $K_2$ would be employed in the future state space and non-linear analyses.

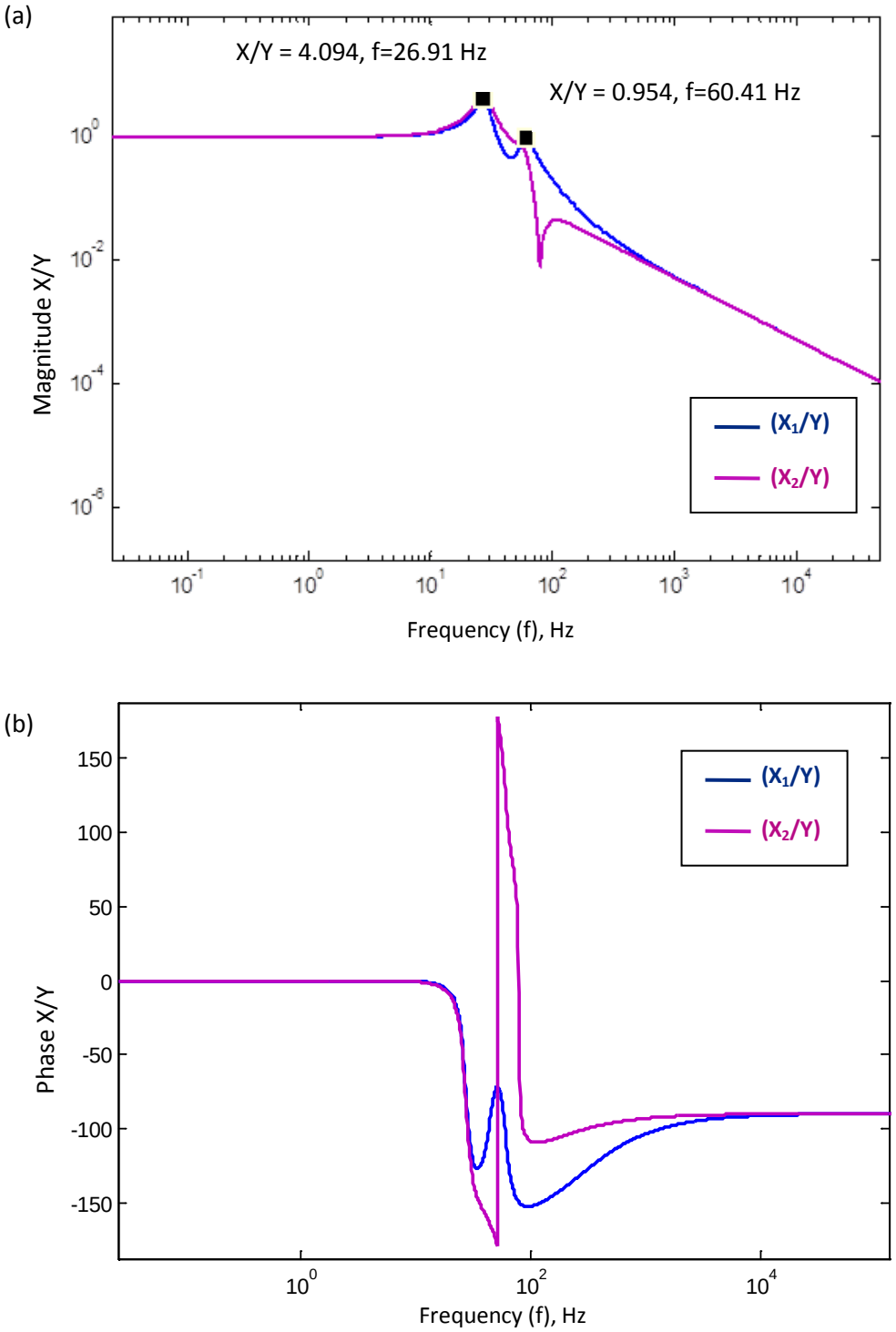


Figure 5.6 Frequency response of 2DOF1D MDK system with $K_1 = K_3 = 80$ N/m and $K_2 = 20$N/m (a) magnitude ($X/Y$) versus frequency and (b) phase versus frequency.

### 5.3.2 State space analysis of 2DOF1D MDK system

Applying the state space method to the 2DOF1D MDK only system, the following state variables, $V_1$, $V_2$, $V_3$ and $V_4$ can be obtained as:

$$V_1 = x_{1,} \tag{5.8}$$

$$V_2 = \dot{x}_1 = \frac{dV_1}{dt}, \tag{5.9}$$

$$V_3 = x_2, \tag{5.10}$$

$$V_4 = \dot{x}_2 = \frac{dV_3}{dt}. \tag{5.11}$$

From equation (5.1) and the above state variables, the acceleration of coil mass 1 can be given by:

$$\ddot{x}_1 = \frac{dV_2}{dt} = \frac{1}{M_1}[D_3\dot{y} + K_3 y - (D_1 + D_3)\dot{x}_1 - (K_1 + K_3)x_1 + D_1\dot{x}_2 + K_1 x_2]$$

$$= \frac{D_3}{M_1}\dot{y} + \frac{K_3}{M_1}y - \frac{(D_1 + D_3)}{M_1}V_2 - \frac{(K_1 + K_3)}{M_1}V_1 + \frac{D_1}{M_1}V_4 + \frac{K_1}{M_1}V_3. \tag{5.12}$$

Similarly, from equation (5.2):

$$\ddot{x}_2 = \frac{dV_4}{dt} = \frac{1}{M_2}[D_2\dot{y} + \dot{K}_2 y - (D_1 + D_2)\dot{x}_2 - (K_1 + K_2)x_2 + D_1\dot{x}_1 + K_1 x_1]$$

$$= \frac{D_2}{M_2}\dot{y} + \frac{K_2}{M_2}y - \frac{(D_1 + D_2)}{M_2}V_4 - \frac{(K_1 + K_2)}{M_2}V_3 + \frac{D_1}{M_2}V_2 + \frac{K_1}{M_2}V_{1.} \tag{5.13}$$

Hence, the state space matrix equation of 2DOF1D can be written as:

$$\begin{bmatrix} \frac{dV_1}{dt} \\ \frac{dV_2}{dt} \\ \frac{dV_3}{dt} \\ \frac{dV_4}{dt} \end{bmatrix} = \begin{bmatrix} 0 & 1 & 0 & 0 \\ \frac{-(K_1+K_3)}{M_1} & \frac{-(D_1+D_3)}{M_1} & \frac{K_1}{M_1} & \frac{D_1}{M_1} \\ 0 & 0 & 0 & 1 \\ \frac{K_1}{M_2} & \frac{D_1}{M_2} & \frac{-(K_1+K_2)}{M_2} & \frac{-(D_1+D_2)}{M_2} \end{bmatrix} \begin{bmatrix} V_1 \\ V_2 \\ V_3 \\ V_4 \end{bmatrix} + \begin{bmatrix} 0 & 0 \\ \frac{D_3}{M_1} & \frac{K_3}{M_1} \\ 0 & 0 \\ \frac{D_2}{M_2} & \frac{K_2}{M_2} \end{bmatrix} \begin{bmatrix} \dot{y} \\ y \end{bmatrix}. \quad (5.14)$$

The theoretical simulation was run to yield the results shown in Figure 5.7 (see also Appendix B for MATLAB code) using the following realistic design values: $M_1 = M_2 = 0.0015$ kg, $D_1 = D_2 = D_3 = 0.05$ Ns/m, $K_1 = K_3 = 80$ N/m and $K_2 = 20$ N/m.

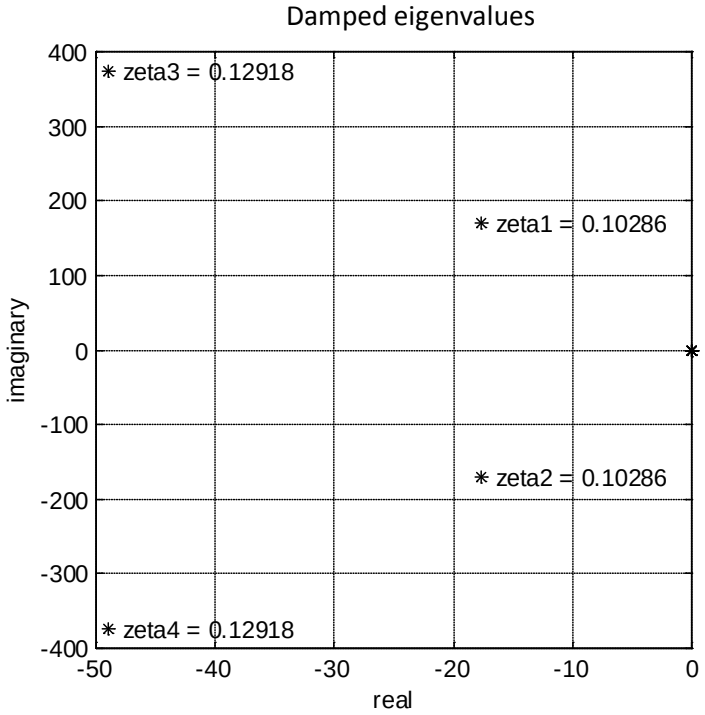


Figure 5.7 Eigenvalues from space state method for 2DOF MDK system.

The resulting eigenvalues obtained were $\lambda_{i=1,2,3,4}$ = -48.93 + 375.6i, -48.93 - 375.6i,-17.74 + 171.55i and -17.74 - 171.55i as shown in Figure 5.7. The corresponding natural frequencies $f_{n1}$ = 27.45Hz and $f_{n2}$ = 60.28Hz were obtained using the equation (4.10) and these matched the peak frequencies observed in the Laplace transform frequency response, as shown in Figure 5.6. The damping ratios were found to be $\zeta_{i,i+1} = 0.129$ and $\zeta_{i+2,i+3} = 0.103$ using equation (4.11) (and see Figure 5.7 above). The close match between the Laplace and the state space values confirms the validity of the theoretical model of 2DOF1D MDK system.

### 5.3.3 Non-linear analysis of 2DOF1D MDK system

Although the simple MDK System was linear, the non-linear analysis was simulated to obtain the time response and to observe any deviations from the approximate linear method.

For this, the following state variables were considered:

$$Z(1) = x_1 \tag{5.15}$$

$$Z(2) = \dot{x}_1 = \frac{dZ(1)}{dt} \tag{5.16}$$

$$Z(3) = x_2 \tag{5.17}$$

$$Z(4) = \dot{x}_2 = \frac{dZ(3)}{dt} \tag{5.18}$$

From equation (5.1) and (5.2):

$$\begin{aligned}\frac{dZ(2)}{dt} &= \frac{1}{M_1}[D_3\dot{y} + K_3 y - (D_1 + D_3)\dot{x}_1 - (K_1 + K_3)x_1 + D_1\dot{x}_2 \\ &\quad + K_1 x_2] \\ &= \frac{D_3}{M_1}\dot{y} + \frac{K_3}{M_1}y - \frac{(D_1 + D_3)}{M_1}Z(2) - \frac{(K_1 + K_3)}{M_1}Z(1) + \frac{D_1}{M_1}Z(4) \\ &\quad + \frac{K_1}{M_1}Z(3) \\ \frac{dZ(4)}{dt} &= \frac{1}{M_2}[D_2\dot{y} + K_2 y - (D_1 + D_2)\dot{x}_2 - (K_1 + K_2)x_2 + D_1\dot{x}_1 \\ &\quad + K_1 x_1]\end{aligned} \tag{5.19}$$

$$= \frac{D_2}{M_2}\dot{y} + \frac{K_2}{M_2}y - \frac{(D_1 + D_2)}{M_2}Z(4) - \frac{(K_1 + K_2)}{M_2}Z(3) + \frac{D_1}{M_1}Z(2) + \frac{K_1}{M_1}Z(1) \quad (5.20)$$

The theoretical simulation was run to yield the following time responses for displacements, $x_1$ and $x_2$ and their corresponding velocities as in Figure 5.8. These were obtained using the same design values, $M_1$ = $M_2$ = $M_3$ = 0.0015 kg, $D_1$ = $D_2$ = $D_3$ = 0.05 Ns/m, $K_1$ = $K_3$ = 80 N/m and $K_2$ = 20 N/m. The peak displacements at the first resonant frequency of 27.45 Hz, observed from the non-linear time domain analyses were $x_1$ = 0.0004048m and $x_2$ = 0.000562 m for the input displacement of $y$ = 0.0001m.

Earlier from Laplace transform analysis, it was observed that at the first resonant frequency of 27.45 Hz, $x_1/y$ = 4.094 and $x_2/y$ = 5.643. Therefore, when the base excitation is $y$ = 0.0001 m, the displacements according to Laplace transforms will be $x_1$ = 0.0001 X 4.094 = 0.000409 m and $x_2$ = 0.0001 X 5.643 = 0.000564 m. The values obtained from both the Laplace transform analyses and the non-linear time domain analyses were very close and agreed with each other thus confirming and establishing the assumed 2DOF1D model.

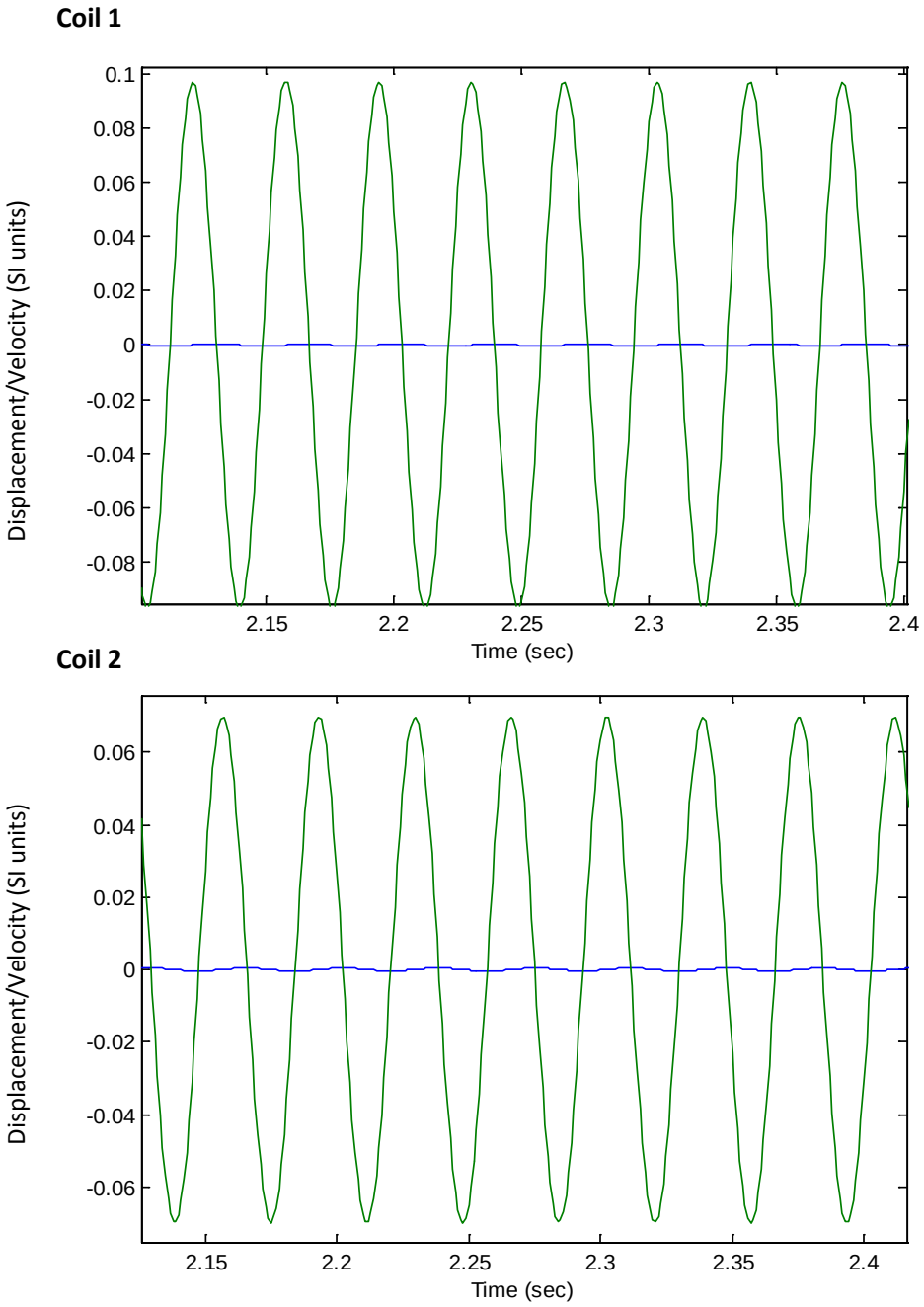


Figure 5.8 Time response from ODE45 method for 2DOF MDK only system.

## 5.4 2DOFID EMVEH MDK RL system derivation

The 2DOFID energy harvester is schematically shown in Figure 5.2. When a 2DOF1D MDK system is coupled with a RL circuit, it forms a complete energy harvester.

Let $x_1$ and $x_2$ be the displacements of the coils, Coil 1 and Coil 2 at any instant *t*. Let $y$ be the displacement of the base at any instant *t*. The magnetic region is moving at the same velocity as the base and hence is at a position $y$ at any instant of time *t*. The positions of coils, $x_1$ and $x_2$ are always with respect to the magnetic region. The magnetic field distribution in the direction of the coil motion is represented in Figure 5.9. The voltages generated by the coils, Coil 1 and Coil 2 are $V_{gen1}$ and $V_{gen2}$ respectively.

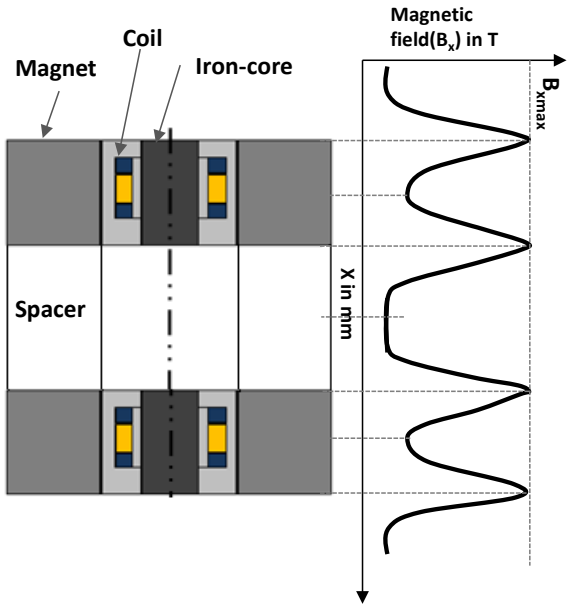


Figure 5.9 Typical magnetic field distributions of two magnets separated by a spacer in 2DOF1D EMVEH. Note that the magnetic field is highest at the either ends of the magnet.

The forces acting on $M_1$ and $M_2$ are similar to the 2DOF – MDK only system, but with additional Lorentz forces. The Lorentz forces are created such that they oppose the direction of motion and hence are electromagnetic damping forces.

Considering these forces, the force equations are:

$$M_1\ddot{x}_1 + (D_1 + D_3)\dot{x}_1 + (K_1 + K_3)x_1 - D_1\dot{x}_2 - K_1x_2 + T(x_1 - y)I_1 = D_3\dot{y} + K_3y \quad (5.21)$$

$$M_2\ddot{x}_2 + (D_1 + D_2)\dot{x}_2 + (K_1 + K_2)x_2 - D_1\dot{x}_1 - K_1x_1 + T(x_2 - y)I_2 = D_2\dot{y} + K_2y \quad (5.22)$$

where $T(x_1 - y)I_1$ and $T(x_2 - y)I_2$ are Lorentz forces, where $T\left(x_{1,2} - y\right)$ is a function of $B\left(x_{1,2} - y\right)$ as in Chapter 4.

Consider $R_1$ and $R_2$ as the resistance values of Coil 1 and Coil 2, $L_1$ and $L_2$ as the inductance of Coil 1 and Coil 2, and the voltage generated by each of these coils is then consumed by their respective RL circuits. In other words, the voltage generated by Coil 1 is given by:

$$V_{gen1} = T(x_1 - y)(\dot{x_1} - \dot{y}) = V_{R_1} + V_{L_1} = RI_1 + L\dot{I}_1. \tag{5.23}$$

Similarly, the voltage generated by Coil 2 is given by:

$$V_{gen2} = T(x_2 - y)(\dot{x_2} - \dot{y}) = V_{R_2} + V_{L_2} = RI_2 + L\dot{I}_2. \tag{5.24}$$

Equations (5.21), (5.22), (5.23) and (5.24) in matrix form give:

$$\begin{bmatrix} M_1 & 0 & 0 & 0 \\ 0 & M_2 & 0 & 0 \\ 0 & 0 & 0 & 0 \\ 0 & 0 & 0 & 0 \end{bmatrix}\begin{bmatrix} \ddot{x}_1 \\ \ddot{x}_2 \\ \dot{I}_1 \\ \dot{I}_2 \end{bmatrix} + \begin{bmatrix} (D_1 + D_3) & -D_1 & 0 & 0 \\ -D_1 & (D_1 + D_2) & 0 & 0 \\ -T(x_1 - y) & 0 & L_1 & 0 \\ 0 & -T(x_2 - y) & 0 & L_2 \end{bmatrix}\begin{bmatrix} \dot{x}_1 \\ \dot{x}_2 \\ \dot{I}_1 \\ \dot{I}_2 \end{bmatrix}$$

$$+ \begin{bmatrix} (K_1 + K_3) & -K_1 & T(x_1 - y) & 0 \\ -K_1 & (K_1 + K_2) & 0 & T(x_2 - y) \\ 0 & 0 & R_1 & 0 \\ 0 & 0 & 0 & R_2 \end{bmatrix}\begin{bmatrix} x_1 \\ x_2 \\ I_1 \\ I_2 \end{bmatrix} \tag{5.25}$$

$$= \begin{bmatrix} D_3 & K_3 \\ D_2 & K_2 \\ -T(x_1 - y) & 0 \\ -T(x_2 - y) & 0 \end{bmatrix}\begin{bmatrix} \dot{y} \\ y \end{bmatrix}.$$

where,

$$T(x_1 - y) = 2\pi nrB(x_1 - y), \tag{5.26}$$

and

$$T(x_2 - y) = 2\pi nrB(x_2 - y) \tag{5.27}$$

,

using the optimum method as discussed in Chapter 4, Table 4.1.

## 5.5 Solving the 2DOF1D MDK RL coupling system

The 2DOFID coupled system of equations can be solved in a similar way to the SDOFID equations in Chapter 4. In a 2DOF1D system, there are two magnetic regions and thus two coupling coefficients.

The first method is to consider the coupling coefficient to be constant, which can be given by:

$$T(x_1 - y) = T(x_2 - y) = 2\pi nrB(x_1 - y) = 2\pi nrB(x_2 - y) = \text{Constant} = T.$$

This makes the coupled equations linear and thus they can be solved by Laplace and state space methods.

The second method is to consider the two coupling coefficients to be the functions of the respective coil positions, $x_1 - y$ and $x_2 - y$ at any instant $t$. This can be given by equations (5.26) and (5.27).

By employing such time-dependent coupling coefficients, the system becomes non-linear. Hence, MATLAB's ODE45, which is based on the numerical Runge-Kutta method of order 4 and 5 was used to solve these coupled equations. To obtain the variation of *B* with respect to the trajectory covered by the coil, ANSOFT was used. The ANSOFT output of *B* versus $x$ was read to the ODE45 to solve the coupled equations and obtain time responses for displacement velocity, current and rate of current for both the coils.

### 5.5.1 Linear –Laplace transform for 2DOF1D MDK RL system

Equation (5.25) becomes

$$\begin{bmatrix} M_1s^2 + (D_1 + D_3)s + (K_1 + K_3) & -D_1s - K_1 & T & 0 \\ -D_1s - K_1 & M_2s^2 + (D_1 + D_2)s + (K_1 + K_2) & 0 & T \\ -Ts & 0 & L_1s + R_1 & 0 \\ 0 & -Ts & 0 & L_2s + R_2 \end{bmatrix} * \begin{bmatrix} X_1(s) \\ X_2(s) \\ I_1(s) \\ I_2(s) \end{bmatrix} = \begin{bmatrix} D_3s + K_3 \\ D_2s + K_2 \\ -Ts \\ -Ts \end{bmatrix} [y] \quad (5.28)$$

where, $T = 2\pi NrB_{max}$ after applying Laplace transforms.

This is of the form, $[A][\alpha] = [B][\beta], \Rightarrow \frac{[\alpha]}{[\beta]} = [A^{-1}][B]$. Thus if

$$A = \begin{bmatrix} a_{11} & a_{12} & a_{13} & a_{14} \\ a_{21} & a_{22} & a_{23} & a_{24} \\ a_{31} & a_{32} & a_{33} & a_{34} \\ a_{41} & a_{42} & a_{43} & a_{44} \end{bmatrix} =$$

$$\begin{bmatrix} M_1 s^2 + (D_1 + D_3)s + (K_1 + K_3) & -D_1 s - K_1 & T & 0 \\ -D_1 s - K_1 & M_2 s^2 + (D_1 + D_2)s + (K_1 + K_2) & 0 & T \\ -Ts & 0 & L_1 s + R_1 & 0 \\ 0 & -Ts & 0 & L_2 s + R_2 \end{bmatrix}$$

$\alpha = \begin{bmatrix} X_1(s) \\ X_2(s) \\ I_1(s) \\ I_2(s) \end{bmatrix}, B = \begin{bmatrix} D_3 s + K_3 \\ D_2 s + K_2 \\ -Ts \\ -Ts \end{bmatrix}$ $and$ $\beta = [y]$. Then, the transfer function matrix is given by:

$$G(s) = \frac{[\alpha]}{[\beta]} = \begin{bmatrix} \frac{x_1(s)}{y(s)} \\ \frac{x_2(s)}{y(s)} \\ \frac{I_1(s)}{y(s)} \\ \frac{I_2(s)}{y(s)} \end{bmatrix} = A^{-1}B. \quad (5.29)$$

A theoretical simulation was run to yield the following results (see Appendix B for MATLAB code) using the following realistic design values of: $M_1$ = $M_2$ = 0.0015 kg, $D_1$ = $D_2$ = $D_3$ = 0.05 Ns/m, $K_1$ = $K_3$ = 80 N/m, $K_2$ = 20 N/m, $R_1$ = $R_2$ = 0.3 Ω, $L_1$ = $L_2$ = 0.016 H. The results of this simulation are given in Figure 5.10.

(a)

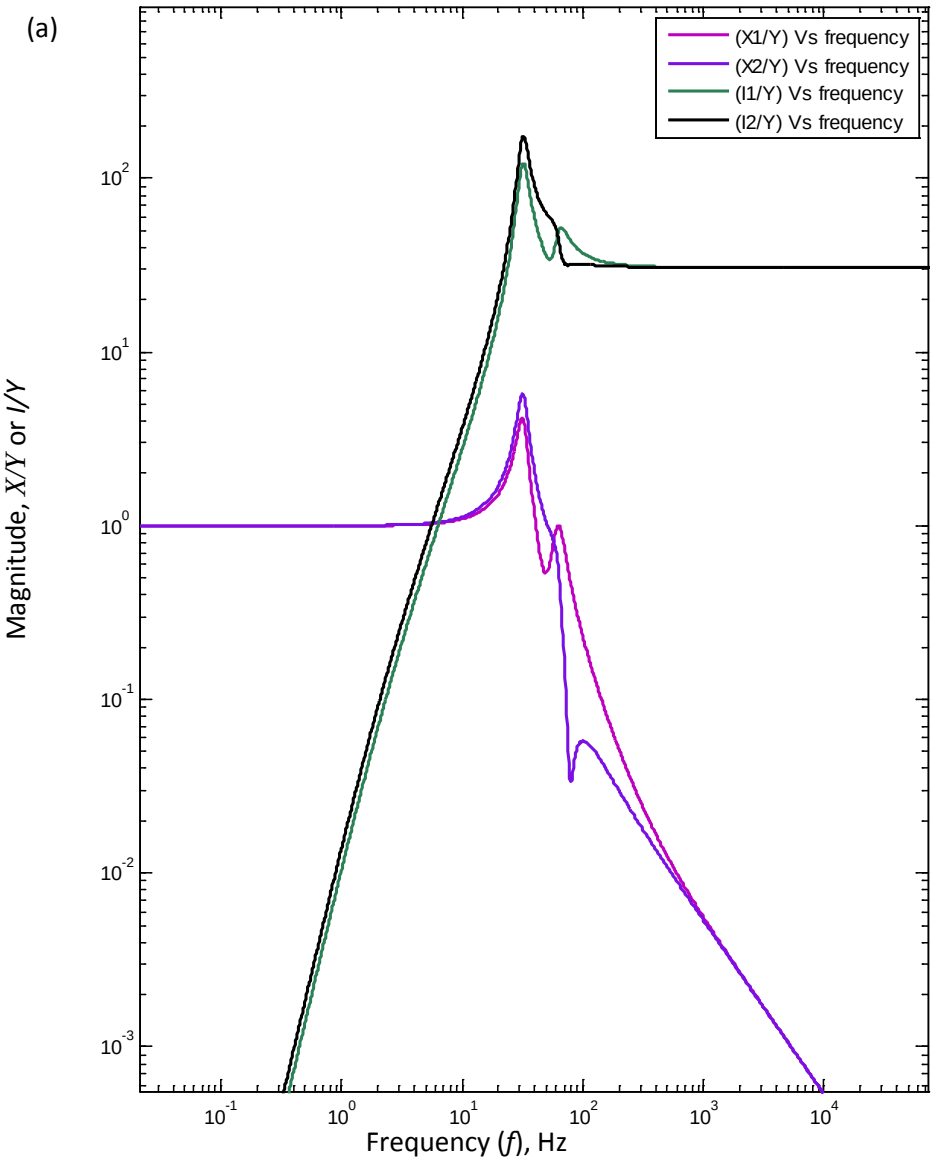
(X1/Y) Vs frequency
(X2/Y) Vs frequency
(I1/Y) Vs frequency
(I2/Y) Vs frequency
Magnitude, X/Y or I/Y
Frequency (f), Hz
10^2
10^1
10^0
10^-1
10^-2
10^-3
10^-1
10^0
10^1
10^2
10^3
10^4

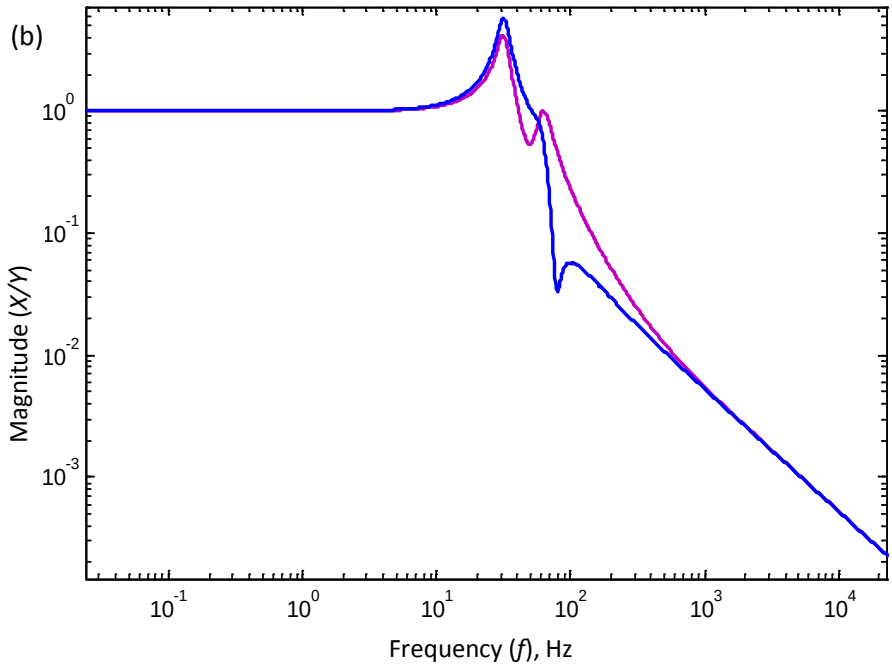
(b)
Magnitude (X/Y)
Frequency (f), Hz

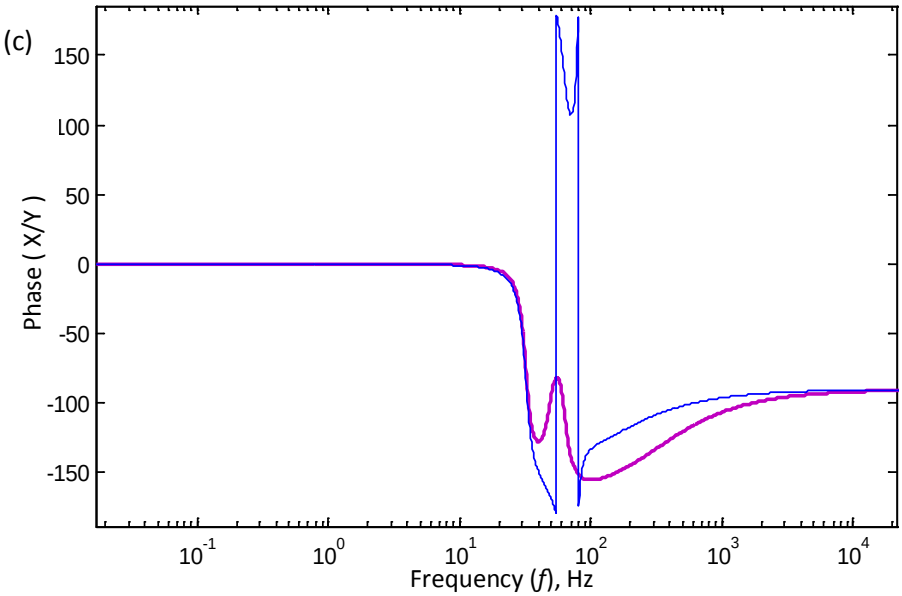
(c)
Phase ( X/Y )
Frequency (f), Hz

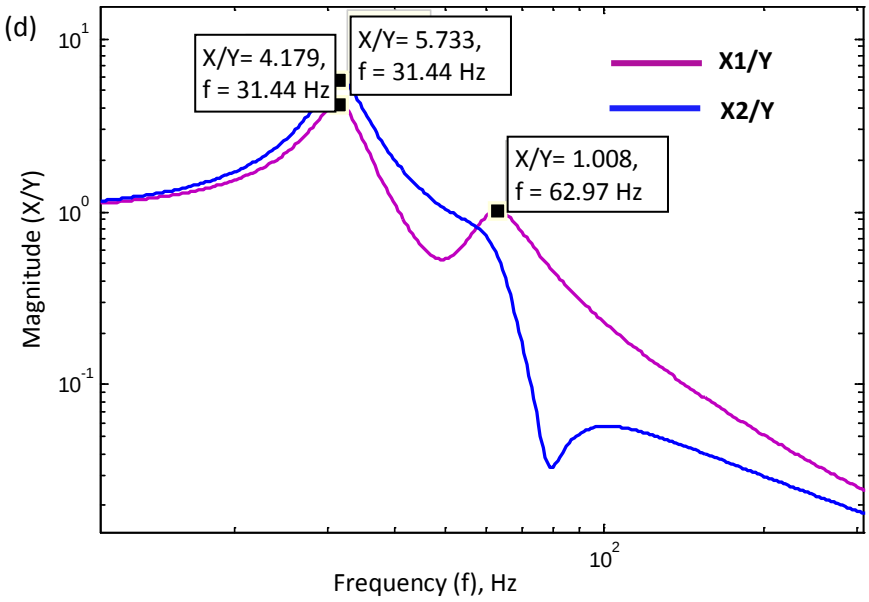
(d)
X/Y= 4.179,
f = 31.44 Hz
X/Y= 5.733,
f = 31.44 Hz
X1/Y
X2/Y
X/Y= 1.008,
f = 62.97 Hz
Magnitude (X/Y)
Frequency (f), Hz

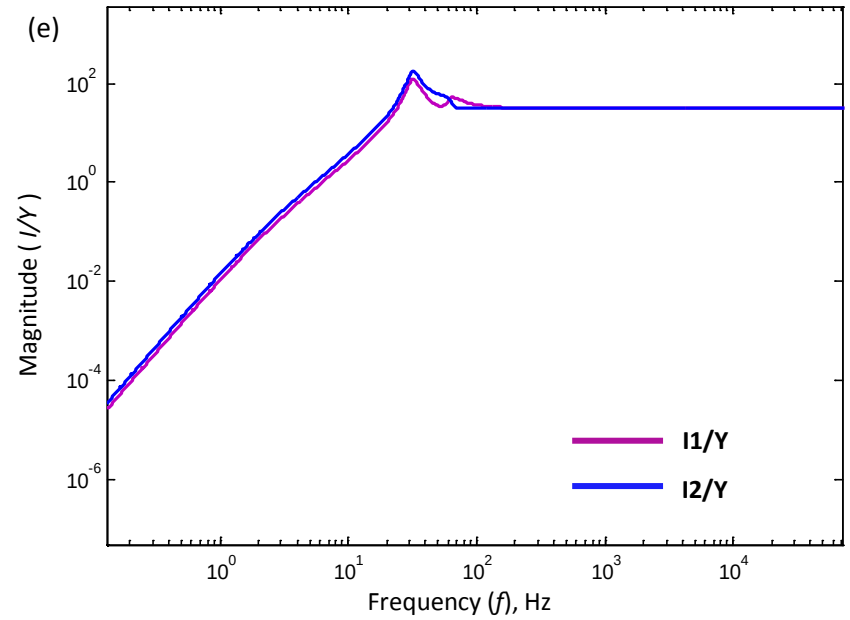
(e)
Magnitude ( I/Y )
Frequency (f), Hz
I1/Y
I2/Y

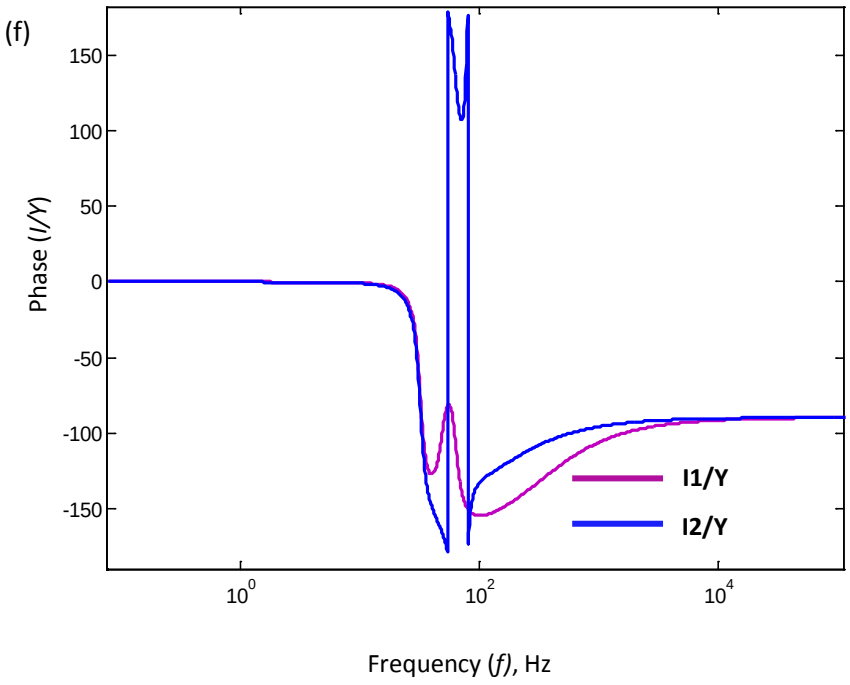
(f)
Phase (I/Y)
Frequency (f), Hz
I1/Y
I2/Y

(g)

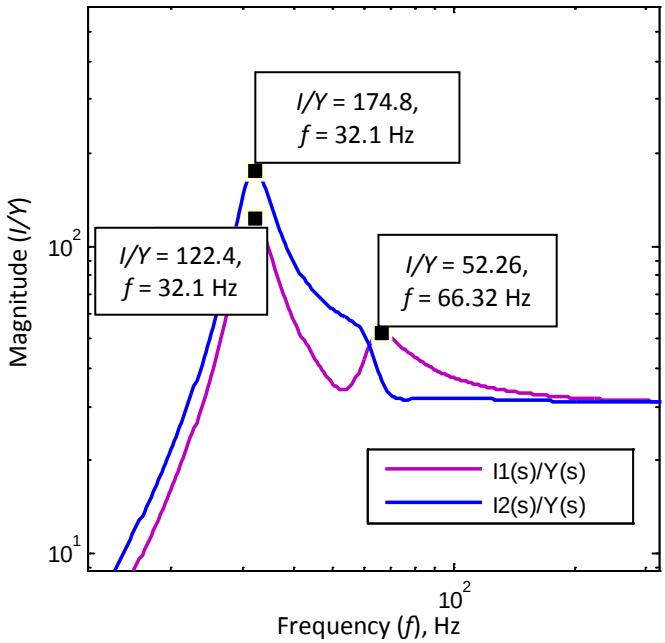
I/Y = 174.8,
f = 32.1 Hz
I/Y = 122.4,
f = 32.1 Hz
I/Y = 52.26,
f = 66.32 Hz
I1(s)/Y(s)
I2(s)/Y(s)
Magnitude (I/Y)
Frequency (f), Hz

(h)

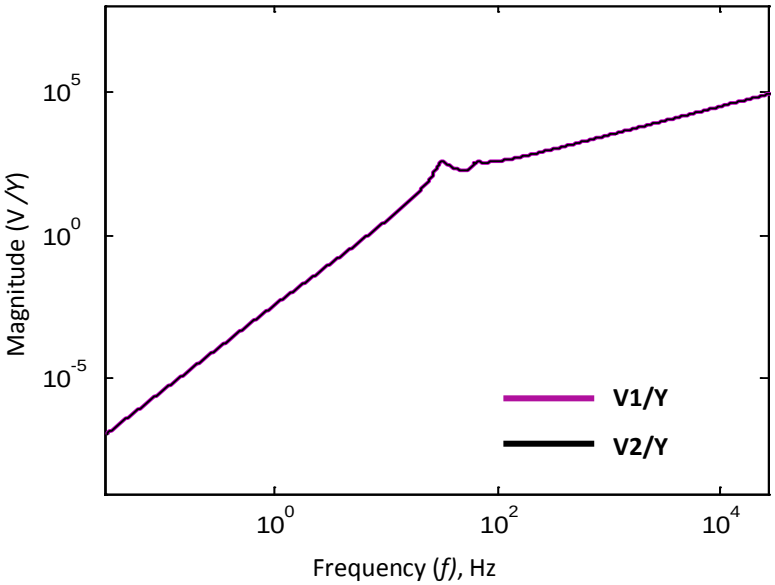
V1/Y
V2/Y
Magnitude (V /Y)
Frequency (f), Hz

(i)

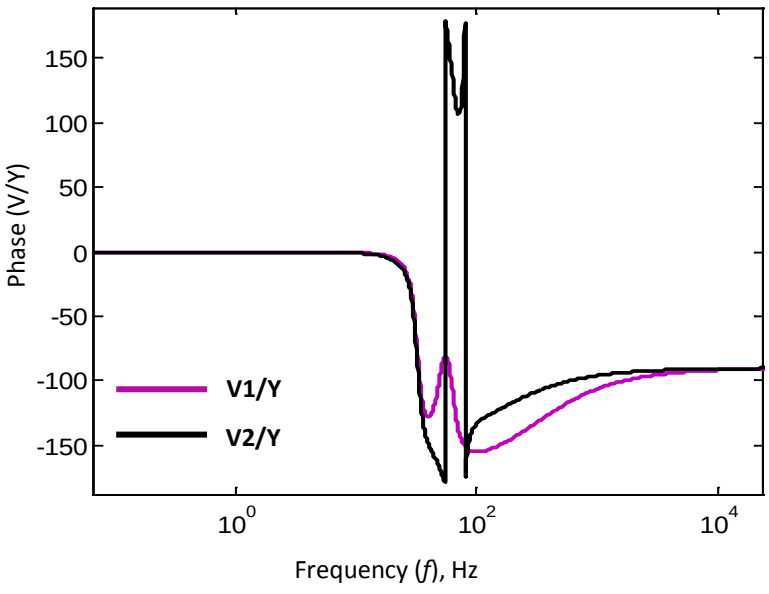
V1/Y
V2/Y
Phase (V/Y)
Frequency (f), Hz

( j )

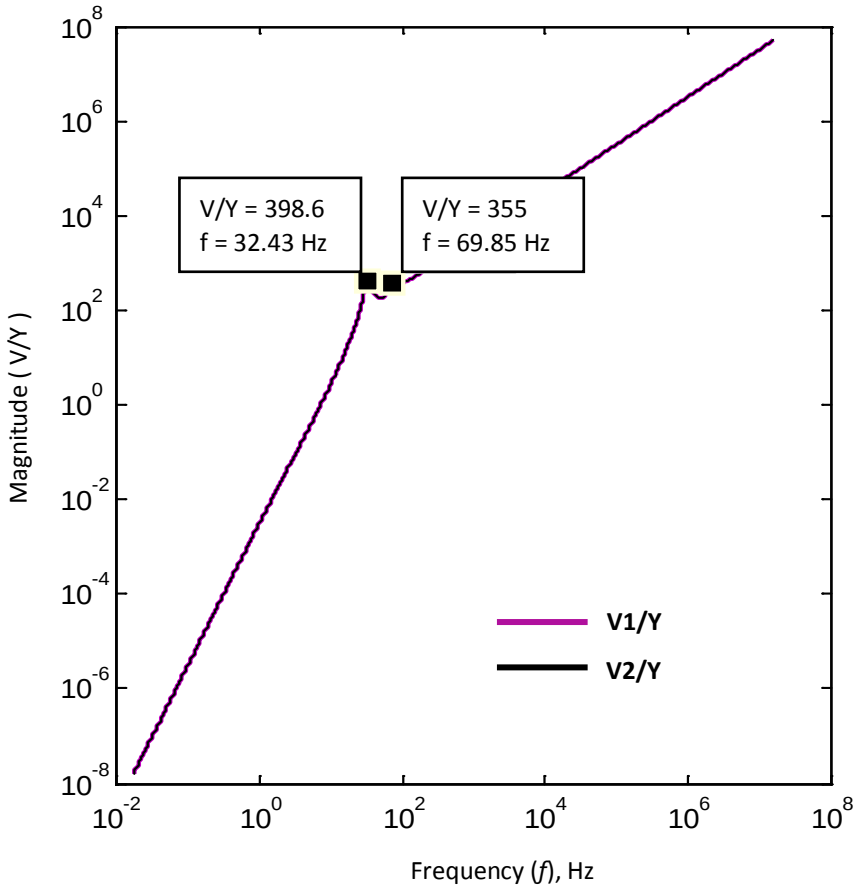


Figure 5.10 (a) to (j) Frequency responses of 2DOF1D MDK RL system:

(a) Summarised frequency responses of coil displacements $X_1$ and $X_2$ and their corresponding induced currents $I_1$ and $I_2$ in a 2DOF1D EMVEH system.

(b) Magnitude frequency response of coil displacement transfer functions, $X_1/Y$ and $X_2/Y$ in a 2DOF1D EMVEH system.

(c) Phase frequency response of coil displacement transfer functions, $X_1/Y$ and $X_2/Y$ in a 2DOF1D EMVEH system.

(d) Figure 5.10(b) magnified to show the peak resonant points.

(e) Magnitude frequency response of coil displacement transfer functions, $I_1/Y$ and $I_2/Y$ in a 2DOF1D EMVEH system.

(f) Phase frequency response of coil displacement transfer functions, $I_1/Y$ and $I_2$/Y in a 2DOF1D EMVEH system.

(g) Figure 5.10(e) magnified to show the peak resonant points.

(h) Magnitude frequency response of coil output voltage transfer functions, $V_1/Y$ and $V_2/Y$ in a 2DOF1D EMVEH system.

(i) Phase frequency response of coil displacement transfer functions, $V_1/Y$ and $V_2/Y$ in a 2DOF1D EMVEH system.

(j) Figure 5.10(h) magnified to show the peak resonant points in a 2DOF1D EMVEH system.

It was observed in Figure 5.10(a) that the 2DOF1D EMVEH showed two resonances corresponding to the motions of masses $M_1$ and $M_2$ respectively. It was observed that the two current frequency responses $I_1/Y$ and $I_2/Y$ corresponded to the mechanical frequency responses $X_1/Y$ and $X_2/Y$.

Although both $x_1$ and $x_2$ had the same frequency for the first resonance, as observed in Figure 5.10(b, d), they were out of phase for the second resonance, as observed in Figure 5.10(c). Similar behaviour was observed with the respective current frequency responses in Figure 5.10(e, f). This suggested that in the second resonance the voltages of individual coils, $V_{gen1}$ and $V_{gen2}$ would be out of phase and this was observed in Figure 5.10(h, i).

It was observed in Figure 5.10(d) that the resonant peaks of $x_1$ and $x_2$ had the same first resonant peak at 31.44 Hz, while only $x_1$ had a second resonant peak at 62.97 Hz. The corresponding current frequency resonances, as observed in Figure 5.10(g), were 32.1 Hz and 66.32 Hz. The differences in the values of the mechanical and electrical resonant peaks of 2DOF1D were similar to the behaviour of the mechanical and electrical resonant peaks observed in SDOF1D EMVEH in the previous chapter. This suggests that in an electrical-mechanical coupled system, the mechanical subsystem is influenced by the electrical subsystem in the form of electrical damping, and the electrical subsystem is influenced by the mechanical velocity affecting the voltage generated by the coil.

For the most effective design of the 2DOF1D energy harvester, these voltages need to be added in phase. This can be achieved by rectifying each of these AC voltages of different phases into DC and adding them later.

### 5.5.2 Linear state space transform for 2DOF1D MDK RL system

State space analysis can be used to solve equation (5.25). State space variables can be defined as:

$$V_1 = x_{1,} \tag{5.30}$$

$$V_2 = \dot{x}_1 = \frac{dV_1}{dt}, \tag{5.31}$$

$$V_3 = x_{2,} \tag{5.32}$$

$$V_4 = \dot{x}_2 = \frac{dV_3}{dt}, \tag{5.33}$$

$$V_5 = I_1, \tag{5.34}$$

$$\dot{I}_1 = \frac{dV_5}{dt}, \tag{5.35}$$

$$V_6 = I_2, \tag{5.36}$$

and $$\dot{I}_2 = \frac{dV_6}{dt}. \tag{5.37}$$

From equation (5.38),

$$\ddot{x}_1 = \frac{dV_2}{dt} = \frac{1}{M_1}[D_3\dot{y} + K_3 y - (D_1 + D_3)\dot{x}_1 - (K_1 + K_3)x_1 + D_1\dot{x}_2 + K_1 x_2 - TI_1]$$

$$= \frac{D_3}{M_1}\dot{y} + \frac{K_3}{M_1}y - \frac{(D_1 + D_3)}{M_1}V_2 - \frac{(K_1 + K_3)}{M_1}V_1 + \frac{D_1}{M_1}V_4 + \frac{K_1}{M_1}V_3 - \frac{T}{M_1}V_5. \tag{5.38}$$

From equation (5.23),

$$\ddot{x}_2 = \frac{dV_4}{dt} = \frac{1}{M_2}[D_2\dot{y} + K_2 y - (D_1 + D_2)\dot{x}_2 - (K_1 + K_2)x_2 + D_1\dot{x}_1 + K_1 x_1 - TI_2]$$

$$= \frac{D_2}{M_2}\dot{y} + \frac{K_2}{M_2}y - \frac{(D_1 + D_2)}{M_2}V_4 - \frac{(K_1 + K_2)}{M_2}V_3 + \frac{D_1}{M_2}V_2 + \frac{K_1}{M_2}V_1 - \frac{T}{M_2}V_6. \tag{5.39}$$

From equations (5.24) and (5.25), $\dot{I}_1$ and $\dot{I}_2$ can also be written as:

$$\dot{I}_1 = \frac{dV_5}{dt} = \frac{T}{L_1}V_2 - \frac{T}{L_1}\dot{Y} - \frac{R_1}{L_1}V_5, \tag{5.40}$$

and

$$\dot{I}_2 = \frac{dV_6}{dt} = \frac{T}{L_2}V_4 - \frac{T}{L_2}\dot{Y} - \frac{R_2}{L_2}V_6. \tag{5.41}$$

Thus in matrix form, the state derivative solution becomes:

$$\begin{bmatrix} \frac{dV_1}{dt} \\ \frac{dV_2}{dt} \\ \frac{dV_3}{dt} \\ \frac{dV_4}{dt} \\ \frac{dV_5}{dt} \\ \frac{dV_6}{dt} \end{bmatrix} = \begin{bmatrix} 0 & 1 & 0 & 0 & 0 & 0 \\ \frac{-(K_1+K_3)}{M_1} & \frac{-(D_1+D_3)}{M_1} & \frac{K_1}{M_1} & \frac{D_1}{M_1} & \frac{-T}{M_1} & 0 \\ 0 & 0 & 0 & 1 & 0 & 0 \\ \frac{K_1}{M_2} & \frac{D_1}{M_2} & \frac{-(K_1+K_2)}{M_2} & \frac{-(D_1+D_2)}{M_2} & 0 & \frac{-T}{M_2} \\ 0 & \frac{T}{L_1} & 0 & 0 & \frac{-R_1}{L_1} & 0 \\ 0 & 0 & 0 & \frac{T}{L_2} & 0 & \frac{-R_2}{L_2} \end{bmatrix} \begin{bmatrix} V_1 \\ V_2 \\ V_3 \\ V_4 \\ V_5 \\ V_6 \end{bmatrix} + \begin{bmatrix} 0 & 0 \\ \frac{D_3}{M_1} & \frac{K_3}{M_1} \\ 0 & 0 \\ \frac{D_2}{M_2} & \frac{K_2}{M_2} \\ \frac{-T}{L_1} & 0 \\ \frac{-T}{L_2} & 0 \end{bmatrix} \begin{bmatrix} \dot{y} \\ y \end{bmatrix}. \quad (5.42)$$

MATLAB software was written to yield the results, as shown in Figure 5.11 (see Appendix B for MATLAB code), using the following realistic values: $M_1 = M_2 = 0.0015$ kg, $D_1 = D_2 = D_3 = 0.05$ Ns/m, $K_1 = K_3 = 80$ N/m, $K_2 = 20$ N/m, $R_1 = R_2 = 0.3$ Ω, $L_1 = L_2 = 0.016$ H.

The eigenvalues obtained were $\lambda_{i=1,2,3,4,5,6}$ = -14.58 + 0i,-18.75 + 0i,-20.42 + 193i,-20.42 - 193i,-48.32 + 378.52i and-48.32 - 378.52i. Their corresponding natural frequencies were $f_1$ = 2.32 Hz, $f_2$ = 2.98 Hz, $f_3$ = 30.89 Hz and $f_4$ = 60.73Hz respectively. It should be noted that the third and fourth natural frequencies are close to the second and third natural frequencies of the Laplace transform, thus the state space results were validated.

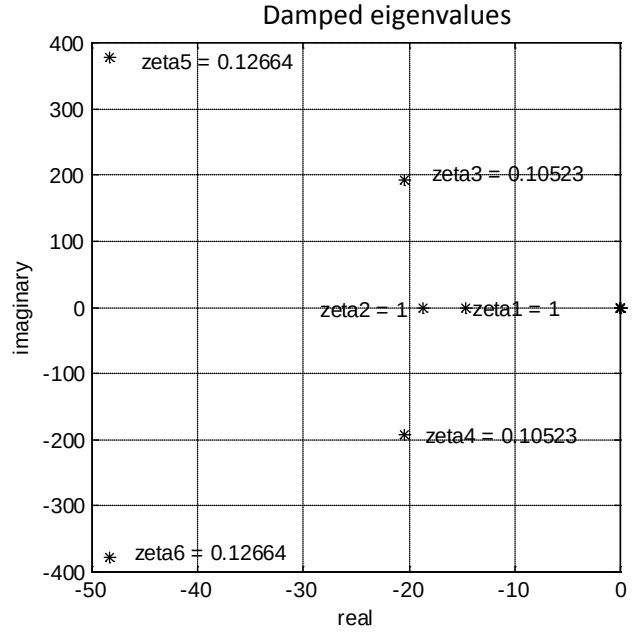


Figure 5.11 Eigenvalues of 2DOF1D MDKRL from state space analysis.

### 5.5.3 Non-linear ODE45–2DOF1D MDK RL analysis

In reality, the coupling coefficients would not be constant but would vary according to the spatially varying magnetic fields; see equations (5.29) and (5.30). This leads to a non-linear treatment of the 2DOF1D MDK RL EMVEH. The coupling coefficients $T(x_1\text{-}y)$ and $T(x_2\text{-}y)$ are the functions of time dependent positions $x_1\text{-}y$ and $x_2\text{-}y$ and can easily be found using numerical magnetostatic analysis. This can be achieved by ANSOFT MAXWELL based magnetostatic analysis. The magnetic field distribution along the direction of coil motion B versus x was obtained as an excel output. Any $B(x, y)$ could be found by interpolation of the value in this ANSOFT output using the MATLAB's command in a similar way to that discussed in equation (4.43).

Consider the state variables given by:

$$Z(1) = x_1, \tag{5.43}$$

$$Z(2) = \dot{x}_1 = \frac{dZ(1)}{dt}, \tag{5.44}$$

$$Z(3) = x_2, \tag{5.45}$$

$$Z(4) = \dot{x}_2 = \frac{dZ(3)}{dt}, \tag{5.46}$$

$$Z(5) = I_1, \tag{5.47}$$

and $$Z(6) = I_2. \tag{5.48}$$

From equation (5.44), this gives:

$$\ddot{x}_1 = \frac{dZ(2)}{dt} = \frac{1}{M_1}[D_3\dot{y} + K_3 y - (D_1 + D_3)Z(2) - (K_1 + K_3)Z(1) + D_1 Z(4) + K_1 Z(3) - T(Z(1) - y)Z(5)]. \tag{5.49}$$

From equation (5.46):

$$\ddot{x}_2 = \frac{dZ(4)}{dt} = \frac{1}{M_2}[D_2\dot{y} + K_2 y - (D_1 + D_2)Z(4) - (K_1 + K_2)Z(3) + D_1 Z(2) + K_1 Z(1) - T(Z(3) - y)Z(6)]. \tag{5.50}$$

From (5.47):

$$\dot{I}_1 = \frac{dZ(5)}{dt} = \frac{1}{L_1}[T(x_1 - y)(\dot{x}_1 - \dot{y}) - R_1 I_1], \tag{5.51}$$

which can be written as:

$$\dot{I}_1 = \frac{dZ(5)}{dt} = \frac{1}{L_1}[T(Z(1) - y)(Z(2) - \dot{y}) - R_1 Z(5)]. \tag{5.52}$$

From (5.48):

$$\dot{I}_2 = \frac{dZ(6)}{dt} = \frac{1}{L_2}[T(x_2 - y)(\dot{x}_2 - \dot{y}) - R_2 I_2], \tag{5.53}$$

which becomes:

$$\dot{I}_2 = \frac{dZ(6)}{dt} = \frac{1}{L_2}[T(Z(3) - y)(Z(4) - \dot{y}) - R_2 Z(6)]. \tag{5.54}$$

The theoretical simulation was run using the following realistic design values of $M_1 = M_2 =$ 0.05 kg, $D_1 = D_2 = D_3 =$ 0.05 Ns/m, $K_1 = K_3 =$ 80 N/m, $K_2 =$ 20 N/m, $R_1 = R_2 =$ 0.3 ohm, $L_1 = L_2 =$ 0.016 H and input base motion amplitude $y$ = 0.1 mm. The results of the simulation are shown in Figure 5.12(a) and Figure 5.12(b) for the first and second modes corresponding to the two resonant peaks. Both $x_1$ and $x_2$ and their corresponding currents $I_1$ and $I_2$ were in phase with each other in mode 1, as shown in Figure 5.12(a) and out of phase at mode 2 as, shown in Figure 5.12(b). The currents $I_1$ and $I_2$ were found to be larger in mode 1 than mode 2 as expected from the Laplace transform results shown in Figure 5.10. The out-of-phase behaviour of the coil current time domain response shown in Figure 5.12(b) appeared to be different from that expected from the Laplace transform analysis. This phase response difference was due to the consideration of the spatial variation of the magnetic field behaviour as a function of the coil location, where the coupling coefficient $T$ was modelled as a function of the position of the coils. For the Laplace transform analysis, this change of coupling coefficient was neglected. This further indicates the necessity to incorporate the non-linear behaviour of the coupling coefficient into the analysis.

(a)

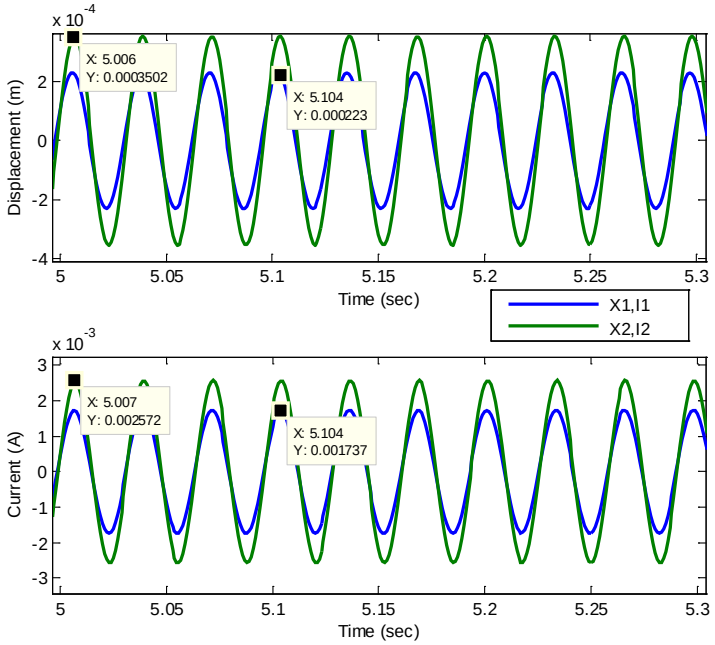


(b)

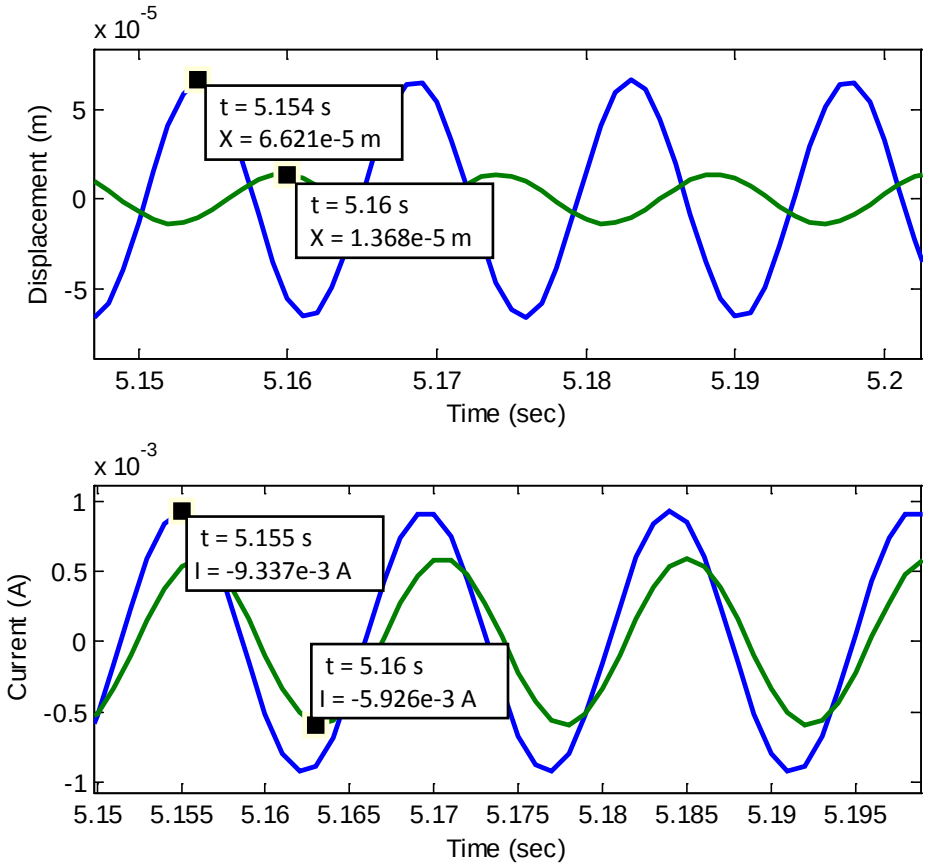


Figure 5.12 Time responses of 2DOF1D MDKRL system (a) at 1st mode at 30.88Hz (b) at 2nd mode at 60.73 Hz.

## 5.6 Power frequency responses of 2DOF1D EMVEH at different amplitudes

In the displacement and the current frequency responses discussed previously in section 5.5, the amplitude Y assumed was 0.1 mm. This small amplitude was assumed in order to compare it with the experimentally achievable amplitude of 0.1 mm, to be discussed in Chapter 6. Hence, the non-linear ODE45 based simulation was performed on the 2DOF1D MDKRL to obtain the current, voltage and the power frequency responses at practical vibration amplitudes of 1 mm to 3 mm. The average power was calculated using equation (3.33).The power factor $\cos\varphi$ was obtained for different frequencies considered in the simulation using equation (3.34). The values obtained are shown in Table 5.2 and are plotted in Figure 5.14. It was observed that for practical amplitudes of 1 mm to 3 mm the power obtained was can easily power sensor /wireless sensor node. However, at higher amplitude and higher frequencies, the acceleration was very high and could be sudden and intense thus demanding a robust design for the energy harvester.

Table 5.2 Theoretical voltage, current and power frequency responses at 1mm to 3mm amplitude.

| | **2DOF1D EMVEH** | | | | | |
|---|---|---|---|---|---|---|
| | **Coil 1** | | | ***Coil 2*** | | |
| ***f* *(Hz)*** | **$V_{rmsth1}$ at 1 mm (mV)** | **$V_{rmsth2}$ at 2 mm (mV)** | **$V_{rmsth3}$ at 3 mm (mV)** | **$V_{rmsth1}$ at 1 mm (mV)** | **$V_{rmsth2}$ at 2 mm (mV)** | **$V_{rmsth3}$ at 3 mm (mV)** |
| 10 | 0.54 | 0.72 | 1.08 | 1.45 | 1.62 | 2.20 |
| 15 | 2.21 | 3.03 | 4.55 | 6.40 | 7.15 | 10.39 |
| 20 | 7.81 | 11.37 | 17.91 | 28.69 | 31.23 | 53.08 |
| 25 | 36.74 | 64.53 | 97.33 | 166.99 | 188.03 | 260.67 |
| 29 | 98.94 | 179.29 | 256.34 | 336.10 | 349.64 | 531.24 |
| 30 | 90.48 | 168.09 | 242.89 | 331.50 | 343.58 | 509.07 |
| 35 | 38.12 | 73.20 | 129.52 | 248.65 | 234.48 | 362.28 |
| 40 | 27.52 | 53.59 | 79.85 | 177.97 | 160.91 | 325.74 |
| 45 | 23.88 | 49.16 | 62.73 | 155.19 | 124.27 | 302.28 |
| 50 | 23.12 | 49.46 | 57.83 | 151.69 | 111.58 | 299.88 |
| 55 | 28.75 | 50.22 | 73.84 | 151.16 | 144.65 | 302.45 |
| 60 | 45.89 | 43.34 | 131.81 | 124.43 | 266.39 | 255.53 |
| 65 | 56.19 | 33.51 | 168.94 | 87.11 | 341.06 | 174.27 |
| 70 | 55.57 | 32.19 | 162.96 | 80.09 | 331.52 | 155.51 |
| | | | | | | |
| ***f* *(Hz)*** | **$I_{rmsth1}$ at 1 mm (mA)** | **$I_{rmsth2}$ at 2 mm (mA)** | **$I_{rmsth3}$ at 3 mm (mA)** | **$I_{rmsth1}$ at 1 mm (mA)** | **$I_{rmsth2}$ at 2 mm (mA)** | **$I_{rmsth3}$ at 3 mm (mA)** |
| 10 | 0.51 | 0.69 | 1.02 | 1.38 | 1.55 | 2.10 |
| 15 | 1.44 | 1.97 | 2.96 | 4.16 | 4.65 | 6.76 |
| 20 | 3.84 | 5.59 | 8.81 | 14.11 | 15.36 | 26.11 |
| 25 | 14.52 | 25.49 | 38.45 | 65.98 | 74.29 | 102.99 |

| | | | | | | |
|---|---|---|---|---|---|---|
| 29 | 33.76 | 61.18 | 87.46 | 114.68 | 119.30 | 181.26 |
| 30 | 29.85 | 55.46 | 80.14 | 109.38 | 113.36 | 167.97 |
| 35 | 10.80 | 20.73 | 36.68 | 70.41 | 66.40 | 102.59 |
| 40 | 6.82 | 13.29 | 19.80 | 44.13 | 39.90 | 80.78 |
| 45 | 5.27 | 10.84 | 13.84 | 34.23 | 27.41 | 66.67 |
| 50 | 4.59 | 9.82 | 11.49 | 30.12 | 22.16 | 59.55 |
| 55 | 5.19 | 9.07 | 13.34 | 27.30 | 26.12 | 54.62 |
| 60 | 7.60 | 7.18 | 21.82 | 20.60 | 44.11 | 42.31 |
| 65 | 8.59 | 5.12 | 25.83 | 13.32 | 52.14 | 26.64 |
| 70 | 7.89 | 4.57 | 23.14 | 11.37 | 47.07 | 22.08 |
| | | | | | | |
| ***f* (Hz)** | **$P_{rmsth1}$ at 1 mm (mW)** | **$P_{rmsth2}$ at 2 mm (mW)** | **$P_{rmsth3}$ at 3 mm (mW)** | **$P_{rmsth1}$ at 1 mm (mW)** | **$P_{rmsth2}$ at 2 mm (mW)** | **$P_{rmsth3}$ at 3 mm (mW)** |
| 10 | 1.810E-04 | 3.265E-04 | 0.001 | 0.001 | 0.002 | 0.003 |
| 15 | 0.002 | 0.004 | 0.008 | 0.016 | 0.020 | 0.070 |
| 20 | 0.016 | 0.034 | 0.085 | 0.219 | 0.259 | 1.386 |
| 25 | 0.342 | 1.054 | 2.398 | 7.059 | 8.949 | 26.846 |
| 29 | 2.113 | 6.940 | 14.184 | 24.386 | 26.390 | 96.293 |
| 30 | 1.759 | 6.071 | 12.676 | 23.612 | 25.363 | 85.508 |
| 35 | 0.283 | 1.041 | 3.261 | 12.016 | 10.686 | 37.166 |
| 40 | 0.103 | 0.389 | 0.864 | 4.291 | 3.507 | 26.313 |
| 45 | 0.065 | 0.274 | 0.446 | 2.727 | 1.749 | 20.153 |
| 50 | 0.054 | 0.246 | 0.336 | 2.311 | 1.251 | 17.858 |
| 55 | 0.075 | 0.228 | 0.492 | 2.063 | 1.888 | 16.520 |
| 60 | 0.170 | 0.152 | 1.400 | 1.248 | 5.721 | 10.811 |
| 65 | 0.241 | 0.086 | 2.182 | 0.580 | 8.891 | 4.643 |
| 70 | 0.226 | 0.076 | 1.942 | 0.469 | 8.036 | 3.434 |

(a)

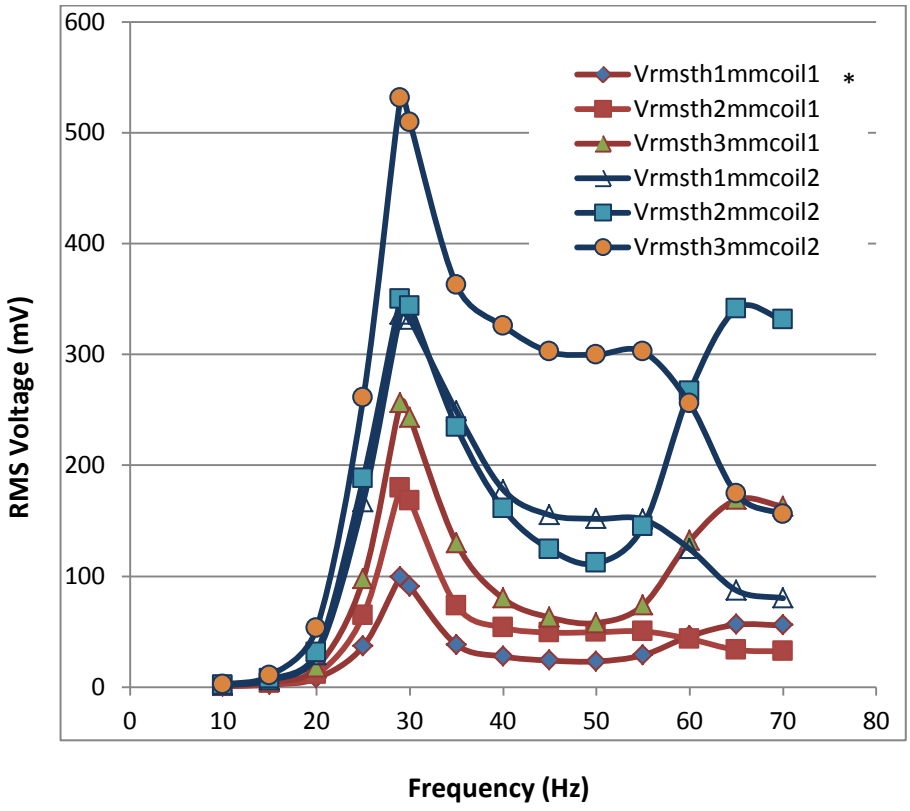

(b)

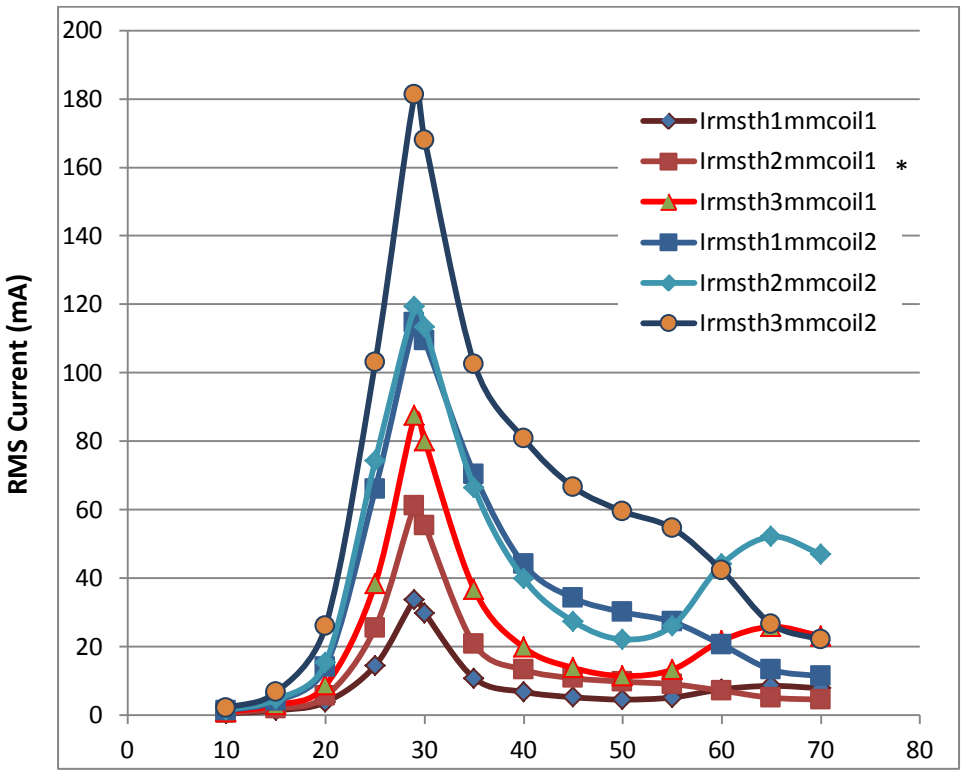


(c)

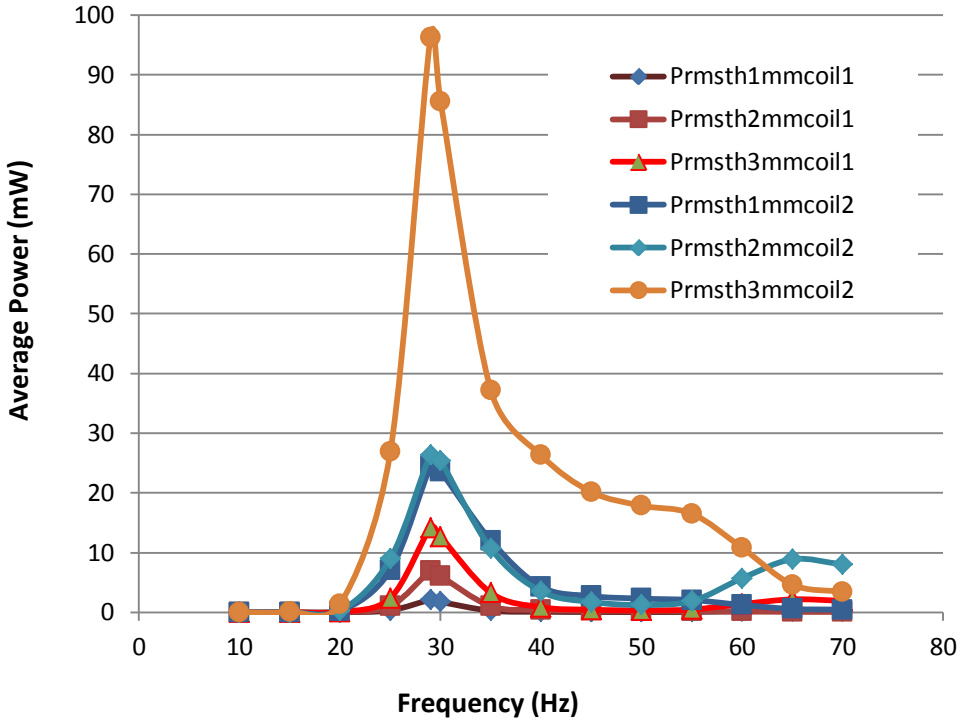


*Note: Vrmsth1mmcoil1 = Theoretical RMS voltage of coil 1 at 1mm amplitude. Similar nomenclature is applicable for the remaining parameters for voltage, current and power values

Figure 5.13 Theoretical (a) voltages in mV, (b) currents in mA and, (c) power in mW of Coil 1 and Coil 2 at amplitudes 1 mm to 3 mm.

## 5.7 Discussion

To understand the 2DOF1D EMVEH, two models were considered. Firstly, a 2DOF1D MDK system that represented only the mechanical system was investigated in order to understand the behaviour of two active electromagnetic inertial masses. Secondly the SDOF1D MDK RL EMVEH system was examined in order to understand the behaviour of the electrical transduction mechanisms and the relationship between the coupled electrical-mechanical systems.

Similar to the SDOF1D EMVEH system, simple linear analyses using Laplace and state space methods were performed on these models, disregarding the spatial variation of the magnetic field. This was followed by non-linear analyses using a hybrid method consisting of the non-linear Runge-Kutta method (MATLAB ODE45 function) and magnetostatic data for spatial variation of the magnetic field.

The results of the Laplace and the state space analyses of the 2DOF1D MDKRL system are summarised, as shown in Table 5.2. According to the Laplace transform analysis, the mass $M_1$ moving at $x_1$ has two resonant peaks with $f_{pk1}$ = 31.44 Hz and $f_{pk2}$ = 62.97 Hz. The mass $M_2$ moving at $x_2$ has one resonant peak with $f_{pk1}$ = 31.44 Hz, while its second resonant peak is not apparent due to damping. The natural frequencies 30.88 Hz and 60.73 Hz obtained from these eigen values corresponded to the Laplace resonant peaks $f_{pk1}$ = 31.44 Hz and $f_{pk2}$ = 62.97 Hz. The difference between the resonant peak values and the resonant frequencies can be attributed to the combined electrical and mechanical damping in the system.

The modes of vibration were explicitly observed in the phase domain of Laplace transforms Figure. 5.11(c and f). Both $x_1$ and $x_2$ and correspondingly $I_1$ and $I_2$ were in phase with each other during the first mode of vibration and out of phase in the second resonance. This was further validated by the observations of the time domain $x_1$, $x_2$, $I_1$ and $I_2$ signals obtained from non-linear analyses, as shown in Figure 5.13. This gives rise to three important conclusions, a) both the linear and the non-linear models exhibit similar behaviour of the 2DOF1D EMVEH system, b) the 2DOF1D EMVEH system has two modes of vibration, of which the first mode has significantly more power compared to the second mode, c) selection of the modes is an important parameter in the design of future 2DOF1D EMVEHs and subsequently the MDOF1D EMVEHs. Although Laplace and state space provided this interesting information, detailed investigations were made from the time domain results of the non-linear ODE solver based analyses.

The non-linear analyses of 2DOF1D MDK RL were simulated for resonant frequencies in the time domain based signal analyses of displacement and current. The observed peak and RMS currents and the derived voltages and power were tabulated and are shown in Table 5.3 and Table 5.4. The electrical impedances of both systems were calculated, using the formula described in equation 4.82 in Chapter 4. It was observed that there were significant deviations in the $x_1$, $x_2$, $I_1$ and $I_2$ values obtained from both the linear and non-linear analyses, as observed in Tables 5.3 and 5.4 where the values were much higher in the linear analyses. This was due to the fact that the spatial variation of the magnetic field was neglected in the linear analyses, and the magnetic field was assumed to be B = 0.65 T throughout, which is not practical. In reality, since the initial positions of both the coils were at the middle of the ring magnets where the magnetic field was very low (0.1 T), and the amplitude of 0.1 mm was too low for the coils to move into higher magnetic field regions, the non-linear analyses showed lesser voltage and power. Hence, it can be concluded that the spatial variation of the magnetic field must be considered to ensure maximum power at resonant frequencies of the 2DOF1D EMVEH system. From the power frequency response analyses, it was observed that considerably higher voltages and power are achievable at vibrations with practical amplitudes. In addition, the maximum power at resonance of one coil was greater than the maximum power of the SDOF1D EMVEH as obtained in section 4.8 of Chapter 4. This indicates that a two-coiled 2DOF1D EMVEH produces more power than combined two SDOF1D EMVEHs. Thus, MDOF1D EMVEH is more effective not only in terms of broadband frequency based power generation but also in terms of power density.

Table 5.3 Summary of linear theoretical simulation results of 2DOF1D MDK RL EMVEH systems at base excitation of 0.1mm.

| | | |
|---|---|---|
| Laplace | $X_1/Y$ peak coordinates | (31.44,4.179)(62.97,1.008) |
| | $X_1/Y$ frequency | 31.44 Hz , 62,97 Hz |
| | $X_1/Y$ magnitude | 4.179,1.008 |
| | $X_1$ | 0.0004 m,0.0001 m |
| | | |
| | $X_2/Y$ peak coordinates | (31.44,5.733) |
| | $X_2/Y$ frequency | 31.44 Hz |
| | $X_2/Y$ magnitude | 5.733 |
| | $X_2$ | 0.00057 m |
| | | |
| | $I_1/Y$ peak coordinates | (32.1,122.4)(66.32,52.26) |
| | $I_1/Y$ frequency | 32.1 Hz,66.32 Hz |
| | $I_1/Y$ magnitude | 122.4,52.26 |
| | $I_1$ | 0.01224 A,0.00523 A |
| | | |

| | | |
|---|---|---|
| | $I_2/Y$ peak coordinates | (32.1,174.8) |
| | $I_2/Y$ frequency | 32.1 Hz |
| | $I_2/Y$ magnitude | 174.8 |
| | $I_2$ | 0.0175 A |
| | $V_1/Y$ peak coordinates | (32.43,398.6)(69.85,355) |
| | $V_1/Y$ frequency | 32.43 Hz,69.85 Hz |
| | $V_1/Y$ magnitude | 398.6,355 |
| | $V_1$ | 0.03986 V,0.0355 V |
| | $V_2/Y$ peak coordinates | (32.43,398.6)(69.85,355) |
| | $V_2/Y$ frequency | 32.43 Hz,69.85 Hz |
| | $V_2/Y$ magnitude | 398.6,355 |
| | $V_2$ | 0.03986 V,0.0355 V |
| State space | Eigen value ,$\lambda_1$ | -48.326 + 378.52i |
| | Eigen value ,$\lambda_2$ | -48.326 - 378.52i |
| | Eigen value ,$\lambda_3$ | -14.585 |
| | Eigen value ,$\lambda_4$ | -20.42 + 193.008i |
| | Eigen value ,$\lambda_5$ | -20.42 - 193.008i |
| | Eigen value ,$\lambda_6$ | -18.75 |
| | Resonant frequency , $f_{n1}$ | 2.32 Hz |
| | Resonant frequency , $f_{n2}$ | 2.98 Hz |
| | Resonant frequency , $f_{n3}$ | 30.88 Hz |
| | Resonant frequency , $f_{n4}$ | 60.73 Hz |

Table 5.4 Summary of non-linear theoretical simulation results of 2DOF1D MDK RL EMVEH System at base excitation of 0.1 mm

| | | **at 30.88 Hz** | | **at 60.73 Hz** | |
|---|---|---|---|---|---|
| | | **Peak** | **RMS** | **Peak** | **RMS** |
| **Displacement (mm)** | $x_1$ | 0.23 | 0.16 | 9.49E-02 | 6.71E-02 |
| | $x_2$ | 0.35 | 0.25 | 5.04E-02 | 3.57E-02 |
| **Current (mA)** | $I_1$ | 1.73 | 1.23 | 0.92 | 0.65 |
| | $I_2$ | 2.57 | 1.82 | 0.82 | 0.58 |
| **Impedance (Ohm)** | $Z_1 = Z_2 = Z$ | 3.12 | 3.12 | 6.11 | 6.11 |
| **Voltage (mV)** | $V_1$ | 5.41 | 3.82 | 5.64 | 3.98 |
| | $V_2$ | 8.02 | 5.67 | 5.00 | 3.54 |
| **Power (mW)** | $V_1I_1\cos\varphi$ | 9.00E-04 | 4.50E-04 | 2.55E-04 | 1.27E-04 |
| | $V_1I_1\cos\varphi$ | 1.98E-03 | 9.89E-04 | 2.01E-04 | 1.00E-04 |

# Chapter 6 Sensitivity analyses of SDOF1D and 2DOF1D EMVEH models

The theoretical linear and non-linear simulation was performed on SDOF1D EMVEH in Chapter 4, and on 2DOF1D EMVEH in Chapter 5. It was understood that the design parameters, namely the coupling coefficient (*T*), mass of the inertial active electromagnetic masses (*M*), damping coefficients (*D*), spring stiffnesses (*K*), total resistance (*R*) and inductance (*L*) of the system significantly contributed to the electromagnetic transduction mechanism of converting vibration into electric energy. Hence, it is necessary to understand how the system behaves when these parameters vary. A series of parametric sensitivity analyses was performed here in this chapter on both the SDOF1D EMVEH and 2DOF1D EMVEH models.

## 6.1 Research methodology

The sensitivity analyses were initially performed on the SDOF1D EMVEH model, followed by the 2DOF1D EMVEH model. For the SDOF1D EMVEH model, the parameters considered were the coupling coefficient (*T*), mass of the inertial active electromagnetic masses (*M*), damping coefficient (*D*), spring stiffness (*K*), resistance (*R*) and inductance (*L*).

For the 2DOF1D EMVEH model, the parameters considered were the coupling coefficient (*T*), mass of the inertial active electromagnetic masses ($M_1$, $M_2$), damping coefficients ($D_1$, $D_2$, $D_3$), spring stiffnesses ($K_1$, $K_2$, $K_3$), resistance ($R_1$, $R_2$) and inductance ($L_1$, $L_2$). Each of these parameters was varied, keeping all the other parameters as constants. For example, the coupling coefficient *T* was varied from 0.004 to 0.0015, keeping the *M, D, K, R* and *L* parameters as constants. The varying design parameter and the constant design parameters were recorded in each of the plots.

The Laplace transform based frequency response analysis method was chosen for the sensitivity analyses although the non-linear ODE45 based time domain response method yielded more accurate results, considering the spatial variation of the magnetic field. This

was due to the fact that the non-linear ODE45 method was very tedious and time consuming with regard to obtaining the voltage responses for each of the desired frequencies. Since the purpose of the sensitivity analyses was only to understand the behaviour of the electrical output frequency responses, the linear Laplace transform frequency response analysis method was considered for both the SDOF1D and 2DOF1D EMVEH models.

## 6.2 Sensitivity analysis of SDOF1D EMVEH

Three types of sensitivity studies were performed on SDOF1D EMVEH by (a) varying the coupling coefficient (*T*), (b) varying the mechanical parameters - mass (*M*), damping coefficient (*D*), and spring stiffness (*K*) and, (c) varying the electrical parameters – resistance (*R*) and inductance (*L*).

### 6.2.1 Varying the coupling coefficient (*T*)

The first sensitivity analysis was conducted to study how the variation of coupling coefficient *T* affects the voltage frequency response. *T* was varied from 0.004 to 0.015 Tm keeping the other design parameters constant with the following values: *M* = 0.0015 kg, *D* = 0.05 Ns/m, *K* = 160 N/m, *R* = 0.3 ohm and *L* = 0.016 H. The voltage frequency response variation for different values of the coupling coefficient (*T*) is shown in Figure 6.1.

Figure 6.1(a) indicates that the voltage output per input base excitation y increases with the increase in the coupling coefficient. This is evident from Faraday's law of electromagnetic induction, since the coupling coefficient depends on the magnetic field strength **B**. Figure 6.1(a, b, c) also suggests that the coupling coefficient does not have any effect on the resonance of the EMVEH system since the resonant peaks of *V/Y, I/Y* and $P/Y^2$ frequency responses were occurring at the same frequency. This observation also implies that the spatial variation of the magnetic field had no effect on the resonance of the SDOF1D EMVEH system. However, the magnitude of *V/Y, I/Y* and $P/Y^2$ increased with the increase of the coupling coefficient. This was obvious since the increase of the coupling coefficient is possible only by increasing the magnetic flux linkage, thus resulting in increased generated voltage.

(a)

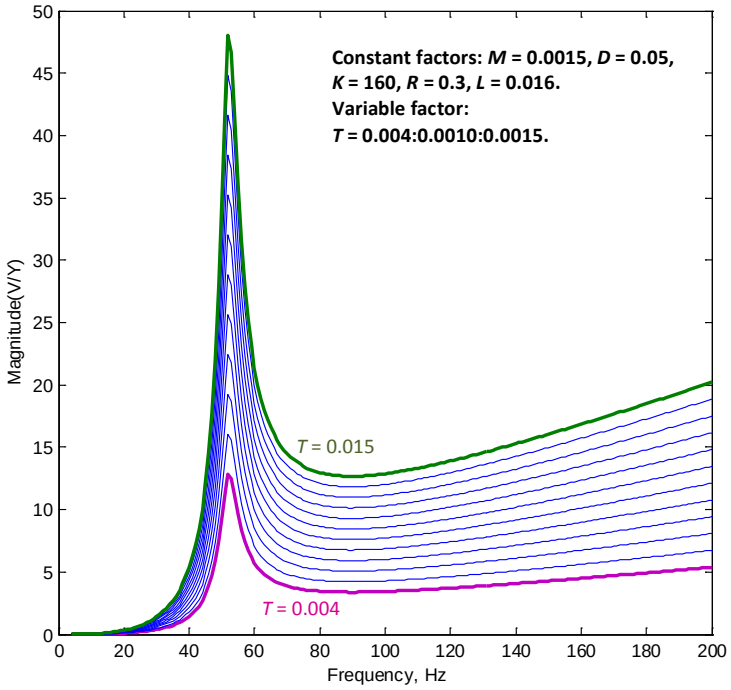
Constant factors: M = 0.0015, D = 0.05,
K = 160, R = 0.3, L = 0.016.
Variable factor:
T = 0.004:0.0010:0.0015.
T = 0.015
T = 0.004
Magnitude(V/Y)
Frequency, Hz
0
5
10
15
20
25
30
35
40
45
50
0
20
40
60
80
100
120
140
160
180
200

(b)

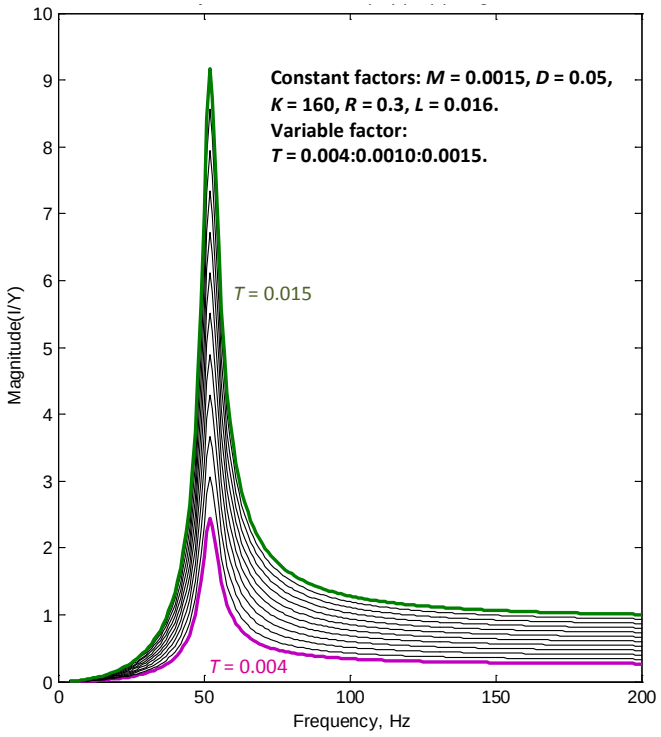
Constant factors: M = 0.0015, D = 0.05,
K = 160, R = 0.3, L = 0.016.
Variable factor:
T = 0.004:0.0010:0.0015.
T = 0.015
T = 0.004
Magnitude(I/Y)
Frequency, Hz
0
1
2
3
4
5
6
7
8
9
10
0
50
100
150
200

(c)

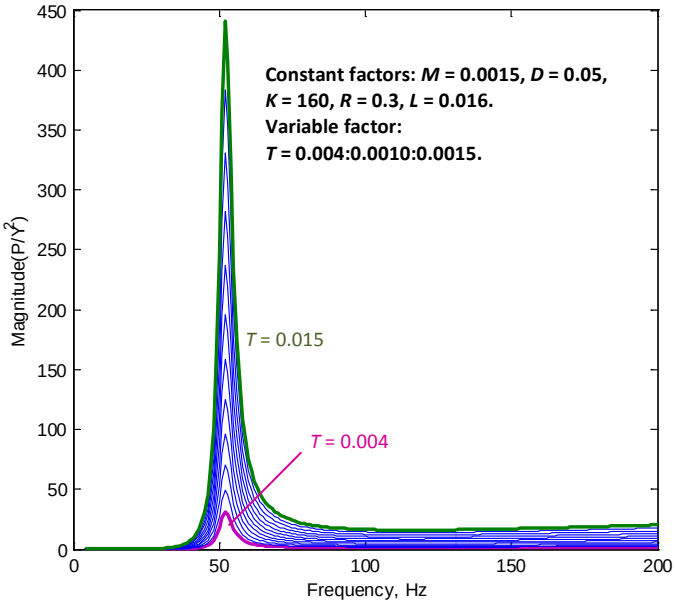


Figure 6.1 Sensitivity test results for SDOF1D EMVEH model – (a) voltage output frequency response, (b) current output frequency response and (c) power output frequency response curves for different values of the coupling coefficient *T*. All magnitudes are in SI units.

### 6.2.2 Varying the mechanical parameters

Similar sensitivity tests were performed for the mechanical parameters Mass (*M*), Mechanical Damping (*D*) and spring stiffness (*K*) and the results are shown in Figure 6.2.

(a)

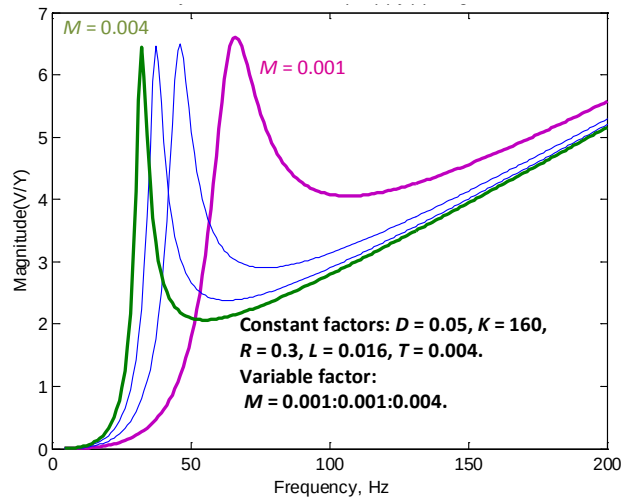

(b)

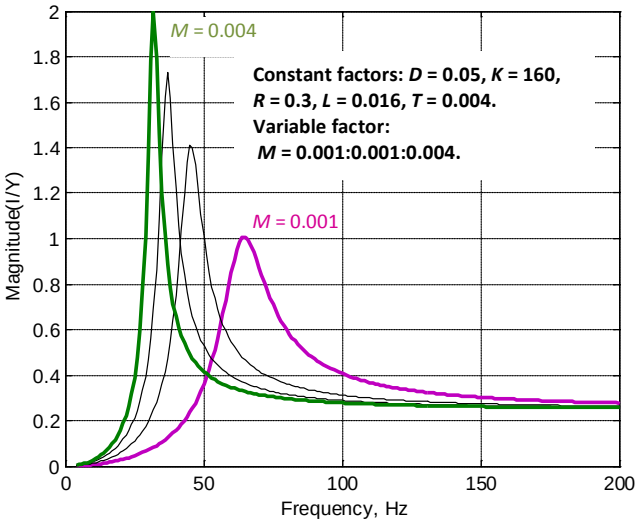
M = 0.004
Constant factors: D = 0.05, K = 160,
R = 0.3, L = 0.016, T = 0.004.
Variable factor:
M = 0.001:0.001:0.004.
M = 0.001
Magnitude(I/Y)
Frequency, Hz

(c)

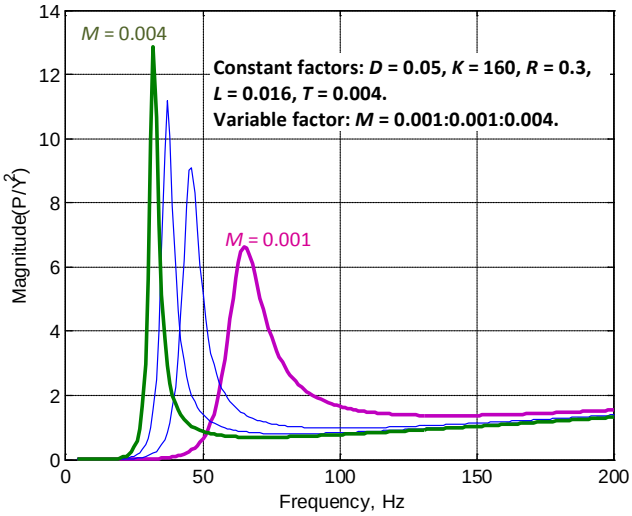
M = 0.004
Constant factors: D = 0.05, K = 160, R = 0.3,
L = 0.016, T = 0.004.
Variable factor: M = 0.001:0.001:0.004.
M = 0.001
Magnitude(P/Y²)
Frequency, Hz

(d)

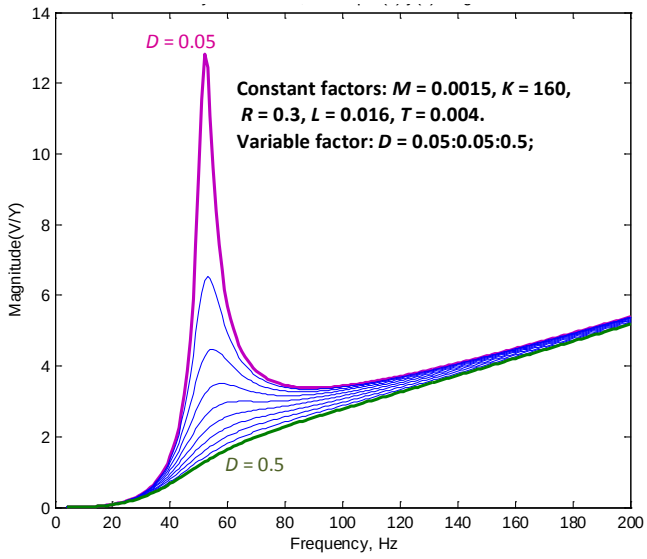
D = 0.05
Constant factors: M = 0.0015, K = 160,
R = 0.3, L = 0.016, T = 0.004.
Variable factor: D = 0.05:0.05:0.5;
D = 0.5
Magnitude(V/Y)
Frequency, Hz

(e)

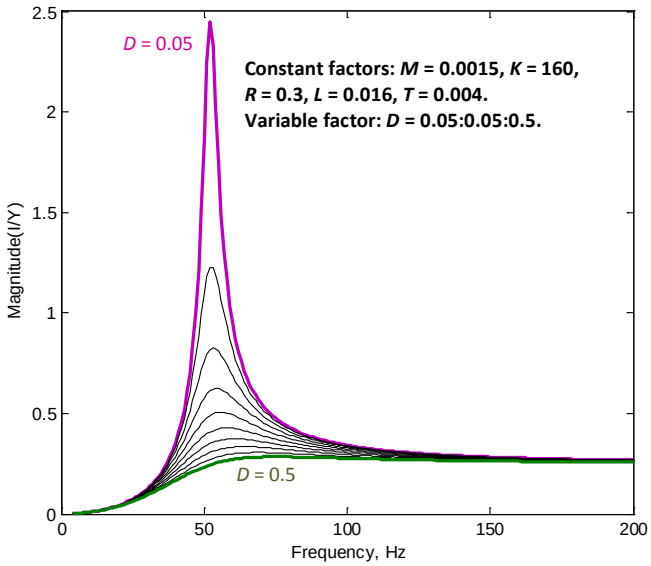
D = 0.05
Constant factors: M = 0.0015, K = 160,
R = 0.3, L = 0.016, T = 0.004.
Variable factor: D = 0.05:0.05:0.5.
D = 0.5
Magnitude(I/Y)
Frequency, Hz
0
0.5
1
1.5
2
2.5
0
50
100
150
200

(f)

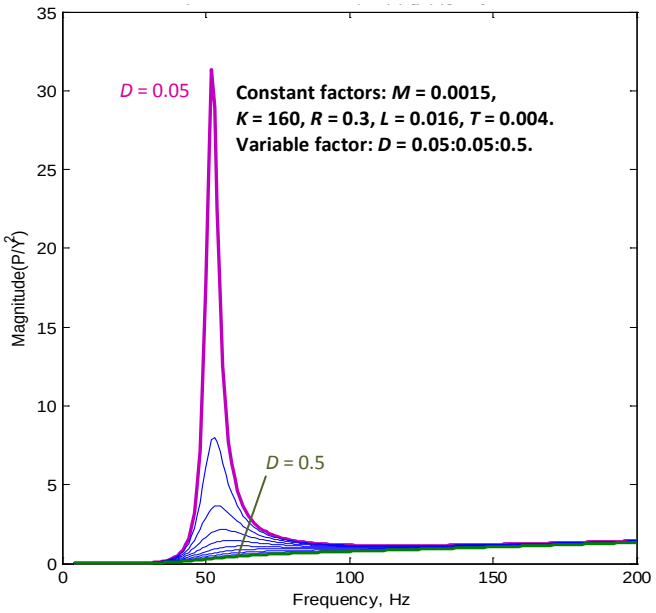
D = 0.05
Constant factors: M = 0.0015,
K = 160, R = 0.3, L = 0.016, T = 0.004.
Variable factor: D = 0.05:0.05:0.5.
D = 0.5
Magnitude(P/Y²)
Frequency, Hz
0
5
10
15
20
25
30
35
0
50
100
150
200

(g)

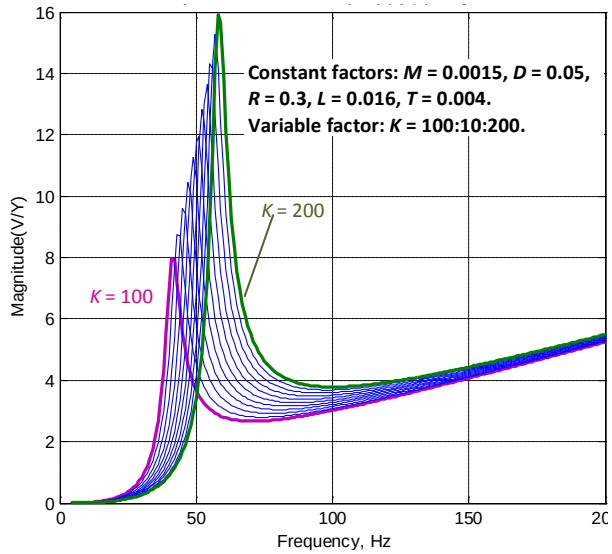
Constant factors: M = 0.0015, D = 0.05,
R = 0.3, L = 0.016, T = 0.004.
Variable factor: K = 100:10:200.
K = 200
K = 100
Magnitude(V/Y)
Frequency, Hz
0
2
4
6
8
10
12
14
16
0
50
100
150
20

(h)

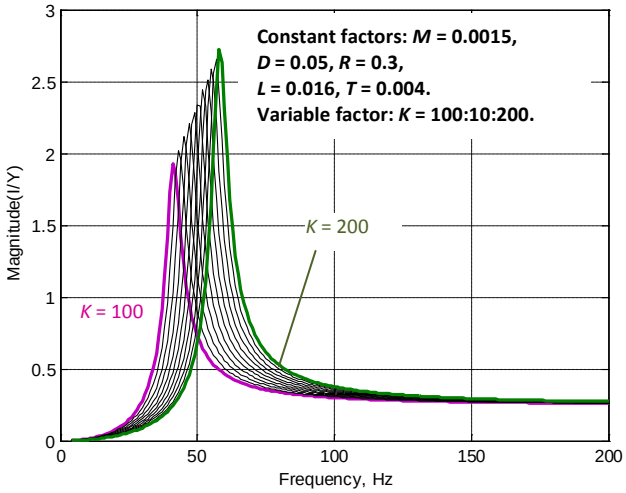
Constant factors: M = 0.0015,
D = 0.05, R = 0.3,
L = 0.016, T = 0.004.
Variable factor: K = 100:10:200.
K = 200
K = 100
Magnitude(I/Y)
Frequency, Hz
0
0.5
1
1.5
2
2.5
3
0
50
100
150
200

(i)

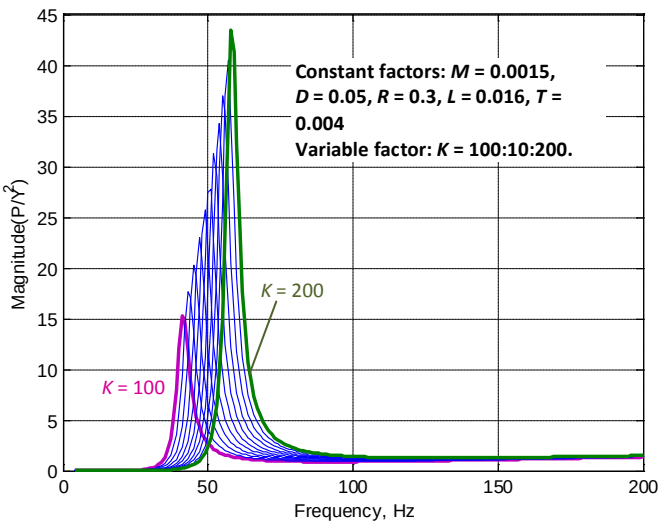


Figure 6.2 Sensitivity test results for SDOF1D EMVEH model – Output frequency response curves for different values of mass(a, b, c), damping (d, e, f) and spring stiffness (g, h, i). All magnitudes are in SI units.

The increase in mass (*M*) resulted in a decrease in resonance frequency as shown in Figure 6.2 (a, b, c). This is evident since the resonance frequency of the mechanical MDK system is inversely proportional to the square root of the mass. While the voltage transfer function *(V/Y)* resonant peaks decreased very little with the increase in *M*, the current *(I/Y)* and power $(P/Y^2)$ transfer functions increased with increase in *M*.

The increase in damping slightly increases the resonant frequency as was observed in Figure 6.2 (d, e, and f). This is negligible in the spring-mass-damping system where the resonance is mainly a function of mass and spring stiffness. However, increased damping resulted in reduced voltage, current and power. The power output depended on the EMF generated and the EMF generated depended on the rate of change of magnetic flux, which in turn depends on the velocity of the coil motion. When the coil motion is severely damped, not only will the magnitude of the outputs decrease, the resonant behaviour tends to fade away from the system.

Contrary to the increase in mass, the increase in spring stiffness (*K*) resulted in an increase in the resonant frequency, as observed in Figure 6.2 (g, h, i). It was also observed in Figure 6.2 (g, h, i) that the voltage, current and power output resonance peaks increased with increases in the spring stiffness.

### 6.2.3 Varying the electrical parameters

The electrical part of the SDOF1D EMVEH system can be either an RL or RLC system. A pure RLC system has an electrical resonance characterised by electrical resonant frequency given by $\sqrt{\frac{1}{LC}}$, while the RL system has no resonance. Since the RL system was preferred over the RLC for the SDOF1D system in Chapter 4, one can anticipate that the electrical system has no effect on the resonance of the overall SDOF1D EMVEH system. To verify this, similar sensitivity tests were performed for the electrical parameters resistance (*R*), and the inductance (L) and the results are shown in Figure 6.3.

(a)

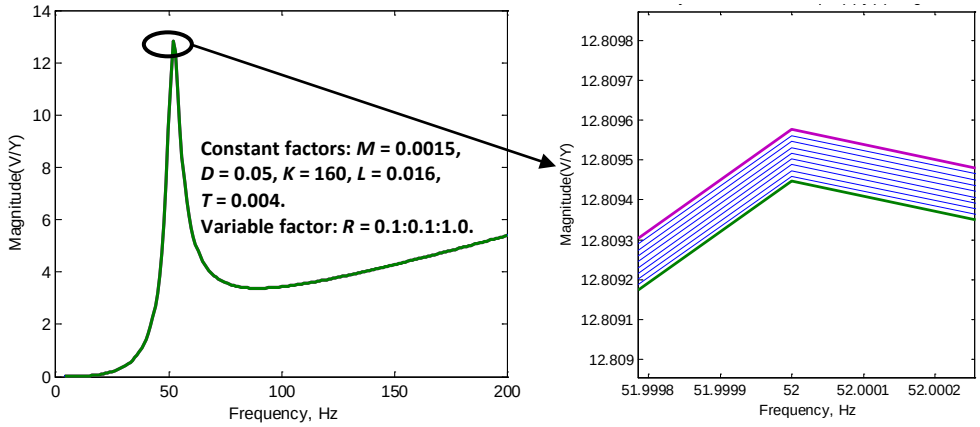


(b)

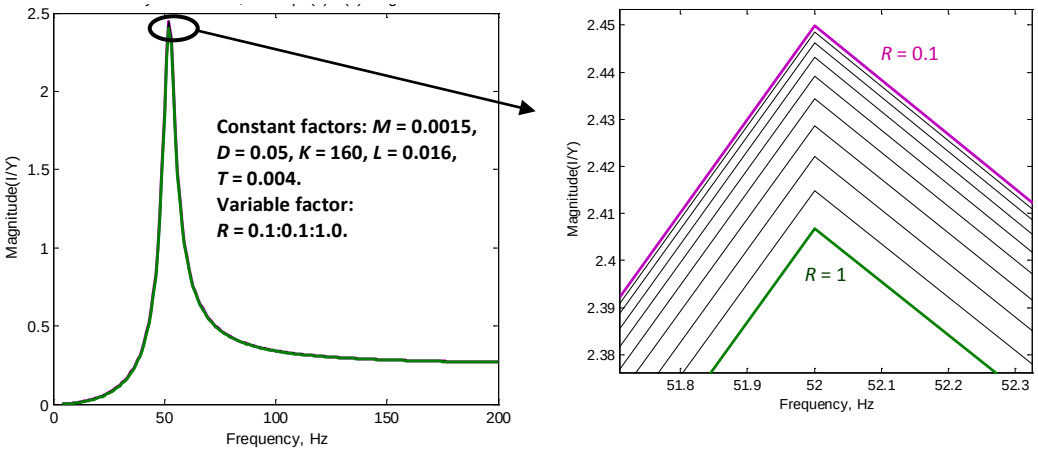

(c)

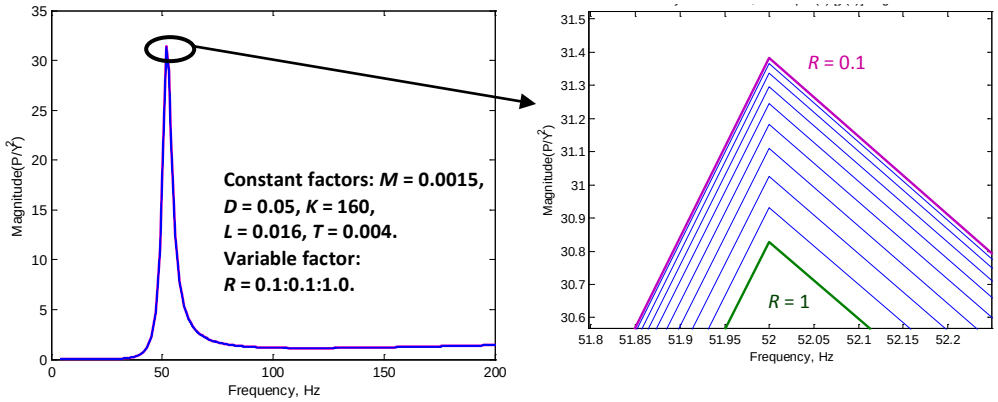
Constant factors: M = 0.0015,
D = 0.05, K = 160,
L = 0.016, T = 0.004.
Variable factor:
R = 0.1:0.1:1.0.
R = 0.1
R = 1
Magnitude(P/Y^2)
Frequency, Hz

(d)

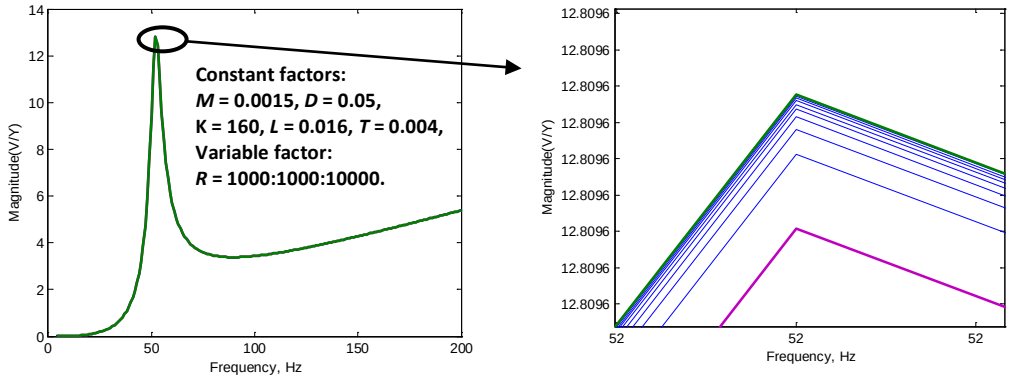
Constant factors:
M = 0.0015, D = 0.05,
K = 160, L = 0.016, T = 0.004,
Variable factor:
R = 1000:1000:10000.
Magnitude(V/Y)
Frequency, Hz

(e)

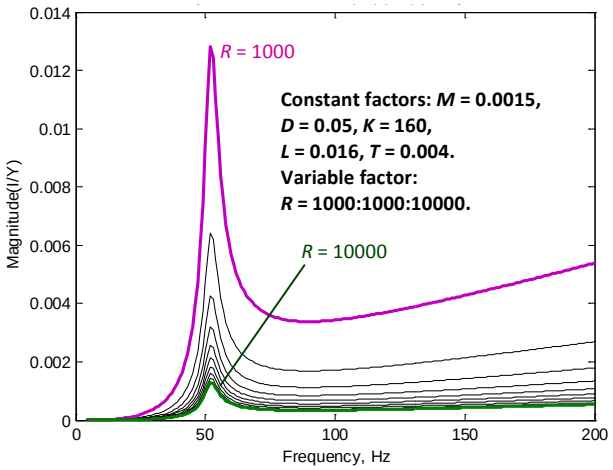
R = 1000
Constant factors: M = 0.0015,
D = 0.05, K = 160,
L = 0.016, T = 0.004.
Variable factor:
R = 1000:1000:10000.
R = 10000
Magnitude(I/Y)
Frequency, Hz

(f)

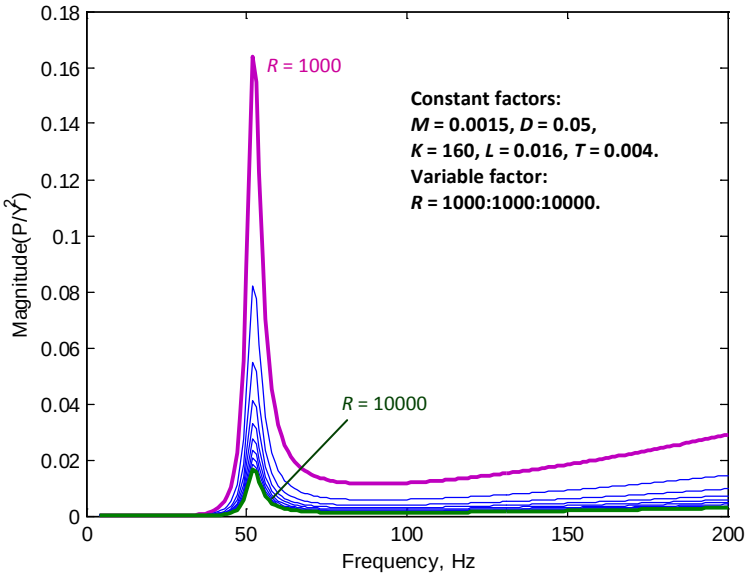
R = 1000
Constant factors:
M = 0.0015, D = 0.05,
K = 160, L = 0.016, T = 0.004.
Variable factor:
R = 1000:1000:10000.
R = 10000
Magnitude(P/Y^2)
Frequency, Hz

(g)

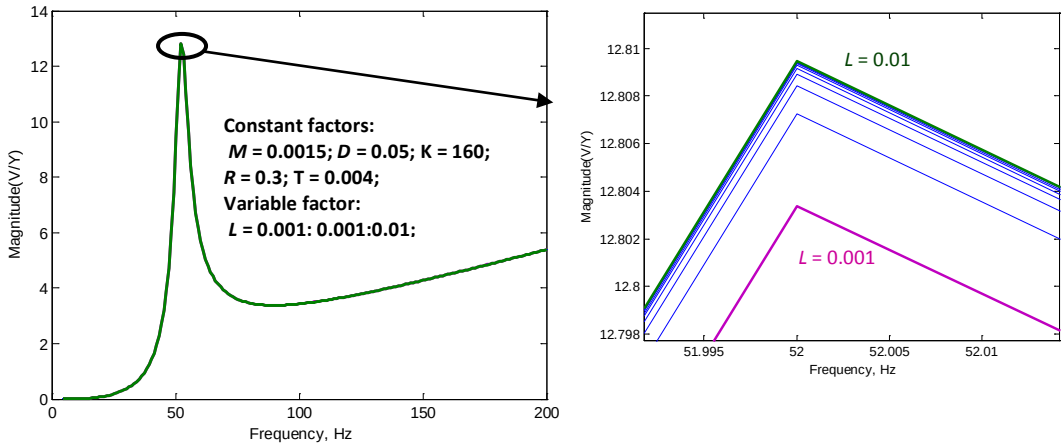
Constant factors:
M = 0.0015; D = 0.05; K = 160;
R = 0.3; T = 0.004;
Variable factor:
L = 0.001: 0.001:0.01;
Magnitude(V/Y)
Frequency, Hz
L = 0.01
L = 0.001

(h)

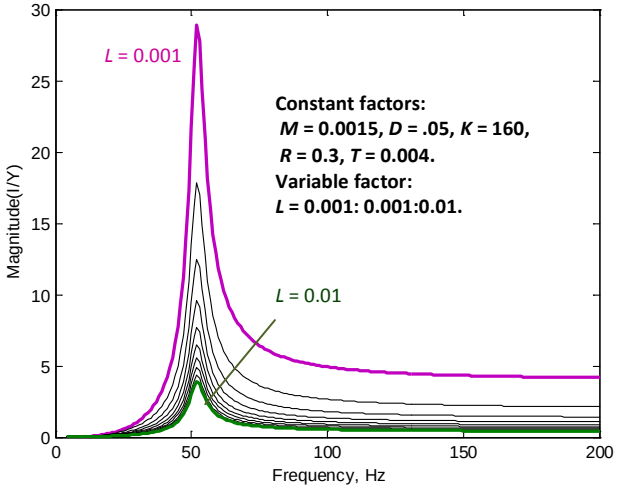
L = 0.001
Constant factors:
M = 0.0015, D = .05, K = 160,
R = 0.3, T = 0.004.
Variable factor:
L = 0.001: 0.001:0.01.
L = 0.01
Magnitude(I/Y)
Frequency, Hz

(i)

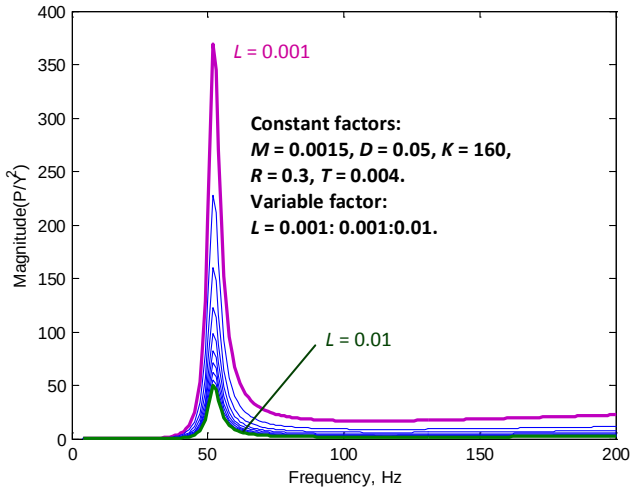
L = 0.001
Constant factors:
M = 0.0015, D = 0.05, K = 160,
R = 0.3, T = 0.004.
Variable factor:
L = 0.001: 0.001:0.01.
L = 0.01
Magnitude(P/Y²)
Frequency, Hz

(j)

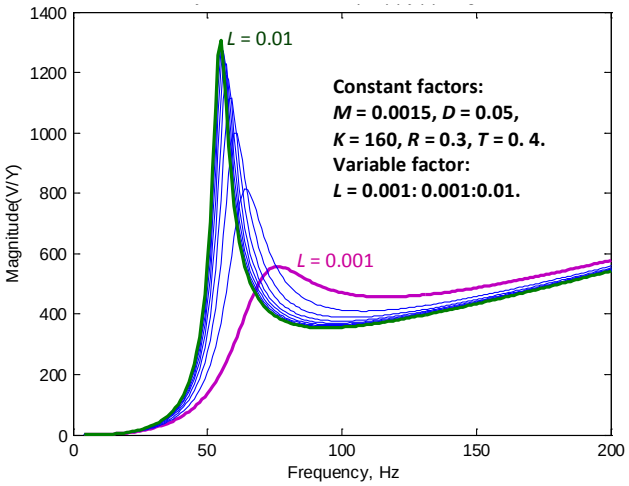
L = 0.01
Constant factors:
M = 0.0015, D = 0.05,
K = 160, R = 0.3, T = 0. 4.
Variable factor:
L = 0.001: 0.001:0.01.
L = 0.001
Magnitude(V/Y)
Frequency, Hz

(k)

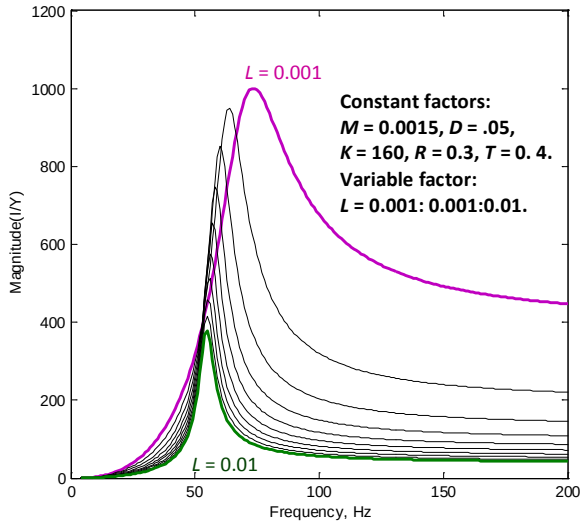
L = 0.001
Constant factors:
M = 0.0015, D = .05,
K = 160, R = 0.3, T = 0. 4.
Variable factor:
L = 0.001: 0.001:0.01.
L = 0.01
Magnitude(I/Y)
Frequency, Hz

(*l*)

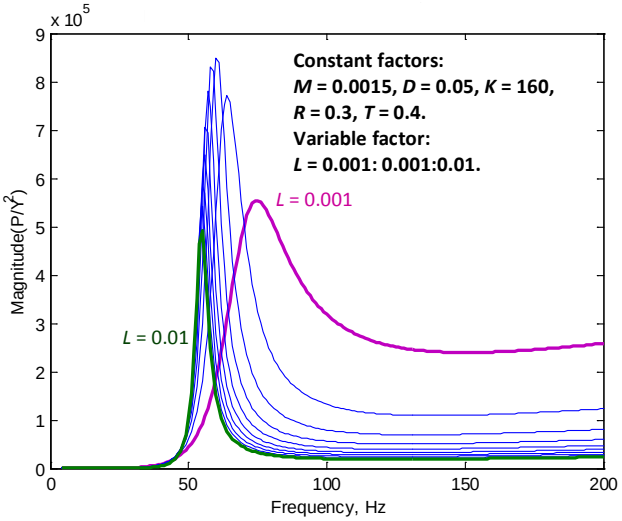


Figure 6.3 Sensitivity test results for SDOF1D EMVEH model – output frequency response curves for different values of internal resistance (a, b, c), external resistance (d, e, f), inductance at low T (g, h, i ) and inductance at high T (j, k, l). All magnitudes are in SI units.

The change of internal resistance from $R$ = 0.1 ohm to $R$ = 1 ohm had negligible or no effect on both magnitudes of current, and voltage and power frequency responses, as shown in Figure 6.3 (a, b, c). The internal resistance had no effect on the resonant frequency of the SDOF1D EMVEH system. When an external load resistance was added, and the total resistance was varied from $R$ = 1000 ohm to $R$ = 10,000 ohm, there was again no change in the resonant frequency as can be observed in Figure 6.3 (d, e, f). While there was no change in the voltage, the induced current decreased, resulting in a decrease in power.

At low levels of coupling coefficient, for example, $T$ = 0.004, inductance ($L$) of the coil had no effect on the voltage, as can be observed in Figure 6.3 (g, h, i). The magnitude of $V/Y$ was almost constant, while the current $(I/Y)$ and power decreased with the increase of inductance. At higher levels of coupling coefficient, as shown in Figure 6.3 (j, k, l), for example, where $T$ = 0.4, the increase in inductance ($L$) increased the magnitude $V/Y$, but decreased the current ($I/Y$) and power outputs ($P/Y^2$). The resonant frequency was also observed to decrease with increasing inductance.

## 6.3 Sensitivity analysis of 2DOF1D EMVEH

Similar to the SDOF1D EMVEH, the linear Laplace transform was considered in order to save time for the sensitivity simulation tests of the 2DOF1D EMVEH. Unlike the SDOF1D EMVEH which was a single-input single-output (SISO) function, the 2DOF1D EMVEH was a single-input multiple-output (SIMO) function with one input variable, the base excitation $y$ and two output variables, $V_1$ and $V_2$ that represented the output voltages of the two coils.

In Chapter 5, it was found that the voltages generated by each of the coils, $V_1$ and $V_2$ were identical in both phase and magnitude when all the springs in 2DOF1D EMVEH had identical spring stiffnesses. Since this was not desirable for broadband energy harvesting, the bottom spring $K_2$ was chosen to be different from $K_1$ and $K_3$. Hence, for sensitivity analyses, only the 2DOF1D EMVEH different spring stiffnesses were considered.

### 6.3.1 Varying the coupling coefficient ($T$)

The first sensitivity analysis was undertaken to study how the variation of coupling coefficient $T$ affects the voltage frequency response. $T$ was varied from 0.004 to 0.015, keeping the other design parameters constant, as shown in Figure 6.4. The behaviour of the voltage frequency response was similar to that of the SDOF1D EMVEH for the varying coupling coefficient $T$, except that there were two resonant peaks. Nevertheless, the resonant peaks occurred at the same two resonant frequencies, indicating that the coupling coefficient had no effect on the resonance of the overall system. Similar to the SDOF1D EMVEH, the magnitudes of the voltage, current and power transfer functions of 2DOF1D EMVEH also increased with the increase in $T$.

(a)

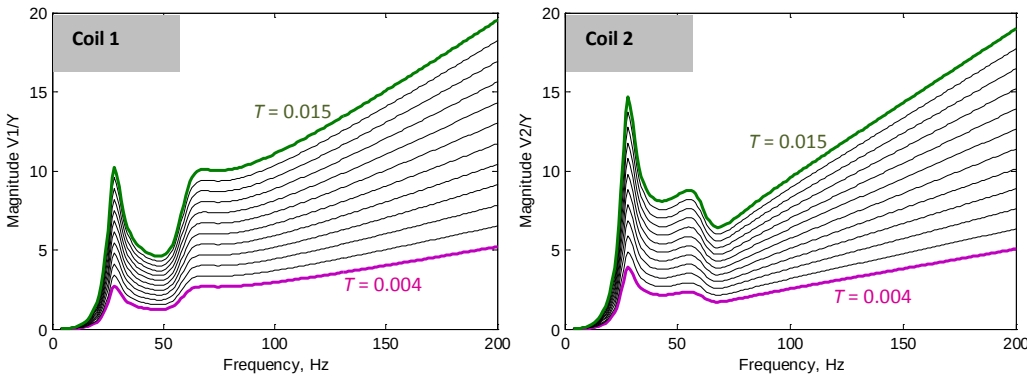


**Constant factors: $M_1 = M_2 = 0.0015$, $D_1 = D_2 = D_3 = 0.05$, $K_1 = K_3 = 80$, $K_2 = 20$, $R_1 = R_2 = R_3 = 0.3$, $L_1 = L_2 = 0.016$.**
**Variable factor: $T = 0.004{:}0.001{:}0.015$.**

(b)

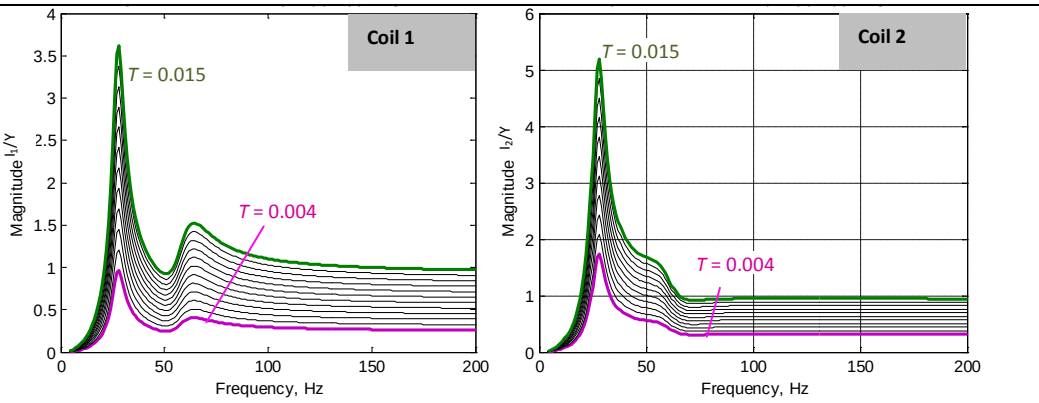


**Constant factors: $M_1 = M_2 = 0.0015$, $D_1 = D_2 = D_3 = 0.05$, $K_1 = K_3 = 80$, $K_2 = 20$, $R_1 = R_2 = R_3 = 0.3$, $L_1 = L_2 = 0.016$.**
**Variable factor: $T = 0.004{:}0.001{:}0.015$.**

(c)

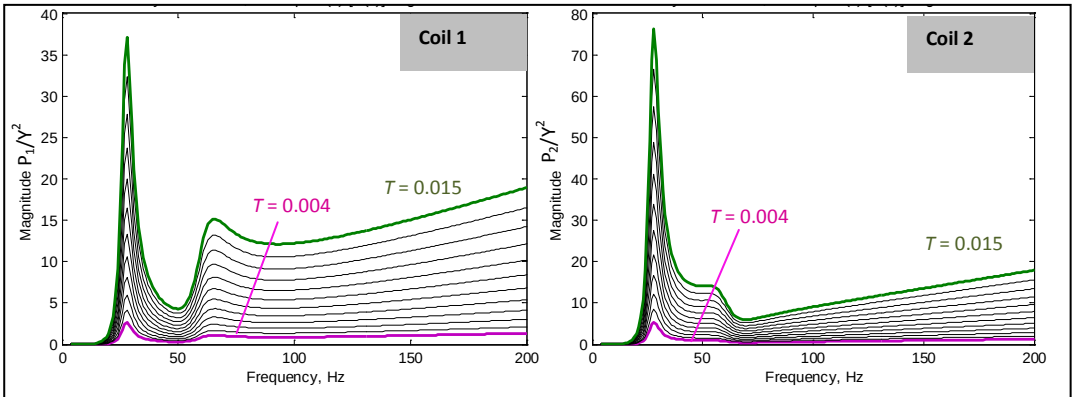


**Constant factors: $M_1 = M_2 = 0.0015$, $D_1 = D_2 = D_3 = 0.05$, $K_1 = K_3 = 80$, $K_2 = 20$, $R_1 = R_2 = R_3 = 0.3$, $L_1 = L_2 = 0.016$.**
**Variable factor: $T = 0.004{:}0.001{:}0.015$.**

Figure 6.4 Sensitivity test results for 2DOF1D EMVEH model different values of the coupling coefficient T for (a) voltage (b) current and (c) power outputs. All magnitudes are in SI units.

From Figure 6.4, it can be observed that the voltage and currents increased with the increase in the coupling coefficient. This was obvious since the induction increased with the magnetic flux linkage and the coupling coefficient was directly proportional to magnetic flux linkage. It was also observed that the second mode of resonance was not apparent at low values of *T*. This suggests that a high value of *T* is desired in the design of an EMVEH to generate power from the second mode of vibration.

### 6.3.2 Varying the mechanical parameters – mass, damping and stiffness.

Similar sensitivity tests were performed for the mechanical parameters mass (*M*), mechanical damping (*D*) and spring stiffness (*K*) and the results are shown in Figure 6.5. It was found that the behaviour of the voltage frequency response curves of the 2DOF1D EMVEH system for changes in values of the mechanical design parameters were similar to that found in the SDOF1D EMVEH system. As can be observed in Figure 6.5 (a, b, c), the increase in values of masses shifted both the resonant peaks towards the low frequency range. As observed in Figure 6.5 (g, h, i), the increase in the values of stiffness shifted the two resonant peaks towards the high frequency range. As observed in Figure 6.5 (d, e, f), the damping coefficient had no effect on the two resonant frequencies of the 2DFO1D EMVEH system although higher damping resulted in reduced resonant behaviour and also affected the magnitude of the voltage current and power transfer functions.

(a)

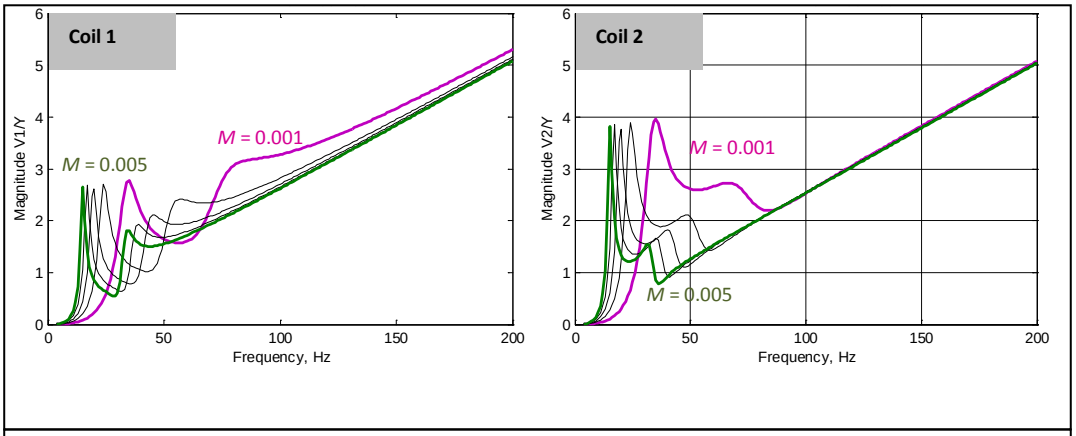


**Constant factors:** $D_1 = D_2 = D_3 = 0.05$, $K_1 = K_3 = 80$, $K_2 = 20$, $R_1 = R_2 = R_3 = 0.3$, $L_1 = L_2 = 0.016$, $T = 0.004$.
**Variable factor:** $M_1 = M_2 = M = 0.001{:}0.001{:}0.005$.

(b)

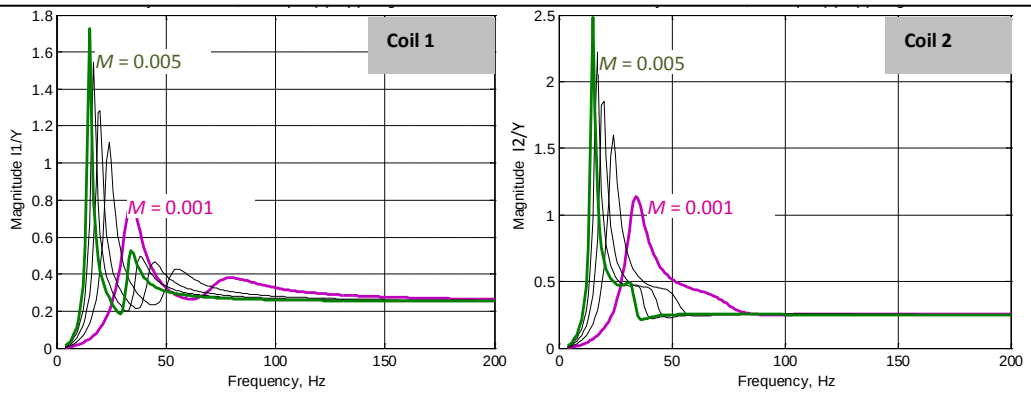


**Constant factors:** $D_1 = D_2 = D_3 = 0.05$, $K_1 = K_3 = 80$, $K_2 = 20$, $R_1 = R_2 = R_3 = 0.3$, $L_1 = L_2 = 0.016$, $T = 0.004$.
**Variable factor:** $M_1 = M_2 = M = 0.001{:}0.001{:}0.005$.

(c)

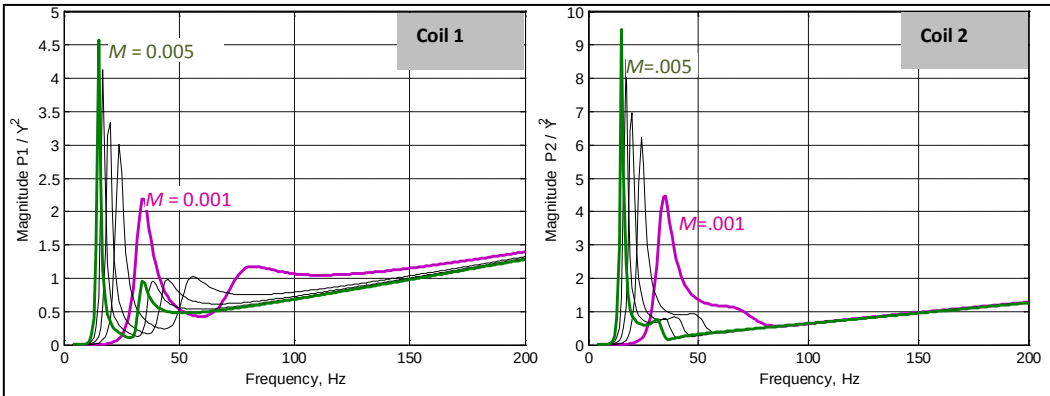


**Constant factors:** $D_1 = D_2 = D_3 = 0.05$, $K_1 = K_3 = 80$, $K_2 = 20$, $R_1 = R_2 = R_3 = 0.3$, $L_1 = L_2 = 0.016$, $T = 0.004$.
**Variable factor:** $M_1 = M_2 = M = 0.001{:}0.001{:}0.005$.

(d)

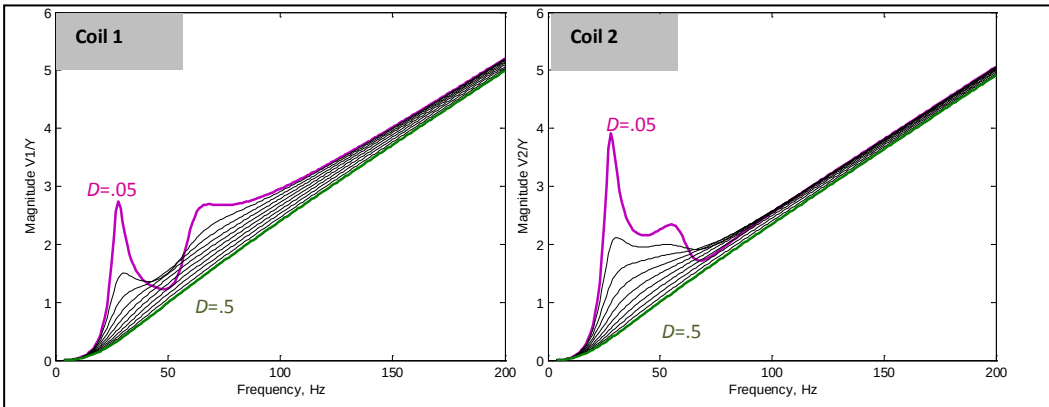


**Constant factors:** $M_1 = M_2 = M = 0.0015$, $K_1 = K_3 = 80$, $K_2 = 20$, $R_1 = R_2 = R_3 = 0.3$, $L_1 = L_2 = 0.016$, $T = 0.004$.
**Variable factor:** $D_1 = D_2 = D_3 = D = 0.05{:}\ 0.05{:}0.5$.

(e)

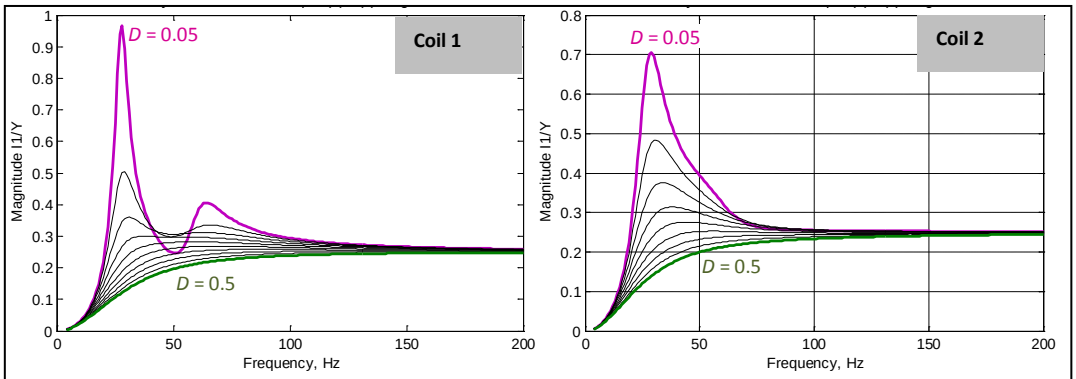


**Constant factors:** $M_1 = M_2 = M = 0.0015$, $K_1 = K_3 = 80$, $K_2 = 20$, $R_1 = R_2 = R_3 = 0.3$, $L_1 = L_2 = 0.016$, $T = 0.004$.
**Variable factor:** $D_1 = D_2 = D_3 = D = 0.05: 0.05: 0.5$.

(f)

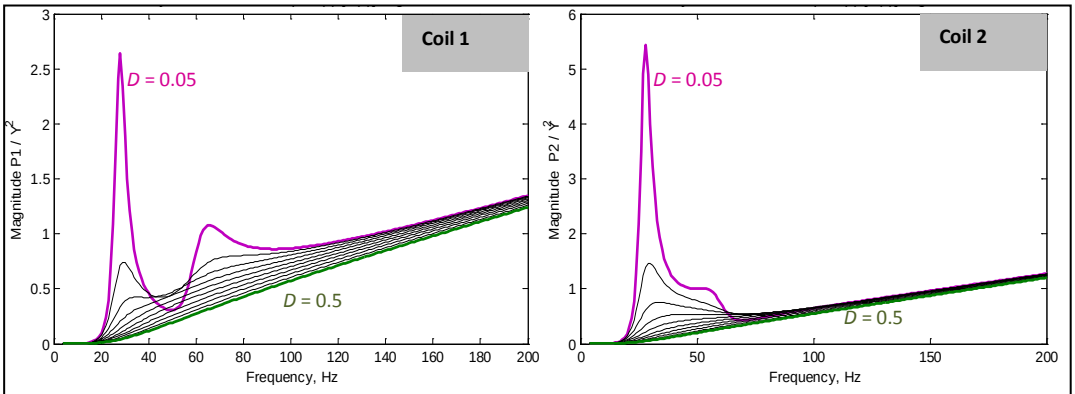


**Constant factors:** $M_1 = M_2 = M = 0.0015$, $K_1 = K_3 = 80$, $K_2 = 20$, $R_1 = R_2 = R_3 = 0.3$, $L_1 = L_2 = 0.016$, $T = 0.004$
**Variable factor:** $D_1 = D_2 = D_3 = D = 0.05: 0.05: 0.5$

(g)

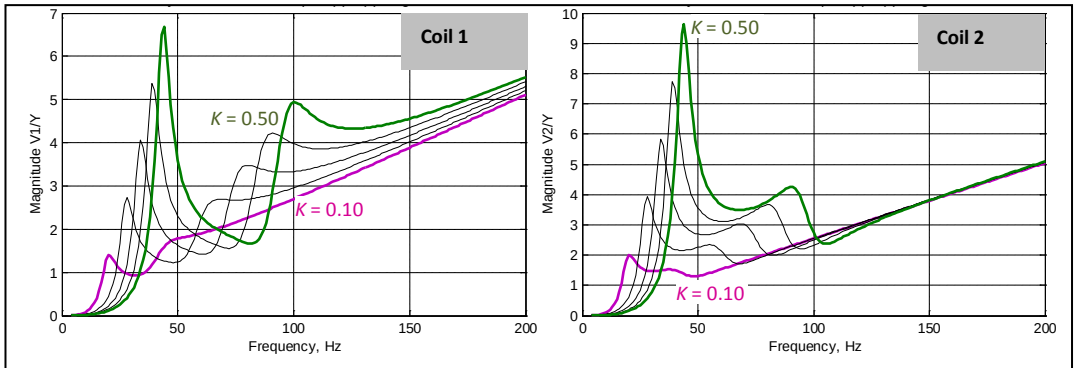


**Constant factors:** $M_1 = M_2 = 0.0015$, $D_1 = D_2 = D_3 = 0.05$, $R_1 = R_2 = R_3 = 0.3$, $L_1 = L_2 = 0.016$, $T = 0.004$.
**Variable factor:** $K_1 = K_3 = 4K$, $K_2 = K$, $K = 10: 10: 50$.

(h)

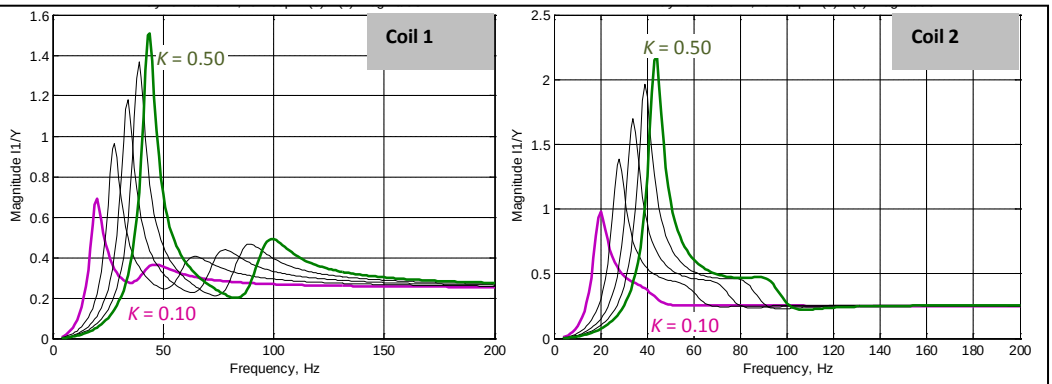


**Constant factors:** $M_1 = M_2 = 0.0015$, $D_1 = D_2 = D_3 = 0.05$, $R_1 = R_2 = R_3 = 0.3$, $L_1 = L_2 = 0.016$, $T = 0.004$.
**Variable factor:** $K_1 = K_3 = 4K$, $K_2 = K$, $K = 10{:}10{:}50$.

(i)

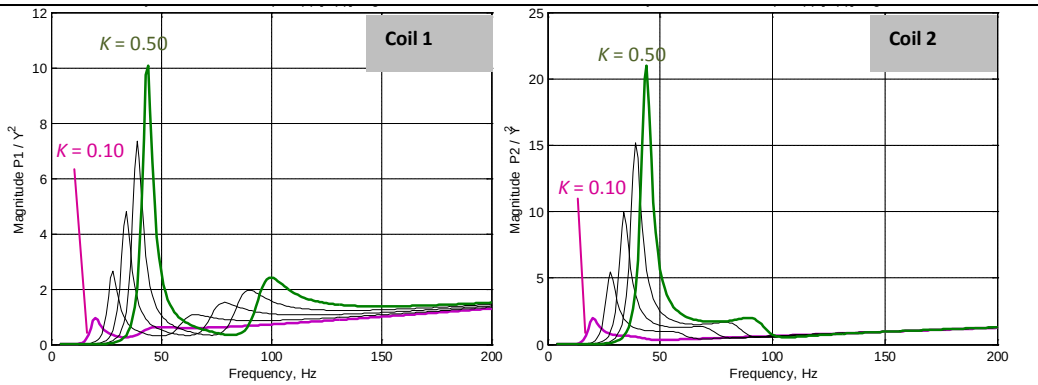


**Constant factors:** $M_1 = M_2 = 0.0015$, $D_1 = D_2 = D_3 = 0.05$, $R_1 = R_2 = R_3 = 0.3$, $L_1 = L_2 = 0.016$, $T = 0.004$.
**Variable factor:** $K_1 = K_3 = 4K$, $K_2 = K$, $K = 10{:}10{:}50$.

Figure 6.5 Sensitivity test results for 2DOF1D EMVEH model – electrical output frequency response curves for different values of mass (a, b, c) , damping (d, e, f) and spring stiffness (g, h, i). All magnitudes are in SI units.

### 6.3.3 Varying the electrical parameters – resistance and inductance.

The similar sensitivity tests were performed for the electrical parameters of resistance (*R*), and inductance (*L*) and the results are shown in Figure 6.6. It was found that the behaviour of the voltage, current and power frequency response curves of the 2DOF1D EMVEH system for changes in values of the electrical design parameters were similar to those found in the SDOF1D EMVEH system.

(a)

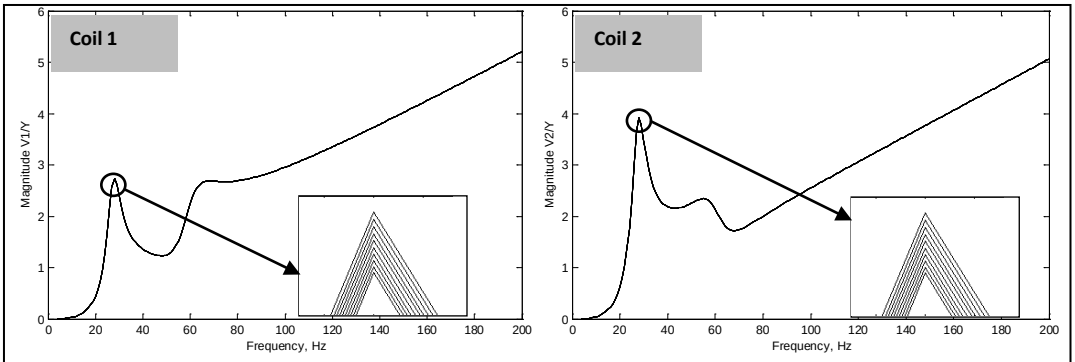


**Constant factors:** $M_1 = M_2 = 0.0015$, $D_1 = D_2 = D_3 = 0.05$, $L_1 = L_2 = 0.016$, $K_1 = K_3 = 80$, $K_2 = 20$, $T = 0.004$.
**Variable factor:** $R_1 = R_2 = R_3 = R = 0.1{:}0.1{:}1.0$.

(b)

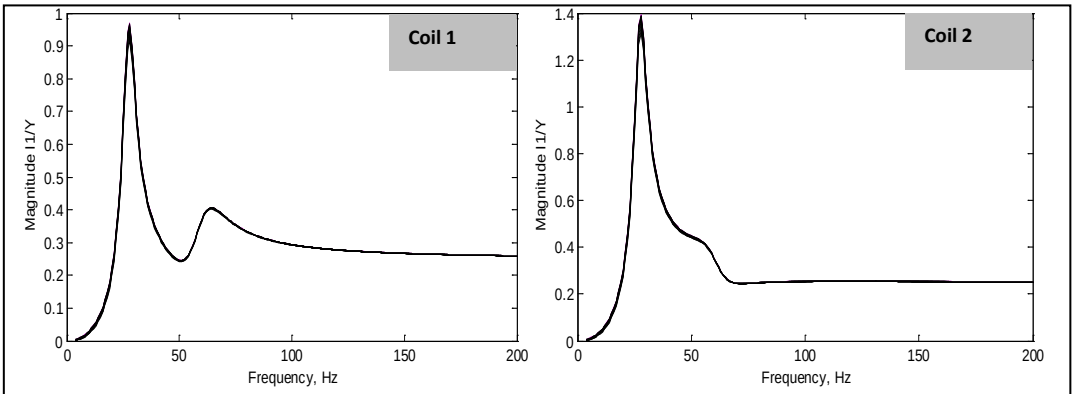


**Constant factors:** $M_1 = M_2 = 0.0015$, $D_1 = D_2 = D_3 = 0.05$, $L_1 = L_2 = 0.016$, $K_1 = K_3 = 80$, $K_2 = 20$, $T = 0.004$.
**Variable factor:** $R_1 = R_2 = R_3 = R = 0.1{:}0.1{:}1.0$.

(c)

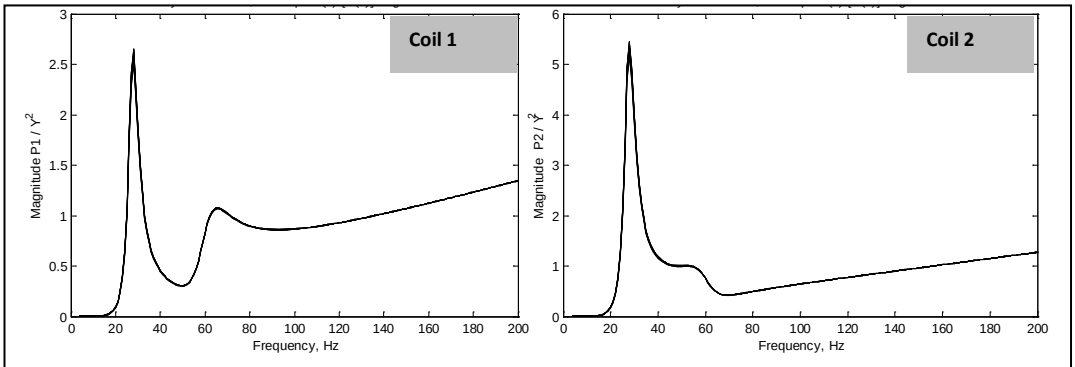


**Constant factors:** $M_1 = M_2 = 0.0015$, $D_1 = D_2 = D_3 = 0.05$, $L_1 = L_2 = 0.016$, $K_1 = K_3 = 80$, $K_2 = 20$, T = 0.004
**Variable factor:** $R_1 = R_2 = R_3$ = R = 0.1:0.1:1.0

(d)

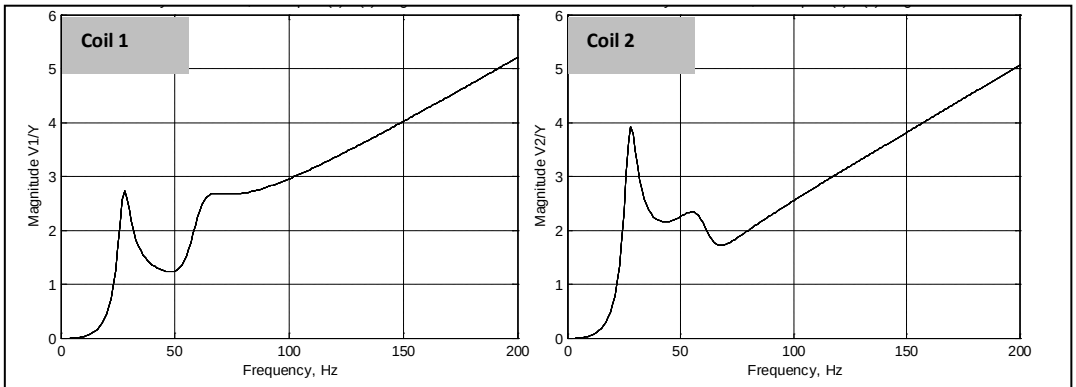


**Constant factors:** $M_1 = M_2 = 0.0015$, $D_1 = D_2 = D_3 = 0.05$, $L_1 = L_2 = 0.016$, $K_1 = K_3 = 80$, $K_2 = 20$, $T = 0.004$.
**Variable factor:** $R_1 = R_2 = R_3 = R$ = 1000:1000:10000.

(e)

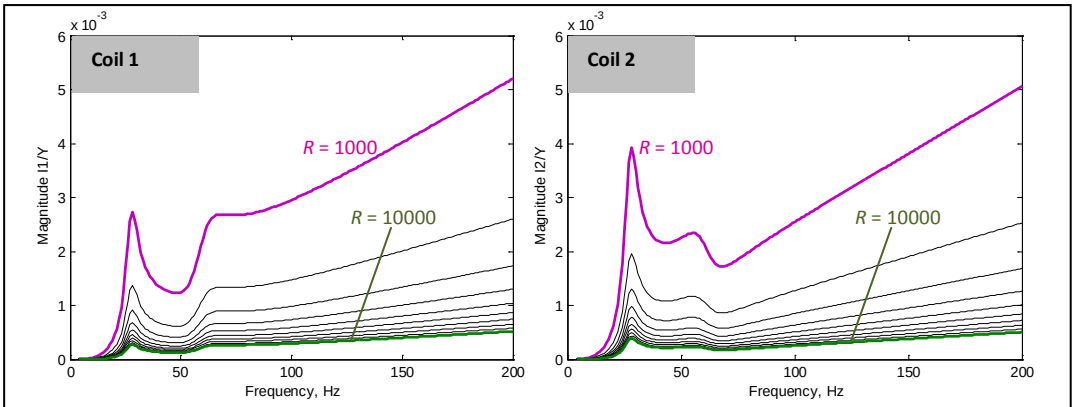


**Constant factors:** $M_1 = M_2 = 0.0015$, $D_1 = D_2 = D_3 = 0.05$, $L_1 = L_2 = 0.016$, $K_1 = K_3 = 80$, $K_2 = 20$, $T = 0.004$.
**Variable factor:** $R_1 = R_2 = R_3 = R$ = 1000:1000:10000.

(f)

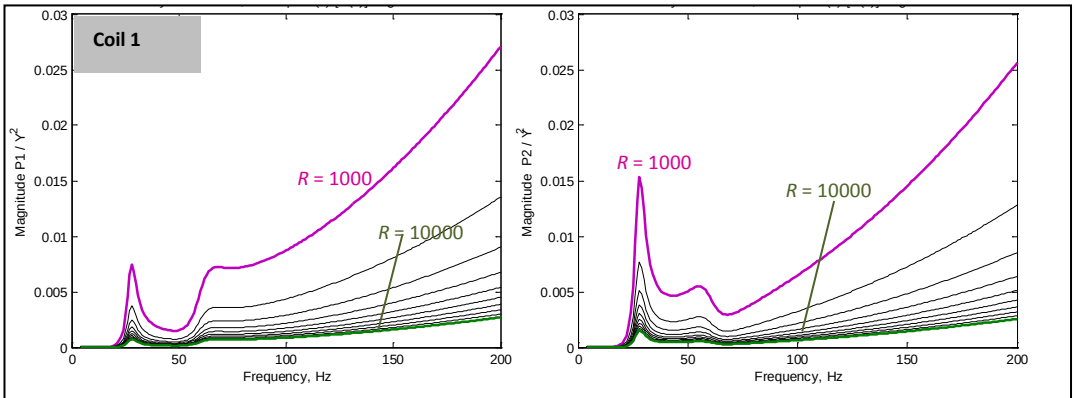


**Constant factors:** $M_1 = M_2 = 0.0015$, $D_1 = D_2 = D_3 = 0.05$, $L_1 = L_2 = 0.016$, $K_1 = K_3 = 80$, $K_2 = 20$, $T = 0.004$.
**Variable factor:** $R_1 = R_2 = R_3 = R$ = 1000:1000:10000.

(g)

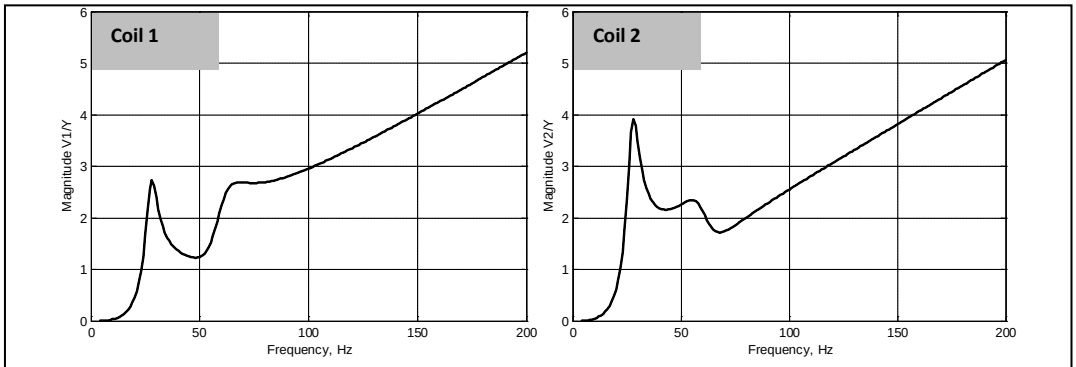


**Constant factors:** $M_1 = M_2 = 0.0015$, $D_1 = D_2 = D_3 = 0.05$, $K_1 = K_3 = 80$, $K_2 = 20$, $R_1 = R_2 = 0.3$, $T = 0.004$.
**Variable factor:** $L_1 = L_2 = L = 0.001{:}0.001{:}0.01$.

(h)

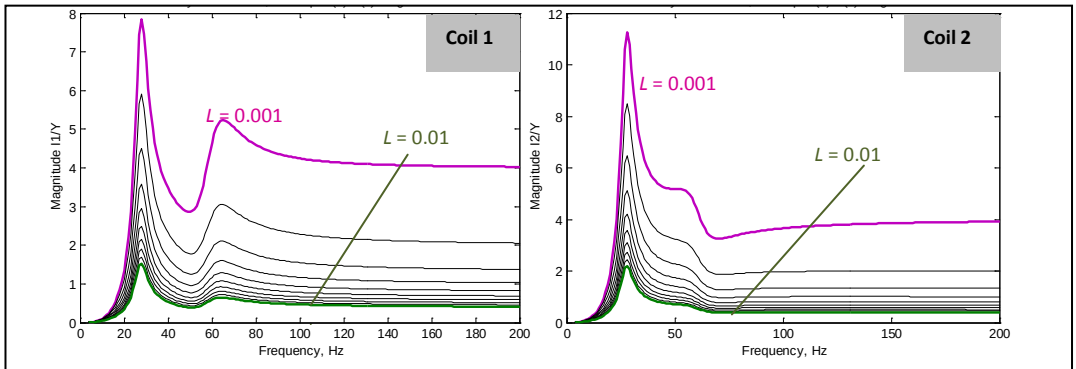


**Constant factors:** $M_1 = M_2 = 0.0015$, $D_1 = D_2 = D_3 = 0.05$, $K_1 = K_3 = 80$, $K_2 = 20$, $R_1 = R_2 = 0.3$, $T = 0.004$.
**Variable factor:** $L_1 = L_2 = L = 0.001{:}0.001{:}0.01$.

(i)

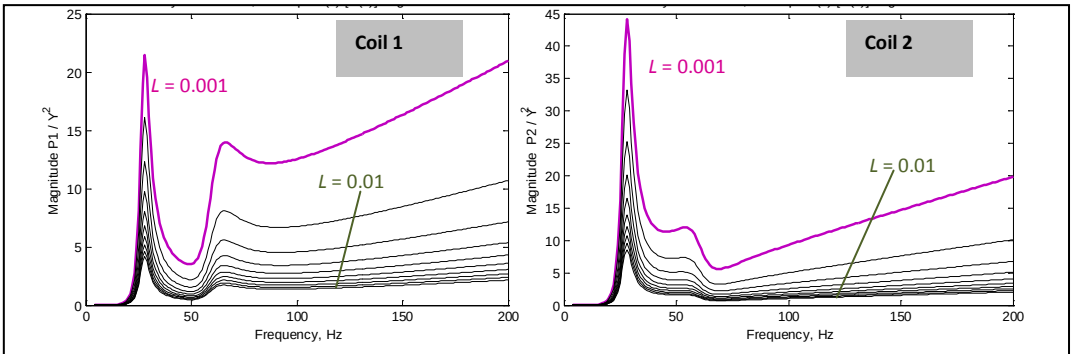


**Constant factors:** $M_1 = M_2 = 0.0015$, $D_1 = D_2 = D_3 = 0.05$, $K_1 = K_3 = 80$, $K_2 = 20$, $R_1 = R_2 = 0.3$, $T = 0.004$.
**Variable factor:** $L_1 = L_2 = L = 0.001{:}0.001{:}0.01$.

(j)

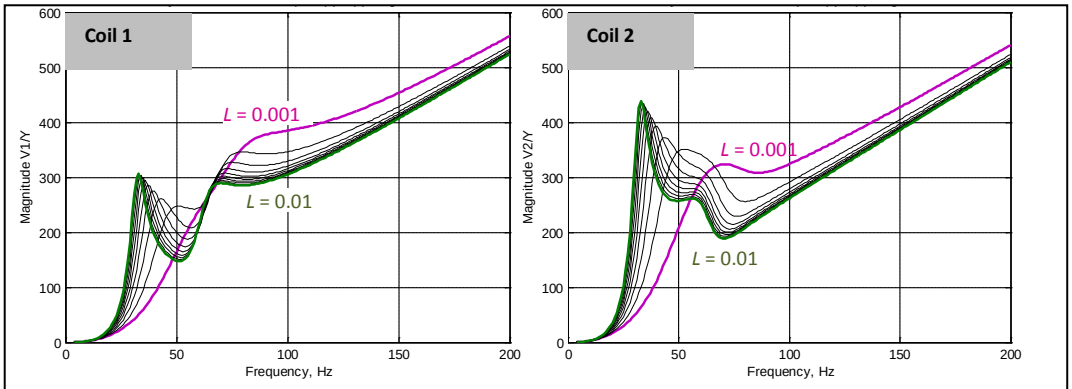


**Constant factors:** $M_1 = M_2 = 0.0015$, $D_1 = D_2 = D_3 = 0.05$, $K_1 = K_3 = 80$, $K_2 = 20$, $R_1 = R_2 = 0.3$, $T = 0.4$.
**Variable factor:** $L_1 = L_2 = L = 0.001{:}0.001{:}0.01$.

(k)

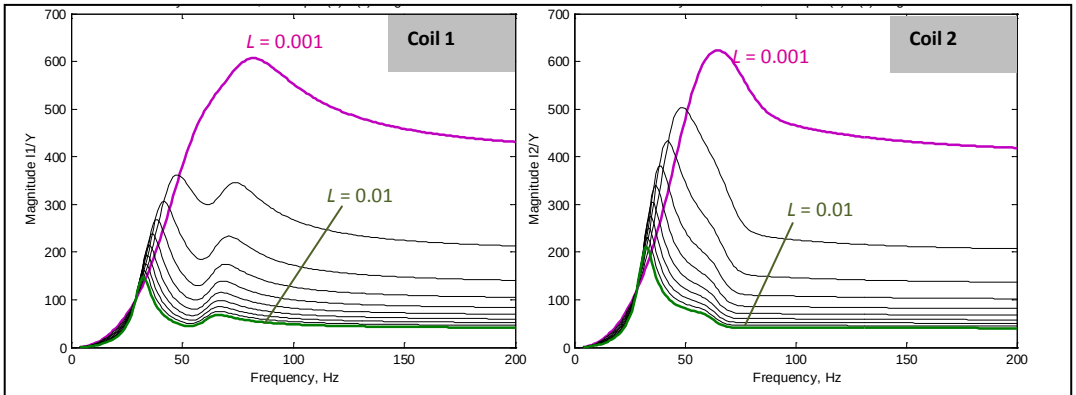


**Constant factors:** $M_1 = M_2 = 0.0015$, $D_1 = D_2 = D_3 = 0.05$, $K_1 = K_3 = 80$, $K_2 = 20$, $R_1 = R_2 = 0.3$, $T = 0.4$.
**Variable factor:** $L_1 = L_2 = L = 0.001{:}0.001{:}0.01$.

(*l*)

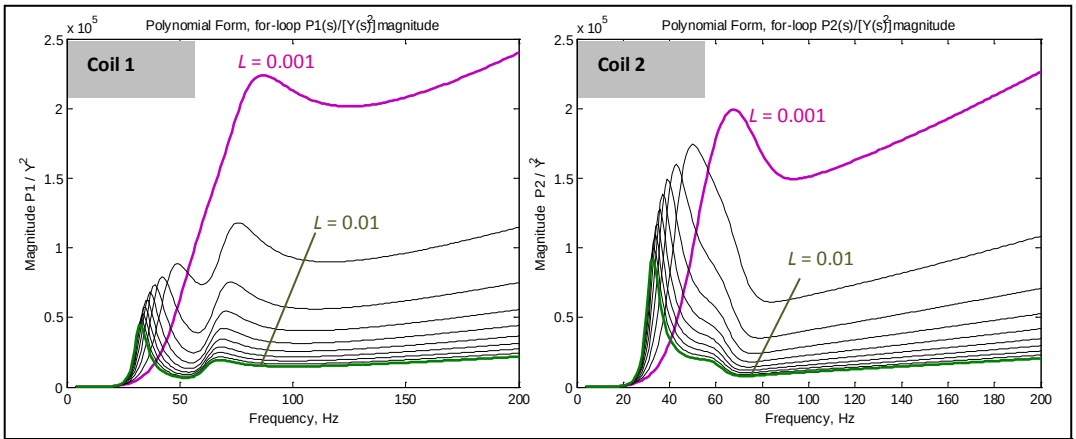


**Constant factors:** $M_1 = M_2 = 0.0015$, $D_1 = D_2 = D_3 = 0.05$, $K_1 = K_3 = 80$, $K_2 = 20$, $R_1 = R_2 = 0.3$, $T = 0.4$.
**Variable factors:** $L_1 = L_2 = L = 0.001{:}0.001{:}0.01$.

Figure 6.6 Sensitivity test results for 2DOF1D EMVEH model – voltage output frequency response curves for different values of (a, b, c) internal resistance (d, e, f) external resistance (g, h, i), inductance at low coupling coefficient $T = 0.004$ (j, k, l), inductance at high coupling coefficient $T = 0.4$.

From Figure 6.6 (a, b, c), it can be observed that the change in internal resistance from 0.1 ohms to 1 ohm had a negligible effect on the voltage, current and power frequency responses. However, when an external resistor was connected and the external resistance was varied from $R$ = 1000 ohms to $R$ = 10000 ohms as in Figure 6.6 (d, e, f), the impedance of the EMVEH system increased, resulting in reduced power along with a reduced current to maintain the same voltage.

It was observed from Figure 6.6 (g, h, i) that at low values of the coupling coefficient ($T$), the inductance ($L$) of the system increased the impedance of the system, thus reducing the current and power while maintaining a constant voltage. At higher values of coupling coefficient ($T$), as observed in Figure 6.6 (j, k, l), the increase in inductance ($L$) decreased the resonant frequency value and more peaking of resonance was observed. Hence, it is desirable to have a high coupling coefficient to observe resonance and hence maximum power occurring at a lower operating frequency.

It may be questionable whether the higher value of the coupling coefficient has any effect on the behaviour of the mechanical parameters. Hence, the coupling coefficient was set to $T$ = 0.4 and the values of the masses ($M_1 = M_2$) were varied from 0.001 kg to 0.005 kg. Once again the behaviour of the voltage response obtained, as seen in Figure 6.7, was similar to the sensitivity test, as explained in Figure 6.5 (a).

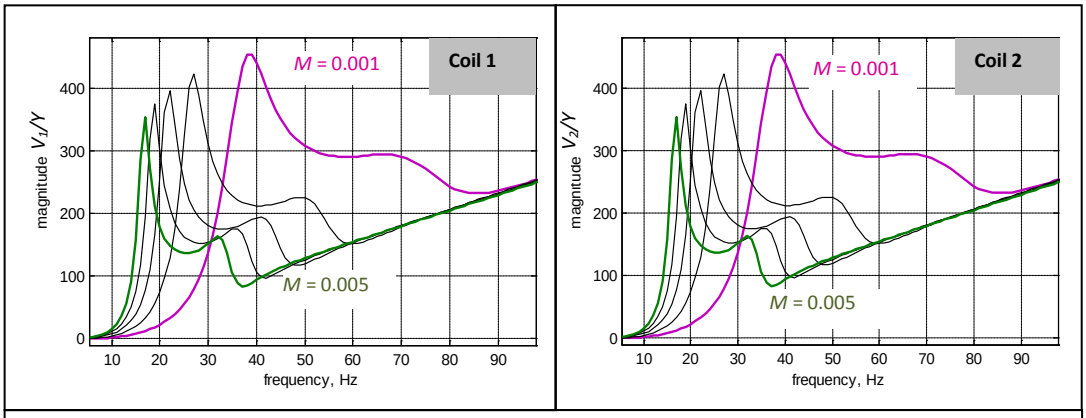


**Constant factors:** $D_1 = D_2 = D_3 = 0.05$, $K_1 = K_2 = K_3 = 80$; $R_1 = R_2 = R_3 = 0.3$, $L_1 = L_2 = 0.016$, $T = 0.4$
**Variable factor:** $M_1 = M_2 = M = 0.0015$

Figure 6.7 Sensitivity test results for 2DOF1D EMVEH model – voltage output frequency response curves for different values of mass at $T$ = 0.4 to check the influence of $T$.

## 6.4 Conclusions

In every test, when the desired parameter was increased whilst keeping the other design parameters constant, the electrical outputs, the resonant frequency and the resonant behaviour varied. The behaviour of both SDOF11D and 2DOF1D EMVEH was similar except for the obvious fact that two resonant peaks were observed in 2DOF1D, compared to the one resonant peak in SDOF1D EMVEH. This similarity in results suggests that future *n* degree-of-freedom-based MDOF1D EMVEHs would follow the same sensitivity behaviours as observed in these two models.

Thus it can be confirmed that the increase in degrees-of-freedom does not have any influence on the sensitivity of the overall EMVEH to each of the design parameters. Hence, the observations regarding both the SDOF1D EMVEH and 2DOF1D EMVEH sensitivity tests were summarised, as presented in Table 6.1.

Table 6.1 Summarised observations of both SDOF1D and 2DOF1D EMVEH sensitivity tests.

| **Input design parameters** | **Output frequency responses** | | | | | |
|---|---|---|---|---|---|---|
| | **Voltage** | | **Current** | | **Power** | |
| | **Magnitude (*V/Y*)** | **Frequency (*f*)** | **Magnitude (*I/Y*)** | **Frequency (*f*)** | **Magnitude ($P/Y^2$)** | **Frequency (*f*)** |
| Coupling coefficient (*T*) | Increases | No change | Increases | No change | Increases | No change |
| Mass (*M*) | Decreases | Decreases | Increases | Decreases | Increases | Decreases |
| Damping (*D*) | Decreases | No change | Decreases | No change | Decreases | No change |
| Spring stiffness (*K*) | Increases | Increases | Increases | Increases | Increases | Increases |
| Internal resistance ($R_i$) | No change | No change | No change | No change | No change | No change |
| Load resistance ($R_i + R_L$) | No change | No change | Decreases | No change | Decreases | No change |
| Inductance(*L*) at low *T* | No change | No change | Decreases | No change | Decreases | No change |
| Inductance(*L*) at high *T* | Increases | Decreases | Decreases | Decreases | Increases | Decreases |

It was found that the coupling coefficient had no effect on the resonant frequency of the overall system. However, the increase in coupling coefficient increased the voltage generated, thus validating Faraday's principle of electromagnetic induction.

The electrical output/base excitation input (*V/Y, I/Y* and $P/Y^2$) behaviour of the SDOF1D/2DOF1D EMVEH was similar to the acceleration output behaviour of the SDOF1D/2DOF1D pure MDK systems since the resonant frequency of the EMVEHs was proportional to $\sqrt{K/M}$. This suggests that the resonance of the overall system is a function of resonances of the individual systems constituted by it, namely the MDK mechanical system and the electrical RL/RLC system. Since the RL system was considered, there was no electrical resonance; hence the overall system resonance was largely influenced by mechanical system resonance.

When external load resistance was used, the impedance of the EMVEH system increased. Due to this, the current flowing through the resistance decreased, and subsequently the power decreased. At high coupling coefficients, the increase in inductance decreased the resonant frequency and the current but increased the power. This study of sensitivity analyses has provided valuable guidance for the design of future MDOF1D energy harvesters. This study provides a reference point for the study of experimentally obtained voltage, current and power frequency responses, to point out deviations of experimentally assumed values of *M, D, K, R, L* and *T*.

# Chapter 7 Experimental validation of SDOF1D and 2DOF1D EMVEH models

In Chapter 4 and Chapter 5, the theoretical models for SDOF1D and 2DOF1D were developed and analysed using simulations. The behaviour of the models was analysed in the sensitivity analyses presented in Chapter 6. To validate the theoretical models, two prototypes, an SDOF1D EMVEH and a 2DOF1D EMVEH were built and tested experimentally. The current chapter focuses on how the prototypes were built and how the experiments were conducted with the resources available. The experimental validation of the SDOF1D and the 2DOF1D was performed to ensure the complete validation of the mathematical models, thus establishing a solid foundation for the generalisation to *n* degrees-of-freedom in Chapter 8.

## 7.1. Experimental methodology

The experimental methodology for the SDOF1D and 2DOF1D is shown in Figure 7.1. Initially, the prototype was designed in a virtual sense using Solidworks 2010 and the design took into account the practical component values for both the SDOF1D EMVEH and the 2DOF1D EMVEH. Most of the parts, particularly the ones relevant to the design parameters *M, D, K, R* and *L* were common to both the SDOF1D and 2DOF1D EMVEHs to ensure a fair comparison. This was followed by manufacturing of the prototypes. At a later stage, the experiments were designed with consideration given to the high accuracy and resolution required for recording and reading the data values. This was followed by the actual experimentation to obtain the SDOF1D experiment and 2DOF1D experiment results.

After running three trials of experiments for both the SDOF1D EMVEH and 2DOF1D EMVEH models, the voltage frequency response curve was deduced. This was obtained for the operating frequency range from the experimental time responses of the experiments, and was compared with the sensitivity analysis data. From this, the key noise parameters and key control parameters were identified. The key noise parameters were those that could not be controlled, such as (a) the electromagnetic interference of the exciter and the lab

building of the experimental setup and (b) the frictional damping between the coil and the magnet since the diametrical clearance was only 1 mm. The key control parameters were those experimental parameters that could be controlled, such as the frequency and data sampling rate. Equivalent *M, D, K, R* and *L* values were assumed, based on the voltage frequency response comparison with the sensitivity analyses. From this, the equivalent theoretical voltage frequency response was deduced and then compared to the experimental voltage frequency response. The experimental results were later compared with the sensitivity analyses to assess the errors in the experimental assumptions, and these are discussed. It was found that the deviations were very small thus substantiating the theoretical models.

The next stage involved a comparison of the SDOF1D with the 2DOF1D EMVEH, so as to understand the performance and frequency characteristic benefits of the 2DOF1D when compared to the SDOF1D EMVEH system.

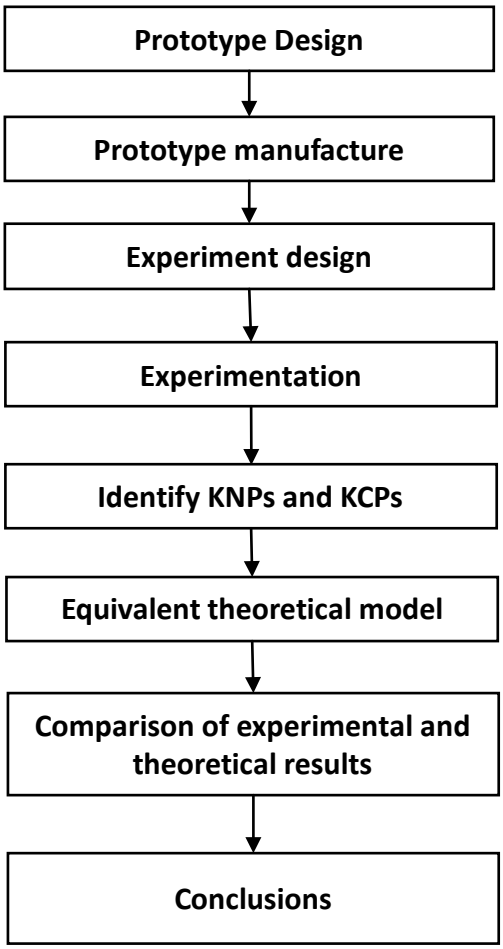


Figure 7.1 Experimental validation methodology for SDOF1D EMVEH and MDOF1D EMVEH.

## 7.2 Prototype design

The prototypes of both the SDOF1D and 2DOF1D EMVEH models were built with common parts for better comparison of both the models. The prototype designs of the SDOF1D and 2DOF1D are as shown in Figure 7.2 and Figure 7.3. The SDOF1D EMVEH model consisted of a central iron-core surrounded by an NdFeB ring magnet. The top and bottom spring holds the coil to the centre when the EMVEH is at rest without vibration. The 2DOF1D EMVEH has a similar setup with a central iron-core, but has two coils and two ring magnets. The two coils are held by a top spring, middle spring and bottom spring.

The coil was made of 14 turns of 0.25 mm copper wire and the iron-core was made from a cast-iron rod. The spring was made of phosphor bronze and the base was made of brass material to ensure no magnetic interference with the magnetic field. Six sigma stack-up tolerance analyses were performed to ensure proper tolerances and fits in the assembly using crystal ball software. The details of the tolerance analyses are provided in Appendix C of this thesis. Detailed drawings of the prototypes are given in Appendix C.

(a)

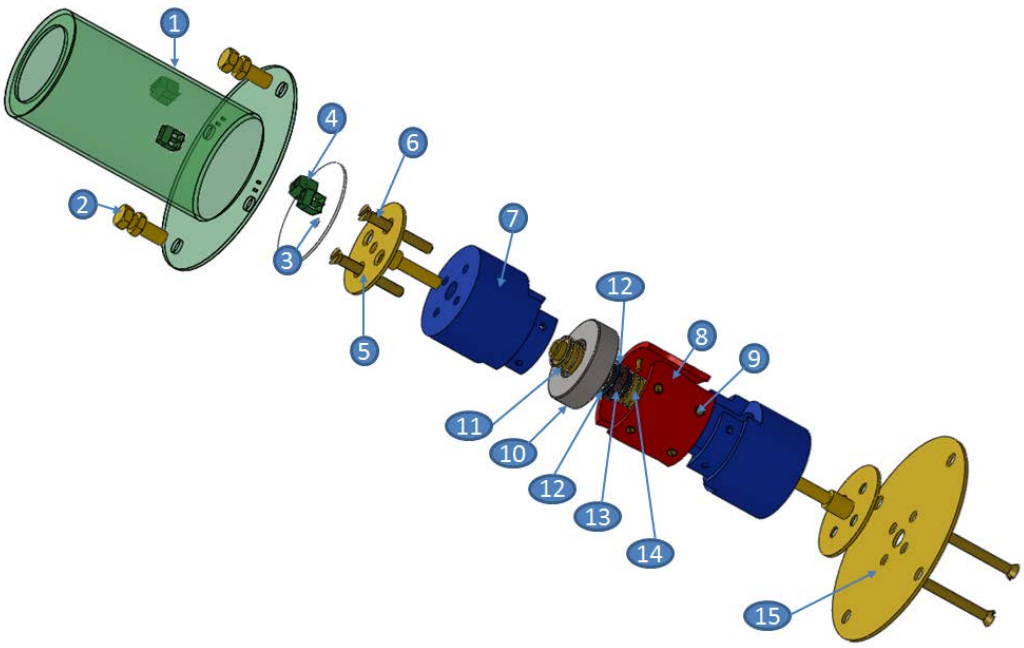

(b)

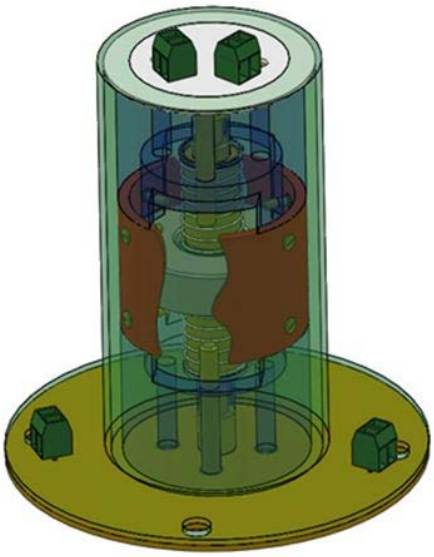

| Part # | SDOF1D assembly parts | Qty |
|---|---|---|
| 1 | SDOF1D cover | 1 |
| 2 | Cover clamping screws | 2 |
| 3 | SDOF1D circuit board | 1 |
| 4 | Wire connectors | 4 |
| 5 | Exciter connector | 2 |
| 6 | Exciter connector screws | 4 |
| 7 | Outer case | 2 |
| 8 | SDOF1D sleeve | 1 |
| 9 | Sleeve screws | 4 |
| 10 | Magnet | 1 |
| 11 | Brass core | 2 |
| 12 | Iron core | 2 |
| 13 | Coil | 1 |
| 14 | SDOF end spring | 2 |
| 15 | Bottom plate | 2 |

(c)

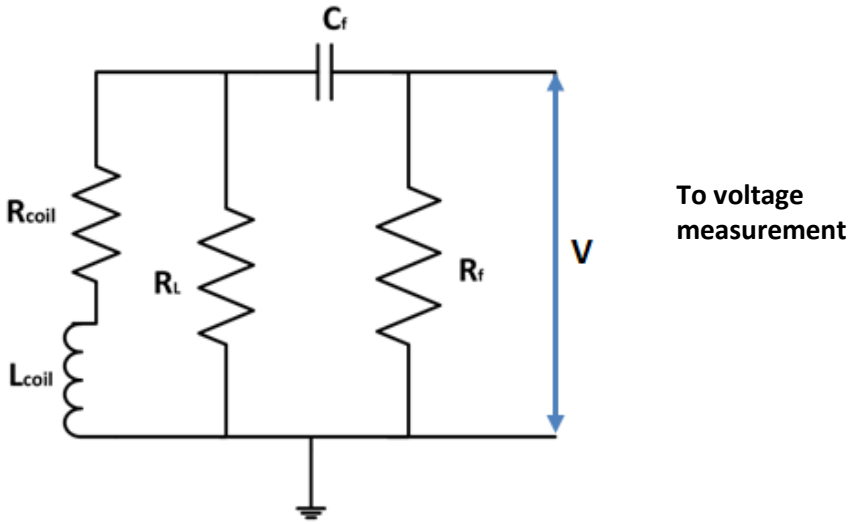


Figure 7.2 Experimental prototype of SDOF1D EMVEH (a) exploded view (b) assembled prototype with bill of materials, (c) the electrical circuit.

(a)

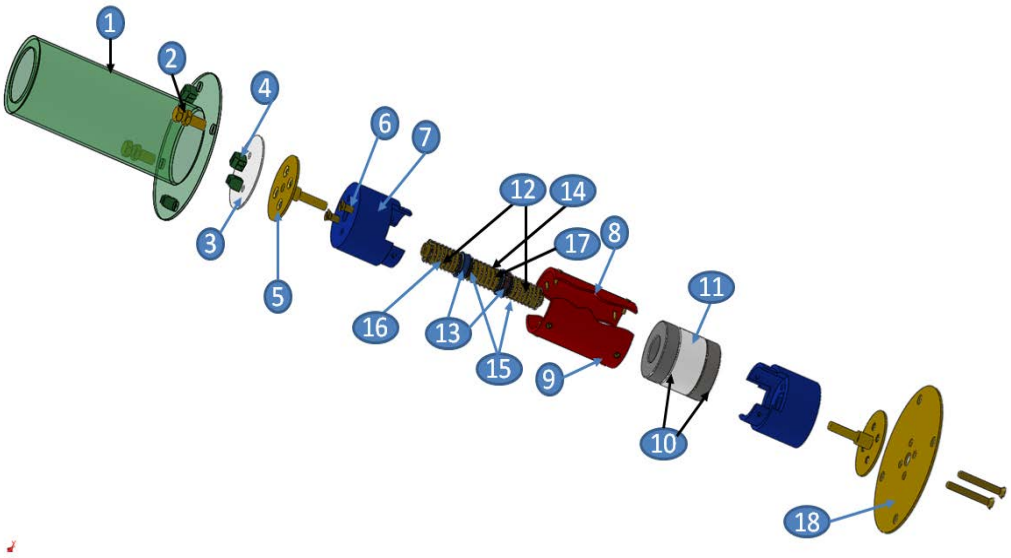


(b)

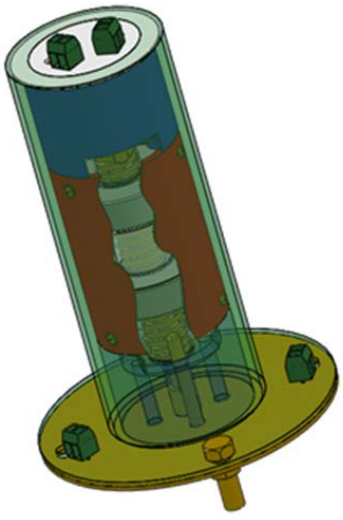

| Part # | 3DOF1D assembly parts | Qty |
|---|---|---|
| 1 | 3DOF1D cover | 1 |
| 2 | Cover clamping screws | 2 |
| 3 | SDOF1D circuit board | 1 |
| 4 | Wire connectors | 4 |
| 5 | Exciter connector | 2 |
| 6 | Exciter connector screws | 4 |
| 7 | Outer case | 2 |
| 8 | 3DOF1D sleeve | 1 |
| 9 | Sleeve screws | 4 |
| 10 | Magnets | 2 |
| 11 | 3MDOF1D spacer | 1 |
| 12 | Brass core end | 2 |
| 13 | Iron core end | 2 |
| 14 | Brass core middle | 1 |
| 15 | Coil | 2 |
| 16 | 3DOF end spring | 2 |
| 17 | 3DOF middle spring | 1 |
| 18 | Bottom Plate | 1 |

(c)

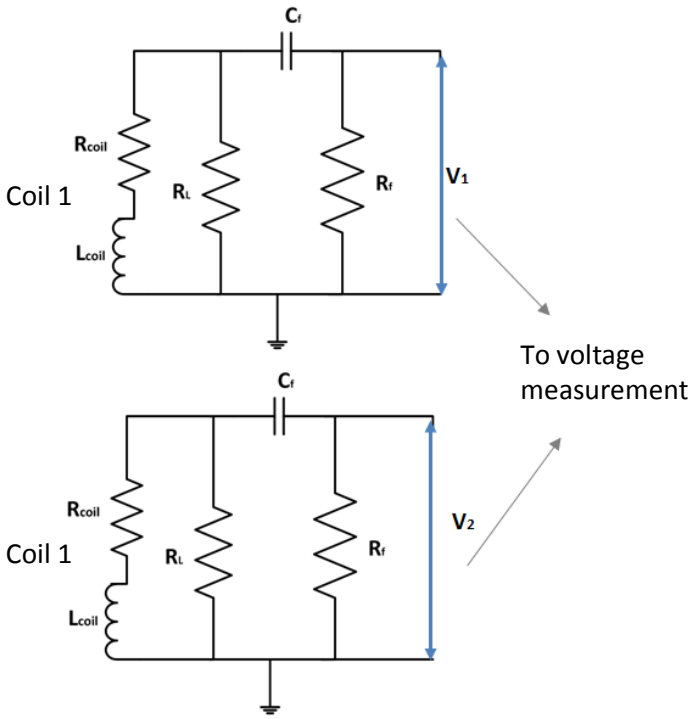


Figure 7.3 Experimental prototype of 2DOF1D EMVEH (a) exploded view, (b) assembled prototype with bill of materials, (c) voltage measuring circuit.

The design parameters of the prototypes of both SDOF1D and 2DOF1D EMVEH were determined by measurement or by assumption, as shown in Table 7.1.

Table 7.1 Determined experimental values of design parameters of SDOF1D and 2DOF1D EMVEH.

| **Experimental prototype values of design parameters** | **Determined by** | **Determined value** |
|---|---|---|
| Masses ($M$, $M_1$, $M_2$) | Directly measured | 0.0015 kg |
| Damping coefficients($D$, $D_1$, $D_2$, $D_3$) | Assumed | 0.05 Ns/m |
| Spring stiffnesses ($K$, $K_1$, $K_2$, $K_3$) | Calculated | 80 N/m |
| Total resistances of the coils ($R$, $R_1$, $R_2$) | Calculated | 0.3 ohm |
| Inductances($L$, $L_1$, $L_2$) | Calculated | 0.016 H |
| Coupling coefficient ($T$) | Magnetostatics | Varies |
| **SDOF1D design parameters** | ***M, D, K, R, L*** | |
| **2DOF1D design parameters** | ***$M_1$, $M_2$, $D_1$, $D_2$, $D_3$, $K_1$, $K_2$, $K_3$, $R_1$, $R_2$, $L_1$, $L_2$*** | |

Initially, the NdFeB N35 grade ring magnets of size 35(OD) X 16(ID) X 10(H) ( in mm units) was purchased. The coil holders were designed based on the inside diameter of these magnets. The mass of the coil with the wire was measured on the weighing scale and was found to be 15g = 0.0015kg. The practical value of 0.05 was assumed for the damping coefficients prior to the experiment. The springs were designed with lengths equal to the distance between the coils in addition to the extra length for initial tension, totalling 30 mm. Phosphor bronze springs were selected due to their non-magnetic property, the springs' modulus of rigidity was 41 GPa.

The mean diameter ($D_s$) of the spring was 13 mm and the diameter of the spring wire ($d_{sw}$) was measured as 0.405 mm. The number of active coils in the spring was 8. The spring stiffness ($K$) was calculated by the formula:

$$K = \frac{G{d_{sw}}^4}{8{D_s}^3 n_a} = \frac{(4.1e{+}11)*(.0004)^4}{8(0.0013)^3(8)} = 78.45 \cong 80 \text{ N/m}. \quad (7.1)$$

The coil was made with a coil diameter ($D_c$) of 15.1 mm and the diameter of the coil wire ($d_w$) was 0.25 mm. The coil wire was made of copper with a resistivity (ρ) of 1.72e-8 Ωm. The length of coil wire used was calculated as:

$$l_{cw} = \pi N D_c = \pi(14)(15.125/1000) = 0.66 \text{ m}. \quad (7.2)$$

The area of the cross-section of the coil wire ($A_{cw}$) was calculated as:

$$A_{cw} = \frac{\pi\, d_w^2}{4} = \frac{\pi(0.00025)^2}{4} = 4.9e-8 \text{ m}^2. \quad (7.3)$$

The resistance of the coil ($R_c$) was calculated as:

$$R_c = \frac{\rho l_{cw}}{A_{cw}} = (1.72\text{e}-8) * \frac{0.66}{4.9e-8} = 0.241\ \Omega. \quad (7.4)$$

The resistance of excess wire ($R_e$) that connected the coil to the voltage measuring circuit was estimated at 0.06Ω. Hence the total internal resistance of the coil was considered as:

$$R = R_c + R_e = 0.24 + 0.06 = 0.3\ \Omega. \quad (7.5)$$

The area of the coil (Ac) was calculated as:

$$A_c = \frac{\pi\, D_c^2}{4} = \frac{\pi\,(15.25e-3)^2}{4} = 0.000183 \text{ m}^2. \quad (7.6)$$

Since the iron-core was installed in the centre of the coil, the permeability of the coil with iron-core is given by:

$$\mu = \mu_0\mu_r = (4\pi \times 10^{-7}) * 1450 = 0.00189 \text{ NA}^{-2}. \quad (7.7)$$

The length of the coil was measured at 4 mm. The inductance (L) of the coil was calculated as:

$$L = \frac{\mu N^2 A}{l_c} = \frac{0.00189 * 14^2 * 0.000183}{0.0004} = 0.016 \text{ H.} \quad (7.8)$$

The value of the coupling coefficient (*T*) was found to vary with respect to $x$ and was found using ANSOFT magnetostatic analysis.

## 7.3 Experimental design

The experiment consisted of two sets of measurements i) time response of SDOF1D EMVEH and ii) time response of 2DOF1D EMVEH. The experimental setup was the same for both of these experiments and is as shown in Figure 7.4.

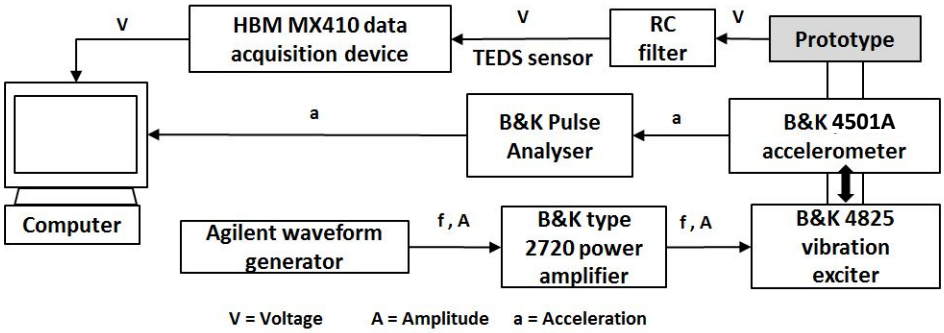


Figure 7.4 Schematic of experimental setup for SDOF1D and 2DOF1D EMVEH.

The experimental setup consisted of the EMVEH prototype (SDOF1D/2DOF1D) being mounted to a B & K Type 4825 vibration exciter. The Agilent waveform generator was connected to the exciter through the B&K Type 2720 power amplifier. The B&K pulse accelerometer was mounted on the flange of the prototype. The acceleration signal cable was connected from the B&K 4501A accelerometer to the B&K pulse analyser for measuring acceleration. When the waveform generator outputs a voltage wave of a particular predetermined amplitude and frequency, it is connected to the power amplifier where it is amplified to the limit acceptable for driving the B & K exciter. The exciter starts vibrating the prototype which is mounted on it. The resulting induced electromagnetic

voltage from the prototype was then connected to the HBM data acquisition device through a RC filter. All the instruments were pre-calibrated.

The detailed pictures of the experiment are included in the Appendix C of this thesis.

## 7.4 Experimental procedure

The experimental procedure was the same for both the SDOF1DEMVEH and MDOF1D EMVEH prototypes. Once the experimental setup was finalised with the assembled prototype, all instruments were powered on. The first step of the experiment was to establish the safe operating range of frequencies and amplitude of the excited base motion. Initially, the waveform generator was adjusted to produce harmonic excitation in the frequency range from 0 Hz - 20 Hz with amplitude of 3 mm. It was observed that the experimental setup started to vibrate violently after 16 Hz. Hence other amplitudes of 0.5 mm and 0.1 mm were considered. It was found that 0.1 mm had a safe operating range over the frequencies 10 Hz-60 Hz for both SDOF1D EMVEH and 2DOF1D EMVEH models and hence was chosen for the experiments. In addition to this, the frequency range from 0 Hz - 10 Hz could not be considered as the accelerometer sensitivity was linear only above 10 Hz.

The waveform generator was adjusted to set the frequency of 10 Hz - 60 Hz for amplitude of 1 mm. The coarse amplitude adjustment was possible using the B&K type 2720 power amplifier and the fine adjustment was made using the waveform generator. The amplitudes were obtained as a function of acceleration voltage as acceleration $a = A\omega^2$ at the maximum peak, where A is the amplitude and $\omega$ is the excitation frequency. The fine and coarse adjustment of the waveform was achieved by bringing the acceleration voltage to the specified voltage for the desired amplitude using the accelerometer calibration sensitivity factor. Once the waveform was set for the desired amplitude and frequency, the time series response of the voltage was recorded in the data acquisition device for a ten second period. The recorded response was then saved as a .CSV or .xlsx file. These experimental time responses were recorded with correct numbering of frequency, amplitude and experiment-set. The responses were recorded for 10 Hz – 60 Hz and 0.1 mm combinations for each of the data sets. Three iterations of the experiment

were performed to ensure repeatability for both SDOF1D EMVEH and 2DOF1D EMVEH models separately.

## 7.5 SDOF1D EMVEH results and validation

Three measurements of voltage RMS outputs of the SDOF1D EMVEH prototype were obtained from the HBM data acquisition device and were plotted for analyses. The key control parameters and key noise parameters were identified by comparing these experimental voltage outputs to the theoretical voltages.

### 7.5.1 SDOF1D EMVEH RMS voltage results

The root mean square voltage output was recorded three times for every frequency point ranging from 10 Hz to 60 Hz in steps of 1 Hz. The measured frequency response of the voltage output of the three trials and their average is shown in the Figure 7.5**.** It was found that there was minimum deviation amongst the three trials. The resonance was observed approximately at a frequency of 54 Hz.

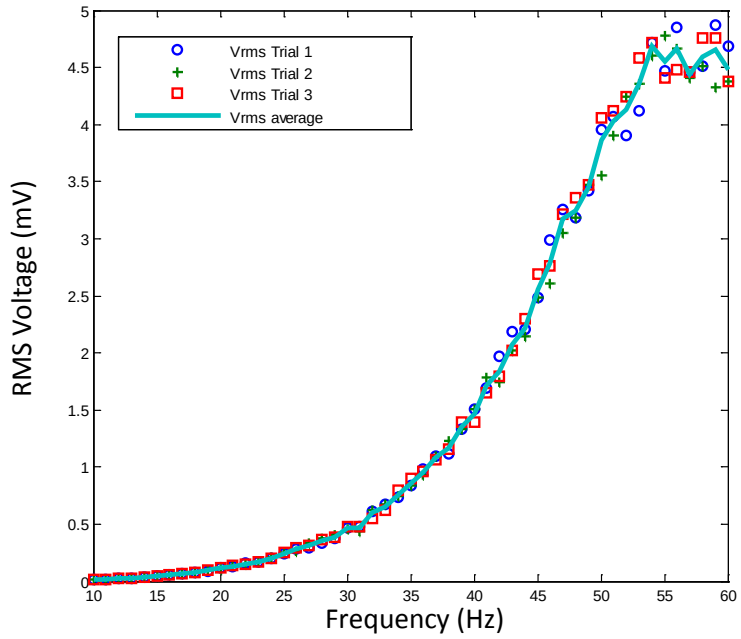


Figure 7.5 SDOF1D EMVEH experimental results – output voltage frequency response.

### 7.5.2 Identifying the key noise parameters and key control parameters from sensitivity analysis

The SDOF1D EMVEH's voltage frequency response obtained from the experiment (as shown in Figure 7.5) was compared with the sensitivity analyses voltage frequency response curves of the SDOF1D EMVEH obtained in Chapter 6. Careful comparison indicated that severe damping was occurring in the experiment. This could have been due to friction between the coil and the magnet, since the clearance between the two was small due to the tight tolerances. The coupling coefficient *T* was also observed to be very low in the experimental curve. This is due to the low number of coils and the fact that the motion of vibration was found to be in the low magnetic spatial variation region.

The equivalent theoretical *M, D, K, R,* and *L* values were determined by both experimental measurement and assumptions based on sensitivity analyses and are shown in Table 7.2.

Table 7.2 Measured and assumed equivalent theoretical values of system parameters.

| **Design Parameter** | **Value** | **Determined by** |
|---|---|---|
| Mass(*M*) | 0.0015 Kg | Measured |
| Damping coefficient(*D*) | 0.2 Ns/m | Assumed –based on comparison with sensitivity test data. |
| Spring stiffness(*K*) | 160 N/m | Trade-off between assumed sensitivity data and measured. |
| Resistance ( *R* ) | 0.3 ohm | Measured. |
| Inductance( *L*) | 0.016H | Trade-off between assumed sensitivity data and measured. |

The equivalent theoretical voltage frequency response curve obtained using the ODE45 non-linear method is shown in Figure 7.6. The natural frequency of the MDK subsystem of SDOF1D EMVEH is calculated as below:

$$f_n = 1/2\pi\sqrt{\frac{K_1+K_2}{M}} = \frac{\sqrt{\frac{(80+80)}{.0015}}}{2\pi} = 52.15 \text{ Hz} \tag{7.9}$$

while the measured natural frequency, as observed in Figure 7.5, was 54 Hz and the equivalent theoretical voltage, as observed in the Figure 7.6, was 55 Hz. All these voltages were very close to each other, thus validating the theoretical model.

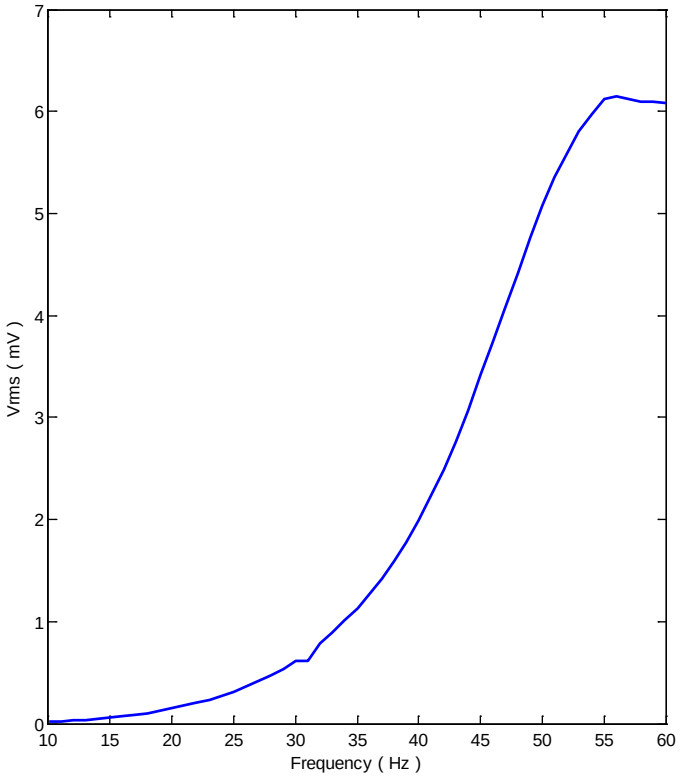


Figure 7.6 Equivalent theoretical voltage frequency response of SDOF1D EMVEH.

### 7.5.3 Comparison of theoretical and experimental results and SDOF1D EMVEH model validation

The experimental output voltage was compared with the equivalent theoretical output voltage obtained from the non-linear analysis discussed in Chapter 5. The comparison is shown in Figure 7.7. MATLAB's curve fitting tool was used to compare the theoretical and experimental voltage outputs at different frequencies. The results of the curve fitting are shown in Figure 7.8. From the curve fitting tool, it was found that the experimental voltage was approximately 75% of the theoretical voltage amplitude. From the sensitivity analysis as per Figure 6.1, this deviation is expected to be due to the coupling coefficient *T*. Thus the experimentally achievable magnetic flux linkage was lower than the anticipated theoretical magnetic flux linkage. This may have been due to eddy current losses, a lower number of coils or the magnetic field assumption as a double sine function for the calculation of *T*. Further controlled experimentation is necessary to understand this deviation. However, the trends of both the experimental and the equivalent theoretical model match each other

since the RMSE was very low as shown in Figure 7.8. Thus the theoretical SDOF1D EMVEH model can be validated as being an appropriate model demonstrating the system behaviour.

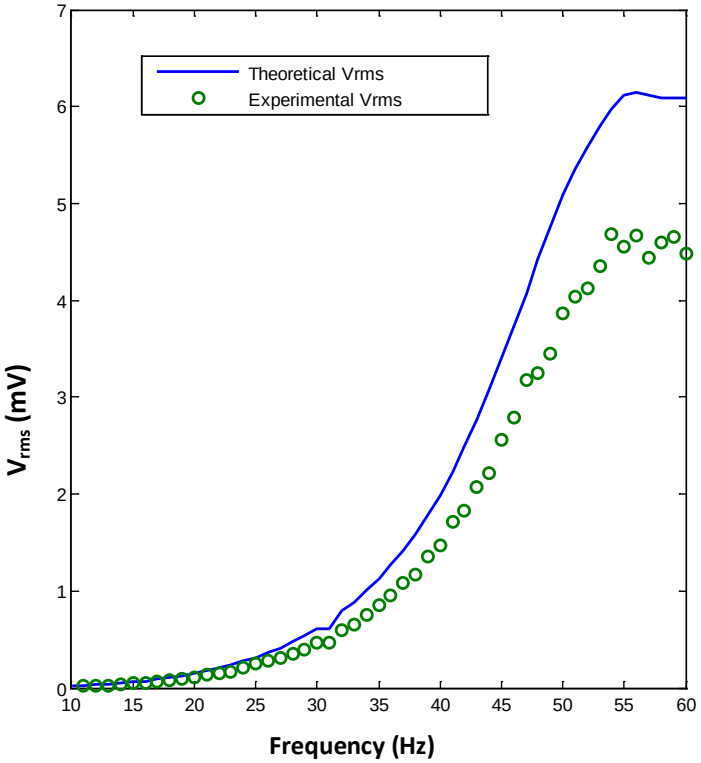


Figure 7.7 Comparison of theoretical and experimental voltage frequency response of SDOF1D EMVEH.

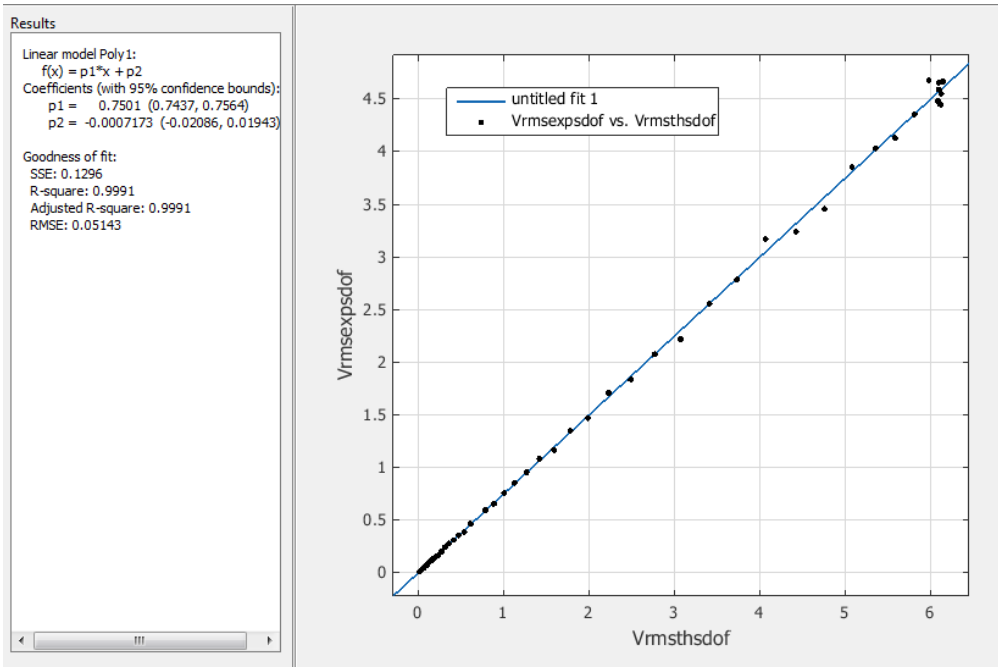


Figure 7.8 Curve fitting test of theoretical RMS voltage frequency response curve with experimental RMS voltage frequency response of SDOF1D EMVEH.

## 7.6 2DOF1D EMVEH results and validation

Similar to the SDOF1D EMVEH, the RMS values of the experimental voltages of all three trials were obtained from the HBM data acquisition device and plotted. The results were then compared to the theoretical results to identify the key noise parameters and key control parameters.

### 7.6.1 2DOF1D EMVEH results

Similar to the SDOF1D experiment, the root mean square voltage output of the 2DOF1D EMVEH prototype was recorded three times for every frequency point ranging from 10 Hz to 60 Hz in steps of 1 Hz. The 2DOF1D EMVEH had two coils where two voltages, namely, $V_{rms1}$ and $V_{rms2}$ were measured separately. The experimental frequency responses of these voltage outputs of the three trials and their average are shown in Figure 7.9a and Figure 7.9b. There was negligible deviation amongst the three readings for both the coils.The 2DOF1D EMVEH prototype was built with three identical springs where the spring stiffnesses were assumed to be same $K_1 = K_2 = K_3 = 80$. Hence, it was anticipated that both the coils would produce identical voltages. However, it was observed that both $V_{rms1}$ and $V_{rms2}$ were slightly different. This may be due to the fact that both the coils had some differences in their fill factor although they were supposed to be identical.

(a)

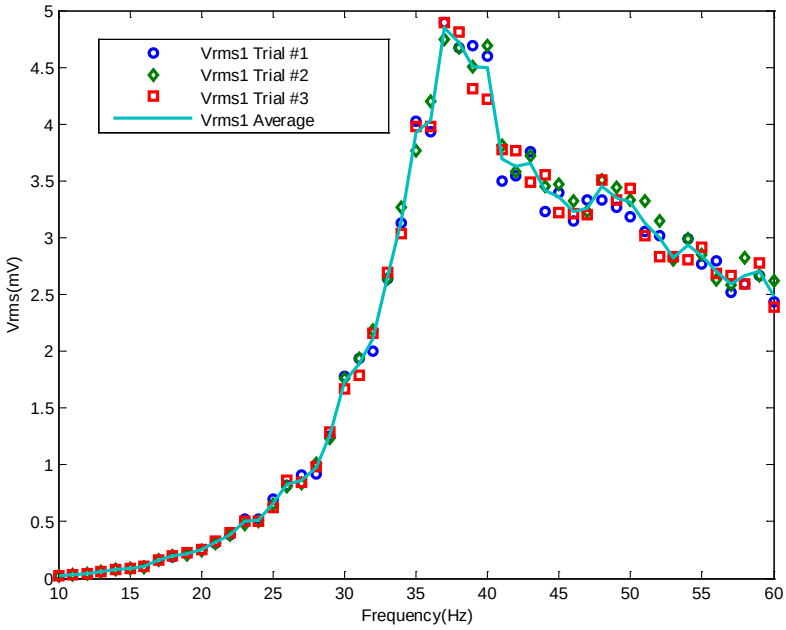

(b)

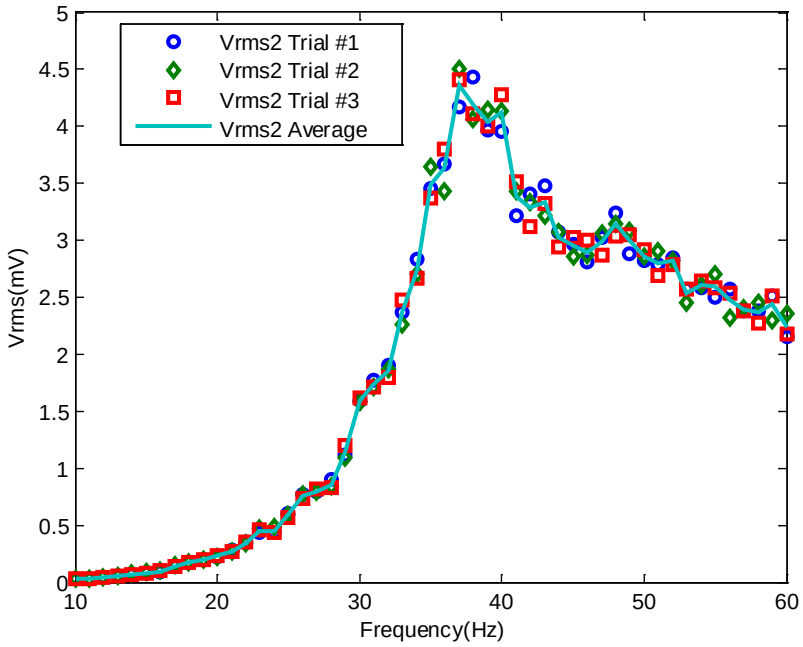


Figure 7.9 2DOF1D EMVEH experimental results - output voltage frequency of (a) top coil and (b) bottom coil.

### 7.6.2 Identifying the key noise parameters and key control parameters from sensitivity analysis

Similar to the SDOF1D EMVEH analysis, the 2DOF1D EMVEH's experimental voltage frequency responses $V_{rms1}$ and $V_{rms2}$ were compared with the sensitivity analyses voltage frequency response curves of the 2DOF1D EMVEH as obtained in Chapter 6. Here too, the damping was very high, due to friction between the coil and the magnet caused by the small clearance between the two from tight tolerances. The equivalent theoretical $M_1$, $M_2$, $D_1$, $D_2$, $D_3$, $K_1$, $K_2$, $K_3$, $R_1$, $R_2$, $L_1$ and $L_2$ values measured and assumed for the equivalent theoretical model are shown in Table 7.3.

Table 7.3 Assumed equivalent theoretical values based on sensitivity analyses.

| Design parameters | Value | Determined by |
|---|---|---|
| Masses ($M_1$, $M_2$) | 0.0015 kg | Measured |
| Damping coefficients ($D_1$, $D_2$, $D_3$) | 0.1 Ns/m | Assumed - based on comparison with sensitivity test data |
| Spring stiffnesses ($K_1$, $K_2$, $K_3$) | 80 N/m | Trade-off between assumed sensitivity data and measured data. |
| Resistances ($R_1$, $R_2$) | 0.3 ohm | Measured |
| Inductance ($L_1$, $L_2$) | 0.016 H | Trade-off between assumed sensitivity data and measured data. |

Hence, the equivalent theoretical voltage frequency response curve obtained using the ODE45 non-linear method is shown in Figure 7.10.

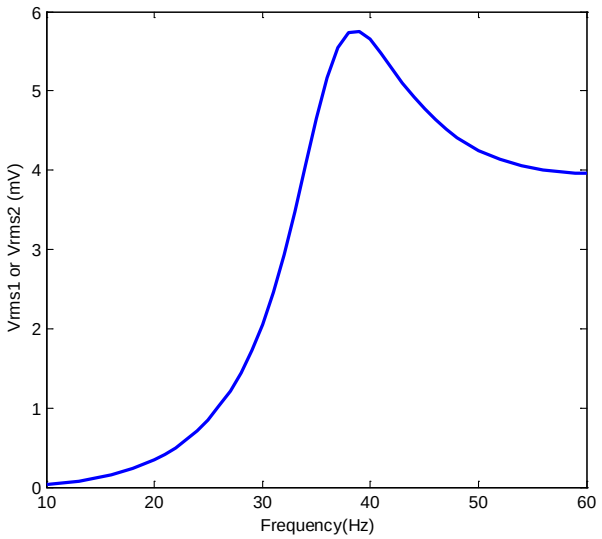


Figure 7.10 Equivalent theoretical voltage frequency response of 2DOF1D EMVEH.

### 7.6.3 Comparison of theoretical and experimental results and model validation

The experimental output voltages were compared with the equivalent theoretical output voltages. The comparison is as shown in Figure 7.11. MATLAB's curve fitting tool was again used to compare the theoretical and experimental voltage outputs at different frequencies. The results of the curve fitting are shown in Figure 7.12. It was observed that the experimental voltages of Coil 1 and Coil 2 were not exactly identical which may be due to

the experimental errors in prototyping. From curve fitness tests performed, as shown in Figure 7.12, it was observed that the experimental voltage was around 0.75 times that of theoretical voltage, with the R-square at 0.98 and root mean square error of about 0.2. The trends of the theoretical and the experimental curves were similar, validating the 2DOF1D EMVEH. Further experimentation is required to reduce the experimental errors.

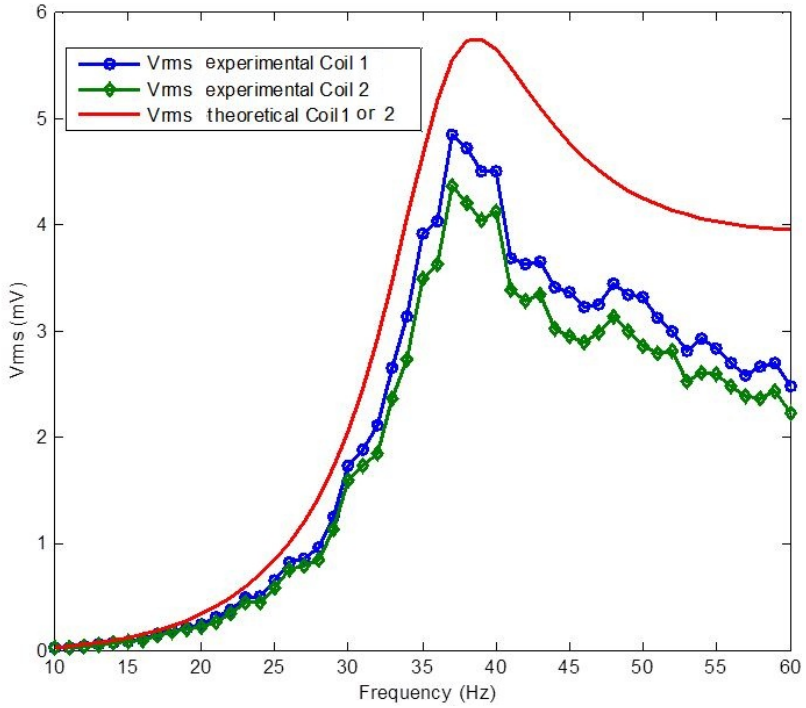


Figure 7.11 Comparison of theoretical and experimental voltage frequency response of 2DOF1D EMVEH.

(a)

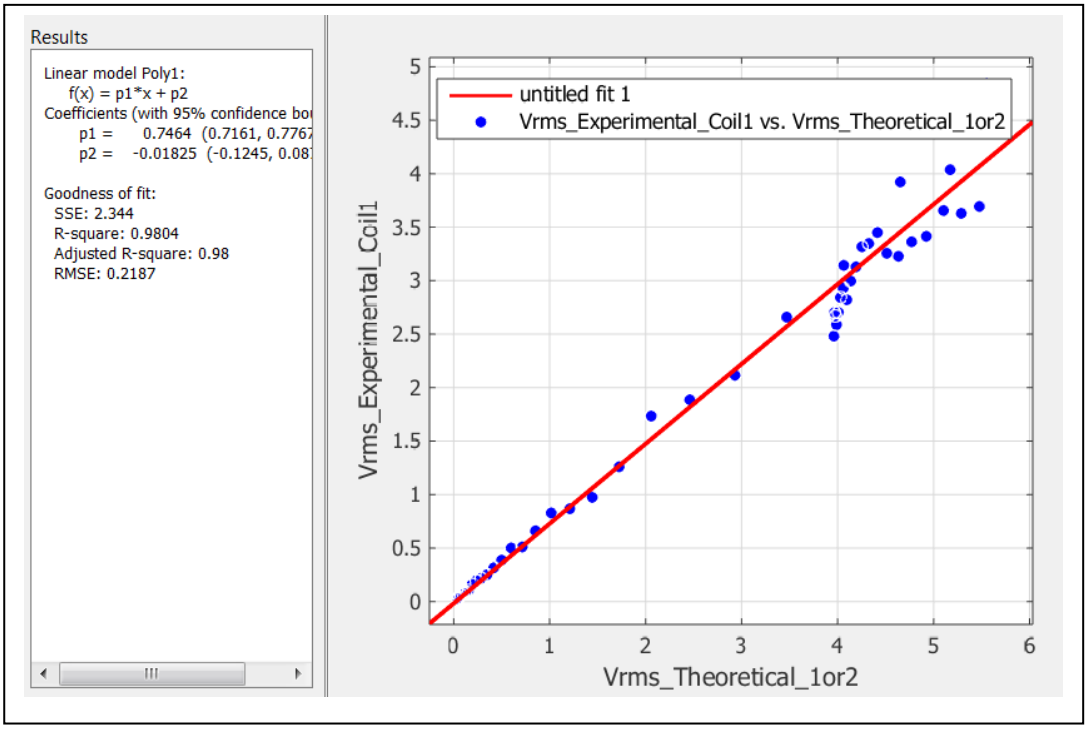

(b)

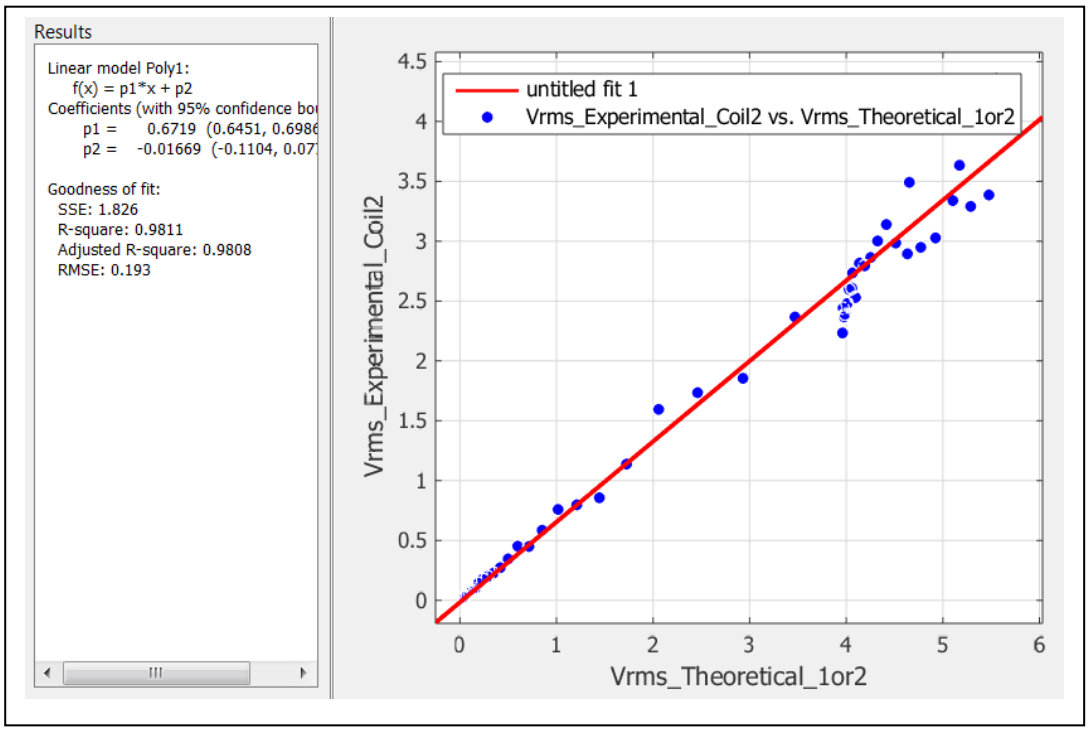


Figure 7.12 Curve fitting test of theoretical RMS voltages (a) Coil 1 and (b) Coil 2 frequency response curves with experimental RMS voltage frequency response of 2DOF1D EMVEH.

## 7.7 Comparison of SDOF1D models and 2DOF1D EMVEH models

From a construction and volume perspective, an SDOF1D EMVEH uses half of the useful parts of 2DOF1D EMVEH. While the SDOF1D EMVEH has only one coil, the 2DOF1D EMVEH has two coils. Therefore it would be fair to compare the power generated by only one coil of 2DOF1D EMVEH with SDOF1D EMVEH. The power characteristics of the SDOF1D EMVEH and the 2DOF1D EMVEH are shown in Figure 7.13.

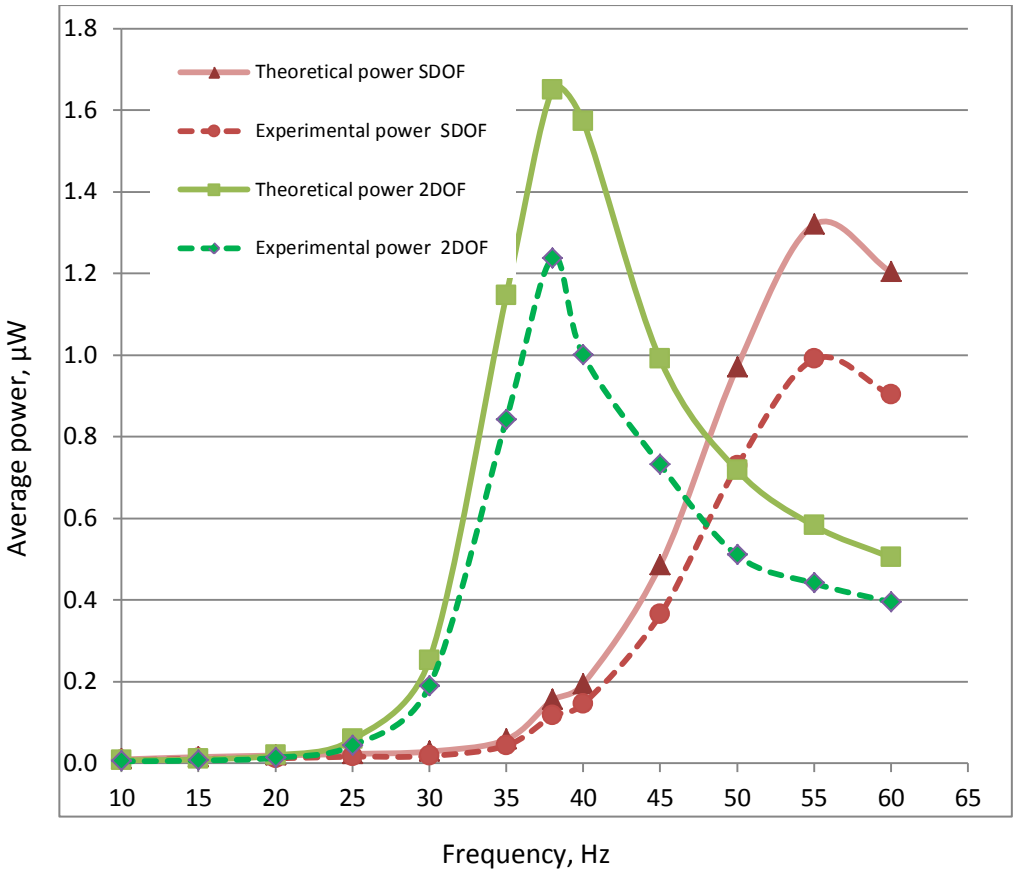


Figure 7.13 Theoretical and experimentally derived power characteristics of SDOF1D EMVEH and 2DOF1D EMVEH models at 0.1 mm amplitude.

It can be observed from Figure 7.13 that the 2DOF1D EMVEH produced more voltage compared to the coil voltage of one coil of the SDOF1D EMVEH both theoretically and experimentally. Also, as per the experiment, the two resonant peaks were not observed on the 2DOF1D EMVEH models. This was obviously because the 2DOF1D EMVEH, having identical spring stiffnesses ($K_1 = K_2 = K_3$) as discussed in the sensitivity analyses of 2DOF1D EMVEH in Chapter 6, was considered to compare it with SDOF1D EMVEH.

If either the top or bottom spring were replaced with a spring of different stiffness to the other two springs, such that $K_1 = K_3 = 80$, $K_2 = 20$, then there would be two resonances, one at 31 Hz and the other at 62 Hz. In order to this the 2DOF1D EMVEH prototype would have required a complete redesign and this was not possible within the time and design constraints of the research. Since the 2DOF1D EMVEH model was already validated, a theoretical comparison of the 2DOF1D EMVEH with different stiffnesses ($K_1 = K_3 = 80$, $K_2 = 20$) and SDOF1D EMVEH was undertaken, as shown in Figure 7.14.

(a)

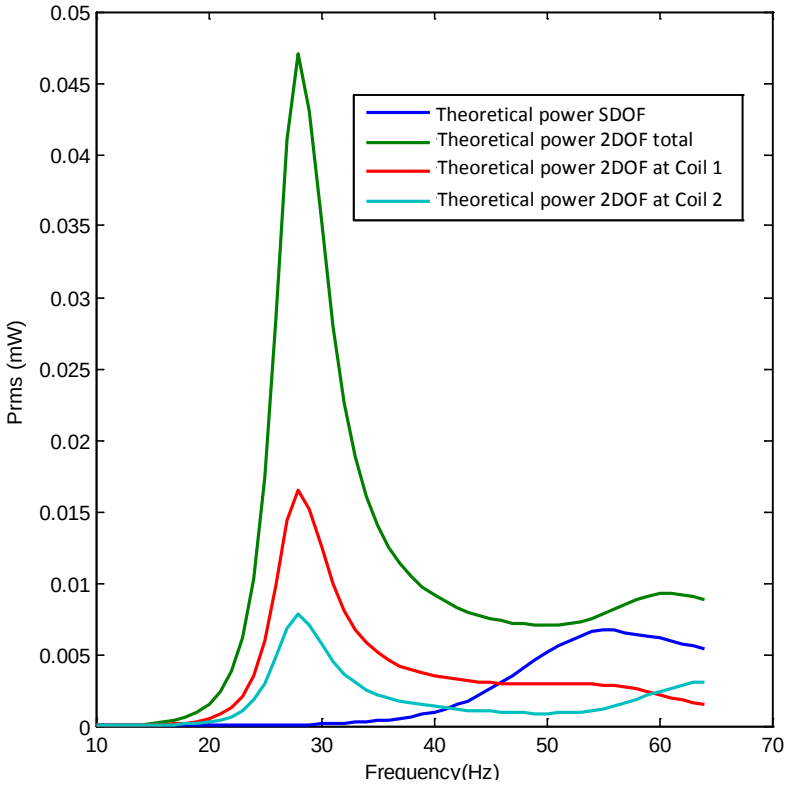


b)

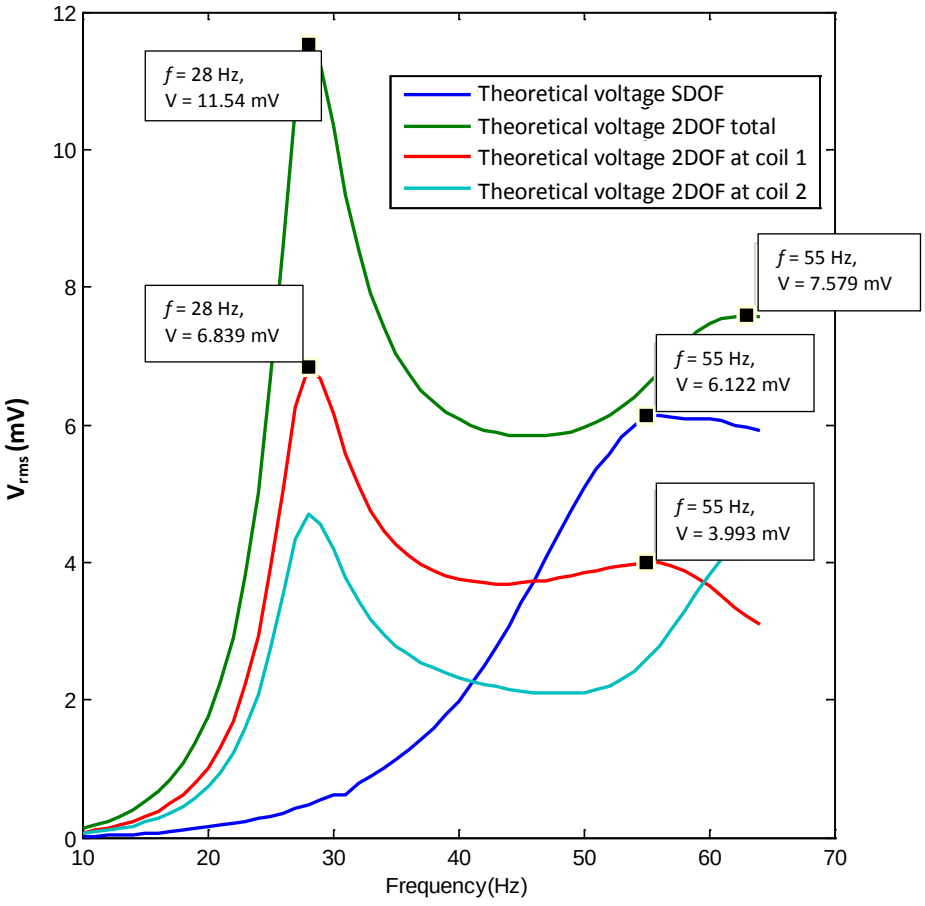


Figure 7.14 Comparison of theoretical power characteristics of SDOF1D and 2DOF1D EMVEHs with different stiffnesses ($K_1 = K_3 = 80$; $K_2 = 20$) (a) Power frequency response. (b) Voltage frequency response at A = 1mm.

From Figure 7.14, it can be observed that a 2DOF1D EMVEH has a broader spectrum response with two resonances, compared to the SDOF1D EMVEH. Figure 7.14 also shows the total voltage and power obtained by adding both voltages in phase with each other. The means of adding the voltages of both the coils with zero phase difference is achievable by suitable voltage regulation. Another means of achieving this voltage regulation is by converting the individual coil voltages of the 2DOF1D EMVEH to DC voltage and adding the DC voltage. The electronic circuit required for adding the individual coil voltages in phase with each other is beyond the scope of this research.

Ideally, the 2DOF1D EMVEH is better than SDOF1D EMVEH in terms of voltage only if the combined voltage of both the coils of 2DOF1D is greater than the twice the voltage of SDOF1D EMVEH. From Fig 7.14 , it was found that the total voltage of both the coils of 2DOF1D was less than twice the voltage of SDOF1D EMVEH at 55 Hz but significant greater than twice the voltage of SDOF1D EMVEH at 31 Hz. This suggests that the only advantage of 2DOF1D EMVEH over the SDOF1D EMVEH is in terms of obtaining a broad range of resonant frequencies for maximum power. In this case, the maximum power of 2DOF1D EMVEH can be obtained at two frequencies 31 Hz and 55 Hz while the SDOF1D EMVEH had maximum power only at 55 Hz. Thus, it is promising for practical applications where both maximum power output per unit volume and broadband resonant frequency based energy harvesters are desired to harvest energy from random industrial vibrations.

## 7.8 Conclusions

The SDOF1D EMVEH and 2DOF1D EMVEH prototypes were designed and developed using ring magnets, coils and circuit elements. An experimental setup was designed and developed to conduct multiple trials on both of these models to obtain the time domain voltage responses at frequencies from 10 Hz to 60 Hz. It was observed that the experimental voltage frequency responses of both SDOF1D and 2DOF1D models showed similar trends to those of the theoretical voltage frequency responses. It was seen that the power generated by a single coil of the 2DOF1D EMVEH was greater than the power generated by the SDOF1D EMVEH due to the resonant behaviour.

The deviations of the theoretical and the experimental voltages can be attributed to experimental errors including (a) the error in assumption of the coupling coefficient, (b) the

error due to neglecting the effect of coil-cylinder contact friction on the damping coefficient, (c) the error due to interference of the flux lines between the magnets, and (d) ambient electromagnetic and vibration interference caused by AC compressors and other devices in the lab. The multiple resonant frequencies were not observed in the operating range of 10 Hz to 60 Hz for the 2DOF1D EMVEH design considered in the experiment. This was due to the use of identical springs. However, the 2DOF1D EMVEH response was shown to be valid since the experimental results were very similar to the theoretical results of 2DOF1D EMVEH with identical spring stiffnesses. Although the alternate design for the 2DOF1D EMVEH with different spring stiffnesses was not possible due to time and resource constraints, it was theoretically validated by having different stiffnesses in the already established 2DOF1D EMVEH. It was observed that 2DOF1D EMVEH with different stiffnesses was beneficial in producing maximum power over a range of frequencies due to its two resonant peaks within the considered operating frequency range.

From this chapter, some important conclusions were established. Firstly the theoretical models of both SDOF1D EMVEH and 2DOF1D EMVEH were valid. However, further experimental controls are necessary to achieve lower deviations from the theoretical values. The mathematical modelling of SDOF1D and 2DOF1D EMVEHs can be further extended to MDOF1D EMVEHs without further experimental validation. Secondly, a 2DOF1D EMVEH was more effective than a SDOF1D EMVEH in terms of generating maximum power. Finally, a 2DOF1D EMVEH with different spring stiffnesses would give more resonant peaks and should be considered in the design of future energy harvesters that target energy harvesting by resonance at multiple frequencies.

# Chapter 8 Theoretical generalisation to multi-degree-of-freedom electromagnetic vibration energy harvesting model (MDOF 1D EMVEH)

In the previous chapter, the 2DOF1D EMVEH system was outlined and discussed in detail, illustrating how it was more beneficial in harnessing vibration energy compared to SDOF1D systems. A 2DOF1D is the most basic form of multi-degree-of-freedom system. However, in the 2DOF1D system, there were only two masses, namely, top mass (top coil) and bottom mass (bottom coil) with both being connected to the base and hence having base excited motion. When a large number of coils are connected in similar fashion, one can find many intermediate masses not directly connected to the base. Hence, the next basic model to be considered is a 4DOF1D system where there are at least two intermediate masses sandwiched between the top and bottom masses, as shown in Figure 8.1.

## 8.1 Research methodology

Initially, a 4DOF1D MDKRL system with four degrees of freedom and one voltage degree of freedom was considered. This represented the generic MDOF1D MDKRL system (since they have intermediate masses unlike the 2DOF1D EMVEH that had only top and bottom coil masses). The differential equations of motion and voltage were derived. These equations were coupled since they had common coupling coefficients. Finally, a coupled matrix equation was formed that represented the 4DOF1D MDKRL system. This was followed by extrapolating the 4DOF1D EMVEH to MDOF1D EMVEH.

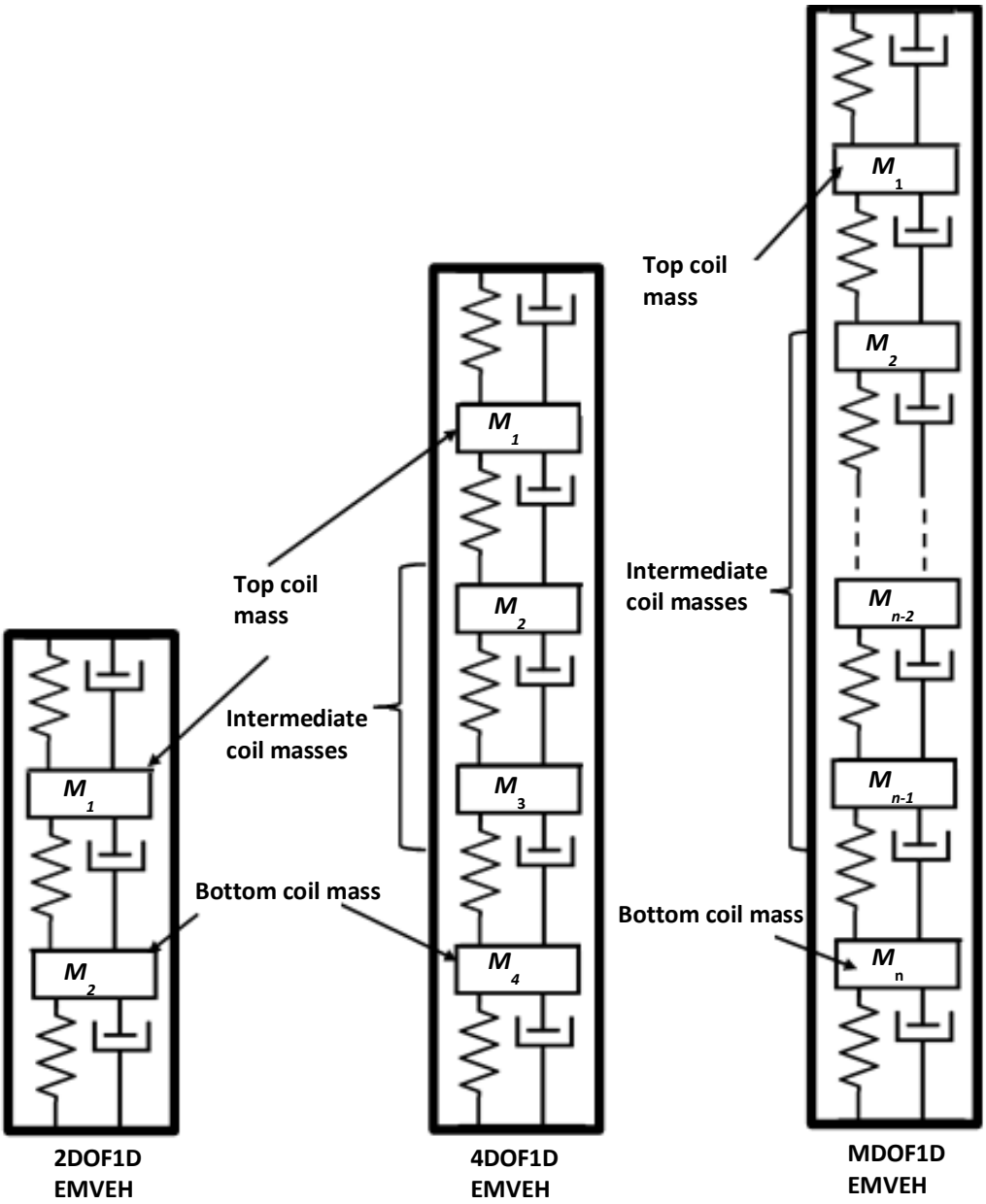


Figure 8.1 General schematic of side by side comparison of 2DOF1D, 4DOF1D and MDOF1D model.

## 8.2 4DOF1D-damped EMVEH model study

A 4DOF1D EMVEH system, as shown in Figure 8.2 was considered. As per Figure 8.2, $M_2$ and $M_3$ are intermediate coils and $M_1$ and $M_4$ represent the top and bottom coils. It was generalised that a MDOF1D system with *n* degrees of freedom could similarly have a top

and bottom coil and (*n* - 2) intermediate coils. The study and derivation of matrix equations for 4DOF1D EMVEH was extrapolated to generalised equations for the MDOF1D system.

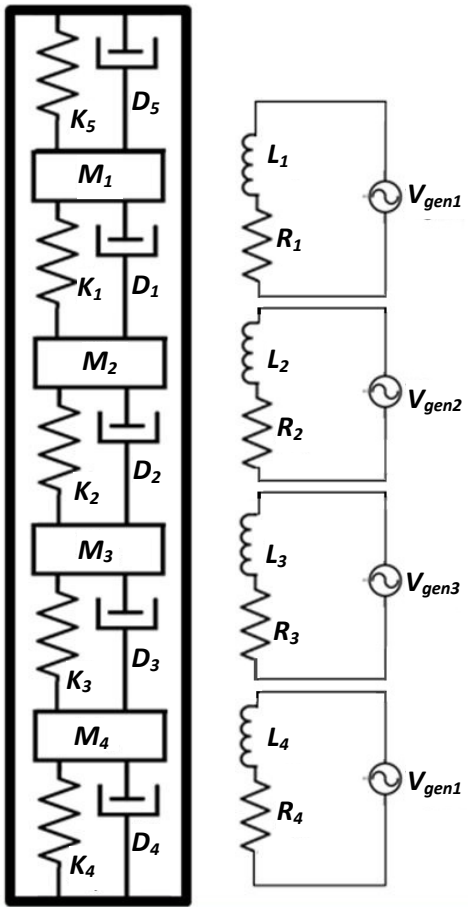


Figure 8.2 4DOF1D MDK-RL EMVEH.

Consider the mechanical part of the 4DOF1D EMVEH. It consists of four masses as shown in Figure 8.3.

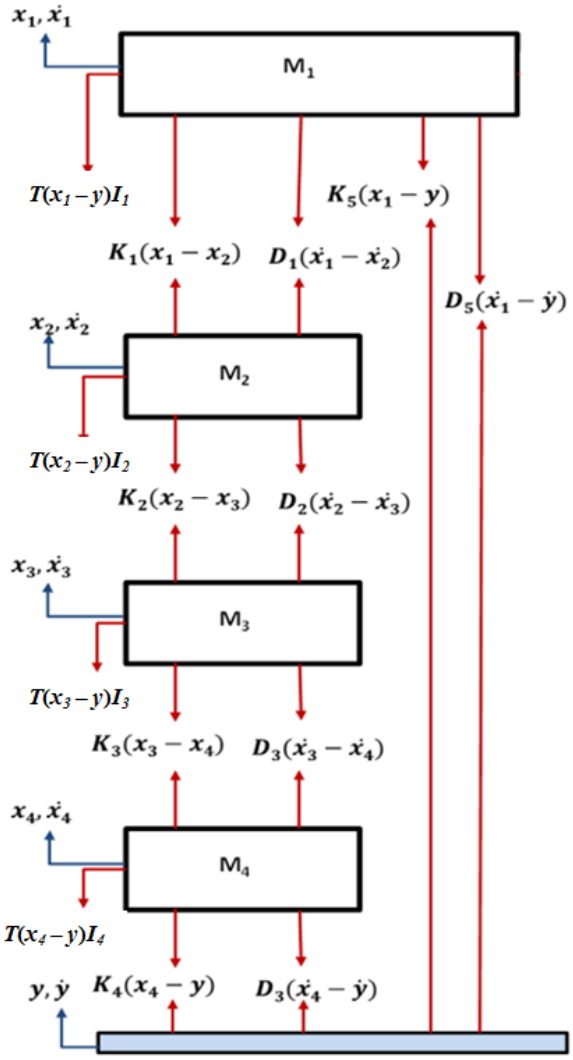


Figure 8.3 Free body diagram of 4DOF1D MDK-RL system.

Applying Newton's second law of motion, the forces at mass $M_1$ become:

$$M_1\ddot{x}_1 = \sum F_{M1}, \tag{8.1}$$

which can be written as:

$$M_1\ddot{x}_1 = -(D_1 + D_5)\dot{x}_1 - (K_1 + K_5)x_1 + D_1\dot{x}_2 + K_1x_2 - T(x_1 - y)I_1 + D_5\dot{y} + K_5y. \tag{8.2}$$

Equation (8.2) can be rearranged as:

$$M_1\ddot{x}_1 + (D_1 + D_5)\dot{x}_1 + (K_1 + K_5)x_1 - D_1\dot{x}_2 - K_1x_2 + T(x_1 - y)I_1 = D_5\dot{y} + K_5y. \tag{8.3}$$

Applying Newton's second law of motion, the forces at mass $M_2$ become:

$$M_2\ddot{x}_2 = \sum F_{M2}. \tag{8.4}$$

This can be written as:

$$M_2\ddot{x}_2 + (D_1 + D_2)\dot{x}_2 + (K_1 + K_2)x_2 - D_2\dot{x}_3 - K_2x_3 - D_1\dot{x}_1 - K_1x_1 + T(x_2 - y)I_2 = 0. \tag{8.5}$$

Similarly, the forces at mass $M_3$ become:

$$M_3\ddot{x}_3 = \sum F_{M3}, \tag{8.6}$$

which can be written as:

$$M_3\ddot{x}_3 + (D_2 + D_3)\dot{x}_3 + (K_2 + K_3)x_3 - D_3\dot{x}_4 - K_3x_4 - D_2\dot{x}_2 - K_2x_2 + T(x_3 - y)I_2 = 0. \tag{8.7}$$

Applying Newton's second law of motion at mass $M_4$ , the forces can be written as:

$$M_4\ddot{x}_4 = \sum F_{M4}, \tag{8.8}$$

which can be written as:

$$M_4\ddot{x}_4 + D_4(\dot{x}_4 - \dot{y}) + K_4(x_4 - y) - D_3(\dot{x}_3 - \dot{x}_4) - K_3(x_3 - x_4) + T(x_4 - y)I_4 = 0. \tag{8.9}$$

Equation (8.9) can be rearranged as:

$$M_4\ddot{x}_4 + D_4\dot{x}_4 + K_4x_4 - D_3(\dot{x}_3 - \dot{x}_4) - K_3(x_3 - x_4) + T(x_4 - y)I_4 = D_4\dot{y} + K_4y. \tag{8.10}$$

Consider each of the four coils having four different RL circuits with resistances $R_1$, $R_2$, $R_3$, $R_4$ and inductances $L_1$, $L_2$, $L_3$, *and* $L_4$ as shown in Figure 8.2.

The voltage generated in circuit 1 consisting of Coil 1 is consumed by its resistance $R_1$ and inductance $L_1$ and is given by:

$$V_{gen1} = T(x_1 - y)(\dot{x}_1 - \dot{y}) = V_{R_1} + V_{L_1} = RI_1 + L\dot{I}_1. \tag{8.11}$$

Similarly, the voltage generated in circuit 2 consisting of Coil 2 is given by:

$$V_{gen2} = T(x_2 - y)(\dot{x}_2 - \dot{y}) = V_{R_2} + V_{L_2} = RI_2 + L\dot{I}_2, \tag{8.12}$$

For circuit 3 consisting of Coil 3 as:

$$V_{gen3} = T(x_3 - y)(\dot{x}_3 - \dot{y}) = V_{R_3} + V_{L_3} = RI_3 + L\dot{I}_3, \tag{8.13}$$

and for circuit 4 consisting of Coil 4 as:

$$V_{gen4} = T(x_4 - y)(\dot{x_4} - \dot{y}) = V_{R_4} + V_{L_4} = RI_4 + L\dot{I_4}. \tag{8.14}$$

The force equations (8.3), (8.5), (8.7) and (8.10) and the voltage equations (8.11 to 8.14) can be written in matrix form as:

$$\begin{bmatrix} M_1 & 0 & 0 & 0 \\ 0 & M_2 & 0 & 0 \\ 0 & 0 & M_3 & 0 \\ 0 & 0 & 0 & M_4 \\ 0 & 0 & 0 & 0 \\ 0 & 0 & 0 & 0 \\ 0 & 0 & 0 & 0 \\ 0 & 0 & 0 & 0 \end{bmatrix} \begin{bmatrix} \ddot{x}_1 \\ \ddot{x}_2 \\ \ddot{x}_3 \\ \ddot{x}_4 \end{bmatrix}$$

$$+ \begin{bmatrix} (D_5 + D_1) & -D_1 & 0 & 0 & 0 & 0 & 0 & 0 \\ -D_1 & (D_1 + D_2) & -D_2 & 0 & 0 & 0 & 0 & 0 \\ 0 & -D_2 & (D_2 + D_3) & -D_3 & 0 & 0 & 0 & 0 \\ 0 & 0 & -D_3 & (D_3 + D_4) & 0 & 0 & 0 & 0 \\ -T(x_1 - y) & 0 & 0 & 0 & L_1 & 0 & 0 & 0 \\ 0 & -T(x_2 - y) & 0 & 0 & 0 & L_1 & 0 & 0 \\ 0 & 0 & -T(x_3 - y) & 0 & 0 & 0 & L_1 & 0 \\ 0 & 0 & 0 & -T(x_4 - y) & 0 & 0 & 0 & L_1 \end{bmatrix} \begin{bmatrix} \dot{x}_1 \\ \dot{x}_2 \\ \dot{x}_3 \\ \dot{x}_4 \\ \dot{I}_1 \\ \dot{I}_2 \\ \dot{I}_3 \\ \dot{I}_4 \end{bmatrix}$$

$$+ \begin{bmatrix} (K_5 + K_1) & -K_1 & 0 & 0 & T(x_1 - y) & 0 & 0 & 0 \\ -K_1 & (K_1 + K_2) & -K_2 & 0 & 0 & T(x_2 - y) & 0 & 0 \\ 0 & -K_2 & (K_2 + K_3) & -K_3 & 0 & 0 & T(x_3 - y) & 0 \\ 0 & 0 & -K_3 & (K_3 + K_4) & 0 & 0 & 0 & T(x_4 - y) \\ 0 & 0 & 0 & 0 & R_1 & 0 & 0 & 0 \\ 0 & 0 & 0 & 0 & 0 & R_2 & 0 & 0 \\ 0 & 0 & 0 & 0 & 0 & 0 & R_3 & 0 \\ 0 & 0 & 0 & 0 & 0 & 0 & 0 & R_4 \end{bmatrix} \begin{bmatrix} x_1 \\ x_2 \\ x_3 \\ x_4 \\ I_1 \\ I_2 \\ I_3 \\ I_4 \end{bmatrix}$$

$$= \begin{bmatrix} D_5 & K_5 \\ 0 & 0 \\ 0 & 0 \\ D_4 & K_4 \\ -T(x_1 - y) & 0 \\ -T(x_2 - y) & 0 \\ -T(x_3 - y) & 0 \\ -T(x_4 - y) & 0 \end{bmatrix} \begin{bmatrix} \dot{y} \\ y \end{bmatrix}. \tag{8.15}$$

This is the coupled equation system for 4DOF1D EMVEH.

## 8.3 Solutions to 4DOF1D MDKRL EMVEH model

Similar to the solution methods for the SDOF1D and the 2DOF1D EMVEHs discussed in Chapter 4 and Chapter 6, the approximate linear methods of Laplace transforms and state space analyses were initially employed, neglecting the spatial variation of the magnetic

field. This was followed by the more accurate non-linear ODE solver to obtain the time domain responses.

It should be noted that the coupling coefficient is considered to be constant by neglecting the spatial variation and is equal to $2\pi nrB_{max}$.

### 8.3.1 Laplace transforms analysis of 4DOF1D MDKRL EMVEH system

Equation (8.15) can be rewritten by applying Laplace transforms using the Laplace operator $s = j\omega$ as:

$$\begin{bmatrix} a_{11}(s) & -D_1s-K_1 & 0 & 0 & T & 0 & 0 & 0 \\ -D_1s-K_1 & a_{22}(s) & -D_2s-K_2 & 0 & 0 & T & 0 & 0 \\ 0 & -D_2s-K_2 & a_{33}(s) & -D_3s-K_3 & 0 & 0 & T & 0 \\ 0 & 0 & -D_3s-K_3 & a_{44}(s) & 0 & 0 & 0 & T \\ -Ts & 0 & 0 & 0 & a_{55}(s) & 0 & 0 & 0 \\ 0 & -Ts & 0 & 0 & 0 & a_{66}(s) & 0 & 0 \\ 0 & 0 & -Ts & 0 & 0 & 0 & a_{77}(s) & 0 \\ 0 & 0 & 0 & -Ts & 0 & 0 & 0 & a_{88}(s) \end{bmatrix} \begin{bmatrix} X_1(s) \\ X_2(s) \\ X_3(s) \\ X_4(s) \\ I_1(s) \\ I_2(s) \\ I_3(s) \\ I_4(s) \end{bmatrix} = \begin{bmatrix} D_5s+K_5 \\ 0 \\ 0 \\ D_4s+K_4 \\ -Ts \\ -Ts \\ -Ts \\ -Ts \end{bmatrix} [y], \quad (8.16)$$

where the diagonal elements are $a_{11}(s) = M_1s^2+(D_5+D_1)s+(K_5+K_1)$, $a_{22}(s) = M_2s^2+(D_1+D_2)s+(K_1+K_2)$, $a_{33}(s) = M_3s^2+(D_2+D_3)s+(K_2+K_3)$,

$a_{44}(s) = M_4s^2+ (D_3+D_4)\ s+ (K_3+K_4)$, $a_{55}(s) = L_1s+R_1$, $a_{66}(s) = L_2s+R_2$, $a_{77}(s) = L_3s+R_3$ *and* $a_{88}(s) = L_4s+R_4$ respectively.

Equation (8.16) is of the form:

$$[A][\alpha] = [B][\beta].$$

Rearranging the equation gives:

$$\frac{[\alpha]}{[\beta]} = [A^{-1}][B].$$

where,

$$A = \begin{bmatrix} a_{11}(s) & \cdots & 0 \\ \vdots & \ddots & \vdots \\ 0 & \cdots & a_{88}(s) \end{bmatrix}, \alpha = \begin{bmatrix} X_1(s) \\ \vdots \\ I_4(s) \end{bmatrix}, B = \begin{bmatrix} D_5s+K_5 \\ \vdots \\ -Ts \end{bmatrix} \text{ and } \beta = [y].$$

The transfer function matrix is then given by:

$$G(s) = \frac{[\alpha]}{[\beta]} = \begin{bmatrix} \frac{X_1(s)}{Y(s)} \\ \frac{X_2(s)}{Y(s)} \\ \frac{X_3(s)}{Y(s)} \\ \frac{X_4(s)}{Y(s)} \\ \frac{I_1(s)}{y(s)} \\ \frac{I_2(s)}{y(s)} \\ \frac{I_3(s)}{y(s)} \\ \frac{I_4(s)}{y(s)} \end{bmatrix} = \begin{bmatrix} G_1(s) \\ G_2(s) \\ G_3(s) \\ G_4(s) \\ H_1(s) \\ H_2(s) \\ H_3(s) \\ H_4(s) \end{bmatrix} = A^{-1}B. \tag{8.17}$$

There are eight useful transfer functions of interest with four displacement transfer functions $G_1(s)$ to $G_4(s)$ and the four current transfer functions $H_1(s)$ to $H_4(s)$.

MATLAB software was written to yield results (see Appendix B for MATLAB code) using the following realistic design values of: $M_{1,2,3,4}$ = 0.0015 kg, $D_{1,2,3,4,5}$ = 0.05 Ns/m, $K_{1,2,3,4,5}$ = 80 N/m, $R_{1,2,3,4,5}$ = 0.3 ohm and $L_{1,2,3,4,5}$ = 0.0016 H. The results of this simulation are given in Figure 8.4(a). It was found that there were only two resonances of interest at 28 Hz and 61 Hz. The transfer functions $X_1/Y$ and $X_2/Y$ were similar in form to each other and so were $X_3/Y$ and $X_4/Y$. Correspondingly, the transfer functions $I_1/Y$ and $I_2/Y$ were also of similar form to each other and so were $I_3/Y$ and $I_4/Y$.

Another Laplace simulation was run by changing the individual mechanical resonances by assigning different spring stiffnesses, $K_1$ = 20 N/m, $K_2$ = 40 N/m, $K_3$ = 60 N/m, $K_4$ = 80 N/m, $K_5$ = 110 N/m. The resulting Laplace transform frequency response is shown in Figure 8.4(b). It was observed that there were four resonance peaks of interest compared to the two resonant peaks with identical mechanical resonances. This indicates that by having different mechanical stiffnesses or even inertial masses, one can obtain a higher number of resonant peaks thus widening the energy harvester bandwidth of operation.

(a)

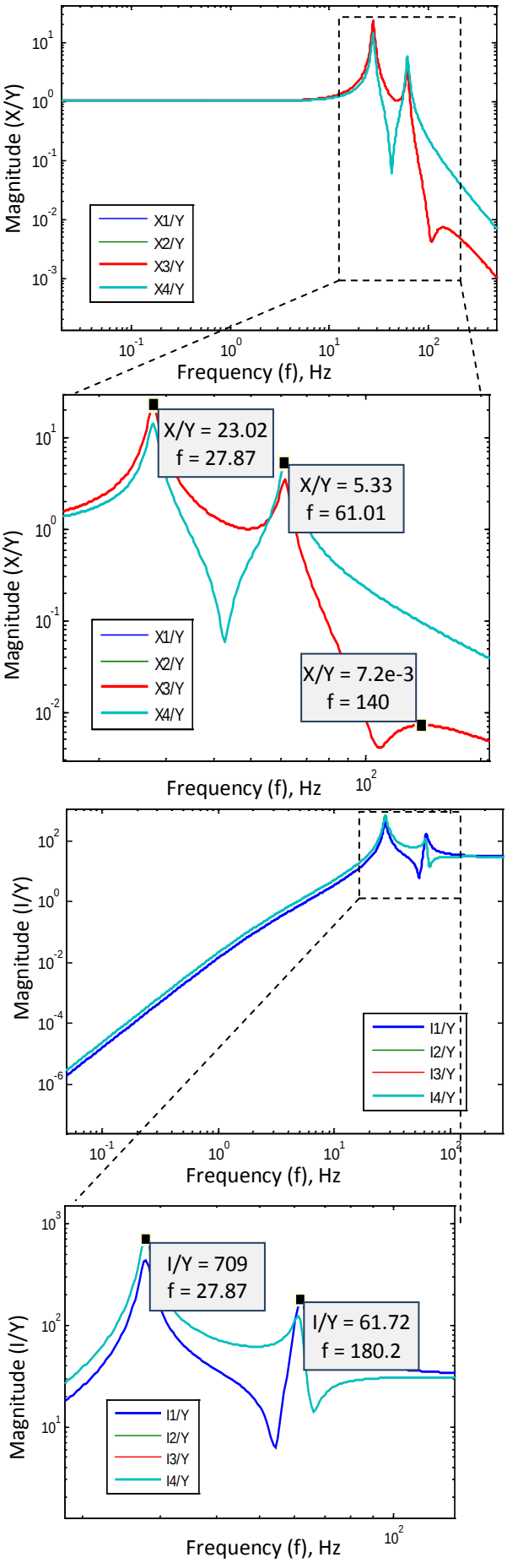
Magnitude (X/Y)
Frequency (f), Hz
X1/Y
X2/Y
X3/Y
X4/Y
X/Y = 23.02
f = 27.87
X/Y = 5.33
f = 61.01
X/Y = 7.2e-3
f = 140
Magnitude (I/Y)
I1/Y
I2/Y
I3/Y
I4/Y
I/Y = 709
f = 27.87
I/Y = 61.72
f = 180.2

(b)

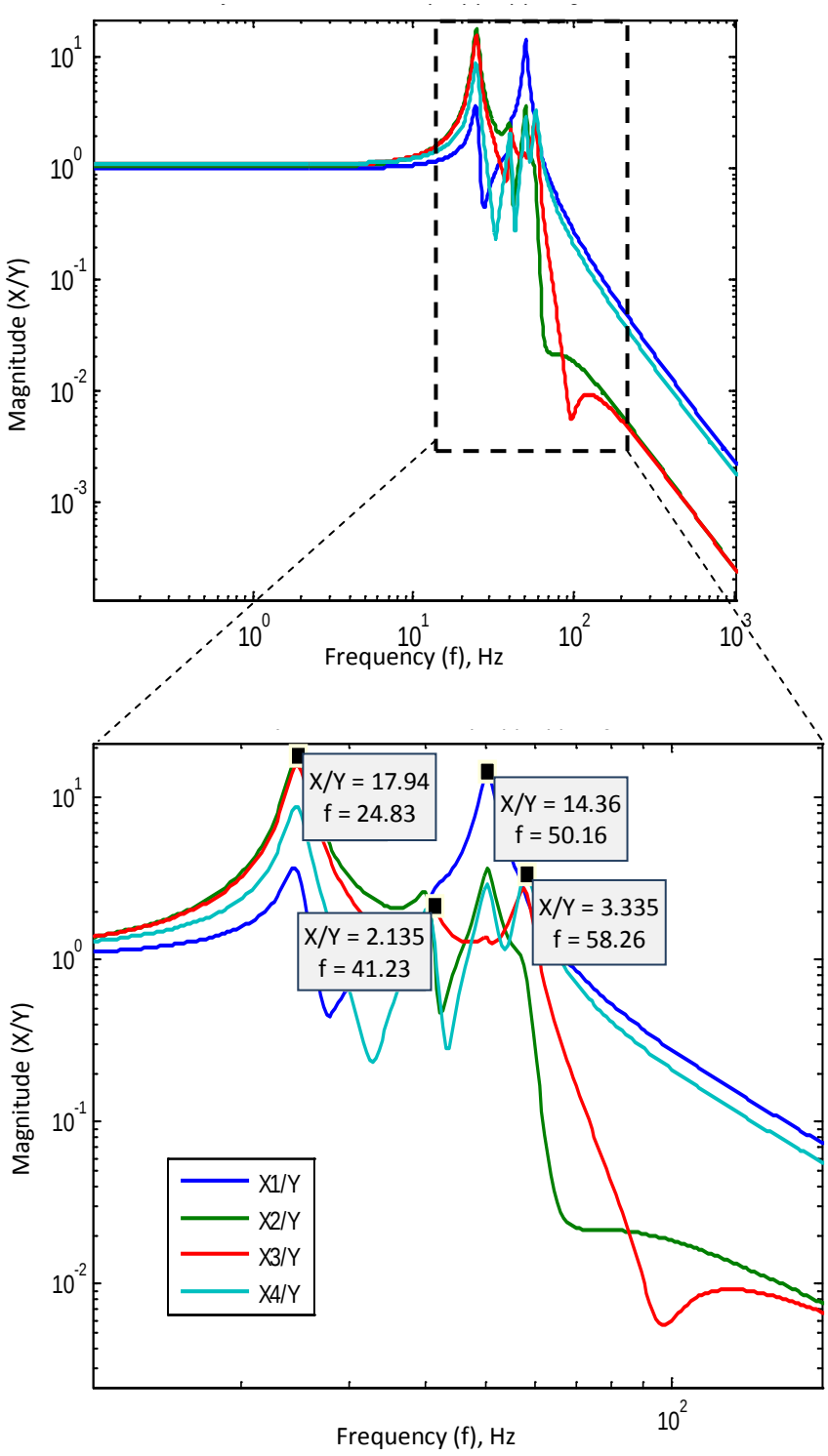
Magnitude (X/Y)
Frequency (f), Hz
X/Y = 17.94
f = 24.83
X/Y = 14.36
f = 50.16
X/Y = 3.335
f = 58.26
X/Y = 2.135
f = 41.23
X1/Y
X2/Y
X3/Y
X4/Y

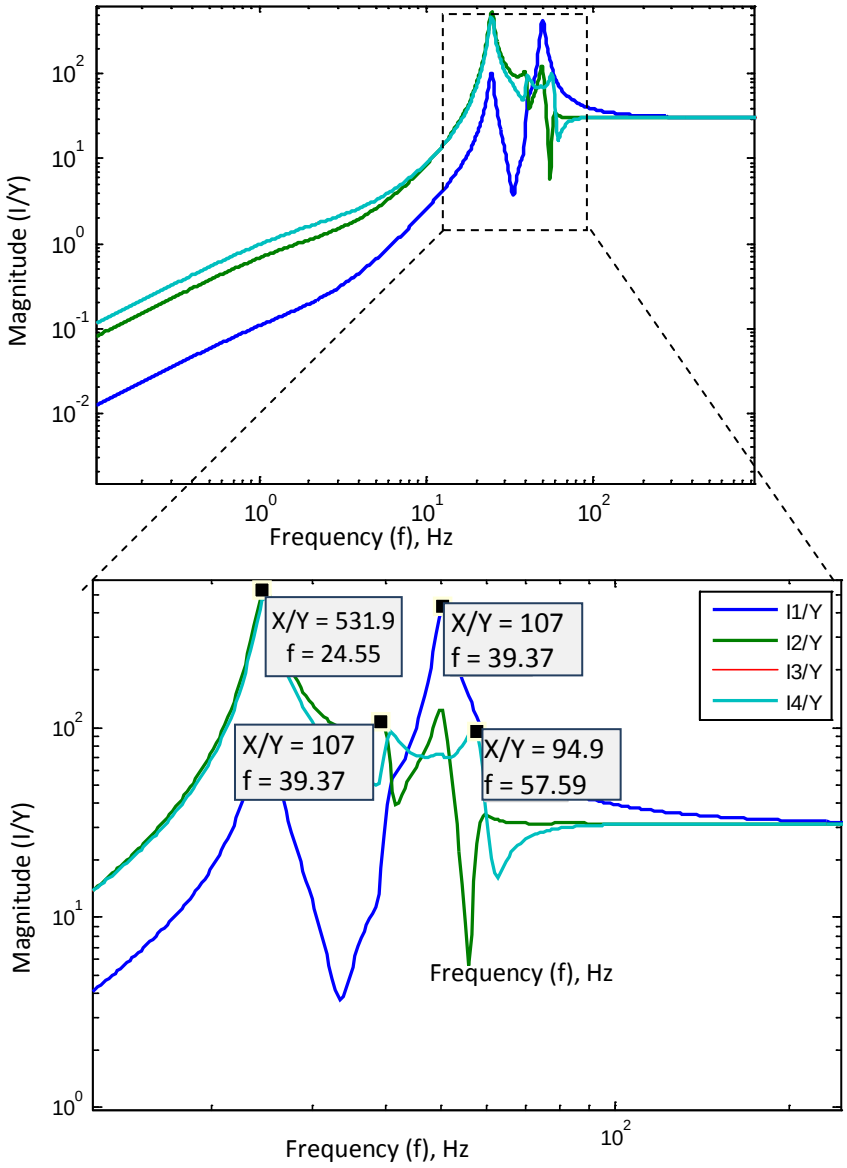


Figure 8.4 Frequency response functions of 4DOF1D EMVEH system – (a) with identical spring stiffnesses ($K_1 = K_2 = K_3 = K_4 = K_5$), (b) with different spring stiffnesses. All transfer functions are in SI units.

It can be observed from Figure 8.4(a) that with identical spring stiffnesses, the entire four spring mass systems exhibited only two resonant peaks owing to their identical mechanical design parameters that constituted their individual mechanical resonances. Hence, the spring stiffnesses were changed to observe different resonant peaks, as shown in Figure 8.4(b). Although the first resonance for all the four coils of different MDKs were the same, the second resonant peaks were different, thus enhancing the broadband power harvesting capability. Unlike the 2DOF1D which had only two resonant peaks, the 4DOF1D can have

four resonant peaks. A careful design optimisation is necessary to ascertain the combinations of MDK values of individual coils, such that multiple resonant peaks can be achievable within the operating frequency range.

### 8.3.2 Linear state space transform for 4DOF1D MDKRL EMVEH system

State space variables can be used to solve equation (8.15). State space variables can be defined as:

$$V_1 = x_{1,} \tag{8.18}$$

$$V_2 = \dot{x}_1 = \frac{dV_1}{dt}, \tag{8.19}$$

$$V_3 = x_{2,} \tag{8.20}$$

$$V_4 = \frac{dV_3}{dt} = \dot{x_{2,}} \tag{8.21}$$

$$V_5 = x_{3,} \tag{8.22}$$

$$V_6 = \dot{x}_3 = \frac{dV_5}{dt}, \tag{8.23}$$

$$V_7 = x_{4,} \tag{8.24}$$

$$V_8 = \frac{dV_7}{dt} = \dot{x_{4,}} \tag{8.25}$$

$$V_9 = I_1, \tag{8.26}$$

$$\dot{I_1} = \frac{dV_9}{dt}, \tag{8.27}$$

$$V_{10} = I_2, \tag{8.28}$$

$$\dot{I_2} = \frac{dV_{10}}{dt}, \tag{8.29}$$

$$V_{11} = I_3, \tag{8.30}$$

$$\dot{I_3} = \frac{dV_{11}}{dt}, \tag{8.31}$$

$$V_{12} = I_4, \tag{8.32}$$

$$\dot{I_4} = \frac{dV_{12}}{dt}. \tag{8.33}$$

From equations (8.19) and (8.21):

$$\ddot{x}_1 = \frac{dV_2}{dt} = \frac{D_5}{M_1}\dot{y} + \frac{K_5}{M_1}y - \frac{(D_5 + D_1)}{M_1}V_2 - \frac{(K_5 + K_1)}{M_1}V_1 + \frac{D_1}{M_1}V_4 + \frac{K_1}{M_1}V_3 - \frac{T}{M_1}V_9 \tag{8.34}$$

$$\ddot{x}_2 = \frac{dV_2}{dt} = -\frac{(D_1 + D_2)}{M_2}V_4 - \frac{(K_1 + K_2)}{M_2}V_3 + \frac{D_2}{M_2}V_6 + \frac{K_2}{M_2}V_5 + \frac{D_1}{M_2}V_2 + \frac{K_1}{M_2}V_1 - \frac{T}{M_2}V_{10}, \tag{8.35}$$

From equation (8.23):

$$\ddot{x}_3 = \frac{dV_3}{dt} = -\frac{(D_2 + D_3)}{M_3}V_6 - \frac{(K_2 + K_3)}{M_2}V_5 + \frac{D_3}{M_3}V_8 + \frac{K_3}{M_3}V_7 + \frac{D_2}{M_3}V_4 + \frac{K_2}{M_3}V_3 - \frac{T}{M_3}V_{11}. \tag{8.36}$$

From equation (8.25):

$$\ddot{x}_4 = \frac{dV_4}{dt} = \frac{D_4}{M_4}\dot{y} + \frac{K_4}{M_4}y - \frac{(D_3 + D_4)}{M_4}V_8 - \frac{(K_3 + K_4)}{M_4}V_7 + \frac{D_3}{M_4}V_6 + \frac{K_3}{M_4}V_5 - \frac{T}{M_4}V_{12}. \tag{8.37}$$

Similarly, $\dot{I}_1, \dot{I}_2, \dot{I}_3$ , $\dot{I}_4$ can also be written as:

$$\dot{I}_1 = \frac{dV_9}{dt} = \frac{T}{L_1}V_2 - \frac{T}{L_1}\dot{Y} - \frac{R_1}{L_1}V_9, \tag{8.38}$$

$$\dot{I}_2 = \frac{dV_{10}}{dt} = \frac{T}{L_2}V_4 - \frac{T}{L_2}\dot{Y} - \frac{R_2}{L_2}V_{10}, \tag{8.39}$$

$$\dot{I}_3 = \frac{dV_{11}}{dt} = \frac{T}{L_3}V_6 - \frac{T}{L_3}\dot{Y} - \frac{R_3}{L_3}V_{11}, \tag{8.40}$$

and $$\dot{I}_4 = \frac{dV_{12}}{dt} = \frac{T}{L_4}V_8 - \frac{T}{L_4}\dot{Y} - \frac{R_4}{L_4}V_{12}. \tag{8.41}$$

Thus in matrix form:

$$[d] = [D_1][V] + [D_2][Y], \tag{8.42}$$

where

$$[d] = \begin{bmatrix} \frac{dV_1}{dt} \\ \vdots \\ \frac{dV_{12}}{dt} \end{bmatrix}, [V] = \begin{bmatrix} V_1 \\ \vdots \\ V_{12} \end{bmatrix}, [Y] = \begin{bmatrix} \dot{y} \\ y \end{bmatrix},$$

which can be expanded as:

$$[D_1] = \begin{bmatrix} 0 & 1 & 0 & 0 & 0 & 0 & 0 & 0 & 0 & 0 & 0 & 0 \\ \frac{-(K_5+K_1)}{M_1} & \frac{-(D_5+D_1)}{M_1} & \frac{K_1}{M_1} & \frac{D_1}{M_1} & 0 & 0 & 0 & 0 & \frac{-T}{M_1} & 0 & 0 & 0 \\ 0 & 0 & 0 & 1 & 0 & 0 & 0 & 0 & 0 & 0 & 0 & 0 \\ \frac{K_1}{M_2} & \frac{D_1}{M_2} & \frac{-(K_1+K_2)}{M_2} & \frac{-(D_1+D_2)}{M_2} & \frac{K_2}{M_2} & \frac{D_2}{M_2} & 0 & 0 & 0 & \frac{-T}{M_2} & 0 & 0 \\ 0 & 0 & 0 & 0 & 0 & 1 & 0 & 0 & 0 & 0 & 0 & 0 \\ 0 & 0 & \frac{K_2}{M_3} & \frac{D_2}{M_3} & \frac{-(K_2+K_3)}{M_3} & \frac{-(D_2+D_3)}{M_3} & \frac{K_3}{M_3} & \frac{D_3}{M_3} & 0 & 0 & \frac{-T}{M_3} & 0 \\ 0 & 0 & 0 & 0 & 0 & 0 & 0 & 1 & 0 & 0 & 0 & 0 \\ 0 & 0 & 0 & 0 & \frac{K_3}{M_4} & \frac{D_3}{M_4} & \frac{-(K_3+K_4)}{M_4} & \frac{-(D_3+D_4)}{M_4} & 0 & 0 & 0 & \frac{-T}{M_4} \\ 0 & \frac{T}{L_1} & 0 & 0 & 0 & 0 & 0 & 0 & \frac{-R_1}{L_1} & 0 & 0 & 0 \\ 0 & 0 & 0 & \frac{T}{L_2} & 0 & 0 & 0 & 0 & 0 & \frac{-R_2}{L_2} & 0 & 0 \\ 0 & 0 & 0 & 0 & 0 & \frac{T}{L_3} & 0 & 0 & 0 & 0 & \frac{-R_3}{L_3} & 0 \\ 0 & 0 & 0 & 0 & 0 & 0 & 0 & \frac{T}{L_4} & 0 & 0 & 0 & \frac{-R_4}{L_4} \end{bmatrix},$$

and,

$$[D_2] = \begin{bmatrix} \frac{D_5}{M_1} & \frac{K_5}{M_1} \\ 0 & 0 \\ 0 & 0 \\ \frac{D_4}{M_4} & \frac{D_4}{M_4} \\ \frac{T}{L_1} & 0 \\ \frac{T}{L_2} & 0 \\ \frac{T}{L_3} & 0 \\ \frac{T}{L_4} & 0 \end{bmatrix}.$$

A theoretical simulation was run to yield the following results (see Appendix B for MATLAB code) using the following realistic values: $M_{1,2,3,4}$ = 0.0015 kg, $D_{1,2,3,4,5}$ = 0.05 Ns/m, $K_{1,2,3,4,5}$ = 80 N/m, $R_{1,2,3,4}$ = 0.300 ohm, $L_{1,2,3,4}$ = 0.016 H and T = 0.492 Tm . The results of the analysis are shown in Figure 8.5.

The eigen values were obtained and their corresponding resonant frequencies for maximum power are shown in Table 8.1. It can be observed that the resonant frequencies of the state space solution are identical to the resonant frequencies peaks observed in the Laplace transform, thus confirming the state space results to be valid.

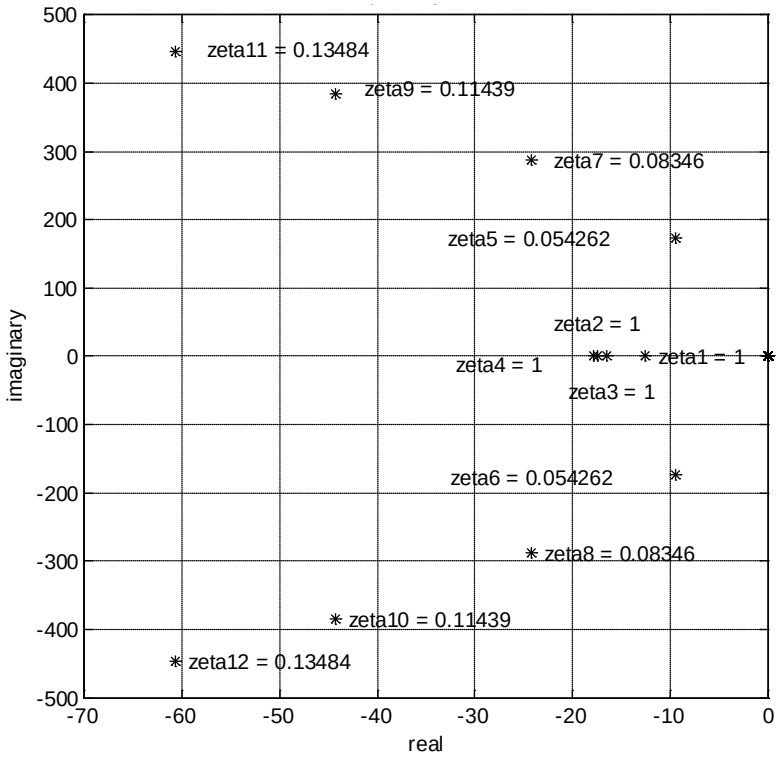


Figure 8.5 Eigenvalues of 4DOF1D MDKRL from state-space analysis with identical spring stiffnesses.

Table 8.1 Eigenvalues and derived resonant frequencies from state-space analysis of 4DOF1D MDKRL EMVEH with identical spring stiffnesses.

| Eigenvalue ($\lambda_i$) | Resonant frequency | |
|---|---|---|
| | ($\omega_i$ in rad/s) | ($f_i$ in Hz) |
| -12.55 + 0i | 12.55 | 2.00 |
| -16.48 + 0i | 16.48 | 2.62 |
| -17.48 + 0i | 17.48 | 2.78 |
| -17.81+ 0i | 17.81 | 2.83 |
| -9.47 + 174.22i | 174.48 | 27.77 |
| -9.47 - 174.22i | 174.48 | 27.77 |
| -24.17 + 288.54i | 289.55 | 46.08 |
| -24.17 - 288.54i | 289.55 | 46.08 |
| -44.27 + 384.48i | 387.02 | 61.60 |
| -44.27 - 384.48i | 387.02 | 61.60 |
| -60.77 + 446.58i | 450.7 | 71.73 |
| -60.77 - 446.58i | 450.7 | 71.73 |

Another Laplace simulation was run by changing the individual mechanical resonances by assigning different spring stiffnesses, $K_1$ = 20 N/m, $K_2$ = 40 N/m, $K_3$ = 60 N/m, $K_4$ = 80 N/m, $K_5$ = 110 N/m. The eigen values obtained and their corresponding resonant frequencies for maximum power are shown in Table 8.2. It can be observed that the resonant frequencies from state space analysis were close to the resonant frequencies observed from the Laplace transform, thus confirming the state space results to be valid. The closeness of the values with the Laplace transform results also validates the 4DOF1D EMVEH model.

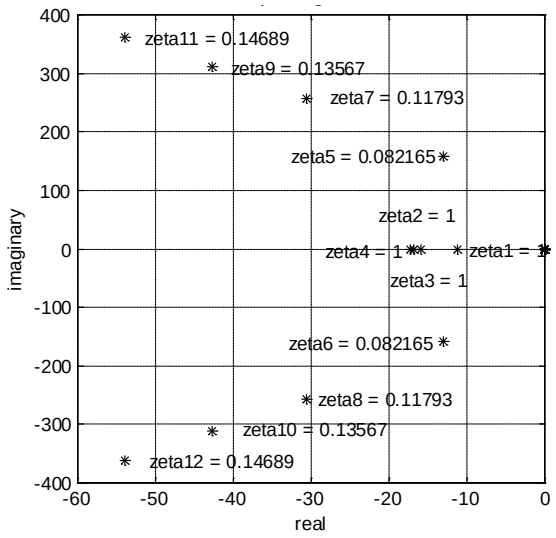


Figure 8.6 Eigenvalues of 4DOF1D MDKRL from state-space analysis with different spring stiffnesses.

Table 8.2 Eigenvalues and derived resonant frequencies from state-space analysis of 4DOF1D MDKRL EMVEH with different spring stiffnesses.

| **Eigenvalue ($\lambda_i$)** | **Resonant frequency** | |
|---|---|---|
| | **($\omega_i$ in rad/s)** | **($f_i$ in Hz)** |
| -11.15 + 0i | 11.16 | 1.78 |
| -15.86+ 0.0i | 15.87 | 2.53 |
| -16.84 + 0i | 16.85 | 2.68 |
| -17.34 + 0i | 17.34 | 2.76 |
| -5.6+ 157.27i | 158.63 | 25.25 |
| -5.6 - 157.27i | 158.63 | 25.25 |
| -7.02 + 256.07i | 259.36 | 41.28 |
| -7.02 - 256.07i | 259.36 | 41.28 |
| -9.6 + 307.07i | 314.81 | 50.10 |
| -9.6 - 307.07i | 314.81 | 50.10 |
| -11.37 + 367.8i | 366.92 | 58.40 |
| -11.37 - 367.8i | 366.92 | 58.40 |

### 8.3.3 Nonlinear ODE45 4DOF1D MDK-RL EMVEH analysis

When the spatial variation of the magnetic field is considered in the 4DOF1D EMVEH system, the coupling coefficients are no longer assumed to be constant, but they are functions of the displacement. Hence the coupling coefficients considered are $T(x_1 - y)$ , $T(x_2 - y)$, $T(x_3 - y)$ and $T(x_4 - y)$ that are functions of displacements $x_1$, $x_2$, $x_3$ and $x_4$ respectively .

Consider the following state variables and state derivatives:

$$Z(1) = x_{1,} \tag{8.43}$$

$$Z(2) = \dot{x}_1 = \frac{dZ(1)}{dt}, \tag{8.44}$$

$$Z(3) = x_{2,} \tag{8.45}$$

$$Z(4) = \frac{dZ(3)}{dt} = \dot{x_{2,}} \tag{8.46}$$

$$Z(5) = x_{3,} \tag{8.47}$$

$$Z(6) = \dot{x}_3 = \frac{dZ(5)}{dt}, \tag{8.48}$$

$$Z(7) = x_{4,} \tag{8.49}$$

$$Z(8) = \frac{dZ(7)}{dt} = \dot{x_{4,}} \tag{8.50}$$

$$Z(9) = I_1, \tag{8.51}$$

$$\dot{I}_1 = \frac{dZ(9)}{dt}, \tag{8.52}$$

$$Z(10) = I_2, \tag{8.53}$$

$$\dot{I}_2 = \frac{dZ(10)}{dt}. \tag{8.54}$$

$$Z(11) = I_3, \tag{8.55}$$

$$\dot{I}_3 = \frac{dZ(11)}{dt}. \tag{8.56}$$

$$Z(12) = I_4, \tag{8.57}$$

$$\dot{I}_4 = \frac{dZ(12)}{dt}. \tag{8.58}$$

From equations (8.44) and (8.46), the state variables become:

$$\ddot{x}_1 = \frac{dZ(2)}{dt} = \frac{D_5}{M_1}\dot{y} + \frac{K_5}{M_1}y - \frac{(D_5 + D_1)}{M_1}Z(2) - \frac{(K_5 + K_1)}{M_1}Z(1) + \frac{D_1}{M_1}Z(4) + \frac{K_1}{M_1}Z(3) - \frac{T}{M_1}Z(9), \tag{8.59}$$

$$\ddot{x}_2 = \frac{dZ(4)}{dt} = -\frac{(D_1 + D_2)}{M_2}Z(4) - \frac{(K_1 + K_2)}{M_2}Z(3) + \frac{D_2}{M_2}Z(6) + \frac{K_2}{M_2}Z(5) + \frac{D_1}{M_2}Z(2) + \frac{K_1}{M_2}Z(1) - \frac{T}{M_2}Z(10), \tag{8.60}$$

From equations (8.48) and (8.50), the state variables become:

$$\ddot{x}_3 = \frac{dZ(6)}{dt} = -\frac{(D_2 + D_3)}{M_3}Z(6) - \frac{(K_2 + K_3)}{M_2}Z(5) + \frac{D_3}{M_3}Z(8) + \frac{K_3}{M_3}Z(7) + \frac{D_2}{M_3}Z(4) + \frac{K_2}{M_3}Z(3) - \frac{T}{M_3}Z(11). \tag{8.61}$$

and

$$\ddot{x}_4 = \frac{dZ(8)}{dt} = \frac{D_4}{M_4}\dot{y} + \frac{K_4}{M_4}y - \frac{(D_3 + D_4)}{M_4}Z(8) - \frac{(K_3 + K_4)}{M_4}Z(7) + \frac{D_3}{M_4}Z(6) + \frac{K_3}{M_4}Z(5) - \frac{T}{M_4}Z(12). \quad (8.62)$$

Similarly, $\dot{I}_1, \dot{I}_2, \dot{I}_3, \dot{I}_4$ can also be written as:

$$\dot{I}_1 = \frac{dZ(9)}{dt} = \frac{T}{L_1}Z(2) - \frac{T}{L_1}\dot{Y} - \frac{R_1}{L_1}Z(9), \quad (8.63)$$

$$\dot{I}_2 = \frac{dZ(10)}{dt} = \frac{T}{L_2}Z(4) - \frac{T}{L_2}\dot{Y} - \frac{R_2}{L_2}Z(10), \quad (8.64)$$

$$\dot{I}_3 = \frac{dZ(11)}{dt} = \frac{T}{L_3}Z(6) - \frac{T}{L_3}\dot{Y} - \frac{R_3}{L_3}Z(11), \quad (8.65)$$

$$\dot{I}_4 = \frac{dZ(12)}{dt} = \frac{T}{L_4}Z(4) - \frac{T}{L_4}\dot{Y} - \frac{R_4}{L_4}Z(12), \quad (8.66)$$

For identical spring stiffnesses based 4DOF1D EMVEH, the displacement and current time domain responses were simulated for two frequencies at a) $f_{n1}$ = 27 Hz, where the first dominant resonant peak was observed as per the Laplace transform analyses and, b) $f_{n2}$ = 46 Hz where the resonance response is lower than the first as per the Laplace transform analyses. Both the displacement and the time responses are given in Figure 8.7. It can be observed that the currents $I_1$, $I_2$, $I_3$ and $I_4$ had the same phase in the first mode, leading to higher displacement and higher current generation. It can be observed in the second mode that the currents $I_3$ and $I_4$ were in different phase from $I_1$ and $I_2$, while $I_1$ and $I_2$ were in phase with one another. In the second mode, there was scrambling of the current signals and lower displacement and lower current generation.

The voltages and power generated by the individual coils at $f_{n1}$= 27 Hz and $f_{n2}$ = 46 Hz were calculated using the formula, $V = I^2 Z \cos\phi$, where $Z$ = impedance of each coil and $\cos\phi = R/Z$ is the power factor for that coil circuit. The results are summarised in Table 8.3 below.

Table 8.3 Theoretically simulated current, voltage and power generated from individual coils of 4DOF1D EMVEH at amplitude 0.1 mm.

| **RMS values** | **at 27 Hz** | **at 46 Hz** |
|---|---|---|
| Current at Coil 1, $I_1$ (mA) | 3.536 | 2.122 |
| Current at Coil 2, $I_2$ (mA) | 7.072 | 2.122 |
| Current at Coil 3, $I_3$ (mA) | 2.829 | 0.707 |
| Current at Coil 4, $I_4$ (mA) | 5.658 | 1.061 |
| Internal resistance of each coil, $R$ (ohm) | 0.3 | 0.3 |
| Inductive reactance of each coil, $X_L$ (ohm) | 2.714 | 4.624 |
| Impedance of each coil, $Z$ (ohm) | 2.731 | 4.634 |
| Voltage at Coil 1, $V_1$ (mV) | 9.657 | 9.832 |
| Voltage at Coil 2, $V_2$ (mV) | 19.313 | 9.832 |
| Voltage at Coil 3, $V_3$ (mV) | 7.725 | 3.277 |
| Voltage at Coil 4, $V_4$ (mV) | 15.45 | 4.916 |
| Power factor, $\cos\varphi = R / Z$ | 0.110 | 0.065 |
| Power generated from Coil 1, $P_1$ (mW) | 3.751E-03 | 1.351E-03 |
| Power generated from Coil 2, $P_2$ (mW) | 5.123E-04 | 2.818E-05 |
| Power generated from Coil 3, $P_3$ (mW) | 1.120E-05 | 6.529E-08 |
| Power generated from Coil 4, $P_4$ (mW) | 9.787E-07 | 3.405E-10 |

It was observed that in the second mode at 46 Hz, the current, voltage and power outputs of all four coils were in different phase and magnitude with respect to each other. By suitably powered electronic means, the individual AC voltages could be rectified to DC and then added to yield the final voltage output.

(a)

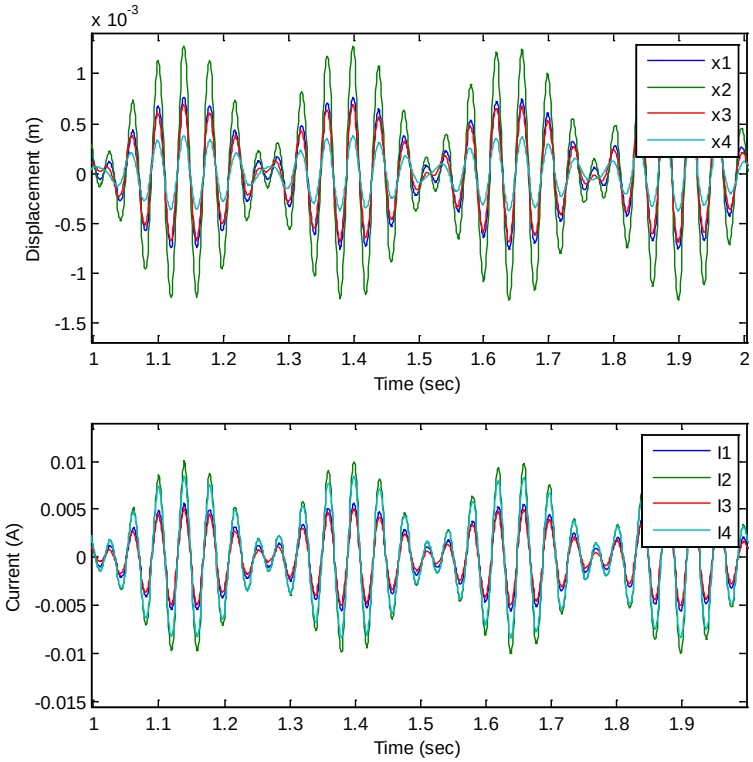


(b)

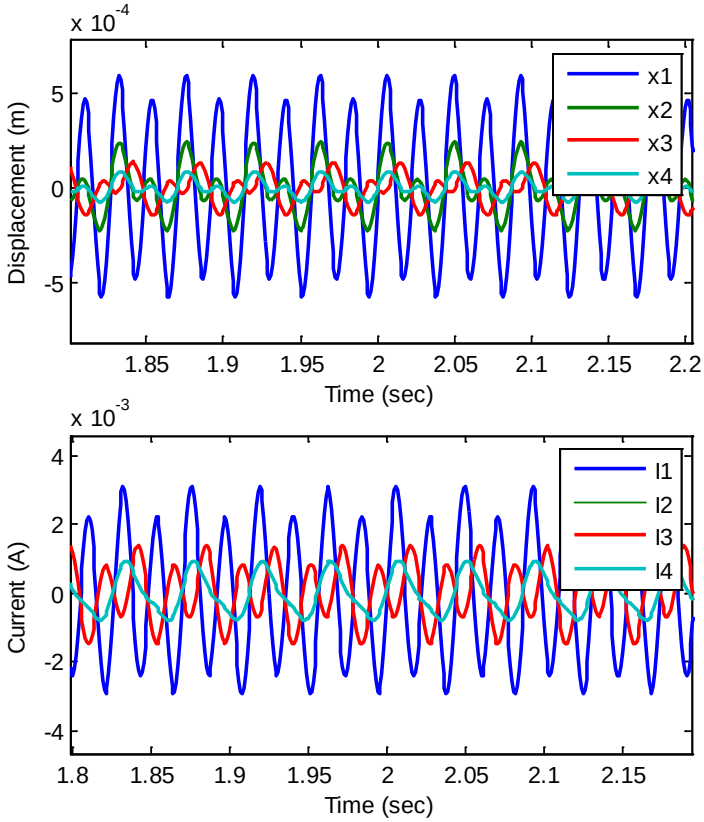


Figure 8.7 Time responses of 4DOF1D-MDKRL system (a) at first mode at 27 Hz, (b) at second mode at 46 HZ.

## 8.4 Generalisation to MDOF1D-damped EMVEH model

Equation (8.15) can be generalised to a multi-degree-of-freedom EMVEH (MDOF1D EMVEH). Consider a MDOF1D EMVEH with n degrees of freedom, as shown in Figure 8.8. Consider *n* number of coils being connected in similar fashion as 4DOF1D, starting with $M_1$ as the top coil mass and $M_n$ as the bottom most coil mass with $M_2$, $M_3$,…$M_{n-1}$ intermediate coils in- between $M_1$ and $M_n$. Consider these *n* coil masses to be connected in series by spring elements $K_1$, $K_2$…$K_{n+1}$ and damping elements $D_1$, $D_2$,…$D_{n+1}$ as shown in Figure 8.8(a). Each of the coils are connected to a resistor and inductor element as shown in Figure 8.8(b).

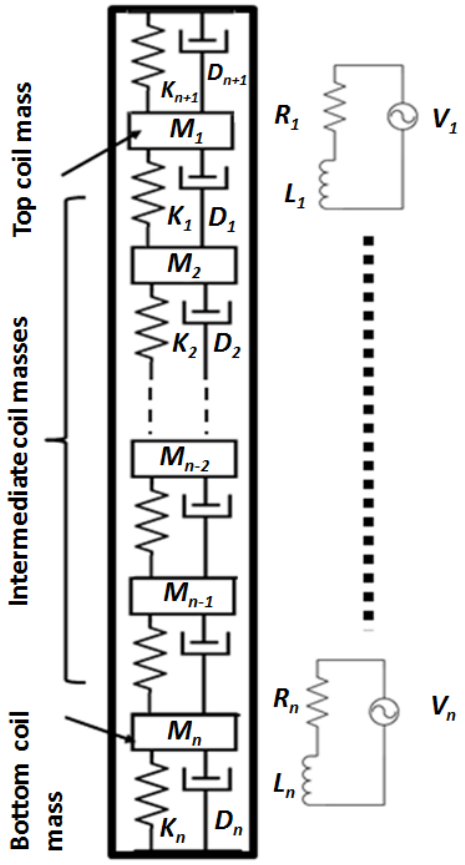


(a) (b)

Figure 8.8 MDOF1D EMVEH with *n* degrees of freedom – a) mechanical system b) electrical system.

The free body diagram of the mechanical system can be written as shown in Figure 8.9.

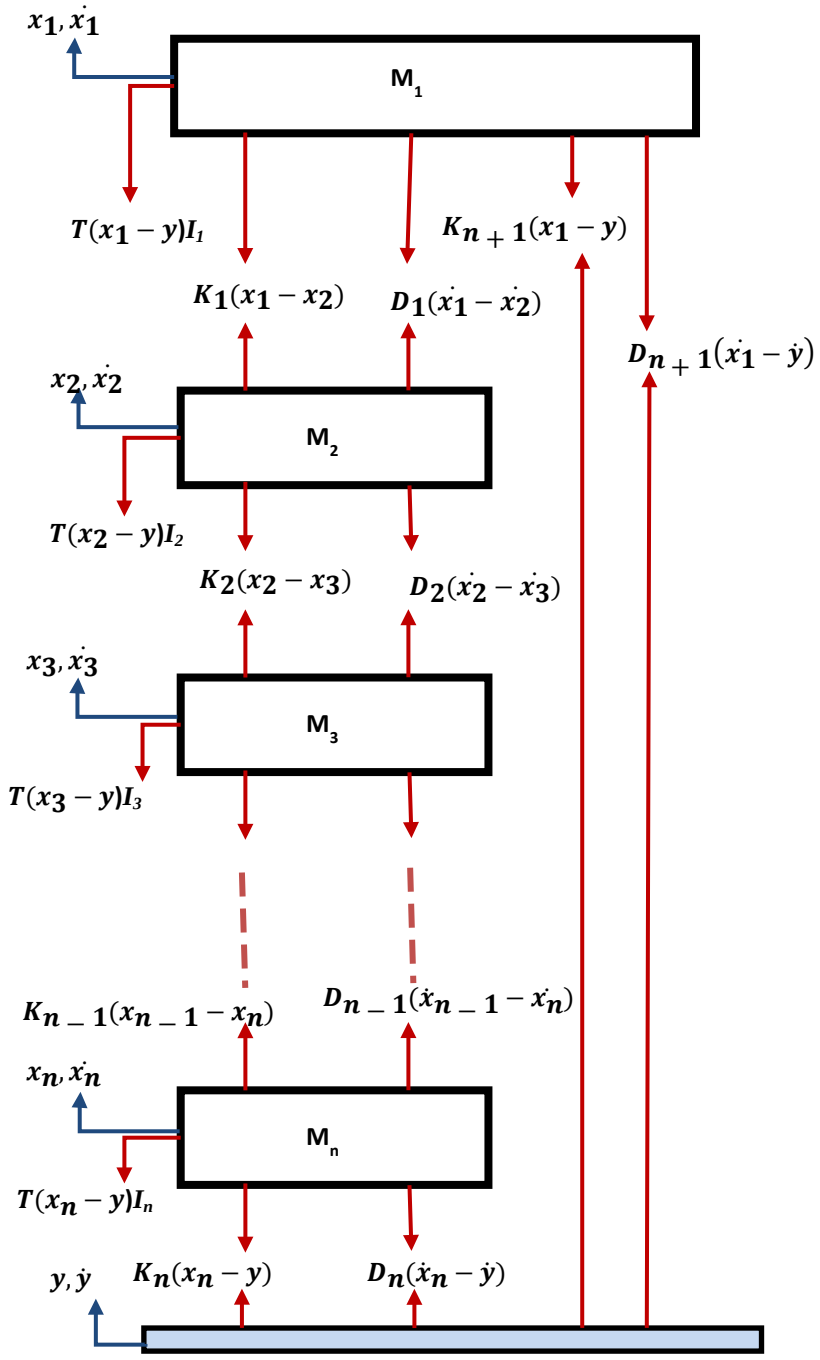


Figure 8.9 Free body diagrams of acting forces of a MDOF1D EMVEH with *n* degrees of freedom.

Applying Newton's second law of motion at mass $M_1$ , the forces can be written as,

$$M_1\ddot{x_1} = \sum F_{M1}, \tag{8.67}$$

which becomes:

$$M_1\ddot{x}_1 = -(D_{n+1} + D_1)\dot{x}_1 - (K_{n+1} + K_1)x_1 + D_1\dot{x}_2 + K_1x_2 - T(x_1 - y)I_1 + D_{n+1}\dot{y} + K_{n+1}y. \quad (8.68)$$

This can be rearranged as,:

$$M_1\ddot{x}_1 + (D_n + D_1)\dot{x}_1 + (K_{n+1} + K_1)x_1 - D_1\dot{x}_2 - K_1x_2 + T(x_1 - y)I_1 = D_{n+1}\dot{y} + K_{n+1}y. \quad (8.69)$$

The force equation at the first intermediate mass, namely $M_2$, becomes:

$$M_2\ddot{x_2} = \sum F_{M2}. \quad (8.70)$$

Similarly, the force equation at mass $M_2$ can be written as:

$$M_2\ddot{x}_2 + (D_1 + D_2)\dot{x}_2 + (K_1 + K_2)x_2 - D_2\dot{x}_3 - K_2x_3 - D_1\dot{x}_1 - K_1x_1 + T(x_2 - y)I_2 = 0. \quad (8.71)$$

The force equation at the last intermediate mass $M_{n-1}$ becomes:

$$M_{n-1}\ddot{x_{n-1}} = \sum F_{M_{n-1}}, \quad (8.72)$$

which can be written as:

$$M_{n-1}\ddot{x}_{n-1} + (D_{n-2} + D_{n-1})\dot{x}_{n-1} + (K_{n-2} + K_{n-1})x_{n-1} - D_{n-1}\dot{x}_n - K_{n-1}x_n - D_{n-2}\dot{x}_{n-2} - K_{n-2}x_{n-2} + T(x_{n-1} - y)I_{n-1} = 0. \quad (8.73)$$

The force equation at the n$^{th}$ mass $M_n$ becomes:

$$M_n\ddot{x_n} = \sum F_{M_n} \quad (8.74)$$

which can be written as:

$$M_n\ddot{x}_n + D_N(\dot{x}_n - \dot{y}) + K_n(x_n - y) - D_{n-1}(\dot{x}_{n-1} - \dot{x}_n) - K_{n-1}(x_{n-1} - x_n) + T(x_n - y)I_n = 0. \quad (8.75)$$

This can be rewritten as:

$$M_n\ddot{x}_n + D_n\dot{x}_n + K_nx_n - D_{n-1}(\dot{x}_{n-1} - \dot{x}_n) - K_{n-1}(x_{n-1} - x_n) + T(x_n - y)I_n = D_n\dot{y} + K_ny, \quad (8.76)$$

Consider each of the $n$ coils having $n$ different RL circuits with resistances $R_1$, $R_2$,…, $R_n$ and inductances $L_1$, $L_2$,…,$L_n$ as shown in Figure 8.3.

The voltage generated in Circuit 1, consisting of Coil 1, is consumed by its resistance $R_1$ and inductance $L_1$ and is given by:

$$V_{gen_1} = T(x_1 - y)(\dot{x_1} - \dot{y}) = V_{R_1} + V_{L_1} = R_1 I_1 + L_1 \dot{I_1}. \quad (8.77)$$

The voltage generated in the circuit $n$ consisting of coil $n$ is consumed by its resistance $R_n$ and inductance $L_n$ and is given by:

$$V_{gen_n} = T(x_n - y)(\dot{x_n} - \dot{y}) = V_{R_n} + V_{L_n} = R_n I_n + L_n \dot{I_n}. \quad (8.78)$$

The force equations and the voltage equations can be written in the matrix form as:

$$\underset{n\,X\,n}{\begin{bmatrix} M \end{bmatrix}} \underset{n\,X\,n}{\begin{bmatrix} x'' \end{bmatrix}} + \underset{2n\,X\,2n}{\begin{bmatrix} D & 0 \\ -T & L \end{bmatrix}} \underset{1\,X\,2n}{\begin{bmatrix} x' \\ I' \end{bmatrix}} + \underset{2n\,X\,2n}{\begin{bmatrix} K & T \\ 0 & R \end{bmatrix}} \underset{1\,X\,2n}{\begin{bmatrix} x \\ I \end{bmatrix}} = \underset{2n\,X\,2n}{\begin{bmatrix} D_K \\ -T_L \end{bmatrix}} \underset{2\,X\,1}{\begin{bmatrix} \dot{y} \\ y \end{bmatrix}} \quad (8.79)$$

where $n$ is the number of degrees of freedom and generally the number of electromagnetic inertial masses such as coils or magnets.

[M] Block is an $n \times n$ diagonal matrix equal to:

$$\begin{bmatrix} M_1 & 0 & .. & 0 & 0 \\ 0 & M_2 & .. & 0 & 0 \\ .. & .. & . & : & : \\ .. & .. & . & : & : \\ .. & .. & .. & 0 & : \\ 0 & 0 & .. & M_{n-1} & 0 \\ 0 & 0 & .. & 0 & M_n \end{bmatrix},$$

[0] block is $n \times$ n matrix of zeroes,

[X"] block is a $1 \times n$ matrix equal to $[\ddot{x}_1 \quad \ddot{x}_2 \quad \cdots \quad \ddot{x}_{n-1} \quad \ddot{x}_n]^T$,

[D] block is a $n \times n$ matrix equal to:

$$\begin{bmatrix} (D_{N+1} + D_1) & -D_1 & 0 & .. & .. & 0 & 0 \\ -D_1 & (D_1 + D_2) & -D_2 & .. & .. & 0 & 0 \\ 0 & : & : & : & .. & . & .. \\ : & : & : & .. & .. & . & .. \\ : & : & .. & .. & .. & . & .. \\ 0 & : & .. & .. & -D_{n-2} & (D_{n-2} + D_{n-1}) & -D_{n-1} \\ 0 & 0 & .. & .. & ... & -D_{n-1} & (D_{n-1} + D_n) \end{bmatrix},$$

[T] block is $n \times n$ diagonal matrix equal to:

$$\begin{bmatrix} T(x_1 - y) & 0 & .. & .. & .. & 0 \\ 0 & T(x_2 - y) & .. & \dots & .. & 0 \\ .. & 0 & .. & .. & .. & .. \\ .. & .. & .. & .. & .. & .. \\ .. & .. & .. & .. & .. & .. \\ 0 & 0 & .. & .. & .. & T(x_{n-1} - y) \end{bmatrix},$$

[-T] block is $n \times n$ matrix equal to the opposite of [T],

[L] block is $n \times n$ matrix equal to:

$$\begin{bmatrix} L_1 & 0 & .. & 0 & 0 \\ 0 & L_2 & .. & 0 & 0 \\ .. & .. & . & : & : \\ .. & .. & . & : & : \\ .. & .. & .. & 0 & : \\ 0 & 0 & .. & L_{n-1} & 0 \\ 0 & 0 & .. & 0 & L_n \end{bmatrix},$$

[X'] block is $1 \times n$ matrix equal to $[\dot{x}_1 \quad \dot{x}_2 \quad \cdots \quad \dot{x}_{n-1} \quad \dot{x}_n]^T$,

[I'] block is $1 \times n$ matrix equal to $[\dot{I}_1 \quad \dot{I}_2 \quad \cdots \quad \dot{I}_{n-1} \quad \dot{I}_n]^T$,

[K] block is n × n matrix equal to:

$$\begin{bmatrix} (K_{n+1} + K_1) & -K_1 & 0 & .. & .. & 0 & 0 \\ -K_1 & (K_1 + K_2) & -K_2 & .. & .. & 0 & 0 \\ 0 & : & : & : & .. & . & .. \\ : & : & : & .. & .. & . & .. \\ : & : & .. & .. & .. & . & .. \\ 0 & : & .. & .. & -K_{n-2} & (K_{n-2} + K_{n-1}) & -K_{n-1} \\ 0 & 0 & .. & .. & \dots & -K_{n-1} & (K_{n-1} + K_n) \end{bmatrix},$$

[R] block is n × n matrix equal to:

$$\begin{bmatrix} R_1 & 0 & .. & 0 & 0 \\ 0 & R_2 & .. & 0 & 0 \\ .. & .. & . & : & : \\ .. & .. & . & : & : \\ .. & .. & .. & 0 & : \\ 0 & 0 & .. & R_{n-1} & 0 \\ 0 & 0 & .. & 0 & R_n \end{bmatrix},$$

[X] block is $1 \times n$ matrix equal to $[x_1 \quad x_2 \quad \cdots \quad x_{n-1} \quad x_n]^T$,

[I] block is $1 \times n$ matrix equal to $[I_1 \quad I_2 \quad \cdots \quad I_{n-1} \quad I_n]^T$,

[$D_K$] block is $2 \times n$ matrix equal to:

$$\begin{bmatrix} D_{n+1} & K_{n+1} \\ 0 & 0 \\ : & : \\ 0 & 0 \\ D_n & K_n \end{bmatrix},$$

[-$T_L$] block is 2 × n matrix equal to:

$$\begin{bmatrix} T(x_1 - y) & 0 \\ T(x_2 - y) & 0 \\ : & : \\ T(x_{n-1} - y) & 0 \\ T(x_n - y) & 0 \end{bmatrix}.$$

The solution to this set of coupled electromechanical equations can be solved in the same manner as the 4DOF1D EMVEH system. The spatial variation of the magnetic field is neglected in linear methods namely the Laplace and the state space methods. The spatial variation can be considered in the non-linear ODE45 method to obtain time domain response of the displacement and its corresponding generated current, power and voltage.

Analogous to the current, voltage and power outputs of 2DOF1D EMVEH with two resonant peaks, the current, voltage and power output frequency responses of an MDOF1D EMVEH will have n resonant peaks where n is the number of degrees of freedom.

## 8.5 Discussion and conclusions

The study of 2DOF1D provided the evidence that having a multiple-degree-of-freedom energy harvester offered significant advantages such as increased power density and broad band power harvesting, but the 2DOF1D was not a perfect multi-degree-of- freedom model since it lacked intermediate masses. Hence the 4DOF1D EMVEH was analysed in detail in this chapter using both linear Laplace/state space and non-linear ODE45 methods. It was observed that 4DOF1D EMVEH had an increased number of resonant peaks owing to many masses and springs.

It was also observed that by having different spring stiffnesses, one can have a greater number of resonant peaks. Thus it can be concluded that an increased number of resonant peaks of the overall electrically-mechanically coupled MDOF1D EMVEH system can be achieved by having multiple system eigenvalues, each different to the others. This can be achieved either by having different spring stiffnesses or different masses, as shown in

Figure 8.10. Extending the same concept to an electrical counterpart, one can have multiple eigenvalues in the electrical circuit. However, since an RL circuit was used, there would be no extra electrical resonances to consider.

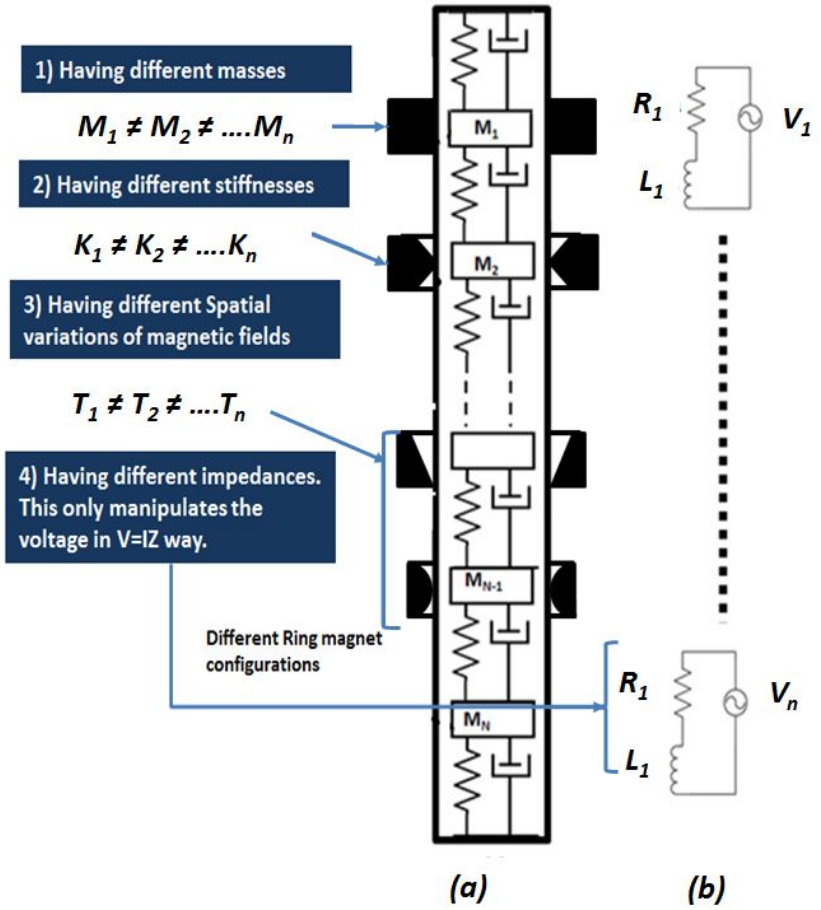


Figure 8.10 Different options to achieve multiple resonances of MDOF1D EMVEH system.

Another way of achieving multiple resonant peaks is by having different spatial variations in the magnetic fields of each individual mass system of the MDOF1D EMVEH system. This can be achieved by having combinations of different magnets, as shown in Figure 8.11. The only variation to the generalised equation (8.79) would be the [T], [-T] and [$-T_L$ ] blocks with each block having different T variations.

Hence, the generalised equation formed in this chapter can be manipulated by many permutations and combinations of the variations of design parameters to obtain a higher number of resonant peaks that will help in achieving maximum power at different frequencies, as shown in Figure 8.11. Thus the EMVEH becomes versatile to achieve maximum power output regardless of the random vibration frequency of the ambient

source at any instant of time. This generalised equation can serve as a framework for the design of future MDOF1D EMVEH energy harvesters.

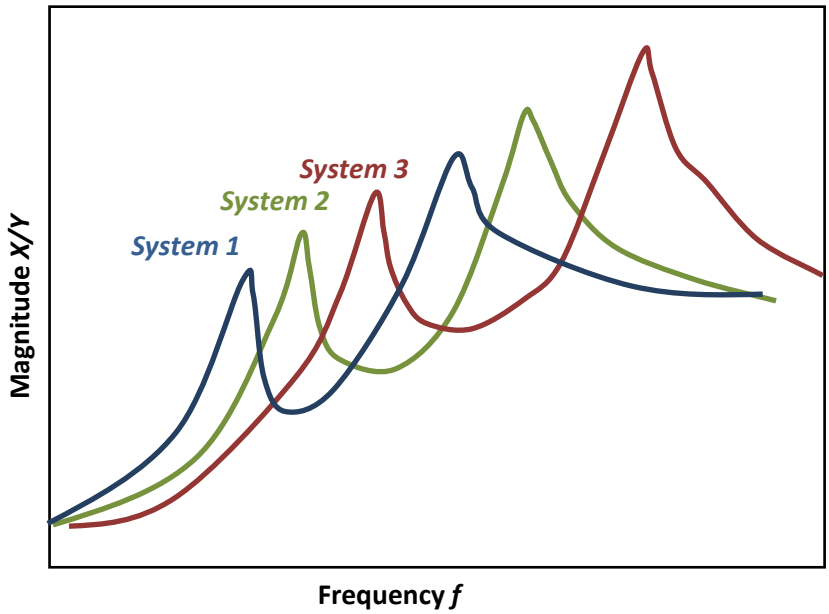


Figure 8.11 Ideal or desired frequency spectrum of individual voltage systems that constitute the MDOF1D EMVEH system.

The MDOF1D EMVEH generalised equation can be used to derive coupled equations of motion from unidirectional energy harvesters. Some vibrations such as those in rotary machines, for example, generators, pumps and motors, have bidirectional vibrations at the bearing supports of the rotating shafts. Equation (8.79) may be further generalised to MDOFMD EMVEHs provided the vibration in one direction is independent and does not affect the vibrations from the other direction. This further generalisation to multi-directionality requires further research.

# Chapter 9 Conclusion

The current chapter summarises the key findings of the MDOF1D EMVEHs and their possible practical applications. The conclusions have been divided into four categories:

- Conclusions concerning the product design of the MDOF1D EMVEH, where the key features of the design of MDOF energy harvesters are discussed. This chapter also briefly discusses the key findings of each of the previous chapters.
- Discussion on the research methodologies and computational methods used and how they can be used in similar systems.
- Applications overview of how the current research can be applied to real-world devices.
- Scope for future research work that discusses improvement and short-term research work that is feasible for improving the design and performance of EMVEHs.

## 9.1 Conclusions regarding MDOF1D EMVEH design

It was found that the MDOF1D EMVEH provides a broad range of resonant frequencies compared to the SDOF1D EMVEHs. This is useful in that a broad range of frequencies is appropriate for use in industrial situations where the available ambient vibrations may be random vibrations or may constitute periodic vibrations operating at uncertain resonant frequencies. While the SDOF1D EMVEH generates maximum power only when the source frequency is nearly equal to the resonant frequency of the system, the MDOF1D EMVEH is capable of generating maximum power for different resonant frequencies.

As concluded in Chapter 3, it was found that one can improve the design of the energy harvester by taking advantage of the spatial variation of the magnetic field. This can be achieved by designing the coil so that it vibrates in the region of maximum magnetic field variation, or alternatively, a varying profile magnet vibrating in a fixed coil may be used. Alternative coil structures and magnetic profiles could be explored further. This exploration of the spatial variation of the magnetic field may be a key consideration in future designs of

other electromagnetic energy harvesters, and possibly extended to other electro-mechanical transduction mechanisms like loudspeakers (reversing the EMVEH principle) and microphones.

The step-by-step mathematical modeling of the basic lumped mass SDOF1D model, as discussed in Chapter 4, provided an insight into both linear and non-linear electromechanical transduction mechanisms and can be applied to future simple electromagnetic energy harvesters with a single degree of freedom. The SDOF1D EMVEH modeling laid the very basic foundations for building mathematical models for the 2DOF1D EMVEH and subsequent generalisation to MDOF1D EMVEH systems. The first step towards upgrading the SDOF1D EMVEH to MDOF1D EMVEH was the 2DOF1D EMVEH system, as discussed in Chapter 5. The theoretical modeling of the 2DOF1D EMVEH provided a foundation for the development of the 4DOF1D EMVEH and subsequent generalisation to MDOF1D EMVEH systems.

Before proceeding to a generalisation regarding the MDOF1D EMVEH, sensitivity analyses were performed for both the basic models including the SDOF1D EMVEH and the 2DOF1D EMVEH as outlined in Chapter 6. This was essential to understand how the main design parameters of the EMVEH, namely the coupling coefficient (*T*), mass (*M*), damping (*D*), spring stiffness (*K*), resistance (*R*) and inductance (*L*) influenced the voltage output of the energy harvester. In future, a similar approach could be used not only to optimise voltage output but also power output and impedance. Chapter 6 was of practical significance with regard to future rapid design and development of the industrial design of MDOF1D EMVEHs.

The prototype builds of the SDOF1D EMVEH and 2DOF1D EMVEH and their subsequent experimentation was outlined in Chapter 7. The experimental results were compared with the sensitivity data and the design parameters were measured to develop equivalent theoretical models. It was observed that the theoretical and experimental models were close to each other, thus validating the formulated SDOF1D and 2DOF1D EMVEH models. Similar experimental methodology could be employed for validating the design of future MDOF EMVEHs. However, it was found that the experimental parameters could be further controlled by improving the prototype and the experiment.

Once the SDOF1D and 2DOF1D EMVEH models were well established by theoretical modeling and experimental validation, the concept of multi-degrees-of-freedom was

extended to 4DOF1D, and subsequently generalised to MDOF1D EMVEH. The final generalised matrix of MDOF1D EMVEH was finally derived and the solution methods were clearly explained. The MDOF1D EMVEH matrix equation provides the basis for the preliminary mathematical modeling of future MDOF1D EMVEHs that is usually carried out before design and development.

It was observed that each of the coils in any MDOF1D EMVEH produced a voltage that may or may not have been in phase with the voltages of the other coils. The difference in phases of individual coils in an MDOF1D EMVEH increases, particularly when different resonant frequencies are desired in the design of the EMVEH to achieve the goal of broadband energy harvesting. There are several alternatives which may be considered when adding coil voltages together. One possibility is to convert each of the individual coil voltages into DC voltages and then adding them. At a particular frequency of ambient vibration, the MDOF1D EMVEH coils that respond with maximum deflection and velocity, according to the modal behaviour of the system, will produce higher voltage and current output compared to the other coils.

## 9.2 Conclusions on research methodologies

The development of the mathematical models from an SDOF1D to an MDOF1D EMVEH system was progressive, in order to obtain a detailed understanding of system behavior caused by individual design parameters *M, D, K, R, L* and *T*. The mathematical models of EMVEHs considered were developed initially using linear methods such as Laplace transform and state space methods. This was undertaken without considering the spatial variation of the magnetic field but eventually graduated to the more accurate non-linear method with due consideration to the spatial variation of the magnetic field.

Throughout the analyses, from the SDOF1D to MDOF1D EMVEH systems, hybrid methodologies constituting analytical and numerical methods were used. The spatial variation of the magnetic field was determined using numerical magnetostatics by ANSOFT MAXWELL and then importing the results of the analytical simulation performed by MATLAB. This hybridisation of analytical and numerical methods was essential to reduce the time-cycle of the analysis. Not only that, in the near future, if complex topologies of spatial magnetic variation (for example, using a conical ring magnet) are used, then it is

inevitable that numerical methods will be used for obtaining spatial variation data. Taking this into account, the current hybrid methodology was developed with a view to producing a simple framework for the design and development of future MDOF EMVEH systems.

The current research also provided a framework for developing non-linear coupled physical systems. Essentially, an EMEVEH is a coupled electro-mechanical system of transduction. The same framework can be applied, with minor amendments, to analogous non-linear coupled systems with either one or more coupling coefficients. In order to simplify the process, MATLAB software could be employed to compute large matrices. If the non-linearity of the coupling coefficients becomes more computationally intensive, approximate linear methods such as Laplace transform and state space methods, as utilised in this research, may be considered.

## 9.3. Applications of MDOF1D EMVEHs

MDOF EMVEH systems can be applied in real-world industrial situations to not only harvest vibrational energy but kinetic energy of any kind that consists of periodic motion or can be converted to periodic motion. The sources of dynamic energy that can be harvested using MDOF1D EMVEH systems can be classified as: (a) vibrations which are typically from low-power sources where the harvested energy runs from microwatts to milliwatts, (b) dynamic renewable energy sources such as wind power and wave power where the harvested energy runs from kilowatts to megawatts.

### 9.3.1 Fields of application

Since the energy generated by vibrations is typically low, the energy is only sufficient to power low-power microelectronics. Therefore, at the micro and meso-scale, MDOF1D EMVEH systems can be designed to harvest energy for micro-electronic devices such as sensors, smart sensors or wireless sensors, since the power generated consists of microwatts to milliwatts. The abovementioned sensors are normally subject to ambient vibrations and include industrial sensors for condition monitoring applications, automotive sensors connected to CAN, and bridge sensors for structural health monitoring.

On a larger scale, the spatially varying MDOF1D EMVEHs can be utilised for the generation of renewable energy by generalising the model to MDOF1D motion energy harvesters where any periodic motion, such as waves, can be harvested for use as electrical energy. Typically these energy sources are in the form of fluid motion such as wind and ocean wave energy. MDOF1D EMVEHs may be used, provided suitable non-periodic kinetic energy is convertible to periodic kinetic energy at the first stage, and periodic kinetic energy is convertible to electrical energy in second stage conversion. This process is beyond the scope of this research as it requires comprehensive research of the inherent irregular nature of fluid motion.

### 9.3.2 Topologies of application

On a micro-scale, cantilever-based topology is often adopted, owing to ease of manufacture at a MEMS level. A concept design of MEMS MDOF EMVEH cell is as shown in Figure 9.1. On a meso and macro-scale, conventional helical spring topology with an electromagnetic, active inertial mass (EAIM), such as a coil or magnet can be used, as shown in the Figure 9.2. Alternatively, a coil spring topology with an EAIM can be used to harvest vibrational energy from torsional vibrations.

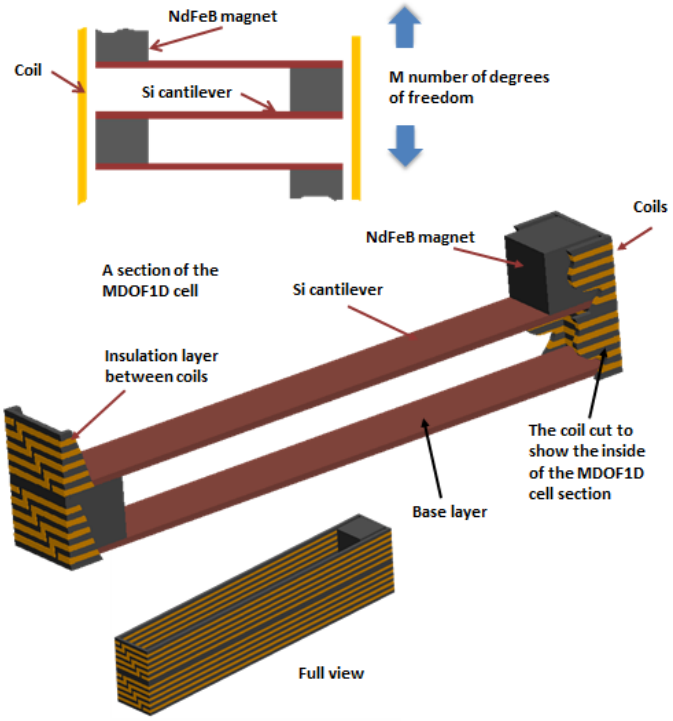


Figure 9.1 Micro-scale topology concept for MDOF1D EMVEH.

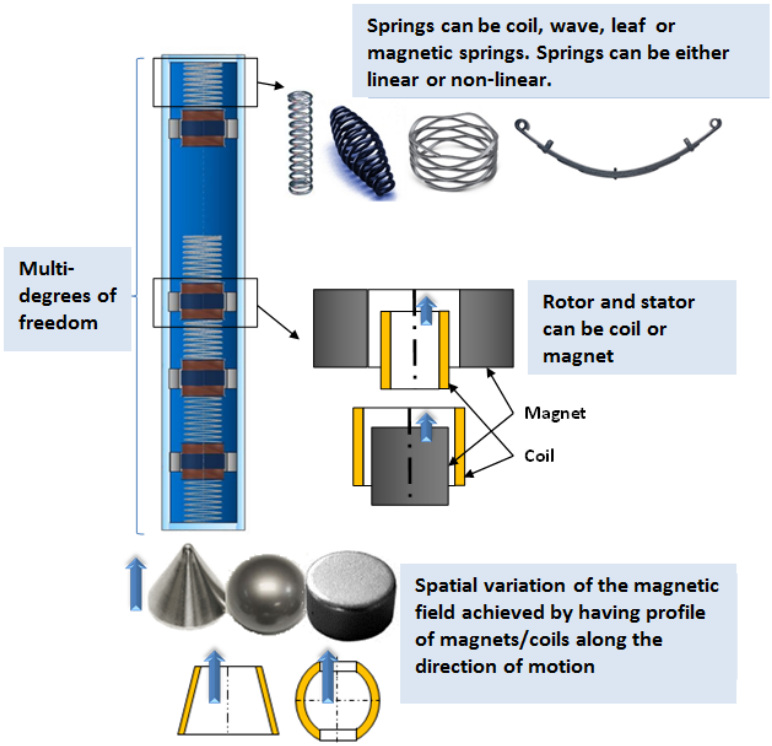


Figure 9.2 Meso-scale and macro-scale topology concepts of MDOF1D EMVEH.

## 9.4 Future work and recommendations

While the scope for future work is vast, since the field of energy harvesting is still in its infancy, only-short term, immediately extendable research work is discussed here. In the immediate future, the comprehensive experiments with the MDOF1D EMVEH system can be improved, where every design parameter can be analysed. Each of the design parameters *M, D, K, R, L* and *T* can be varied to investigate their sensitivity with respect to overall voltage and power output. In a MDOF1D EMVEH, the individual AC currents developed in each of the coils are in different phase with each other. Hence suitable power electronics need to be designed for adding the individual currents.

The MDOF1D EMVEH can be built as a cell with a number of springs and inertial masses, as shown in Figure 9.3. As shown in the concept, each MDOF1D EMVEH consists of a cell with a top and bottom connector similar to AA or AAA batteries. The advantage of a battery-like structure is that it can be added to, similar to the usual method of adding batteries to obtain more voltage. The addition of individual voltages in different coils that constitute the MDOF1D EMVEH cell, power regulation and rectification circuit can be built into each cell. The output voltage would have DC voltage with positive and negative polarities on either ends through a modified bipolar design, as shown in Figure 9.4. Unlike traditional batteries with polarities on one side only, the MDOF EMVEH cell would have both polarities on either side of the cell.

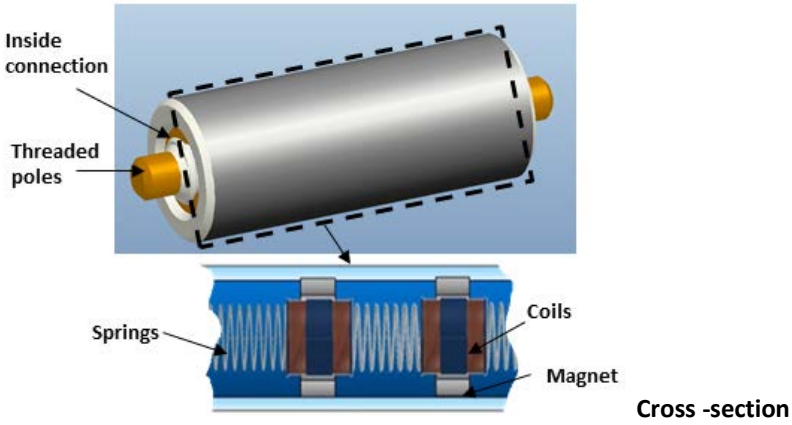


Figure 9.3 MDOF1D EMVEH Cell concept.

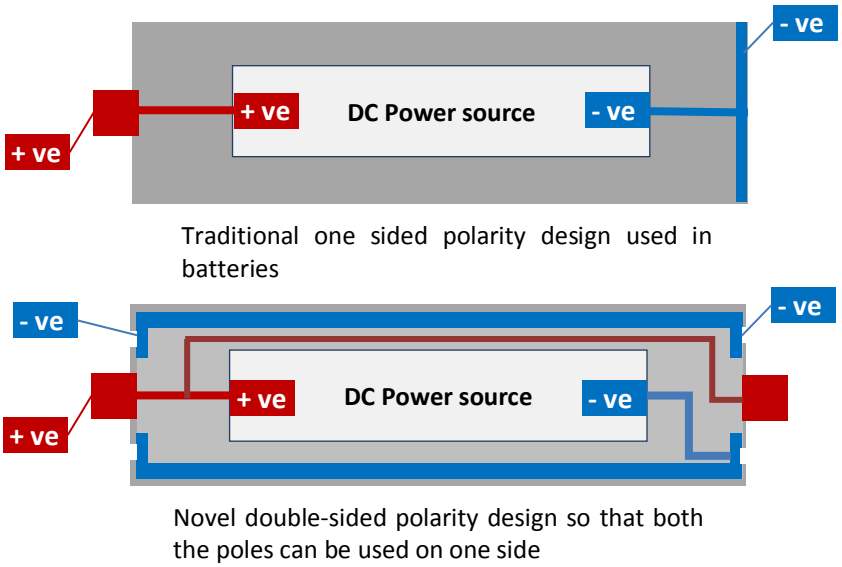


Figure 9.4 Cross-sectional schematic of novel bipolar design of DC power for EMVEH concept.

To connect two MDOF cells in series, series connectors are used. This makes the design modular, whereby it can be flexibly added to by additional EMVEHs, according to energy availability and requirements (Figure 9.5).

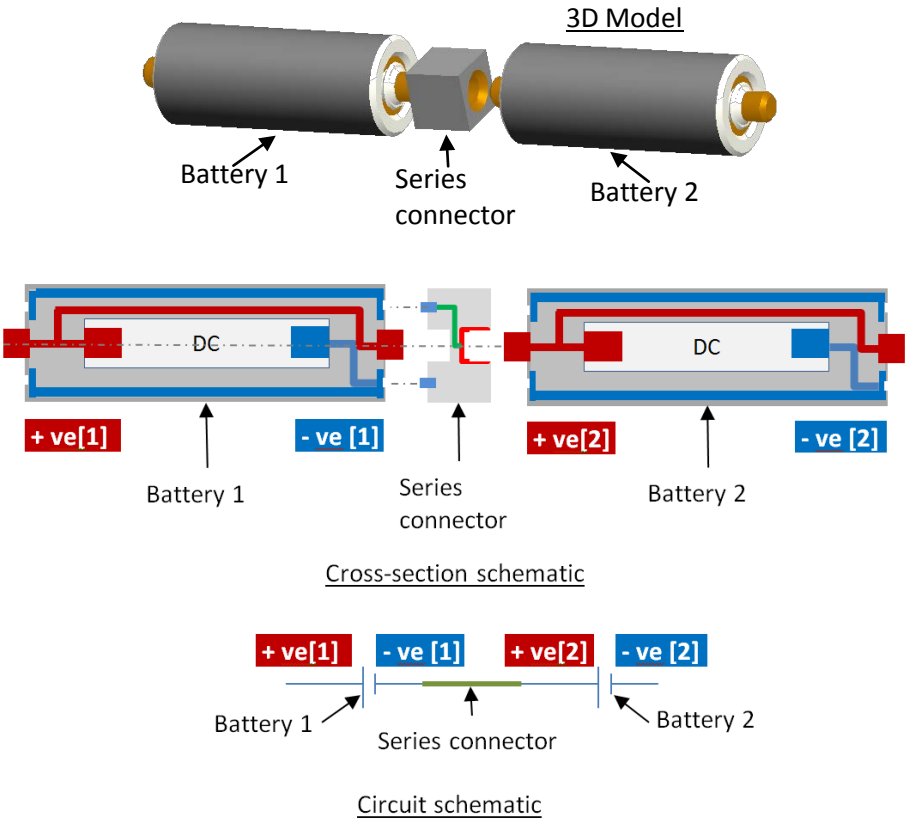


Figure 9.5 Schematics of Series Connector to connect MDOF EMVEH cells in series.

It is also possible to add a bi-axial connector to connect two MDOF1D EMVEH cells in mutually perpendicular directions along a plane, as shown in Figure 9.6. A bi-axial-bipolar connector can be designed in similar lines of the series connector to connect two DC sources in series by connecting the opposite poles of the two different directions in series.

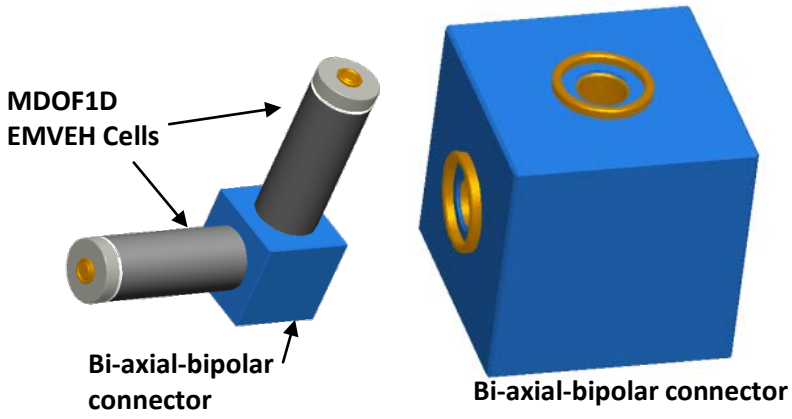


Figure 9.6 Bi-axial MDOF EMVEH cell concept.

The MDOF1D EMVEH systems can be extended to MDOF3D systems, as shown in Figure 9.7. The multi-directionality of MDOF EMVEH systems is possible when three MDOF cells are in mutually perpendicular directions, thus harvesting energy in X, Y and Z directions. This type of configuration is necessary, as most of the rotary machines have energy in all three orthogonal directions, with one direction being typically the most dominant compared to the other two directions. A cubical connector that connects all the three X, Y and Z MDOF cells is shown in Figure 9.7. The three MDOF cells are screwed to the tri-axial connector that receives both the poles of each MDOF cell. The tri-axial connector is designed such that internally it connects all three X, Y and Z DC voltages of three MDOF1D EMVEH cells in series.

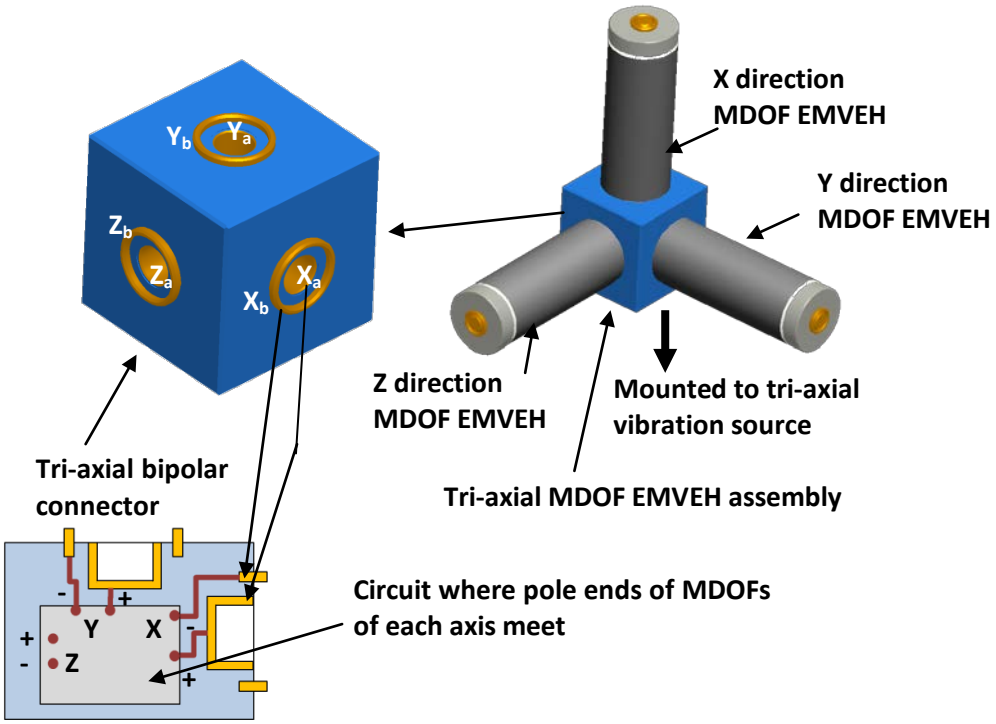


Figure 9.7 A MDOF3D EMVEH concept.

The possibility of connecting many MDOF cells in series, in two directions along a plane and in all three directions, motivates a further step to build a MDOF EMVEH energy frame, as shown in Figure 9.8. A MDOF EMVEH energy frame is an array of MDOF cells in either two or three directions formed by connecting several MDOF cells in series, and in two or three directions. It is feasible, from the above design, to create energy frames of various configurations with MDOFs in parallel and/or series combinations in all three directions. The external wiring of the connections can be minimised using intelligent design connectors.

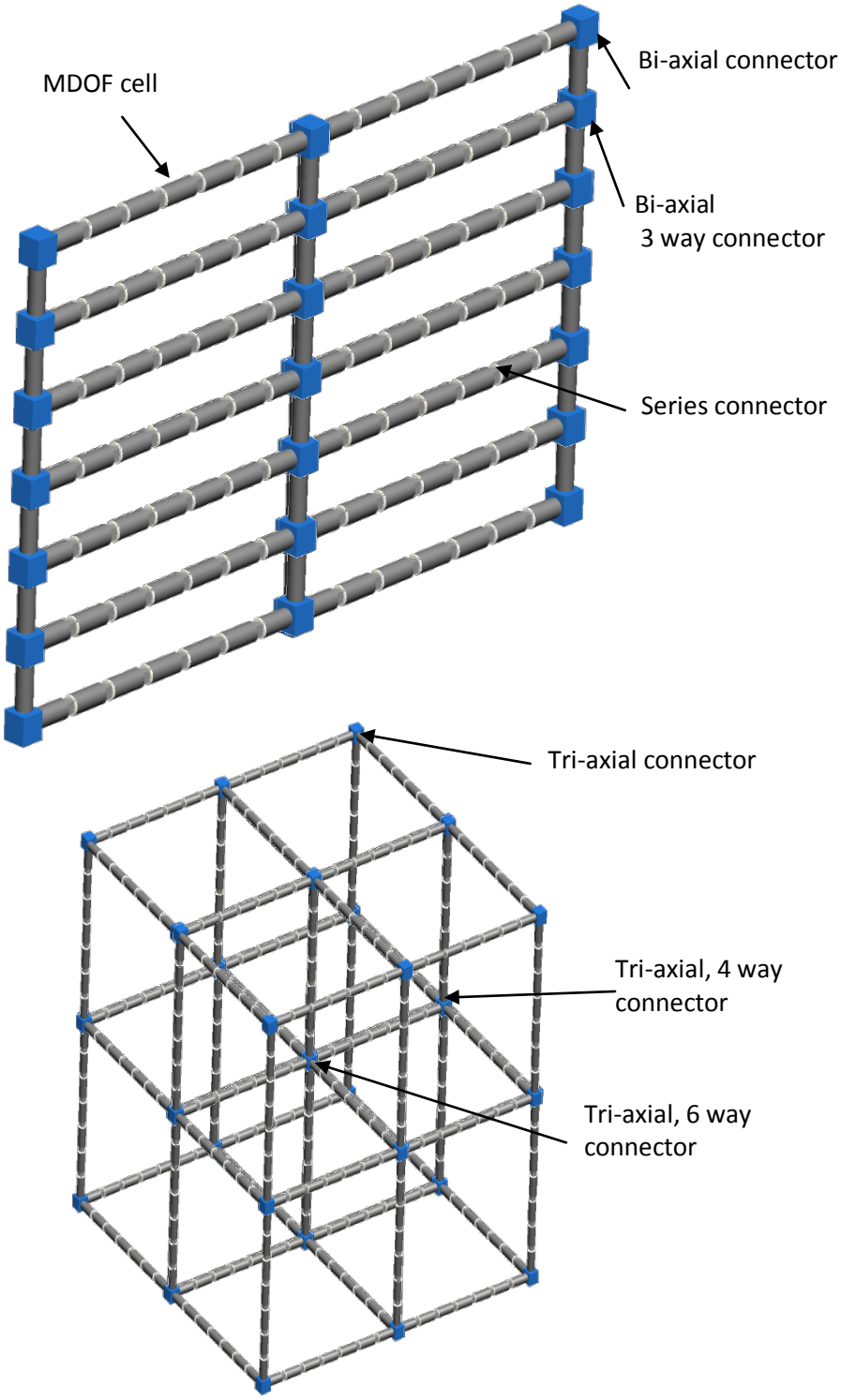


Figure 9.8 Concept of planar and tri-axial energy frames made of array of MDOF EMVEH cells.

# References


Arroyo, E., & Badel, A. (2011). Electromagnetic vibration energy harvesting device optimization by synchronous energy extraction. Sensors and Actuators A: Physical, 171(2), 266-273. doi:http://dx.doi.org/10.1016/j.sna.2011.06.024

B&K (1976). Piezoelectric accelerometers and vibration amplifiers-Theory and application Handbook.

Barton, D. A. W. (2010). "Energy harvesting from vibrations with a nonlinear oscillator." Journal of Vibration, Acoustics, Stress, and Reliability in Design 132(2): 021009.

Beckwith, T. G., R.D. Marangoni, and J.H.L. V (2007). Mechanical Measurements, Pearson Prentice Hall.

Beeby, S. P. and T. O'Donnell (2009). Electromagnetic Energy Harvesting.

Beeby, S. P., M. J. Tudor, N. M. White (2006). "Energy harvesting vibration sources for microsystems applications." Measurement Science and Technology 17(12): Page R175.

Bhuiyan, R. H., R. A. Dougal, Ali.M (2010). "A Miniature Energy Harvesting Device for Wireless Sensors in Electric Power System." Sensors Journal, IEEE 10(7): Page 1249-1258.

Bin Ab Rahman, M. F., & Swee Leong, K. (2011, 19-20 Dec. 2011). Investigation of useful ambient vibration sources for the application of energy harvesting. Paper presented at the 2011 IEEE Student Conference on Research and Development (SCOReD). doi:10.1109/SCOReD.2011.6148771.

Bonisoli, E., A. Canova, Freschi, F. , Moos , S., Repetto, M . , Tornincasa, S.. (2010). "Dynamic Simulation of an Electromechanical Energy Scavenging Device." IEEE Transactions on Magnetics, 46(8): Page 2856-2859.

Bouendeu, E., A. Greiner, Greiner, A. , Smith, P.J. , Korvink, J.G. (2011). "A Low-Cost Electromagnetic Generator for Vibration Energy Harvesting." Sensors Journal, IEEE 11(1): Page 107-113.

Cao, X., W. J. Chiang, Chiang, Wen-Jen , Ya-Chin King , Yi-Kuen Lee (2007). "Electromagnetic energy harvesting circuit with feed forward and feedback DC–DC PWM boost converter for vibration power generator system." IEEE Transactions on Power Electronics, 22(2): Page 679-685.

Cepnik, C., O. Radler, O. Radlerb, S. Rosenbaumb, T. Ströhlab, U. Wallrabea. (2011). "Effective optimization of electromagnetic energy harvesters through direct computation of the electromagnetic coupling." Sensors and Actuators A: Physical 167(2): Page 416-421.

Challa, V. R., M. G. Prasad, Fisher. F.T. (2011). "Towards an autonomous self-tuning vibration energy harvesting device for wireless sensor network applications." Smart Materials and Structures 20(2): 025004.

Chandrakasan, A., R. Amirtharajah, Goodman, J. , Rabiner, W. (1998). Trends in low power digital signal processing. IEEE International Symposium on Circuits and Systems, 1998. ISCAS '98.

Chen, H., T. N. Cong, Haisheng Chena, b, Thang Ngoc Conga, Wei Yanga, Chunqing Tanb, Yongliang Lia, Yulong Dinga,. (2009). "Progress in electrical energy storage system: A critical review." Progress in Natural Science 19(3): Page 291-312.

Chye, W.C.; Dahari, Z.; Sidek, O.; Miskam, M.A., "Electromagnetic micro power generator — A comprehensive survey," Industrial Electronics & Applications (ISIEA), 2010 IEEE Symposium on , vol., no., pp.376,382, 3-5 Oct. 2010, doi: 10.1109/ISIEA.2010.5679438

Dayal, R. and L. Parsa (2012). Hybrid start-up strategy for low voltage electromagnetic energy harvesting systems. Applied Power Electronics Conference and Exposition (APEC), 2012 Twenty-Seventh Annual IEEE.

Dragunov, V. P. and D. I. Ostertak (2012). "Microelectromechanical converters." Russian Microelectronics 41(2): Page 107-121.

Dudney, N. J. (2009). Thin film batteries for energy harvesting. Energy Harvesting Technologies. D. J. I. Shashank Priya, Springer: Page 355-363.

S. Priya and D. J. Inman (2008) Energy Harvesting Technologies. Springer US: Page 129-161.

Eren, H. (2005). Wireless Sensors and Instruments: Networks, Design, and Applications, Taylor and Francis Group.

Falconi, C. (2009). "Studying piezoelectric nanowires and nanowalls for energy harvesting." Sensors and Actuators. B, Chemical 139(2): Page 511.

Fang, H. B. and B. Hua (2006). "A MEMS-based piezoelectric power generator for low frequency vibration energy harvesting." Chinese Physics Letters 23(3): Page 732.

Fang, H. B. (2011). System and method for providing a piezoelectric electromagnetic hybrid vibrating energy harvester. US, WO 02/084754 A2 (Oct, 2002). 12107422.

Feenstra, J. (2008). "Energy harvesting through a backpack employing a mechanically amplified piezoelectric stack." Mechanical Systems and Signal Processing 22(3): Page 721.

Ferrari, M. (2008). "Piezoelectric multifrequency energy converter for power harvesting in autonomous microsystems." Sensors and Actuators. A, Physical 142(1): Page 329.

Alessandra Flammini, Paolo Ferrari, Daniele Marioli, Emiliano Sisinni, Andrea Taroni, Wired and wireless sensor networks for industrial applications, Microelectronics Journal, Volume 40, Issue 9, September 2009, Pages 1322-1336, ISSN 0026-2692, http://dx.doi.org/10.1016/j.mejo.2008.08.012.

Fondevilla, N., Serre, C.; Martinez, S., Perez-Rodriguez, A., Morante, Joan Ramon, Martincic, E., Montserrat, Josep, Esteve, Jaume, (2008). "Electromagnetic inertial microgenerators for vibrational energy scavenging: Implementation of a Si technology based modular process for optimised." Integration Issues of Miniaturized Systems - MOMS, MOEMS, ICS and Electronic Components (SSI), 2008 2nd European Conference & Exhibition on: Page 1-8.

Frayne, S. M (2009). Generator utilizing fluid-induced oscillations. US, DE 10241854 (Apr, 2003);

Gambier, P., Anton, S.R. , Kong. N, Erturk. A, Inman, D. J. (2012). "Piezoelectric, solar and thermal energy harvesting for hybrid low-power generator systems with thin-film batteries." Measurement Science and Technology 23(1): 015101.

Gatti, R., & Howard, I. (2012). Electromagnetic Energy Harvesting by Spatially Varying the Magnetic Field. In F. L. Gaol & Q. V. Nguyen (Eds.), Proceedings of the 2011 2nd International Congress on Computer Applications and Computational Science. (Vol. 144, pp. 403-409): Springer Berlin Heidelberg. Retrieved from http://dx.doi.org/10.1007/978-3-642-28314-7_54 doi:10.1007/978-3-642-28314-7_54

Gilbert, J. and F. Balouchi (2008). "Comparison of energy harvesting systems for wireless sensor networks." International Journal of Automation and Computing 5(4): Page 334-347.

Glynne Jones, P. (2004). "An electromagnetic, vibration-powered generator for intelligent sensor systems." Sensors and Actuators. A, Physical 110(1-3): Page 344.

Golding, A. R. M. V. C. A. and J. E. S. F. C. A. Rasmussen (2009). Adaptive and personalized navigation system. US, US 7053830 B2

Grant Instruments (2012). Squirrel Portable Data Loggers, CAS Dataloggers. 2012.

Green, R. J., Rihawi, Z. ; Mutalip, Z.A. ; Leeson, M.S. ; Higgins, M.D. (2012). Networks in automotive systems: The potential for optical wireless integration. 14th International Conference on Transparent Optical Networks (ICTON), 2012.

Gungor, V. C. and G. P. Hancke (2009). "Industrial Wireless Sensor Networks: Challenges, Design Principles, and Technical Approaches." IEEE Transactions on Industrial Electronics, 56(10): Page 4258-4265.

H. Brock Kolls, P. P. A. (2005). Global network based vehicle safety and security telematics. US, US 6389337 B1 (May, 2002) Kolls. 10134907.

Hachman, M. (2011). "Google's Self-Driving Car Challenge: 1 Million Miles, By Itself." Retrieved 03/09/2012, 2012, from http://www.pcmag.com/article2/0,2817,2395049,00.asp.

Hadas, Z., Zouhar, J., Singule, V., Ondrusek, C. (2008). Design of energy harvesting generator base on rapid prototyping parts. Power Electronics and Motion Control Conference, 2008. EPE-PEMC 2008. 13th, IEEE.

Hatipoglu, G. and H. Ürey (2010). "FR4-based electromagnetic energy harvester for wireless sensor nodes." Smart Materials and Structures 19(1): 015022.

Howells, C. A. (2009). "Piezoelectric energy harvesting." Energy Conversion and Management 50(7): 1847.

Jia, D., J. Liu, Y. Zhou. (2009). "Harvesting human kinematical energy based on liquid metal magnetohydrodynamics." Physics Letters A 373(15): Page 1305-1309.

Jiang, Y., S. Masaoka, Masaoka, S., Uehara, M., T. Fujita, K. Higuchi, K. Maenaka. (2011). "Micro-structuring of thick NdFeB films using high-power plasma etching for magnetic MEMS application." Journal of Micromechanics and Microengineering 21(4): 045011.

Joyce, B. S., Farmer, J., & Inman, D. J. (2013). Electromagnetic energy harvester for monitoring wind turbine blades. Wind Energy, n/a-n/a. doi:10.1002/we.1602

Kai Sun, G. Q. L., Xiao Yu Xu (2012). "No-Load Analysis of Permanent Magnet Spring Nonlinear Resonant Generator for Human Motion Energy Harvesting." Applied Mechanics and Materials Mechanical and Electronics Engineering III (October 2011): Page 2778-2782.

Kerzenmacher, S., J. Ducréeb, R. Zengerlea, b, F. von Stettena. (2008). "Energy harvesting by implantable abiotically catalyzed glucose fuel cells." Journal of Power Sources 182(1): Page 1-17.

Khaligh, A., Z. Peng, C. Zheng (2010). "Kinetic Energy Harvesting Using Piezoelectric and Electromagnetic Technologies: State of the Art." IEEE Transactions on Industrial Electronics, 57(3): Page 850-860.

Khan, F., F. Sassani, B. Stoeber. (2010). "Copper foil-type vibration-based electromagnetic energy harvester." Journal of Micromechanics and Microengineering 20(12): 125006.

Kim, S.-I., D. H. Lee, Y.P Lee, Y.S. Chang, M. Park (2008). "Low frequency properties of micro power generator using a gold electroplated coil and magnet." Current Applied Physics 8(2): Page 138-141.

Ko Ko, W., Xinhui, W., Dasgupta, S., Wong Jun, W., Kumar, R., & Panda, S. K. (2010, 17-19 Nov. 2010). Efficient solar energy harvester for wireless sensor nodes. Paper presented at the IEEE International Conference on Communication Systems (ICCS), 2010 doi:10.1109/iccs.2010.5686355

Kuehne, I. (2008). "Power MEMS—A capacitive vibration-to-electrical energy converter with built-in voltage." Sensors and Actuators. A, Physical 142(1): Page 263.

S. Kulkarni, E. Koukharenkob, R. Torahb, J. Tudorb, S. Beeby, T. O'Donnella, S. Roy (2008). "Design, fabrication and test of integrated micro-scale vibration-based electromagnetic generator." Sensors and Actuators A: Physical 145–146(0): Page 336-342.

Leen, G. and D. Heffernan (2002). "Expanding automotive electronic systems." Computer 35(1): Page 88-93.

Lefeuvre, E., A. Badel, C. Richard, L. Petit, D. Guyomar (2006). "A comparison between several vibration-powered piezoelectric generators for standalone systems." Sensors and Actuators A: Physical 126(2): Page 405-416.

Li, P., Y. Wen, P. Liu , X. Li , C. Jia (2008). An electromagnetic energy harvesting circuits for self-powered wireless sensor network. IEEE 10th International Conference on Control, Automation, Robotics and Vision, 2008(ICARCV 2008).

Liu, J. Q. (2008). "A MEMS-based piezoelectric power generator array for vibration energy harvesting." Microelectronics Journal 39(5): Page 802.

Marin, A., Turner, J., Ha, D. S., & Priya, S. (2013). Broadband electromagnetic vibration energy harvesting system for powering wireless sensor nodes. Smart Materials and Structures, 22(7), 075008. Retrieved from http://stacks.iop.org/0964-1726/22/i=7/a=075008

Marzencki, M., Y. Ammar, S. Basrour (2008). "Integrated power harvesting system including a MEMS generator and a power management circuit." Sensors and Actuators A: Physical 145–146(0): Page 363-370.

Miki, S., T. Fujita, Kotoge, T. , Jiang, Y.G. , Uehara, M. , Kanda, K. , Higuchi, K. , Maenaka, K.. (2012). Electromagnetic energy harvester by using buried NdFeB. IEEE 25th International Conference on Micro Electro Mechanical Systems (MEMS), 2012.

Minartz, T., D. Molka, M. Knobloch, S. Krempel, T. Ludwig, W. E. Nagel, B. Mohr, H. Falter (2012). eeClust: Energy-Efficient Cluster Computing.

Minazara, E., D. Vasic, F. Costa, G. Poulin. (2006). "Piezoelectric diaphragm for vibration energy harvesting." Ultrasonics 44, Supplement(0): Page e699-e703.

Mu, T., & Minghao, T. (2010, 23-25 Sept. 2010). LEACH-B: An Improved LEACH Protocol for Wireless Sensor Network. Paper presented at the 6th International Conference on Wireless Communications Networking and Mobile Computing (WiCOM), 2010 doi:10.1109/wicom.2010.5601113.

NISP Labs' online real vibrations database Retrieved 03/03/2013, 20132, from http://realvibrations.nipslab.org/.

Neri, Igor,F. Travasso,R. Mincigrucci,H. Vocca,F. Orfei,L.Gammaitoni (2012) "A real vibration database for kinetic energy harvesting application." Journal of Intelligent Material Systems and Structures 23.18 (2012): 2095-2101 doi: 10.1177/1045389X12444488

NokiaResearchCenter. "The Morph Concept" Retrieved 03/09/2012, 2012, from http://research.nokia.com/morph.

Notter, D. A., M. Gauch , R. Widmer , P. Wäger , A. Stamp , R. Zah, H. Althaus (2010). "Contribution of Li-Ion Batteries to the Environmental Impact of Electric Vehicles." Environmental Science & Technology 44(17): Page 6550-6556.

O'Donnell, T., C. Saha, S. Beeby, J. Tudor. (2007). "Scaling effects for electromagnetic vibrational power generators." Microsystem Technologies 13(11): Page 1637-1645.

Owens, B. A. M. and B. P. Mann (2012). "Linear and nonlinear electromagnetic coupling models in vibration-based energy harvesting." Journal of Sound and Vibration 331(4): Page 922-937.

Papotto, G., F. Carrara, G. Palmisano, (2011). "A 90-nm CMOS Threshold-Compensated RF Energy Harvester." IEEE Journal of Solid-State Circuits, 46(9): 1985-1997.

Park, J. C. (2010). "Micro-Fabricated Electromagnetic Power Generator to Scavenge Low Ambient Vibration." IEEE Transactions on Magnetics 46(6): 1937-1942.

Pereyma, M. (2007). Overview of the modern state of the vibration energy harvesting devices. IEEE International Conference on Perspective Technologies and Methods in MEMS Design, 2007. MEMSTECH 2007.

Perpetuum, P. (2012). "Getting Started with Vibration Energy Harvesting." Retrieved 24/09/2012, 2012, from http://www.perpetuum.com/resources/.

Perrig, A., J. Stankovic, D. Wagner (2004). "Security in wireless sensor networks." Commun. ACM 47(6): Page 53-57.

Pimentel, D., P. Musilek, A. Knight, J. Heckenbergerova. (2010). Characterization of a wind flutter generator. 9th International Conference on Environment and Electrical Engineering (EEEIC), 2010.

Poulin, G., E. Sarraute, F. Costa. (2004). "Generation of electrical energy for portable devices: Comparative study of an electromagnetic and a piezoelectric system." Sensors and Actuators A: Physical 116(3): Page 461-471.

F. L. Gaol and Q. V. Nguyen, Springer Berlin / Heidelberg(2011). Proceedings of the 2011 2nd International Congress on Computer Applications and Computational Science. 144: Page 403-409.

Pushparaj, V. L., M. M. Shaijumon, A. Kumar, S. Murugesan, L. Ci, R. Vajtai , R. J. Linhardt, O. Nalamasu, P. M. Ajayan. (2007). "Flexible energy storage devices based on nanocomposite paper." Proc Natl Acad Sci U S A 104(34): 13574-13577.

Ramasur, D. and G. P. Hancke (2012). A wind energy harvester for low power wireless sensor networks. IEEE International Instrumentation and Measurement Technology Conference (I2MTC), 2012.

Roundy, S. (2003). "A study of low level vibrations as a power source for wireless sensor nodes." Computer communications 26(11): 1131.

Roundy, S., & Takahashi, E. (2013). A planar electromagnetic energy harvesting transducer using a multi-pole magnetic plate. Sensors and Actuators A: Physical, 195(0), 98-104. doi:http://dx.doi.org/10.1016/j.sna.2013.03.018

Ruff, T. M. P. E.(2007) Advances in Proximity Detection Technologies for Surface Mining Equipment,National Institute for Occupational Safety and Health.

Saha, C. R., T. O'Donnell, N. Wang, P. McCloskey (2008). "Electromagnetic generator for harvesting energy from human motion." Sensors and Actuators A: Physical 147(1): Page 248-253.

Saha, C. R., T. O'Donnell, H. Loder, S. Beeby, J. Tudor (2006). "Optimization of an electromagnetic energy harvesting device." IEEE Transactions on Magnetics, 42(10): Page 3509-3511.

Salem, M. S., A. Zekry, H.F. Ragai, (2007). Effect of parallel capacitance in increasing output power of electrostatic MEMS converters. IEEE International Conference on Microelectronics, 2007. ICM 2007.

Sapiński, B. (2010). "Vibration power generator for a linear MR damper." Smart Materials and Structures 19(10): 105012.

Sari, I., T. Balkan, H. Kulah. (2008). "An electromagnetic micro power generator for wideband environmental vibrations." Sensors and Actuators A: Physical 145–146(0): Page 405-413.

Sari, I., T. Balkan, H. Kulah. (2010)."An Electromagnetic Micro Power Generator for Low-Frequency Environmental Vibrations Based on the Frequency Upconversion Technique." Journal of Microelectromechanical Systems, 19(1): Page 14-27.

Shen, W.A., S. Zhu, Y. Xu. (2012)."An experimental study on self-powered vibration control and monitoring system using electromagnetic TMD and wireless sensors." Sensors and Actuators A: Physical 180(0): Page 166-176.

Shuenn-Yuh, L., H. Cheng-Han, C. Yang. (2012). "Wireless Front-End With Power Management for an Implantable Cardiac Microstimulator." IEEE Transactions on Biomedical Circuits and Systems, 6(1): Page 28-38.

Sidek, O., M. A. Khalid, M.Z. Ishak, M.A. Miskam,(2011).Design and simulation of SOI-MEMS electrostatic vibration energy harvester for micro power generation. International Conference on Electrical, Control and Computer Engineering (INECCE), 2011.

Taithongchai, T. and E. Leelarasmee (2009). Adaptive electromagnetic energy harvesting circuit for wireless sensor application. 6th International Conference on Electrical Engineering/Electronics, Computer, Telecommunications and Information Technology, 2009. ECTI-CON 2009., IEEE.

Tang, X. and L. Zuo (2011). "Enhanced vibration energy harvesting using dual-mass systems." Journal of Sound and Vibration 330(21): Page 5199-5209.

TI (2012). TMS320C5000 DSP/BIOS Application Programming Interface (API) Reference Guide.

TI. (2012). "C5000™ Audio Capacitive Touch BoosterPack." Retrieved 03/09/2012, 2012, from http://www.ti.com/tool/430boost-c55audio1.

TI. (2012). "Energy Harvesting." Retrieved 03/09/2012, 2012, from http://www.ti.com/ww/en/apps/energy-harvesting/index.shtml?DCMP=MSP430_Energy&HQS=Other+OT+430energy.

TI. (2012). "FRAM – Ultra-Low-Power Embedded Memory." Retrieved 03/09/2012, 2012, from http://www.ti.com/ww/en/mcu/fram_ultra_low_power_embedded_memory/index.htm?DCMP=FRAM&HQS=Other+BA+fram-b.

TI. (2012). "MSP430™ Ultra-Low Power 16-Bit Microcontrollers." Retrieved 03/09/2012, 2012, from http://www.ti.com/lsds/ti/microcontroller/16-bit_msp430/overview.page?DCMP=MCU_other&HQS=msp430.

Triet, L., K. Mayaram, T.S Fiez,(2006).Efficient Far-Field Radio Frequency Power Conversion System for Passively Powered Sensor Networks. Custom Integrated Circuits Conference, 2006. CICC '06. IEEE.

Ulaby, F. T. (2005). Electromagnetics for Engineers, Pearson Printice Hall.

Von Büren, T. and G. Tröster (2007). "Design and optimization of a linear vibration-driven electromagnetic micro-power generator." Sensors and Actuators A: Physical 135(2): Page 765-775.

Vo, M. N., & Noras, M. A. (2013). Energy Harvesting from Electromagnetic Field Surrounding A Current Carrying Conductor. Paper presented at the Proc. ESA Annual Meeting on Electrostatics 2013.

Vullers, R. J. M., R. V. Schaijk, H.J. Visser, J. Penders,C.V. Hoof (2010). "Energy Harvesting for Autonomous Wireless Sensor Networks." Solid-State Circuits Magazine, IEEE 2(2): Page 29-38.

Wang, D.A., C.Y. Chiu, H. Pham. (2012). "Electromagnetic energy harvesting from vibrations induced by Kármán vortex street." Mechatronics 22(6): Page 746-756.

Wang, L. and F. G. Yuan (2007). Energy harvesting by magnetostrictive material (MsM) for powering wireless sensors in SHM, 14th International Symposium of SPIE Smart Structures and Materials & NDE and Health Monitoring.

Wang, L. and F. G. Yuan (2008). "Vibration energy harvesting by magnetostrictive material." Smart Materials and Structures 17(4): Page 045009.

Wang, Z. (2007). "Voltage generation from individual BaTiO3 nanowires under periodic tensile mechanical load." Nano letters 7(10): Page 2966.

Wang, D.-A., Chiu, C.-Y., & Pham, H.-T. (2012). Electromagnetic energy harvesting from vibrations induced by Kármán vortex street. Mechatronics, 22(6), 746-756. doi:http://dx.doi.org/10.1016/j.mechatronics.2012.03.005

Williams, C. and R. B. Yates (1996). "Analysis of a micro-electric generator for microsystems." Sensors and Actuators A: Physical 52(1): Page 8-11.

Wischke, M., M. Masur, P. Woias. (2010). "Electromagnetic vibration harvester with piezoelectrically tunable resonance frequency." Journal of Micromechanics and Microengineering 20(3): Page 035025.

Xin, L. and Y. Shuang-Hua (2010). Thermal energy harvesting for WSNs. IEEE International Conference on Systems Man and Cybernetics (SMC), 2010.

Xinping, C., C. Wen-Jen, Y. King , Y. Lee (2007). "Electromagnetic Energy Harvesting Circuit With Feed forward and Feedback DC-DC PWM Boost Converter for Vibration Power Generator System." IEEE Transactions on Power Electronics, 22(2): Page 679-685.

Yang, B., C. Lee, W. Xiang, J. Xie, J.H. He, R.K. Kotlanka1, S.P Low, H. Feng(2009). "Electromagnetic energy harvesting from vibrations of multiple frequencies." Journal of Micromechanics and Microengineering 19(3): Page 035001.

Yong, Z., S. O. R. Moheimani, M.R Yuce (2011)."A 2-DOF MEMS Ultrasonic Energy Harvester." Sensors Journal, IEEE 11(1): Page 155-161.

Yuan, L., X. Xiao,D. Tianpeng , J. Zhong1, X. Zhang, Y. Shen., B. Hu, Y. Huang, J. Zhou, Z.L. Wang, (2012). "Paper-Based Supercapacitors for Self-Powered Nanosystems." Angewandte Chemie 124(20): Page 5018-5022.

Zhongjie, L., Lei, Z., Luhrs, G., Liangjun, L., & Yi-xian, Q. (2013). Electromagnetic Energy-Harvesting Shock Absorbers: Design, Modeling, and Road Tests. Vehicular Technology, IEEE Transactions on, 62(3),Page 1065-1074. doi:10.1109/tvt.2012.2229308

Zhu, D., S. Roberts,J. Tudor, S.Beeby. (2010). "Design and experimental characterization of a tunable vibration-based electromagnetic micro-generator." Sensors and Actuators A: Physical 158(2): Page 284-293.

Zhu, S., W. Shen, Y. Xu. (2012). "Linear electromagnetic devices for vibration damping and energy harvesting: Modeling and testing." Engineering Structures 34(0): Page 198-212.

Zimmermann, T., A. Frey, M. Schreiter, J. Seidel, I. Kuehne (2012). MEMS-based piezoelectric energy harvesting modules for distributed automotive tire sensors. 9th International Multi-Conference on Systems, Signals and Devices (SSD), 2012.

Zorlu, O., E. T. Topal, H.Kulah. (2011). "A Vibration-Based Electromagnetic Energy Harvester Using Mechanical Frequency Up-Conversion Method." Sensors Journal, IEEE 11(2): Page 481-488.

Zurbuchen, A., A. Pfenniger, A. Stahel, C.T. Stoeck, S. Vandenberghe, V.M. Koch, R.Vogel (2012). "Energy Harvesting from the Beating Heart by a Mass Imbalance Oscillation Generator." Annals of Biomedical Engineering: Page 1-11.

**To the best of my knowledge and belief this thesis contains no material previously published by any other person except where due acknowledgement has been made. This thesis contains no material which has been accepted for the award of any other degree or diploma in any university.**

# Appendix A - Impedance Head Calibration

The most critical part of the experiment was to ensure that the transducer that measures the acceleration was correctly calibrated. The selected sensor- B&K 8001 accelerometer was calibrated using a calibrated B&K accelerometer, type 4507B.

The underlying assumption for calibration was that the peak acceleration reading of the calibrator (B&K 4507B accelerometer) ($a_{pk\text{-}PA}$) is equal to the peak acceleration reading of the Impedance head ($a_{pk\text{-}IH}$) to be calibrated. This can be expressed as,

$$a_{pk-PA} = p.a_{pk-IH,} \quad (1)$$

where p is the calibration factor, and

$$a_{pk-PA} = A\omega^2 \quad (2)$$

where A is the amplitude of displacement.

It was observed when measuring peak acceleration and peak amplitude that equation (1) was not satisfied until 7Hz. Hence, equation (2) becomes

$$a_{pk-PA} = \gamma A\omega^2, \quad (3)$$

where, ϒ represents the accelerometer correction factor≈1 (above 7Hz). From the Impedance head, the RMS voltage ($V_{rms}$) was measured and recorded representing the acceleration voltage signal of the accelerometer. This was proportional to the RMS acceleration and can be written as,

$$V_{rms} = G.a_{rms}, \quad (4)$$

where, G represents the proportional factor or Gain or amplification factor in the charge amplifier.

In this experiment, the Gain (G) was set to 1000 V/ms$^{-2}$ for 5 and 6 Hz, 100V/ms$^{-2}$ for 7 to 11 Hz and 10V/ms$^{-2}$ for 11 to 30Hz to achieve appropriate amplifications for more accurate readings.

Equation (4) can also be written as,

$$V_{pk-IH} = G.a_{pk-IH}. \tag{5}$$

Substituting $V_{pk-IH} = \sqrt{2}.V_{rms-IH}$ in (5) gives,

$$a_{pk-IH} = \frac{\sqrt{2}.V_{rms-IH}}{G}. \tag{6}$$

Equations (4) and (6) in equation (3) yields,

$$\gamma A\omega^2 = p.\frac{\sqrt{2}.V_{rms-IH}}{G}. \tag{7}$$

Therefore, the acceleration can be given by,

$$A = \left(\frac{\sqrt{2}.\mathrm{p}}{\gamma\omega^2 G}\right).V_{rms-IH} = \beta.V_{rms-IH}\ , \tag{8}$$

where, $\beta = \left(\frac{\sqrt{2}.\mathrm{p}}{\gamma\omega^2 G}\right)$ was known as the calibration factor. It can be noted that the calibration factor will vary with Gain (G) setting on the charge amplifier and the angular frequency (ω) set on the waveform generator. Therefore the methodology for calibration settings prior to the experiment was: a) to find β for all values from 6 to 31 Hz which was the frequency range of interest with required combinations of Gain settings and correction factor. b) to divide the expected amplitude (say 1mm) by β. This gives the expected RMS voltage for the acceleration amplitude. During the experiment, the expected accelerometer voltage was targeted to achieve the required acceleration amplitude for that frequency.

# Appendix B –MATLAB Codes

Most of the MATLAB codes were written similar to the coding principles of the book-Vibration simulation using MATLAB and ANSYS authored by Michael Hatch, M. R. (Vol. 10), A Chapman & Hall/ CRC Press publication. The MATLAB codes used in this book can be found in MATLAB central at http://www.mathworks.in/MATLABcentral/fileexchange/2186 as accessed on 26/01/2013.

For Laplace and state space MATLAB programs: This appendix contains only those parts of the MATLAB codes for Laplace and state space analysis that are relevant to this thesis and written by the author of this thesis due to copyright reasons. The rest of the codes can be adopted from Hatch, M. R. (2000), Vibration simulation using MATLAB and ANSYS (Vol. 10). Chapman & Hall/CRC.

## MATLAB Code for Laplace transform Frequency responseSDOF1D MDK analysis (Analysis 1 of Chapter 4)

```
M = 0.0015;
D= 0.1;
K=160;
 a = M*s^2+D*s+K;
b = D*s+K;
% Calculate the magnitude and phase of frequency response
z(cnt) = b/a;
loglog(f,zmag,'k-')
 semilogx(f,zphs,'k*-')
```

## MATLAB Code for StatespaceSDOF1D MDK analysis (Analysis 2 of Chapter 4)

```
M = 0.0015;
D= 0.10;
K=160;
aphys = [  0      1
           -K/M    -D/M ];
[xm,lambda] = eig(aphys);
```

## MATLAB Code for Non Linear ODE45 Time domain based SDOF1D MDK analysis (Analysis 3 of Chapter 4)

```
% MATLAB file type: function files - sdof1dmdk_ode.m and sdof1dmdk_dot.m and T.m

% sdof1dmdk_ode.m
function [t,z]=sdof1dmdk_ode
% ODE45 SDOF1D MDKRLC system:
 tspan=0:0.0001:5;
z0=[0;0;0;0];
options = odeset('RelTol',1e-10,'AbsTol',1e-15');
[t,z] = ode45(@sdof1dmdk_dot, tspan, z0,options);

% State variables
x=z(:,1);
xdot=z(:,2);
 xlswrite('ODE45.xlsx',z,'sheet1');
 plot(t,x,t,xdot);xlabel('Time (sec)'); ylabel('Displacement/velocity (in SI units)')

% sdof1dmdk_dot.m

function dzdt = sdof1dmdk_dot(t,z)
global M D K

M = .0015;
D = 0.05;
K = 14.683;
f=15;
A=0.003;
w=2*pi*f;

% Defining the input Ys of the system
y=A*sin(w*t);
ydot=A*w*cos(w*t);

%Variable T(z(1))
dzdt = zeros(size(z));
dzdt(1) = z(2);
dzdt(2) = (1/M)*(D*ydot+K*y-D*z(2)-K*z(1));

end

%  function file name T.m
%  Spatial variation of the magnetic field

function [Tx] = T( x )

% This B Vs X spatial variation was obtained by curvefitting the ANSOFT B vs X
magnetostatic data using the CFTOOL
```

$B_x$= 0.378*sin(9.052*x+1.572) + 0.2302*sin(694.8*x-1.571);

Tx=2*pi*14*.007375*$B_x$;

end

## MATLAB Code for Laplace transform Frequency responseSDOF1D MDK RLC analysis (Analysis 4 of Chapter 4)

```
% assign values for masses, damping, and stiffnesses

M = 0.00149;
D= 0.05;
K=14.68;
R=0.100854;
L=.054;
C=1e-9;
%T=2*pi*16*.007375*Bmax where Bmax =Maximum value of B = .663T
T=0.4916;

% define the frequency responses to be evaluated-m1 not connected to m3
a11 = M*s^2+D*s+K;
a12 = T;
a21 = -C*T*s^2;
a22=L*C*s^2+R*C*s+1;
b1=D*s+K;
b2=-C*T*s^2;

A=[a11 a12;a21 a22];

den(cnt) = det(A);

% Z1=X(s)/Y(s)
z1bf(cnt) = (a22*b1-a12*b2)/den(cnt);
% Z2=I(s)/Y(s)
z2bf(cnt) = (a11*b2-a21*b1)/den(cnt);
```

## MATLAB Code for StatespaceSDOF1D MDK RLC analysis (Analysis 5 of Chapter 4)

```
% Define the values of masses, springs, dampers

M = 0.0015;
D= 0.1;
K=160;
```

```
R=0.3;
L=0.016;
C=1e-9;
T=0.4916;


% Define the system matrix, aphys, in physical coordinates

aphys = [  0     1       0                          0
       -K/M    -D/M     -T/M          0
        0      0        0           1
    -(K*T)/(M*L)  -(D*T)/(M*L)  -((T^2)/(M*L))-(1/(C*L))  -R/L];

% Solve for the eigenvalues of the system matrix

[xm,lambda] = eig(aphys);
```

## MATLAB Code for Non Linear ODE45 Time domain based SDOF1D MDK RLC analysis (Analysis 6 of Chapter 4)

```
% sdof1d.m function file

function dzdt = sdof1d_dot(t,z)
global M D K R L C

M = .0015;
D = 0.05;
K = 160;
R = 100.1;
L = 0.054;
C = 1e-9;
f=15;
A=0.0001;
w=2*pi*f;

%Defining the input Ys of the system
y=A*sin(w*t);
ydot=A*w*cos(w*t);
ydotdot=-A*w*w*sin(w*t);

%Variable T(z(1)-y)
dzdt = zeros(size(z));
dzdt(1) = z(2);
dzdt(2) = (1/M)*(D*ydot+K*y-D*z(2)-K*z(1)-T(z(1)-y)*z(3));
dzdt(3) = z(4);
dzdt(4) = (T(z(1)-y)*D*ydot)/(M*L) + (T(z(1)-y)*K*y)/(M*L)-(T(z(1)-y)*D*z(2))/(M*L)-...
(T(z(1)-y)*K*z(1))/(M*L)-((T(z(1)-y)^2)*z(1)*z(3))/L  -(T(z(1)-y)/L)*(z(1)*ydotdot)  -(R/L)*z(4)-
z(3)/(C*L);
End
```

```
% sdof1d_ode.m function file

function [t,z]=sdof1d_ode(z0)
% ODE45 SDOF1D MDKRLC system:

tspan=[0 1];
% z0=[0;0;0;0];
options = odeset('RelTol',1e-5,'AbsTol',1e-5');
[t,z] = ode45(@sdof1d_dot, tspan, z0,options);

% State variables
x=z(:,1);
xdot=z(:,2);
i=z(:,3);
idot=z(:,4);

xlswrite('ODE45.xlsx',z,'sheet1');
Title('Time response of SDOF1D MDKRLC Simple coil')

subplot(2,2,1),plot(t,x); xlabel('Time (sec)'); ylabel('Displacement (m)')
subplot(2,2,2),plot(t,xdot);xlabel('Time (sec)'); ylabel('Velocity (m)')
subplot(2,2,3),plot(t,i);xlabel('Time (sec)'); ylabel('Current (A)')
subplot(2,2,4),plot(t,idot);xlabel('Time (sec)'); ylabel('Rate of current (A/s)')

%  function file name T.m
%  Spatial variation of the magnetic field

function [Tx] = T( x )

% This B Vs X spatial variation was obtained by curvefitting the ANSOFT B vs X
magnetostatic data using the CFTOOL

Bx= 0.378*sin(9.052*x+1.572) + 0.2302*sin(694.8*x-1.571);

Tx=2*pi*14*.007375*Bx;

end
```

## MATLAB Code for Laplace transforms Frequency response SDOF1D MDK RL analysis (Analysis 7 of Chapter 4)

```
% assign values for masses, damping, and stiffnesses

M = .0015;
D= .05;
K= 160;
R=.3;
L=.016;
 T=0.4916;
```

```
% Define a vector of frequencies to use, radians/sec.

%  define the frequency responses to be evaluated-m1 not connected to m3
a11 = M*s^2+D*s+K;
a12 = T;
a21 = -T*s;
a22=L*s+R;
b1=D*s+K;
b2=-T*s;


A=[a11 a12;a21 a22];

den(cnt) = det(A);

% calculate the magnitude and phase of each frequency response

% Z1=X(s)/Y(s)
z1bf(cnt) = (a22*b1-a12*b2)/den(cnt);

% Z2=I(s)/Y(s)
z2bf(cnt) = (a11*b2-a21*b1)/den(cnt);
```

## MATLAB Code for State space SDOF1D MDK RL analysis (Analysis 8 of Chapter 4)

```
%         define the values of masses, springs, dampers

M = 0.001468;
D= 0.05;
K=15.32;
R=0.178;
L=.00127;

T=0.4916;


% define the system matrix, aphys, in physical coordinates

aphys = [  0      1        0
          -K/M    -D/M     -T/M
            0     T/L      -R/L ];

% solve for the eigenvalues of the system matrix

[xm,lambda] = eig(aphys);
```

## MATLAB Code for Non Linear ODE45 Time domain based SDOF1D MDK RL analysis (Analysis 9 of Chapter 4)

```
% Frequency reading function file readf.m

% Get f from user and store it in excel file f.xls

global f
f=input('Enter frequency');
xlswrite('f.xls',f,'sheet1','A1');

xl=2*pi*f*0.016;
r=0.3;
%impedence
z=sqrt(xl^2+r^2);
xlswrite('f.xls',z,'sheet1','A2');

% sdof1d_dot.m function file

function dzdt = sdof1d_dot(t,z)

global M D K R L f

M = .0015;
D = 0.2;
K = 160;
R = 0.3;
L = 0.016;

A=0.0001;
w=2*pi*f;

%Defining the input Ys of the system
y=A*sin(w*t);
ydot=A*w*cos(w*t);

%Variable T(z(1)-y)
dzdt = zeros(size(z));
dzdt(1) = z(2);
dzdt(2) = (1/M)*(D*ydot+K*y-D*z(2)-K*z(1)-T(z(1)-y)*z(3));
dzdt(3) = (1/L)*(T(z(1)-y)*(z(2)-ydot)-R*z(3));
end

% sdof1d_ode.m function file

function [t,z]=sdof1d_ode
% ODE45 SDOF1D MDKRLC system:

tspan=[0 1];
z0=[0;0;0];
```

```
options = odeset('RelTol',1e-5,'AbsTol',1e-5');
[t,z] = ode45(@sdof1d_dot, tspan, z0,options);

% State variables
x=z(:,1);
xdot=z(:,2);
i=z(:,3);

xlswrite('ODE45.xlsx',i,'sheet1');

subplot(3,1,1),plot(t,x); xlabel('Time (sec)'); ylabel('Displacement (m)')
subplot(3,1,2),plot(t,xdot);xlabel('Time (sec)'); ylabel('Velocity (m)')
subplot(3,1,3),plot(t,i);xlabel('Time (sec)'); ylabel('Current (A)')

%T.m file same as before
```

## MATLAB Code for Laplace transform Frequency response2DOF1D MDK analysis (Analysis 1 of Chapter 5)

```
M1 = .0015;
M2 = .0015;
D1 = .05;
D2 = .05;
D3 = .05;
K1=80;
K2=80;
K3=80;

% define the frequency responses to be evaluated
a11 = M1*s^2+(D1+D3)*s+K1+K3;
a22 = M2*s^2+(D1+D2)*s+K1+K2;
a12=-D1*s-K1;
a21=-D1*s-K1;
b1=D3*s+K3;
b2=D2*s+K2;

A=[a11 a12 ;a21 a22];
B=[b1;b2];

den(cnt) = det(A);

% calculate the magnitude and phase of each frequency response

% Z1=X1(s)/Y(s)
z1bf(cnt) = (a22*b1-a12*b2)/den(cnt);
% Z2=X2(s)/Y(s)
z2bf(cnt) = (a11*b2-a21*b1)/den(cnt);
```

## MATLAB Code for Statespace2DOF1D MDK analysis (Analysis 2 of Chapter 5)

```
% define the values of masses, springs, dampers

M1= 0.0015;
M2= 0.0015;
D1=0.05;
D2=0.05;
D3=0.05;
K1=80;
K2=80;
K3=80;

% define the system matrix, aphys, in physical coordinates

a11=0;a12=1;a13=0;a14=0;
a21=-(K1+K3)/M1;
a22=-(D1+D3)/M1;
a23=K1/M1;
a24=D1/M1;
a31=0;a32=0;a33=0;a34=1;
a41=K1/M2;
a42=D1/M2;
a43=-(K1+K2)/M2;
a44=-(D1+D2)/M2;

aphys = [  a11  a12  a13 a14
                     a21  a22  a23 a24
          a31  a32  a33 a34
          a41  a42  a43 a44];

% solve for the eigenvalues of the system matrix

[xm,lambda] = eig(aphys);
```

## MATLAB Code for Non Linear ODE45 Time domain based 2DOF1D MDK analysis (Analysis 3 of Chapter 5)

```
%readf.m file,T.m file,Vrmsth.m file same as for SDOF1D analyses.

% mdof1d_dot.m function file
```

```
function dzdt = mdof1d_dot(t,z)

global M1 D1 K1 M2 D2 K2 D3 K3 f

M1 = .0015;
M2 = .0015;

D1 = 0.05;
D2 = 0.05;
D3 = 0.05;

K1 = 80;
K2 = 80;
K3 = 20;
A=0.0001;
w=2*pi*f;

%Defining the input Ys of the system
y=A*sin(w*t);
ydot=A*w*cos(w*t);

% %Variable T(z(1))
dzdt = zeros(size(z));

dzdt(1) = z(2);

dzdt(2) = (1/M1)*(D3*ydot+K3*y-(D1+D3)*z(2)-(K1+K3)*z(1)+D1*z(4)+K1*z(3));

dzdt(3) = z(4);

dzdt(4) = (1/M2)*(D2*ydot+K2*y-(D1+D2)*z(4)-(K1+K2)*z(3)+D1*z(2)+K1*z(1));

end

% mdof1d_ode.m function file

function [t,z]=mdof1d_ode
% ODE45 SDOF1D MDKRLC system:

tspan=0:0.001:5;
z0=[0;0;0;0;0];
options = odeset('RelTol',1e-10,'AbsTol',1e-15');
[t,z] = ode45(@mdof1d_dot, tspan, z0,options);

% State variables
x1=z(:,1);
x1dot=z(:,2);
x2=z(:,3);
x2dot=z(:,4);
```

```
% xlswrite('ODE45.xlsx',z,'sheet1');

subplot(2,2,1),plot(t,x1); xlabel('Time (sec)'); ylabel('Displacement 1 (m)')
subplot(2,2,2),plot(t,x1dot);xlabel('Time (sec)'); ylabel('Velocity 1 (m/s)')
subplot(2,2,3),plot(t,x2); xlabel('Time (sec)'); ylabel('Displacement 2 (m)')
subplot(2,2,4),plot(t,x2dot);xlabel('Time (sec)'); ylabel('Velocity 2 (m/s)')
```

## MATLAB Code for Laplace transform Frequency response with identical spring stiffnesses 2DOF1D MDKRL analysis (Analysis 1 of Chapter 5)

## and

## MATLAB Code for Laplace transform Frequency response with different spring stiffnesses 2DOF1D MDKRL analysis (Analysis 2 of Chapter 5)

```
% only the stiffnesses block of code changes between Analysis 1 and Analysis 2
%one of the blocks is made inactive by commenting them.

%"Polynomial Form, for-loop" frequency response plotting
%assigns values for masses, damping, and stiffnesses

M1 = .0015;
M2 = .0015;

% with identical spring

Stiffnesses 2DOF1D MDKRL analysis (Analysis 1 of Chapter 5)

K1 = 80;
K2 = 80;
K3 = 80;

%% with different springs

%stiffnesses2DOF1D MDKRL analysis (Analysis 2 of Chapter 5)

%K1 = 80;
%K2 = 80;
%K3 = 20;


D1=0;
D2=0;
D3=0;

R1 = 0.3;
R2 = 0.3;

L1 = 0.016;
```

```
L2 = 0.016;

T=.4916;


% define the frequency responses to be evaluated-m1 not connected to m3

a11 = M1*s^2+(D1+D3)*s+K1+K3;
a12=-D1*s-K1;
a13=T;
a14=0;
a21=-D1*s-K1;
a22 = M2*s^2+(D1+D2)*s+K1+K2;
a23=0;
a24=T;
a31=-T*s;
a32 = 0;
a33 = L1*s+R1;
a34=0;
a41=0;
a42=-T*s;
a43=0;
a44=L2*s+R2;


b1=D3*s+K3;
b2=D2*s+K2;
b3=-T*s;
b4=-T*s;


A=[a11 a12 a13 a14;a21 a22 a23 a24;a31 a32 a33 a34;a41 a42 a43 a44];
B=[b1;b2;b3;b4];

den(cnt) = det(A);

% inverse of A
invA=inv(A);

Z=A\B;

%calculate the magnitude and phase of each frequency response

% Z1=X1(s)/Y(s)
z1bf(cnt) = Z(1);
% Z2=X2(s)/Y(s)
z2bf(cnt) = Z(2);
% Z3=I1(s)/Y(s)
z3bf(cnt) = Z(3);
% Z4=I2(s)/Y(s)
z4bf(cnt) = Z(4);
```

```
% Z5=V1(s)/Y(s)=[I1(s)/Y(s)]*Z(s)
z5bf(cnt) = z3bf(cnt)*a33 ;
% Z6=V2(s)/Y(s)=[I2(s)/Y(s)]*Z(s)
z6bf(cnt) = z3bf(cnt)*a44 ;
%Z7=V(s)/Y(s)=V1(s)+V(s)/Y(s)
z7bf(cnt) = z5bf(cnt)+ z6bf(cnt) ;
```

## MATLAB Code for State space 2DOF1D MDKRL analysis (Analysis 3 of Chapter 5)

```
% define the values of masses, springs, dampers

M1=.0015;
M2=.0015;
D1=.05;
D2=.05;
D3=.05;
K1=80;
K2=20;
K3=80;
L1=.016;
R1=.3;
L2=.016;
R2=.3;

% T=2*pi*16*.007375*Bmax where Bmax =Maximum value of B = .663T
   T=0.4916;


% define the system matrix, aphys, in physical coordinates

a11=0;a12=1;a13=0;a14=0;a15=0;a16=0;
a21=-(K1+K3)/M1;
a22=-(D1+D3)/M1;
a23=K1/M1;
a24=D1/M1;
a25=-T/M1;
a26=0;
a31=0;a32=0;a33=0;a34=1;a35=0;a36=0;
a41=K1/M2;
a42=D1/M2;
a43=-(K1+K2)/M2;
a44=-(D1+D2)/M2;
a45=0;
a46=-T/M2;
a51=0;
a52=T/L1;
a53=0;
a54=0;
```

```
a55=-R1/L1;
a56=0;
a61=0;
a62=T/L2;
a63=0;
a64=0;
a65=0;
a66=-R2/L2;


aphys = [  a11  a12  a13 a14 a15 a16
             a21  a22  a23 a24 a25 a26
         a31  a32  a33 a34 a35 a36
         a41  a42  a43 a44 a45 a46
         a51  a52  a53 a54 a55 a56
         a61  a62  a63 a64 a65 a66 ];

% solve for the eigenvalues of the system matrix

[xm,lambda] = eig(aphys);
```

## MATLAB Code for Non Linear ODE45 Time domain based 2DOF1D MDKRL analysis (Analysis 4 of Chapter 5)

```
% Frequency reading file

clear all;
clc;

%Get f from user and store it in excel file f.xls

global f
f=input('Enter frequency');
xlswrite('f.xls',f,'sheet1','A1');

xl1=2*pi*f*0.016;
r1=0.3;
z1=sqrt(xl1^2+r1^2);
xlswrite('f.xls',z1,'sheet1','A2');

xl2=2*pi*f*0.016;
r2=0.3;
z2=sqrt(xl2^2+r2^2);
xlswrite('f.xls',z2,'sheet1','A2');

% xl3=2*pi*f*0.016;
% r3=0.3;
% z3=sqrt(xl3^2+r3^2);
% xlswrite('f.xls',z3,'sheet1','A3');
%
```

```
% xl4=2*pi*f*0.016;
% r4=0.3;
% z4=sqrt(xl4^2+r4^2);
% xlswrite('f.xls',z4,'sheet1','A4');


% mdof1d_dot.m file

function dzdt = mdof1d_dot(t,z)

global M1 D1 K1 M2 D2 K2 D3 K3 R1 R2 L1 L2 f

M1 = .0015;
M2 = .0015;

D1 = 0.05;
D2 = 0.05;
D3 = 0.05;
K1 = 80;
K2 = 20;
K3 = 80;

R1 = 0.3;
R2 = 0.3;
L1 = 0.016;
L2 = 0.016;

A=0.0001;
w=2*pi*f;

%T=2*pi*16*.0073125*0.70=0.4916;

T=0.4916;

%Defining the input Ys of the system

y=A*sin(w*t);
ydot=A*w*cos(w*t);


%Variable T(z(1))

dzdt = zeros(size(z));

dzdt(1) = z(2);

dzdt(2) = (1/M1)*(D3*ydot+K3*y-(D1+D3)*z(2)-(K1+K3)*z(1)+D1*z(4)+K1*z(3)-T(z(1)-y)*z

(5));

dzdt(3) = z(4);
```

```
dzdt(4) = (1/M2)*(D2*ydot+K2*y-(D1+D2)*z(4)-(K1+K2)*z(3)+D1*z(2)+K1*z(1)-T(z(3)-y)*z

(5));

dzdt(5) = (1/L1)*(T(z(1)-y)*(z(2)-ydot)-R1*z(5));
dzdt(6) = (1/L2)*(T(z(3)-y)*(z(4)-ydot)-R2*z(6));

end

% mdof1d_ode.m function file

function [t,z]=mdof1d_ode
% ODE45 SDOF1D MDKRLC system:

tspan=0:0.001:15;
z0=[0;0;0;0;0;0];
options = odeset('RelTol',1e-7,'AbsTol',1e-7');
[t,z] = ode45(@mdof1d_dot, tspan, z0,options);

% State variables
x1=z(:,1);
x1dot=z(:,2);
x2=z(:,3);
x2dot=z(:,4);
i1=z(:,5);
i2=z(:,6);

xlswrite('ODE45.xlsx',i1,'sheet1');
xlswrite('ODE45.xlsx',i2,'sheet2');

subplot(2,1,1),plot(t,x1,t,x2); xlabel('Time (sec)'); ylabel('Displacement 1 (m)')
subplot(2,1,2),plot(t,i1,t,i2);xlabel('Time (sec)'); ylabel('Current (A)')
```

## MATLAB Code for Sensitivity tests of SDOF1D and 2DOF1D EMVEH (Chapter 6)

For Sensitivity tests the MALTLAB programs of Laplace transform analyses of SDOF1D EMVEH and 2DOF1D EMVEHs were used with an additional for loop of the varying parameter. An example is provided of how this was done.

```
%Example of modifying Laplace transform analysis to Sensitivity test
%Analysis_2DOF1D_MDKRL_SingleCoil.m file

% "Polynomial Form, for-loop" frequency response plotting
% assign values for masses, damping, and stiffnesses
```

```
D1=0.05;
D2=0.05;
D3=0.05;

K1=80;
K2=20;
K3=80;

L1=.016;
L2=.016;
R1=.3;
R2=.3;
T=0.4916;



for M=0.001:0.001:0.005; % Sensitivity parameter is varied keeping other parameters constant
M1=M;
M2=M;

a11 = M1*s^2+(D1+D3)*s+K1+K3;
a12=-D1*s-K1;
a13=T;
a14=0;
a21=-D1*s-K1;
a22 = M2*s^2+(D1+D2)*s+K1+K2;
a23=0;
a24=T;
a31=-T*s;
a32 = 0;
a33 = L1*s+R1;
a34=0;
a41=0;
a42=-T*s;
a43=0;
a44=L2*s+R2;


b1=D3*s+K3;
b2=D2*s+K2;
b3=-T*s;
b4=-T*s;


A=[a11 a12 a13 a14;a21 a22 a23 a24;a31 a32 a33 a34;a41 a42 a43 a44];
B=[b1;b2;b3;b4];

den(cnt) = det(A);
```

```
 % inverse of A
 invA=inv(A);

Z=A\B;


% calculate the magnitude and phase of each frequency response

% Z1=X1(s)/Y(s)
z1bf(cnt) = Z(1);
% Z2=X2(s)/Y(s)
z2bf(cnt) = Z(2);
% Z3=I1(s)/Y(s)
z3bf(cnt) = Z(3);
% Z4=I2(s)/Y(s)
z4bf(cnt) = Z(4);
% Z4=V1(s)/Y(s)=[I1(s)/Y(s)]*Z(s)
z5bf(cnt) = z3bf(cnt)*a33 ;
% Z4=V2(s)/Y(s)=[I2(s)/Y(s)]*Z(s)
z6bf(cnt) = z4bf(cnt)*a44 ;
```

## MATLAB Code for Laplace transform Frequency response4DOF1D MDK RL analysis (Analysis 7 of Chapter 8)

```
% "Polynomial Form, for-loop" frequency response plotting
% assign values for masses, damping, and stiffnesses

M1 = .0015;
M2 = .0015;
M3 = .0015;
M4 = .0015;


K1 = 20;
K2 = 40;
K3 = 60;
K4 = 80;
K5 = 110;

D1=.01;
D2=.01;
D3=.01;
D4=.01;
D5=.01;

R1 = 0.3;
R2 = 0.3;
```

```
R3 = 0.3;
R4 = 0.3;

L1 = 0.016;
L2 = 0.016;
L3 = 0.016;
L4 = 0.016;


T=.4916;

% define the frequency responses to be evaluated-m1 not connected to m3

a11=M1*s^2+(D5+D1)*s+(K5+K1);
a12=-D1*s-K1;
a13=0;
a14=0;
a15=T;
a16=0;
a17=0;
a18=0;

a21=-D1*s-K1;
a22=M2*s^2+(D1+D2)*s+(K1+K2);
a23=-D2*s-K2;
a24=0;
a25=0;
a26=T;
a27=0;
a28=0;

a31=0;
a32=-D2*s-K2;
a33=M3*s^2+(D2+D3)*s+(K2+K3);
a34=-D3*s-K3;
a35=0;
a36=0;
a37=T;
a38=0;

a41=0;
a42=0;
a43=-D3*s-K3;
a44=M4*s^2+(D5+D1)*s+(K5+K1);
a45=0;
a46=0;
a47=0;
a48=T;

a51=-T*s;
a52=0;
```

```
a53=0;
a54=0;
a55=L1*s+R1;
a56=0;
a57=0;
a58=0;

a61=0;
a62=-T*s;
a63=0;
a64=0;
a65=0;
a66=L2*s+R2;
a67=0;
a68=0;

a71=0;
a72=0;
a73=-T*s;

a74=0;
a75=0;
a76=0;
a77=L3*s+R3;
a78=0;


a81=0;
a82=0;
a83=0;
a84=-T*s;
a85=0;
a86=0;
a87=0;
a88=L4*s+R4;

b1=D5*s+K5;
b2=0;
b3=0;
b4=D4*s+K4;
b5=-T*s;
b6=-T*s;
b7=-T*s;
b8=-T*s;



A=[a11 a12     a13     a14     a15     a16     a17     a18;
```

```
a21     a22     a23     a24     a25     a26     a27     a28;

a31     a32     a33     a34     a35     a36     a37     a38;

a41     a42     a43     a44     a45     a46     a47     a48;

a51     a52     a53     a54     a55     a56     a57     a58;

a61     a62     a63     a64     a65     a66     a67     a68;

a71     a72     a73     a74     a75     a76     a77     a78;

a81     a82     a83     a84     a85     a86     a87     a88];



B=[b1;b2;b3;b4;b5;b6;b7;b8];

den(cnt) = det(A);

% inverse of A
invA=inv(A);

Z=A\B;

% calculate the magnitude and phase of each frequency response

%Calculate displacements
% Z1=X1(s)/Y(s)
 z1bf(cnt) = Z(1);
% Z2=X2(s)/Y(s)
z2bf(cnt) = Z(2);
% Z3=X3(s)/Y(s)
z3bf(cnt) = Z(3);
% Z4=X2(s)/Y(s)
z4bf(cnt) = Z(4);

%Calculate currents
% Z5=I1(s)/Y(s)
z5bf(cnt) = Z(5);
% Z6=I2(s)/Y(s)
z6bf(cnt) = Z(6);
% Z7=I3(s)/Y(s)
z7bf(cnt) = Z(7);
% Z8=I4(s)/Y(s)
z8bf(cnt) = Z(8);


end                 %       end of for-loop
```

## MATLAB Code for Statespace4DOF1D MDK RL analysis (Analysis 8 of Chapter 8)

```
%       define the values of masses, springs, dampers

M1=.0015;
M2=.0015;
M3=.0015;
M4=.0015;

D1=.01;
D2=.01;
D3=.01;
D4=.01;
D5=.01;

K1=80;
K2=80;
K3=80;
K4=80;
K5=80;

L1=.016;
L2=.016;
L3=.016;
L4=.016;
L5=.016;

R1=.3;
R2=.3;
R3=.3;
R4=.3;
R5=.3;

%T=2*pi*16*.007375*Bmax where Bmax =Maximum value of B = .663T
T=0.4916;


%       define the system matrix, aphys, in physical coordinates

a1_1= 0;
a1_2=1;
a1_3= 0;
a1_4= 0;
a1_5= 0;
a1_6= 0;
a1_7= 0;
a1_8= 0;
```

```
a1_9=  0;
a1_10=  0;
a1_11=  0;
a1_12=  0;

a2_1=-(K5+K1)/M1;
a2_2=-(D5+D1)/M1;
a2_3= K1/M1;
a2_4= D1/M1;
a2_5=  0;
a2_6=  0;
a2_7=  0;
a2_8= 0;
a2_9= -T/M1;
a2_10= 0;
a2_11=  0;
a2_12= 0;

a3_1= 0;
a3_2= 0;
a3_3= 0;
a3_4=1;
a3_5= 0;
a3_6= 0;
a3_7= 0;
a3_8= 0;
a3_9= 0;
a3_10= 0;
a3_11= 0;
a3_12= 0;

a4_1= K1/M2;
a4_2=D1/M2;
a4_3=-(K1+K2)/M2;
a4_4=-(D1+D2)/M2;
a4_5= K2/M2;
a4_6=D2/M2;
a4_7= 0;
a4_8=0;
a4_9= 0;
a4_10=-T/M2;
a4_11= 0;
a4_12= 0;

a5_1=0;
a5_2=0;
a5_3=0;
a5_4=0;
a5_5=0;
a5_6=1;
a5_7=0;
```

```
a5_8=0;
a5_9=0;
a5_10=0;
a5_11=0;
a5_12=0;

a6_1=0;
a6_2=0;
a6_3=K2/M3;
a6_4=D2/M3;
a6_5=-(K2+K3)/M3;
a6_6=-(D2+D3)/M3;
a6_7= K3/M3;
a6_8=D3/M3;
a6_9=0;
a6_10= 0;
a6_11=-T/M3;
a6_12=0;

a7_1=0;
a7_2=0;
a7_3=0;
a7_4=0;
a7_5=0;
a7_6=0;
a7_7=0;
a7_8=1;
a7_9=0;
a7_10=0;
a7_11=0;
a7_12=0;

a8_1=0;
a8_2=0;
a8_3=0;
a8_4=0;
a8_5=K3/M4;
a8_6=D3/M4;
a8_7=-(K3+K4)/M4;
a8_8=-(D3+D4)/M4;
a8_9= 0;
a8_10=0;
a8_11=0;
a8_12=-T/M4;

a9_1= 0;
a9_2=T/L1;
a9_3= 0;
a9_4= 0;
a9_5=0;
a9_6=0;
```

```
a9_7=0;
a9_8=0;
a9_9=-R1/L1;
a9_10= 0;
a9_11=0;
a9_12=0;

a10_1=0;
a10_2=0;
a10_3=0;
a10_4=T/L2;
a10_5=0;
a10_6=0;
a10_7=0;
a10_8=0;
a10_9=0;
a10_10=-R2/L2;
a10_11=0;
a10_12=0;

a11_1=0;
a11_2=0;
a11_3=0;
a11_4=0;
a11_5=0;
a11_6= T/L3;
a11_7=0;
a11_8=0;
a11_9=0;
a11_10=0;
a11_11=-R3/L3;
a11_12=0;

a12_1=0;
a12_2=0;
a12_3=0;
a12_4=0;
a12_5=0;
a12_6=0;
a12_7=0;
a12_8= T/L4;
a12_9=0;
a12_10=0;
a12_11=0;
a12_12= -R4/L4;



aphys = [a1_1     a1_2     a1_3     a1_4     a1_5     a1_6     a1_7     a1_8     a1_9
```

```
a1_10   a1_11   a1_12
a2_1    a2_2    a2_3    a2_4    a2_5    a2_6    a2_7    a2_8    a2_9    a2_10   a2_11

a2_12
a3_1    a3_2    a3_3    a3_4    a3_5    a3_6    a3_7    a3_8    a3_9    a3_10   a3_11

a3_12
a4_1    a4_2    a4_3    a4_4    a4_5    a4_6    a4_7    a4_8    a4_9    a4_10   a4_11

a4_12
a5_1    a5_2    a5_3    a5_4    a5_5    a5_6    a5_7    a5_8    a5_9    a5_10   a5_11

a5_12
a6_1    a6_2    a6_3    a6_4    a6_5    a6_6    a6_7    a6_8    a6_9    a6_10   a6_11

a6_12
a7_1    a7_2    a7_3    a7_4    a7_5    a7_6    a7_7    a7_8    a7_9    a7_10   a7_11

a7_12
a8_1    a8_2    a8_3    a8_4    a8_5    a8_6    a8_7    a8_8    a8_9    a8_10   a8_11

a8_12
a9_1    a9_2    a9_3    a9_4    a9_5    a9_6    a9_7    a9_8    a9_9    a9_10   a9_11

a9_12
a10_1   a10_2   a10_3   a10_4   a10_5   a10_6   a10_7   a10_8   a10_9   a10_10  a10_11

a10_12
a11_1   a11_2   a11_3   a11_4   a11_5   a11_6   a11_7   a11_8   a11_9   a11_10  a11_11

a11_12
a12_1   a12_2   a12_3   a12_4   a12_5   a12_6   a12_7   a12_8   a12_9   a12_10  a12_11

a12_12
];

%       solve for the eigenvalues of the system matrix

[xm,lambda] = eig(aphys);
```

## MATLAB Code for Non Linear ODE45 Time domain based 4DOF1D MDK RL analysis (Analysis 9 of Chapter 8)

```
%Get f from user and store it in excel file f.xls

global f
f=input('Enter frequency');
xlswrite('f.xls',f,'sheet1','A1');

xl1=2*pi*f*0.016;
r1=0.3;
```

```
z1=sqrt(xl1^2+r1^2);
xlswrite('f.xls',z1,'sheet1','A2');

xl2=2*pi*f*0.016;
r2=0.3;
z2=sqrt(xl2^2+r2^2);
xlswrite('f.xls',z2,'sheet1','A2');

xl3=2*pi*f*0.016;
r3=0.3;
z3=sqrt(xl3^2+r3^2);
xlswrite('f.xls',z3,'sheet1','A3');

xl4=2*pi*f*0.016;
r4=0.3;
z4=sqrt(xl4^2+r4^2);
xlswrite('f.xls',z4,'sheet1','A4');


% function file fivedof1d_dot.m

function dzdt = fivedof1d_dot(t,z)

global M1 M2 M3 M4 D1 D2 D3 D4 D5 K1 K2 K3 K4 K5 R1 R2 R3 R4 L1 L2 L3 L4 f

M1 = .0015;
M2 = .0015;
M3 = .0015;
M4 = .0015;

D1 = 0.01;
D2 = 0.01;
D3 = 0.01;
D4 = 0.01;
D5 = 0.01;

K1 = 20;
K2 = 40;
K3 = 60;
K4 = 80;
K5 = 110;

R1 = 0.3;
R2 = 0.3;
R3 = 0.3;
R4 = 0.3;

L1 = 0.016;
L2 = 0.016;
L3 = 0.016;
L4 = 0.016;
```

```
A=0.0001;
w=2*pi*f;
% t=2*pi*16*.0073125*0.70;

%Defining the input ys of the system
y=A*sin(w*t);
ydot=A*w*cos(w*t);


% %Variable t(z(1))
dzdt = zeros(size(z));

dzdt(1)=z(2);

dzdt(2)=(1/M1)*(D5*ydot          +K5*y-(D5+D1)*z(2)-(K5+K1)*z(1)+D1*z(4)+K1*z(3)-T(z(1)-
y)*z(9));

dzdt(3)=z(4);

dzdt(4)=(1/M2)*(-(D1+D2  )*z(4)-(K1+K2  )*z(3)+D2*z(6)+K2*z(5)+D1*z(2)+  K1*z(3)-T(z(3)-
y)*z(10));

dzdt(5)=z(6);

dzdt(6)=(1/M3)*(-(D2+D3 )*z(6)-(K2+K3)*z(5) + D3*z(8)+K3*z(7) + D2*z(4)+ K2*z(5)-T(z(5)-
y)*z(11));

dzdt(7)=z(8);

dzdt(8)=(1/M4)*(D4*ydot  +  K4*y-(D3+D4  )*z(8)-(K3+K4  )*z(7)+  D3*z(6)+  K3*z(5)-T(z(7)-
y)*z(12));

dzdt(9)=(1/L1)*(T(z(1)-y)*z(2)-T(z(1)-y)*ydot -R1*z(9));

dzdt(10)=(1/L2)*(T(z(3)-y)*z(4)-T(z(3)-y)*ydot -R2*z(10));

dzdt(11)=(1/L3)*(T(z(5)-y)*z(6)-T(z(5)-y)*ydot -R3*z(11));

dzdt(12)=(1/L4)*(T(z(7)-y)*z(4)-T(z(7)-y)*ydot -R4*z(12));

end

function [t,z]=fivedof1d_ode
% ODE45 SDOF1D MDKRLC system:

tspan=0:0.001:15;
z0=[0;0;0;0;0;0;0;0;0;0;0;0];
options = odeset('RelTol',1e-7,'AbsTol',1e-7');
[t,z] = ode45(@fivedof1d_dot, tspan, z0,options);
```

```
% State variables
x1=z(:,1);
x1dot=z(:,2);
x2=z(:,3);
x2dot=z(:,4);
x3=z(:,5);
x3dot=z(:,6);
x4=z(:,7);
x4dot=z(:,8);

i1=z(:,9);
i2=z(:,10);
i3=z(:,11);
i4=z(:,12);


xlswrite('ODE45.xlsx',i1,'sheet1');
xlswrite('ODE45.xlsx',i2,'sheet2');
xlswrite('ODE45.xlsx',i3,'sheet3');
xlswrite('ODE45.xlsx',i4,'sheet4');

subplot(2,1,1),plot(t,x1,t,x2,t,x3,t,x4); xlabel('Time (sec)'); ylabel('Displacement (m)')
subplot(2,1,2),plot(t,i1,t,i2,t,i3,t,i4);xlabel('Time (sec)'); ylabel('Current (A)')

% Read frequency file

clear all;
clc;

%Get f from user and store it in excel file f.xls

global f
f=input('Enter frequency');
xlswrite('f.xls',f,'sheet1','A1');

xl1=2*pi*f*0.016;
r1=0.3;
z1=sqrt(xl1^2+r1^2);
xlswrite('f.xls',z1,'sheet1','A2');

xl2=2*pi*f*0.016;
r2=0.3;
z2=sqrt(xl2^2+r2^2);
xlswrite('f.xls',z2,'sheet1','A2');

xl3=2*pi*f*0.016;
r3=0.3;
z3=sqrt(xl3^2+r3^2);
xlswrite('f.xls',z3,'sheet1','A3');

xl4=2*pi*f*0.016;
```

```
r4=0.3;
z4=sqrt(xl4^2+r4^2);
xlswrite('f.xls',z4,'sheet1','A4');


% Vrmsth5dof.m file

i1= xlsread('ODE45.xlsx','sheet1','A200:A2000');
i1rms=std(i1)*1000;
Vrms1=i1rms*z1;

i2= xlsread('ODE45.xlsx','sheet2','A200:A2000');
i2rms=std(i2)*1000;
Vrms2=i2rms*z2;

i3= xlsread('ODE45.xlsx','sheet3','A200:A2000');
i3rms=std(i3)*1000;
Vrms3=i3rms*z3;

i4= xlsread('ODE45.xlsx','sheet4','A200:A2000');
i4rms=std(i4)*1000;
Vrms4=i4rms*z4;

Prms1= Vrms1*i1rms;
Prms2= Vrms2*i2rms;
Prms3= Vrms3*i3rms;
Prms4= Vrms4*i4rms;

i1rms;
i2rms;
i3rms;
i4rms;

Vrms1;
Vrms2;
Vrms3;
Vrms4;

Prms1;
Prms2;
Prms3;
Prms4;
```

The values of the design parameters for all the codes of *M, D, K, R, L* and *T* are as described in the Chapters.

# Appendix C –Prototypes and Experiments

## Experiment 1 – SDOF1D Undamped EMVEH (As Discussed in Chapter #3) prototypes

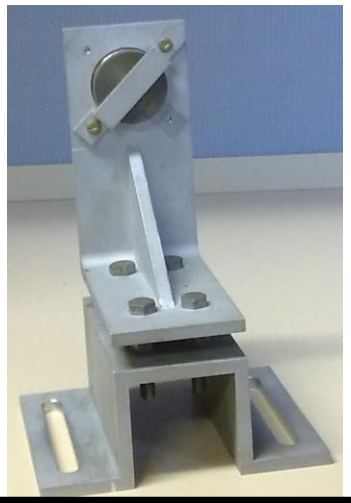

C.1 Magnet and Iron core Assembly.

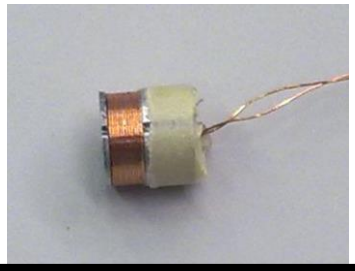

C.2 Coil.

C.3 Magnet and Iron core.

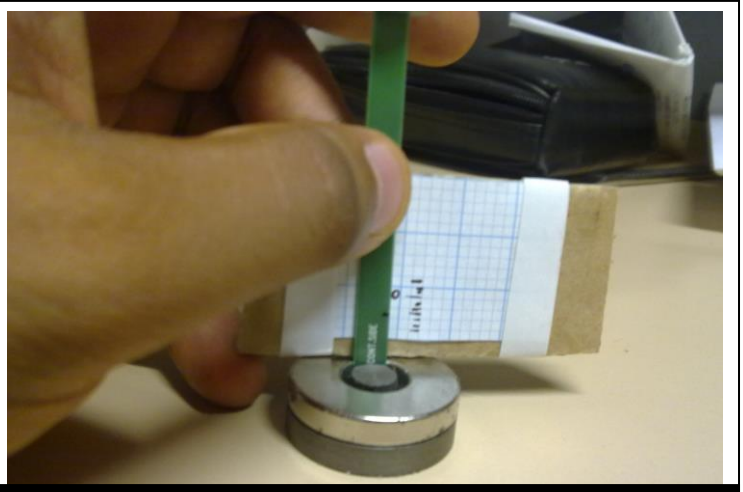

C.3 Approximate measurement of Magnetic field strength at the direction of coil motion using Gauss meter.

## Experiment 2 – SDOF1D Undamped EMVEH (As Discussed in Chapter #3) Experiment

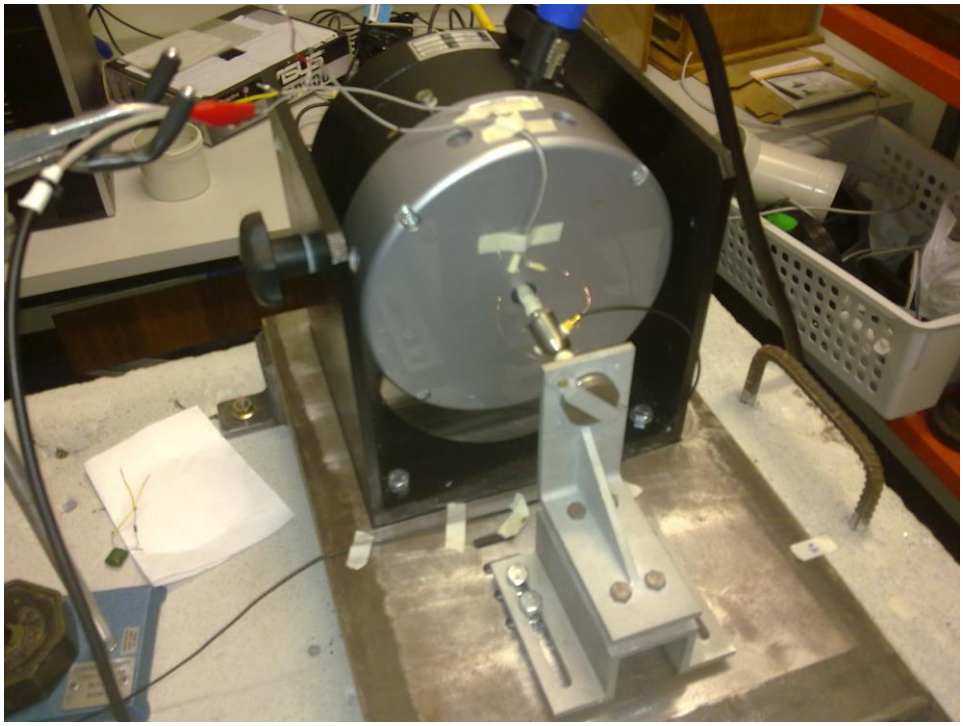

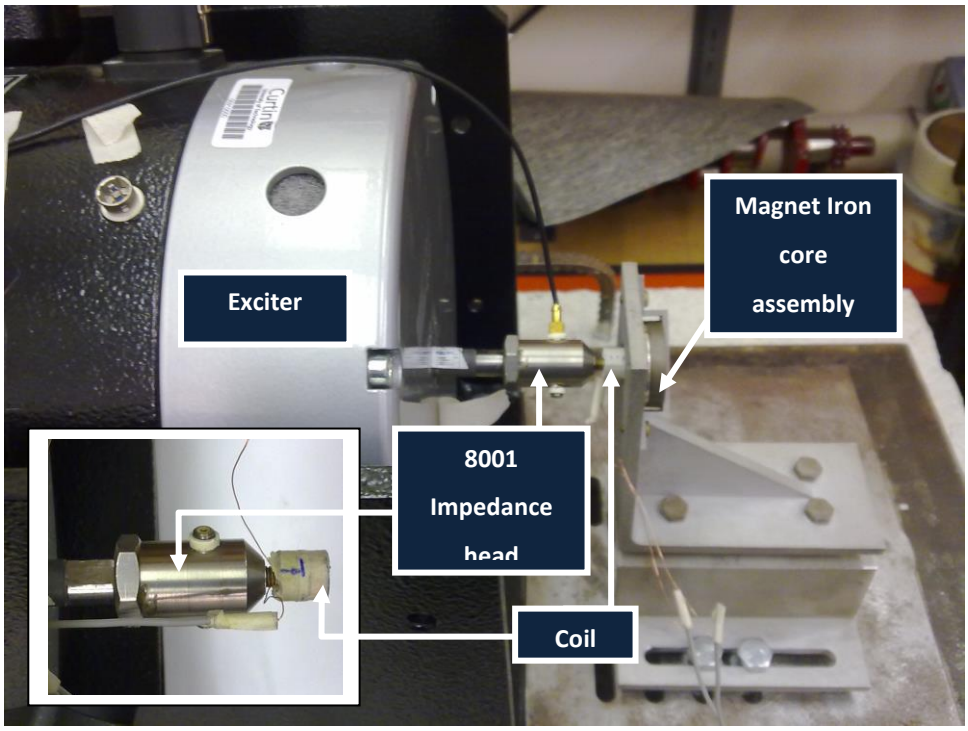


C.4 The coil is mounted to B&K 8001 impedance head and then mounted to the vibration exciter. The coil moves in and out of the Magnet-iron core assembly in the gap between Iron core and magnet.

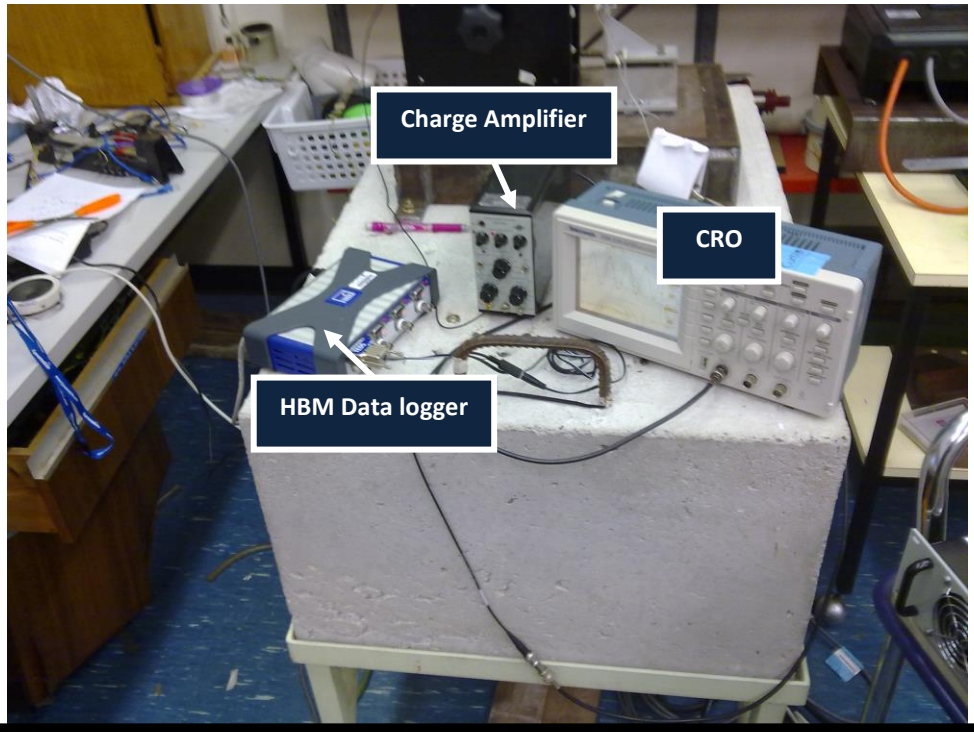


C.5 The HBM Data logger is connected to the PC for visualising the Voltage generated by the prototype. The CRO is connected to the 8001 impedance head through the B&K Charge amplifier to measure the acceleration signal .


C.6 The Waveform Generator is connected to the Exciter through a B&K Power amplifier. The Frequency and the amplitude is set using the waveform generator.

## Experiment 2 – SDOF1D and 2DOF1D EMVEH (As Discussed in Chapter # 6) prototypes

C.7 The common parts for both SDOF1D EMVEH and 2DOF1D EMVEH prototypes .For 2DOF1D EMVEH ,2 ring magnets separated by Nylon spacer were used. There were 2 iron cores for 2DOF1D EMVEH.

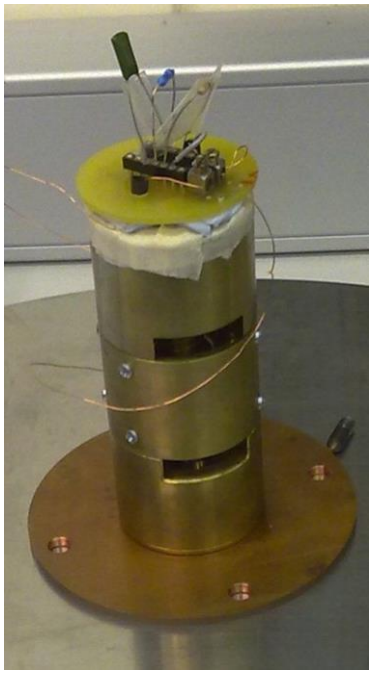

C.8 The initial mounting design was to have the circuit on top of the prototype .But it was found to be a bad design since even the circuit started to vibrate.

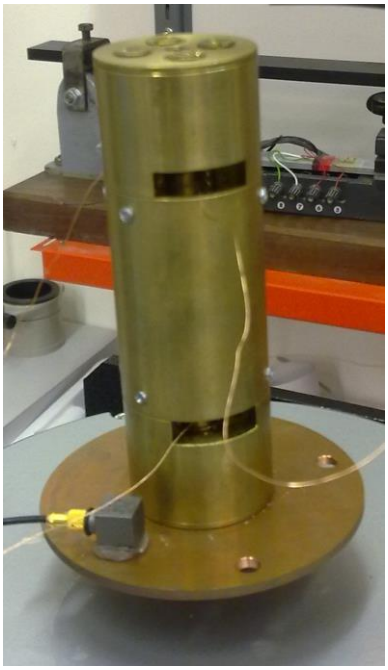

C.9 Hence the circuit was isolated from the vibrating prototype and only the prototype was mounted on the exciter.

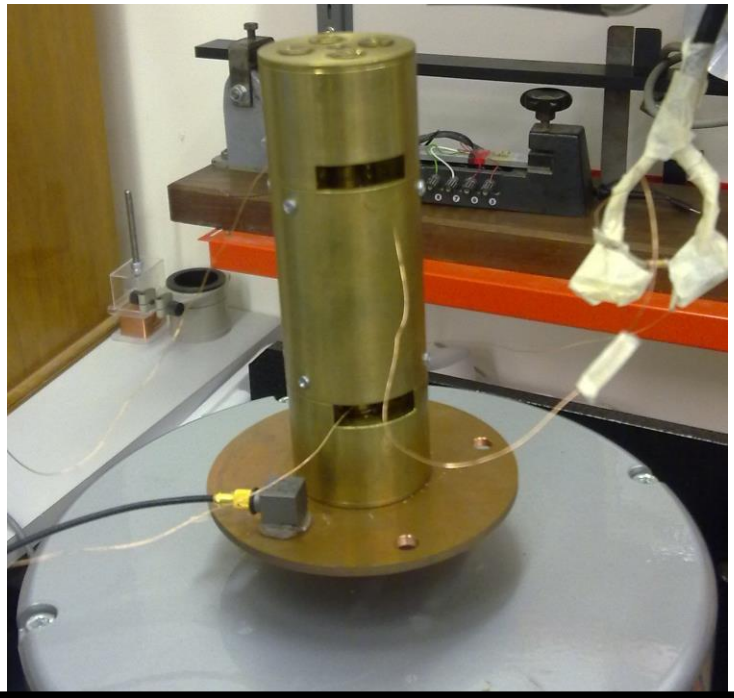

C.10 The B&K accelerometer was used for measuring acceleration. The Pulse accelerometer was connected to B&K Pulse analyser. The output of the coil voltages were connected to the HBM Data logger.

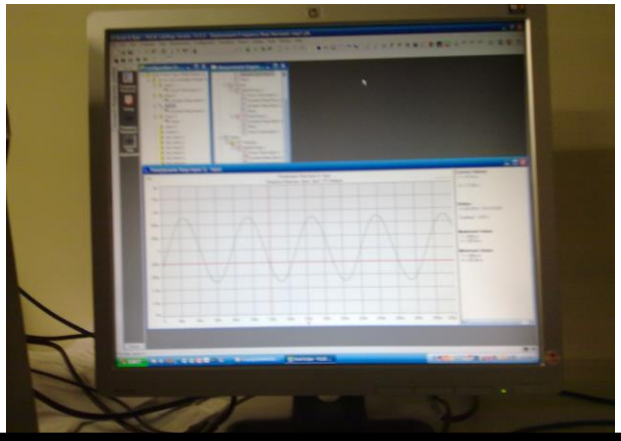

C.11 Measuring B&K pulse acceleration using Pulse analyser.

The remaining setup was similar to experiment 1 where the exciter was connected to the Agilent waveform generator through the power amplifier, the output voltages were connected to the HBM data analyser.